Studies of the low-energy quasiparticle excitations in high-temperature superconducting cuprates with scanning tunneling spectroscopy and magnetization measurements

Thesis by

Andrew David Beyer

In Partial Fulfillment of the Requirements

for the Degree of

Doctor of Philosophy

California Institute of Technology

Pasadena, California

June 5th, 2009

(Submitted June 10, 2009)

Dedicated to Meredith, my family, and my friends.

Acknowledgements

I would like to acknowledge many people for helping me in one way or another during my time at Caltech. The work in this thesis would not have been possible without the support of a great many people. Additionally, I would like to thank the Intel Corporation for supporting me through an Intel Foundation Fellowship and the Gordon and Betty Moore Foundation and the Kavli Foundation for the financial support in the construction of the cryogenic STM/SEM.

Thank you, Meredith, my sweet and lovely wife. You have always been there to support me and pushed me to do fun things outside of lab. I am sorry you are so far away from your family, and I appreciate the sacrifice you made in coming to Caltech. You make me happy, I love you dearly, and I look forward to many more years as your husband.

Thank you to Nai-Chang Yeh, my graduate advisor, for your support and dedication to research in the lab. Research on high-temperature cuprate superconductors requires someone with a wide breadth of knowledge to understand the complex behavior of the cuprate superconductors, and you are the ideal person to lead such research. You taught me how to endure through the difficulties and frustrations associated with publishing papers in such a contentious field of research, how to think for myself, how to communicate effectively, and how to be a dedicated scientist. In short, I learned how to be a proper scientist from you, and I am thankful for the lessons that I learned.

Ben, I love you, and you are a great brother. Thank you for the encouragement and for teaching me to be persistent in finishing up my degree. Thank you, Mom and Dad, for raising me and providing me with love and support. Thank you, Grandpa, for teaching me that God is subtle, and that he will always be there for me.

Thank you to Memaw and Papoo (Cleo and Juanita Schneider), Phyllis Cunningham, Jonathan Cunningham, Terry and Kathy Cunningham, and Jessica, Matt, and Brenna Shelton for letting me take Meredith far from Texas and for your love and support.

Thank you to Eric and Michelle Schulze and for moral support, for being great friends, and for your service to the United States in the military. Eric, you have been there for me through thick and thin. I really appreciate your interest in my research and your pep-talks along the way toward getting my degree. Thank you to Blake “Stormin’ Moorman” Dumas for encouraging me during graduate school and for being a great friend since we were kids. I am grateful for your interest in my research and your great sense of humor. Thank you to Geoffrey Baldwin for all of your support, for late-night frozen yogurt runs, and for watching Texas win the National Championship in Pasadena with Meredith and me. Thank you also for telling the story about Steven Weinberg and me; your check is in the mail.

Thank you, Cameron Hughes, for being my colleague and a great friend in the lab. Because we came to Caltech the same year, we were lucky enough to endure the trials of graduate life together. I wish you the best of luck on your research, your next job, and your future culinary exploits.

I would also like to thank Marcus Teague for being a great friend and colleague. It would not have been possible to get such great results without your help working alongside me on the STM measurements in this thesis. You also have a wonderful sense of dark humor and have provided me with many opportunities to go beer-drinking and discuss life.

Thank you, Mike Grinolds, for your help in the STM measurements presented here. You really impressed me with your enthusiasm and intelligence, and I am sure you will be a great scientist.

I would also like to thank all the previous graduate students and post-docs who shared their

knowledge and encouraged me along the way, including Ching-Tzu Chen, Ted Corcovilos, Vivien Zapf, and Slobodan Mitrovic. You taught me many laboratory skills and provided extremely helpful guidance.

Nils Asplund, you provided me with a lot of encouragement, you gave me common sense advice for getting experiments to work, and did a great job of machining the parts for the STM, the STM/SEM, and many of the parts for the bulk measurement probes used in this thesis. Your skills were extremely vital to the work done here. I also enjoyed going hunting with you this year and appreciate your inviting me to go.

I would like to thank all the undergraduates who did SURF projects with me, including Guglielmo Lockhart, Timothy Ward, Victor Alvarez, Michael Grinolds, and Huan Yang. In addition to being extremely helpful in lab, you all reminded me how to be enthusiastic about physics and research.

Thank you to the Taiwanese students, including Juven Wang, Shu-Ping Lee, Benli Yu, and Jason Horng, for your vital contribution to the simulations in this thesis. A lot was done in one month with your enthusiasm and dedication, and I appreciate your hard work.

Among the faculty and staff at Caltech, I would like to thank Nai-Chang, Jim Eisenstein, Eric Black, Axel Scherer, Michael Roukes, Guy Derose, and Jamil Tahir-Kheli for your help in discussing my research. I would also like to thank my thesis defense committee of Jonas Zmuidzinas, Alexei Kitaev, Jim Eisenstein, and Nai-Chang. Your time and effort are greatly appreciated. I would especially like to thank Nai-Chang, Jim Eisenstein, Ken Libbrecht, Eric Black, and Vivien Zapf for the letters of recommendation that you wrote for me.

Thank you, Nathan Franklin for being my mentor through the Intel Foundation Fellowship program and giving me a lot of advice on applying for jobs. Thank you to Nick Samiotes and Chris Platt for providing me with great information for the STM/SEM and helping me to purchase the right equipment. Thank you to Mary Sikora for your immense help to me in all things KNI. Thank you to Loly Ekmekjian for your friendly and excellent help in taking care of purchases and paperwork.

Thank you to Terry Scott for teaching me how to run a milling machine, a lathe, and many other machines in the machine shop. You are a great machinist and I appreciate your constant willingness to help. Thank you to Richard Paniagua for helping me organize the construction of parts in the Physics Department Machine Shop.

Thank you to the many friends I made during my time at Caltech, including Shahin Rahman, Jack and Lindsey Sayers, Ian Krajbich, John Keith, James and Keiko Maloney, Brad Cenko, Christie Canaria, Rob Ward, Marie-Helene Rousseau, Emily Barrett, Dylan and Madeleine Nieman, Dan Busby, Brooke Glass-O'Shea, Dan Pragel, Tommy Miller, Nicola Wilkins-Miller, Kirk McKenzie, Ella Cameron, Cécile Vangeleyn, Glenn Devine, and Jan, Katerina and Símon Veverka. You all made graduate school even more enjoyable. I loved playing softball with the Sunday Nighters, playing touch football, bowling at All-Star Lanes, the mini-Ryder Cup, the Triballathons, the BWMA events, running marathons, and watching B-movies with you all.

In addition, thank you to my floorball friends including, Swaminathan Krishnan, Matt Kelley, Kana Takematsu, Jon Erickson, Ivan Grudinin, Luigi Perotti, Monty Nandra, Juha Varjonen, Vince Faso, Steve Wilburn, Jan-Erik Paris, Gerald Lelais, Swaroop Mishra, Chris Hoag, Jeff Rysinski, Sanjay Vinayagamoorthy, Raffael Dickreuter, Pavel Kohout, Marcus and Jonas Davidsson, Jonas Fornander, Lauris Laurins, Edgar Penaloza, Espen Olsen, Aki Tanaka, Calle Carlson, Eric Rosen, Mats Lindroth, Peter Kim, Richard Lindroth, Sergey Bystrov, Victor Chou, Erin Harnden, and Daniel Kolodrubetz. Floorball would not have been as fun without you all. Special thanks to Erik Larsson: you are a great friend and I enjoyed growing floorball in Southern California with you.

Thank you to Pastor Barry Foerster and Pastor Roger Sonnenberg for helping me along the way as a Christian. Finally, I would like to thank God for blessing me with many great friends and experiences while at Caltech.

Abstract

This thesis details the investigation of the unconventional low-energy quasiparticle excitations in both hole-and electron-type cuprate superconductors through experimental studies and theoretical modeling. The experimental studies include spatially resolved scanning tunneling spectroscopy (STS) experiments and bulk magnetization measurements, and the theoretical modeling involves developing a phenomenology that incorporates coexisting competing orders and superconductivity in the ground state of the cuprates.

Magnetic field and temperature dependent evolution of the spatially resolved quasiparticle excitation spectra in the electron-type cuprate $\mathrm{La_{0.1}Sr_{0.9}CuO_2}$ (La-112), the simplest structured cuprate superconductor with $\mathrm{T}_C = 43$ K, are investigated experimentally for the first time. For temperature (T) less than the superconducting transition temperature (T_C), and in zero field, the quasiparticle spectra of La-112 exhibits gapped behavior with two coherence peaks and no satellite features. For magnetic field measurements at $\mathrm{T} \ll \mathrm{T}_C$, vortices are observed in La-112, which is the first direct observation of vortices among electron-type cuprate superconductors. Moreover, pseudogap-like spectra are revealed inside the core of vortices, where superconductivity is suppressed. The intra-vortex pseudogap-like spectra are characterized by an energy gap of $\mathrm{V}_{PG} = (8.5 \pm 0.6)$meV, while the inter-vortex quasiparticle spectra show larger peak-to-peak gap values characterized by $\Delta_{pk-pk}(\mathrm{H}) \geq V_{PG}$, and $\Delta_{pk-pk}(0)$=(12.2$\pm$0.8)meV $\geq \Delta_{pk-pk}(H > 0)$. The quasiparticle spectra are found to be gapped at all locations up to the highest magnetic field examined (H = 6T) and reveal an apparent low-energy cutoff at the V_{PG} energy scale. This finding is in stark contrast to the vortex-state quasiparticle spectra in conventional superconductors, where the intra-vortex spectra near vortex cores exhibit a sharp zero-bias conductance peak due to the complete suppression of superconductivity and the presence of continuous bound quasiparticle states. The lack of a zero-bias peak and the observation of pseudogap-like spectra in the intra-vortex quasiparticle spectra of La-112 suggest that superconductivity alone cannot describe the STS results.

Similar studies of the magnetic field and temperature dependent evolution of the spatially resolved quasiparticle excitation spectra in the hole-type cuprate $\mathrm{YBa_2Cu_3O_{7-\delta}}$ (Y-123) have also been carried out. The quasiparticle spectra for $\mathrm{T} \ll \mathrm{T}_C(\sim 93\ \mathrm{K})$ show satellite features at an energy higher than the superconducting gap, and the superconducting gap is found to be associated with a set of coherence peaks for $\mathrm{H} = 0$. The coherence peaks are homogeneous, with a energy gap given by $\Delta_{SC} = (20 \pm 1)$meV, and may be attributed to superconductivity. The satellite features are less homogeneous, with a effective gap energy $\Delta_{eff} = (37.8 \pm 2.0)$meV. The application of magnetic fields reveal vortices in Y-123, and the intra-vortex quasiparticle spectra show two energy gaps, with one gap at the pseudogap energy scale $\mathrm{V}_{PG} \sim 32$meV and the other gap at the subgap energy scale $\Delta' \sim 7 - 12\mathrm{meV} < \Delta_{SC}$. In contrast, the inter-vortex quasiparticle spectra reveal only one energy gap at $\Delta_{SC} \sim 20$meV. A dramatic shift in the peak-to-peak gaps, $\Delta_{pk-pk}(\mathrm{H})$, from Δ_{SC} to both V_{PG} and Δ' with increasing magnetic field is observed. In addition, higher spatial resolution STS measurements were performed in Y-123 to investigate the spatial dependence of the quasiparticle spectra in more detail. The experimental resolution allowed Fourier-transformed local density of states analysis to be performed. Energy-dependent dispersive diffraction modes attributable to quasiparticle scattering interferences (QPI) were seen, as well as three energy-independent modes not due to QPI. The energy-independent modes corresponded to periodic real-space conductance modulations along the Cu-O bonding and the nodal directions attributable to a pair-density wave, a charge-density wave, and a spin-density wave. The totality of data in Y-123 suggests that the ground state of Y-123 contains competing orders coexisting with superconductivity and not superconductivity alone.

In addition to the STS experiments, the effects of unconventional quasiparticle excitations on macroscopic superconductivity and vortex phase diagrams are investigated from bulk magnetization measurements on several different families of superconducting cuprate samples. Evidence for strong field-induced quantum phase fluctuations and quantum criticality are observed in the vortex phase diagrams of all samples considered. The origin of the apparent quantum criticality and strong field-induced quantum phase fluctuations due to the nearby presence of competing orders is discussed.

Finally, a “two-gap” phenomenological model, describing the excitations from a ground state of coexisting superconductivity and a competing order, is used to quantitatively model the unconventional quasiparticle excitations observed in the measurements of the local tunneling density of states and the angle-resolved photoemission spectroscopy (ARPES) experiments. The phenomenological model is found to provide consistent accounts for the quasiparticle tunneling data from our measurements in La-112 and Y-123, as well as experimental data by others on different cuprates.

Contents

List of Figures

Chapter 1

Introduction

The high-temperature cuprate superconductors are type-II superconductors with the highest known values of superconducting transition temperature, T_C (maximum $T_C \sim 165K$ under pressure), to date; however, the mechanism of superconductivity and the physical phenomena displayed by the cuprates remain a mystery, despite their discovery by Bednorz and Müeller over 20 years ago [1]. The superconducting cuprates are derived by doping antiferromagnetic Mott insulators with electrons or holes, and superconductivity arises over a limited range of doping in either case. The highest value of T_C occurs at the so-called optimal doping level, and cuprates with doping less than or greater than optimal doping are referred to as underdoped or overdoped, respectively. The physical phenomena displayed by hole-type superconducting cuprates differ significantly from those displayed by the electron-type superconducting cuprates. Therefore, the phenomena among the cuprates are non-universal.

Among the non-universal phenomena in cuprates, the low-energy quasiparticle excitations remain one of the least understood physical properties. More specifically, cuprate quasiparticle excitations exhibit unconventional properties compared to conventional Bogoliubov quasiparticle excitations. Underdoped and optimally doped hole-type cuprates exhibit the so-called pseudogap [2, 3, 4, 5] and Fermi arc [6, 7, 8] phenomena above T_C, while these quasiparticle excitation phenomena are absent in electron-type cuprates. Neutron scattering experiments in the electron-type cuprates observe spin excitations commensurate with the lattice structure [9, 10, 11, 12], while hole-type cuprates display incommensurate spin excitations according to neutron scattering measurements [13, 14, 15, 16]. Quasiparticle excitations in a magnetic field for both hole- and electron-type cuprates are unconventional [17, 18, 19, 20, 3, 21, 22] compared to the Bogoliubov quasiparticle excitations in conventional type-II superconductors [23, 24, 25].

In addition to superconductivity, many other competing orders are theoretically conjectured to exist in the ground state of the cuprates upon doping the antiferromagnetic Mott insulating parent (undoped) state [26, 27, 28, 29, 30, 31], and these competing orders may provide additional excitations, along with Bogoliubov quasiparticles, to explain the unconventional and non-universal quasiparticle excitations in the cuprates. However, it is also possible that the strange quasiparticle excitations simply arise from disordered superconductivity in the cuprates [8, 3, 32, 33]. An important objective of the experimental work presented here was to empirically determine whether the quasiparticle excitations in cuprates are due to superconductivity alone or if both competing orders and superconductivity are relevant.

In this chapter, we review the known material properties and phase diagrams of the cuprates as a function of doping, discuss the current experimental and theoretical progress to understand the non-universal and unconventional quasiparticle excitations in cuprates, and describe our approach to investigate the low-energy quasiparticle excitations in hole- and electron-type high-temperature cuprate superconductors. The objective is to determine if the quasiparticle excitations arise from a ground state of superconductivity alone or from a ground state of superconductivity and competing orders.

1.1 Electronic phase diagram and crystalline structure of high-temperature cuprate superconductors

The undoped parent compounds of cuprate superconductors are antiferromagnetic Mott insulators. Mott insulators exhibit strong on-site Coulomb repulsion such that a configuration with only one electron per unit cell is the most energetically favorable at half-filling. The overall consequence of the strong on-site Coulomb repulsion in this scenario is that the materials behave as insulators,

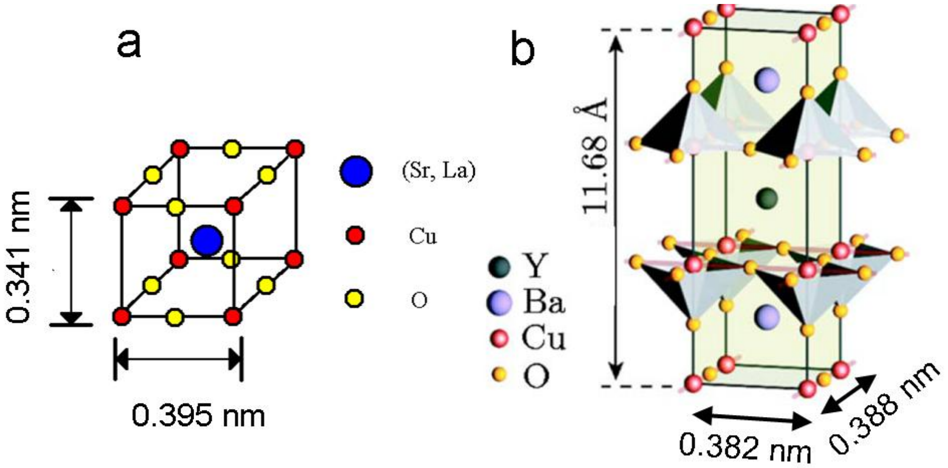

Figure 1.1: Unit cell crystalline structure of: (a) Electron-type: $La_{0.1}Sr_{0.9}CuO_2$ (La-112). (b) Hole-type: $YBa_2Cu_3O_{7-\delta}$ (Y-123). Y-123 figure reproduced and adapted from Ref. [3].

whereas electronic bandstructure calculations would have predicted them to be metallic.

A common feature of the cuprates is the presence of CuO_2 planes, and holes or electrons are doped into these planes, leading to the formation of superconducting states at certain doping levels. (The crystal structures of La-112 and Y-123 are shown in Fig. 1.1 to illustrate the CuO_2 planes and give examples of cuprate unit cells.) Doped Mott insulators are known to exhibit strong electronic correlations among carriers and have ground states that are sensitive to doping level. The pairing symmetry of the superconducting order parameter in the cuprates is observed to be unconventional, with many samples exhibiting $d_{x^2-y^2}$-wave (d-wave) superconductivity [34]. However, all cuprates do not exhibit pure d-wave superconductivity. For example, the orthorhombicity of Y-123 leads to doping dependent (d+s)-wave symmetry [35]. Further, the dominant pairing state, whether s-wave or d-wave, of electron-doped cuprates as a function of doping is a source of debate in the literature [36, 37, 38, 39, 40, 41, 42].

The generic phase diagram of cuprates is shown in Fig. 1.2, where AFM denotes antiferromagnetism, SC denotes superconductivity, FL denotes Fermi-liquid like behavior, and MFL denotes marginal Fermi-liquid behavior. The marginal Fermi liquid is characterized by single-particle and transport scattering rates that are linear in frequency until the energy is approximately equal to the thermal energy [43]. The antiferromagnetic state occurs below the Néel temperature, T_N, while

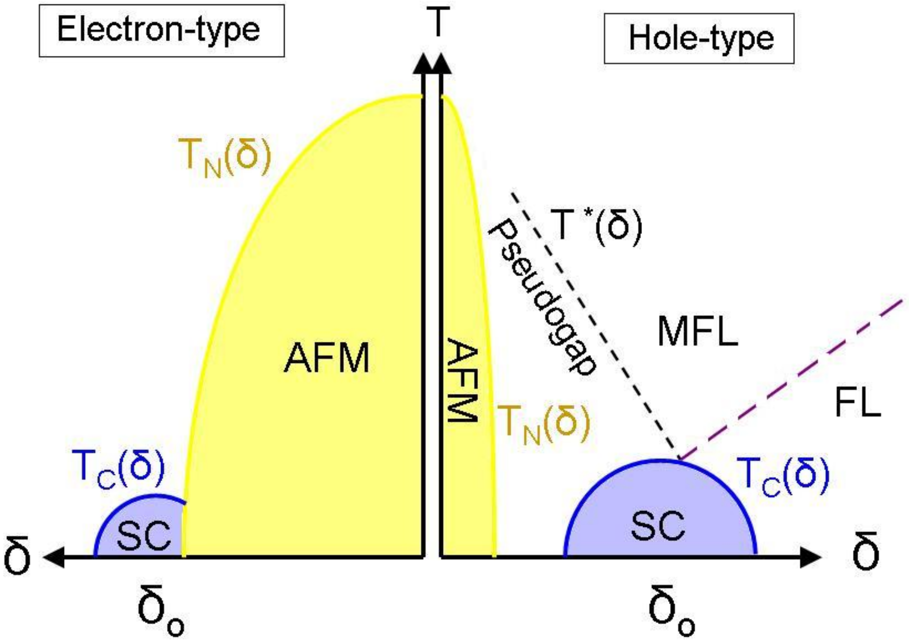

Figure 1.2: The generic phase diagram of the high-temperature cuprate superconductors: Both electron- and hole-type cuprate phase diagrams are shown together. Notation: AFM–antiferromagnetism [$T_N(\delta)$–Néel temperature], SC–superconductivity [T_C–superconducting transition temperature], MFL–marginal Fermi liquid [43], FL–Fermi-liquid like, δ_0–optimal doping

superconductivity occurs below T_C. The pseudogap temperature is characterized by T^* in the phase diagram.

The phase diagram of the cuprates is not symmetric among hole- and electron-type cuprates. The presence of the pseudogap phenomena on the hole-type side of the phase diagram is not reproduced on the electron-type side of the phase diagram. (The pseudogap is the observation of a soft gap in the quasiparticle density of states spectra that persists above T_C in underdoped to slightly overdoped hole-type cuprates. It exhibits no coherence peaks and is referred to as a soft gap because the quasiparticle density of states are suppressed, but non-zero, below the pseudogap energy.) Furthermore, the AFM region of the phase diagram extends out to meet the superconducting "dome" in electron-type cuprates, while clear separation is observed between the superconducting "dome" and AFM on the hole-type side of the phase diagram.

The type of doping, whether holes or electrons, and the location of dopants play a strong role in the orders that arise in the ground state of cuprates. From photoemission studies it is known that, in electron-type cuprates, electrons are primarily doped onto the d-orbital of Cu, turning Cu^{2+} into Cu^{+} [44, 45]. In contrast, holes are primarily doped onto the oxygen p-orbital in hole-type cuprates [46, 47, 48]. Doping holes onto the oxygen-p orbital creates ferromagnetic coupling between neighboring Cu sites, which leads to significant spin frustration as the insulating antiferromagnetic Mott parent state is doped. Clear separation between the antiferromagnetic and superconducting states as a function of doping is seen. In contrast, electrons doped onto Cu sites create spinless Cu^{+} ions that dilute the antiferromagnetic phase exhibited by the insulating Mott parent state. As a result, the antiferromagnetic region of the electron-type phase diagram extends farther out in doping and meets the superconducting region of the phase diagram, as shown in Fig. 1.2. The difference in dopant location is also important because frustration or dilution of the antiferromagnetic background could easily tune the physical parameters of the cuprates to favor one or more type of order in the ground state. Further, the ground state could differ in hole- and electron-type cuprates. Competing orders and superconductivity could also have different energy scales in hole- and electron-type cuprates. Further insight into the differences in the location of dopant and the differences in doping with holes or electrons could help explain the non-universal and unconventional phenomena among electron- and hole-type cuprates.

1.2 Non-universal behavior of hole- and electron-type high-temperature superconducting cuprates

The pseudogap and Fermi arc phenomena are unconventional quasiparticle excitations in hole-type cuprates that are absent in electron-type cuprates; spin excitations observed by neutron scattering in cuprates also appear unconventional, with electron- and hole-type cuprates exhibiting commensurate gapped spin excitations and incommensurate gapped spin excitations, respectively. The origin of these non-universal quasiparticle excitations remains the subject of experimental and theoretical research, which we review here.

The pseudogap phenomena refers to the observation of a soft gap without coherence peaks in the quasiparticle excitation spectra above T_C in hole-type cuprates. The pseudogap temperature is denoted by T* and its doping dependence is shown schematically in Fig. 1.2. Evidence for the pseudogap or direct observation of the pseudogap in hole-type cuprates has been reported in tunneling measurements [2, 3, 4, 49], ^{63}Cu spin-lattice relaxation rate and ^{63}Cu Knight shift NMR experiments [50, 51, 52, 53, 54, 55, 56], optical conductivity experiments [50, 57], Raman scattering experiments [58, 59, 60] and angle resolved photoemission spectroscopy (ARPES) measurements [6, 7]. Examples of the pseudogap from tunneling measurements and ARPES measurements are shown in Figs. 1.3a and 1.3b. A more extensive review of the pseudogap phenomena in hole-type cuprates may be found in Ref. [50]. Research into the origin of the pseudogap in quasiparticle excitations is ongoing.

In contrast, electron-type cuprates do not show a pseudogap above T_C in zero magnetic field, as evidenced, for example, by tunneling and ARPES experiments [39, 61, 62, 63, 17, 64, 41]. An example of the lack of pseudogap in the one-layer electron-type cuprate $Pr_{1.85}Ce_{0.85}CuO_{4-y}$ (PCCO) is shown in Fig. 1.3c. However, "hidden pseudogap"-like quasiparticle excitation spectra have been observed under the superconducting dome in doping dependent grain-boundary tunneling experiments on $Pr_{2-x}Ce_xCuO_{4-y}$ (PCCO) and $La_{2-x}Ce_xCuO_{4-y}$ (LCCO) when a magnetic field $H > H_{C2}$ is applied to suppress superconductivity [17]. The "hidden pseudogap" quasiparticle spectra as a function of magnetic field are reproduced in Fig. 1.3d for reference. It is possible that the pseudogap is present in both hole- and electron-type cuprates and has a non-universal energy scale among hole- and electron-type cuprates, such that the pseudogap is effectively hidden under the superconducting dome for electron-type cuprates.

Intimately related to the pseudogap is the observation of Fermi arcs in hole-type cuprates. The Fermi arc phenomena are observed as an incomplete recovery of the full Fermi surface for temperature in the range $T_C < T < T^*$ in hole-type cuprates. The phenomena is most notably observed in $Bi_2Sr_2CaCu_2O_x$ (Bi-2212) as a function of doping [6, 8, 7]. The persistence of gapped quasiparticle spectral density functions near the $(\pm\pi, 0)$ and $(0, \pm\pi)$ portions of the Brillouin zone above T_C in hole-type cuprates are the source of the incomplete recovery of the Fermi surface. An example of

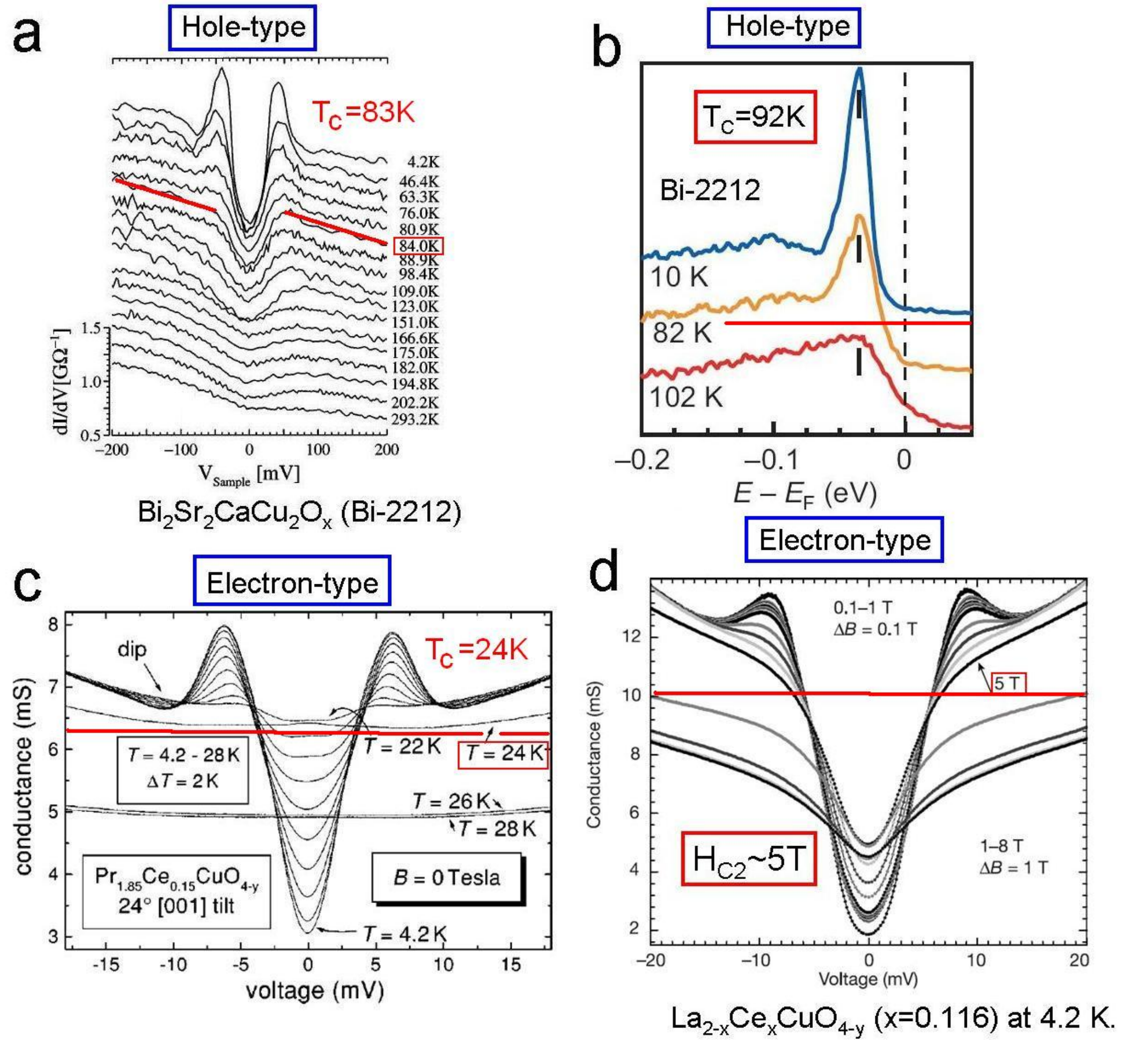

Figure 1.3: Examples of pseudogap phenomena in cuprate superconductors: (a) Pseudogap phenomena in hole-type $Bi_2Sr_2CaCu_2O_x$ (Bi-2212) from scanning tunneling microscopy experiments [2]. [Figure reproduced from Ref [2].] (b) Pseudogap phenomena observed in ARPES measurements on hole-type Bi-2212 [6]. The temperature dependent ARPES signals obtained near the $(0, \pm\pi)$ and $(\pm\pi, 0)$ regions of the Brillouin zone along the Fermi surface are shown. The observed ARPES intensity, which is related to the spectral density function, remains gapped for temperatures above T_C. [Figure reproduced from Ref [6].] (c) Lack of a pseudogap observed above T_C in the one-layer electron-type $Pr_{1.85}Ce_{0.85}CuO_{4-y}$ from break-junction measurements. [Figure reproduced from Ref [61].] (d) "Hidden-pseudogap" spectra revealed in the one-layer electron-type cuprate $La_{1.85}Ce_{0.85}CuO_{4-y}$ as magnetic field is increased above $H_{C2} \sim 5 - 6T$ for $T \ll T_C$, from break-junction experiments [17]. A soft-gapped spectra without coherence peaks and with suppression of the quasiparticle density of states persists up to the highest magnetic fields considered. [Figure reproduced from Ref [17].] (Red lines denote spectra taken at the superconducting transition temperature, T_C in (a), (b), and (c), while the red line in (d) denotes the upper critical field, H_{C2}.)

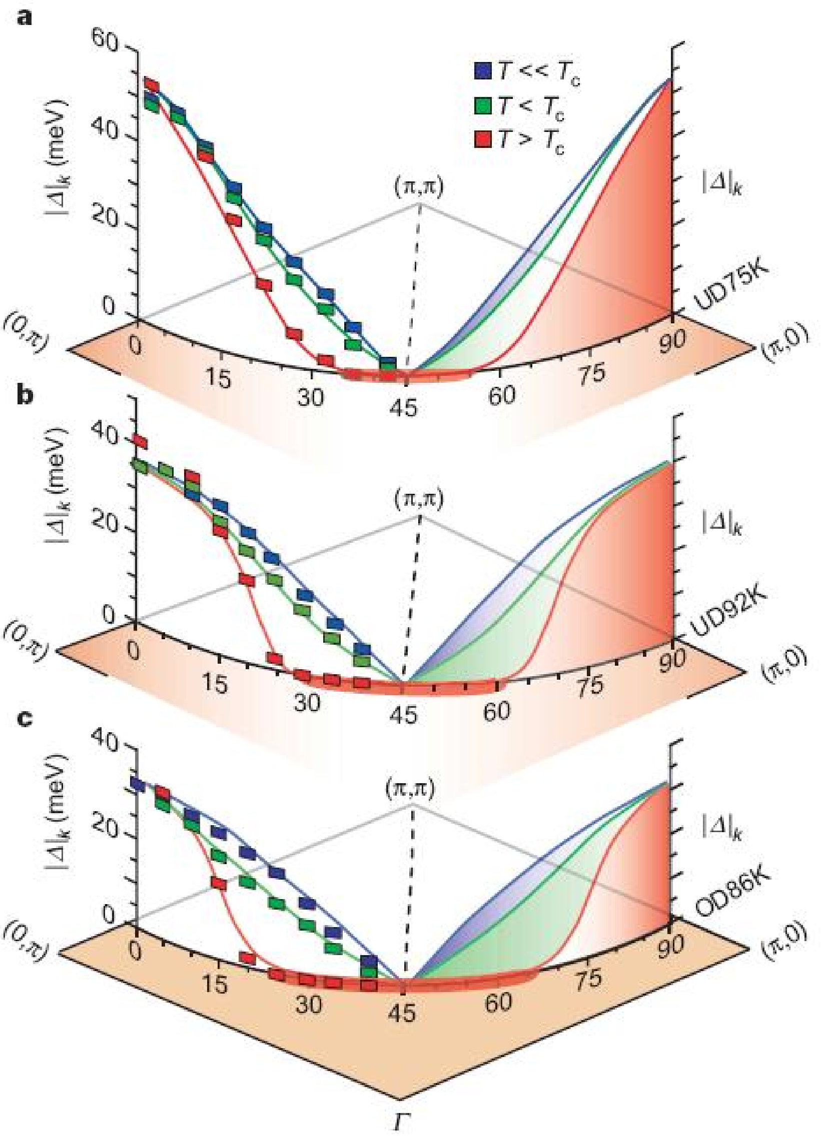

Figure 1.4: Examples of the Fermi arc evolution with doping in Bi-2212: The measured gap-(Δ_k-)vs.-angle(-θ_k) values relative to the $(\pi, 0)$ direction of the Brillouin in Bi-2212 along the Fermi surface for different doping levels are shown. (a) Underdoped, T$_C$=75K, (b) Slightly underdoped, T$_C$=92K, (c) Overdoped, T$_C$=86K. Gapped behavior persists near the $(\pi, 0)$ and $(0, \pi)$ regions of the Brillouin zone. The Fermi surface is recovered over an arc length less than $\pi/2$ for T$_C$ < T < T*. [Figure reproduced from Ref. [6].]

the Fermi arc phenomena in Bi-2212 [6] is reproduced in Fig. 1.4. If the full normal state Fermi surface were recovered in Bi-2212, it would manifest as a complete arc of gapless excitations with arc length of $\pi/2$ in each quadrant of the Brillouin zone above T$_C$. However, the Fermi surface is not fully recovered above T$_C$, and an arc, whose length increases with doping, is observed instead.

Neutron scattering experiments show distinct differences in spin excitations depending on whether holes or electrons are the dopants in a given cuprate. Neutron scattering experiments on the hole-type $La_{2-x}Sr_xCuO_{4-y}$ reveal incommensurate spin correlations in the superconducting state, with a temperature independent spin gap observed both below and above T_C [13, 14, 15]. In contrast, the one-layer electron-type cuprate $Nd_{2-x}Ce_xCuO_{4-y}$ (NCCO) [9] displayed commensurate spin correlations and a temperature dependent spin gap in neutron scattering experiments [9]. Furthermore, the spin gap of NCCO was observed to be a maximum of about 4meV as $T\rightarrow 0$ and disappeared as $T\rightarrow T_C$ [9]. The spin gap in both hole- and electron-type cuprates may possibly be related to the pseudogap, as both the spin gap and pseudogap are absent above T_C in electron-doped cuprates and present above T_C in hole-doped cuprates. The "hidden pseudogap"-like spectra observed in the tunneling spectra of break junctions may also share the same origin as the spin gap in neutron scattering experiments. Enhancement of a static commensurate magnetic order by application of a magnetic field up to 9T in electron-doped $Pr_{0.89}LaCe_{0.11}CuO_4$ (PLCCO) is observed [10], and the authors of Ref. [11] report a commensurate "quasi-2D spin-density wave" enhanced by the application of a magnetic field equal to 5T in underdoped $Pr_{0.88}LaCe_{0.12}CuO_4$. Neither the orders observed by neutron scattering nor the pseudogap are suppressed by moderate magnetic fields. However, the results are not conclusive in favor of a tie between the pseudogap and the spin gap. It has been cautioned that secondary material phases formed during oxygen reduction in the formation of one-layer electron-doped cuprates, paramagnetism of Nd^{3+} or Pr^{3+}, and whether or not holes are the actual carriers in one-layer electron-doped cuprates should be considered in analysis and conclusions [65, 66]. Fortunately, these issues do not arise in the data presented for the electron-type cuprate $La_{0.1}Sr_{0.9}CuO_2$ (La-112) data presented here because oxygen reduction is not required to achieve optimal doping, La-112 is free from magnetic ions, and thermopower measurements are consistent with electrons as the relevant carriers in La-112[67].

1.3 Additional unconventional properties of high-temperature superconducting cuprates

The pseudogap, Fermi arc, and neutron scattering phenomena are due to non-universal and unconventional quasiparticle excitations in the superconducting cuprates. In addition to these phenomena, experiments have observed other unconventional quasiparticle excitations in the cuprates that have not been adequately characterized as universal or non-universal among hole- and electron-type cuprates. The additional unconventional excitations include: the demonstration of nano-scale inhomogeneity in the quasiparticle excitation spectra of some cuprates [68, 49, 4], the observance of pseudogap-like quasiparticle spectra in the core of vortices [18, 20, 69], and the revelation of energy-dependent and energy-independent diffraction modes in Fourier-transformed local density of states (FT-LDOS) measurements in zero and finite magnetic fields.

Nano-scale variations in the quasiparticle excitation spectra of cuprates have been observed in certain hole-type cuprates, but the universality of this phenomena among either hole- or electron-type cuprates is unclear. The nano-scale variations are manifested over length scales of a few nm and exhibit strongly varying peak widths as a function of energy. Specifically, strong spectral inhomogeneity in the peak-to-peak energy gaps, Δ_{pk-pk} appears to vary on the order of 30meV in some hole-type cuprates. Such nano-scale variations have been observed in Bi-2212 [49, 68, 3], $(Bi_{1-y}Pb_y)_2Sr_2CuO_{6+x}$ [(BiPb)-2201] [4], and $Bi_2Sr_{2-x}La_xCuO_{6+\delta}$ (LaBi-2201) [70], and examples of the inhomogeneity studies are reproduced in Fig. 1.5. The inhomogeneous spectra observed in these systems has raised many questions as to the origin of the phenomena. Most notably, the average gaps observed in the quasiparticle excitation spectra do not mimic the same temperature dependence as the bulk T_C values [33, 49, 4, 8], and it is debateable [33, 8, 26, 27, 28, 29, 30, 31] if the peaks (some are rounded at higher energies, some are sharper at lower energies, and others consist of both large rounded peaks together with small peaks or "kinks" at lower energies) observed are necessarily due to superconductivity alone. Furthermore, the hole-type cuprates that exhibit such variations have some of the largest electronic anisotropy values among the cuprates (the ab-plane to c-axis superconducting coherence length ratio $\sim$ 20 or higher). Therefore, the variations could be due to an increased interaction with disorder in these highly anisotropic systems. In fact, even among the same family of Bi-2212 samples, different surface preparations have been shown to yield different degrees of inhomogeneity for the same nominal doping level [71]. Evidence of more homogeneous gaps as a function of position from measurements on hole-type Y-123 [35] and electron-type $Pr_{0.88}LaCe_{0.12}CuO_4$ (PLCCO) [63] with scanning tunneling microscopy (STM) suggest that the inhomogeneity observed is not universal among the hole-type or electron-type cuprates. It is possible that competing orders, besides superconductivity, contribute to the peak locations and are more susceptible to disorder. For example, the results of Ref. [4], observed two gaps in the $T \ll T_C$ spectra, with the strongly varying pseudogap-like spectra masking the second gap at a lower energy. By normalizing out the pseudogap, the second gap was revealed more clearly and observed to be homogeneous and mimic the behavior of the bulk T_C values. Namely, the second gap value decreases with increasing temperature and vanishes at T_C. This behavior is reproduced in Fig. 1.6.

Cuprate superconductors are known as extreme type-II superconductors, and unconventional quasiparticle excitations are also observed in the vortex state of cuprate superconductors. In conventional type-II superconductors, vortices order into the Abrikosov vortex lattice [72, 23, 24, 25] for $T < T_C$ and $H_{C1} < H < H_{C2}$, where H_{C2} is the upper critical field and H_{C1} is the lower critical field that corresponds to the threshold field for vortices. Direct measurements by Hess et al. [23, 24, 25] of the vortex lattice in a conventional type-II superconductor $NbSe_2$ were accomplished with spatially resolved scanning tunneling spectroscopy of the quasiparticle excitation spectra. The quasiparticle spectra outside of vortex cores (inter-vortex spectra) were observed to be similar to the zero field excitation spectra, displaying a gapped spectra with peaks at the superconducting gap, Δ. The spectra near the center of the vortex cores exhibited a zero-bias conduction peak, which have since been theoretically attributed to bound quasiparticle states in the core of vortices [73, 74, 75, 76]. In contrast, the quasiparticle spectra inside the hole-type cuprates Bi-2212 and Y-123 exhibit two gaps in the core of vortices and no zero-bias conduction peak. One gap resembles the pseudogap, while the other gap energy is below the zero field superconducting gap and referred to as the subgap

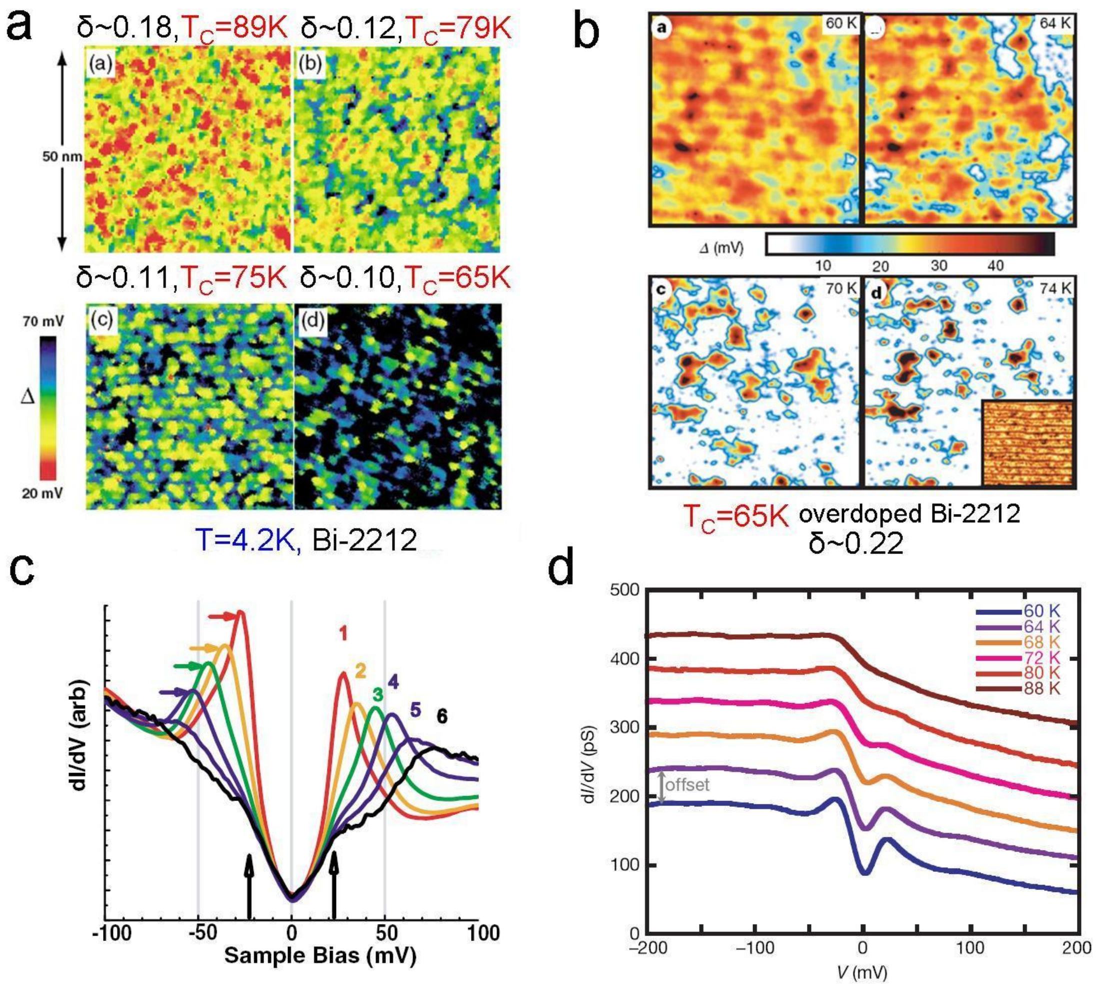

Figure 1.5: Observation of an inhomogeneous gap in Bi-2212 as function of doping and temperature: (a) Inhomogeneous gaps observed in Bi-2212 for various doping levels for T $\ll$ T$_C$. [Figure reproduced and adapted from Ref. [68].] (b) Temperature dependent evolution of inhomogeneous gaps in Bi-2212 from below to above T$_C$. [Figure reproduced and adapted from Ref. [49].] (c) Quasiparticle excitation spectra corresponding to the colors in (a). [Figure reproduced from Ref. [68].] (d) Evolution of representative quasiparticle excitation spectra with temperature from (b). [Figure reproduced from Ref. [49].]

energy. Examples of spectra inside and outside of vortex cores in Y-123 and Bi-2212 are reproduced in Fig. 1.8. The origin of the two-gap features in the intra-vortex spectra is unknown.

In addition to the unconventional vortex state quasiparticle spectra, energy-dependent and energy-independent conductance modulations have been observed from real space and in the Fourier transformed local density of states (FT-LDOS) studies on high-temperature superconducting cuprates. A conductance modulation of $4a_0 \times 4a_0$ lattice constants, independent of energy, was observed in Bi-2212 inside vortex cores in a magnetic field of H = 5T. Here a_0=0.385nm is the planar lattice constant of Bi-2212. Additionally, energy-dependent diffraction modes that disperse with energy were observed in Bi-2212 at zero [68] and finite magnetic fields [77]. The energy-dependent diffraction modulations have been theoretically attributed to quasiparticle scattering interferences due to the joint density states of the quasiparticle excitations that vary with energy [78, 79]. However, the energy-independent $4a_0 \times 4a_0$ conductance modulations are not accounted for using the same theoretical approach [78, 79]. Further measurements in Bi-2212 [80] and $Ca_{2-x}Na_xCuO_2Cl_2$ [81] have revealed $4a_0 \times 4a_0$ conductance modulations imaged both in real space and in FT-LDOS analysis at zero magnetic field. Additionally, other energy independent diffraction modes with incommensurate periodicities have been observed in $Bi_{2-y}Pb_ySr_{2-z}La_zCuO_{6+x}$ [82] and La-Bi2201 [70]. The origin of the energy-independent modes remains a subject of research to date.

1.4 Interpretations of non-universal and unconventional quasiparticle phenomena: preformed pairs versus competing orders

In order to account for the various unconventional and non-universal phenomena in high-temperature superconducting cuprates, two theoretical conjectures emerge. One scenario, which we refer to as the “one-gap” model [8, 33, 32, 3], supposes that the observed physical phenomena are the result of disordered superconductivity that arises below T*, and the cuprate only becomes ordered below T_C. More specifically, the “one-gap” model is commonly referred to as the “pre-formed” pair scenario

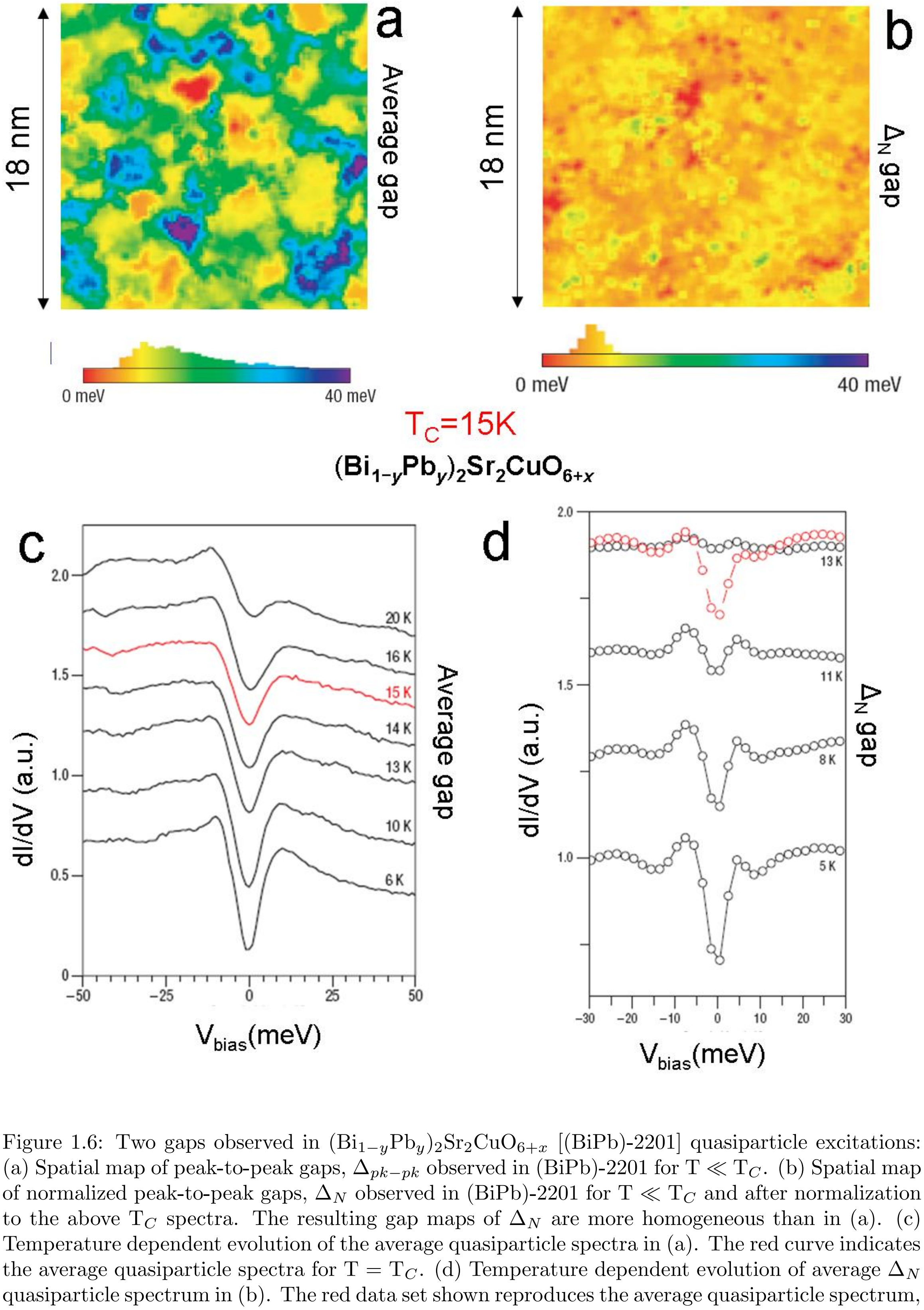

Figure 1.6: Two gaps observed in $(\mathrm{Bi}_{1-y}\mathrm{Pb}_y)_2\mathrm{Sr}_2\mathrm{CuO}_{6+x}$ [(BiPb)-2201] quasiparticle excitations: (a) Spatial map of peak-to-peak gaps, Δ_{pk-pk} observed in (BiPb)-2201 for T $\ll$ T_C. (b) Spatial map of normalized peak-to-peak gaps, Δ_N observed in (BiPb)-2201 for T $\ll$ T_C and after normalization to the above T_C spectra. The resulting gap maps of Δ_N are more homogeneous than in (a). (c) Temperature dependent evolution of the average quasiparticle spectra in (a). The red curve indicates the average quasiparticle spectra for $\mathrm{T} = \mathrm{T}_C$. (d) Temperature dependent evolution of average Δ_N quasiparticle spectrum in (b). The red data set shown reproduces the average quasiparticle spectrum, without normalization, near T_C. [Figures reproduced and adapted from Ref. [4].]

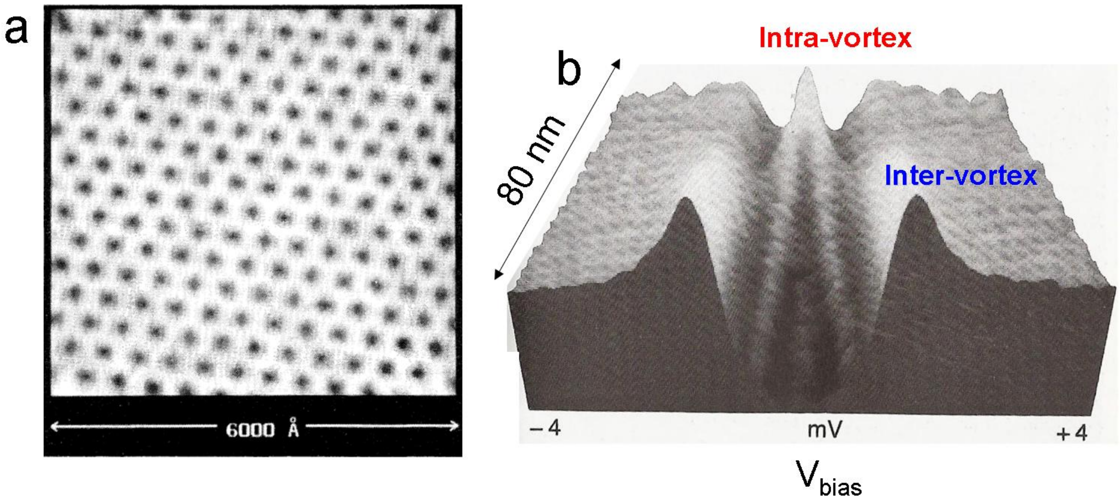

Figure 1.7: Vortex state quasiparticle spectra in a conventional type-II superconductor $NbSe_2$: (a) Spatial map of dI/dV at V_{bias} =1.3mV. The Abrikosov vortex lattice is evident [72]. [Figure reproduced from Ref. [23].] (b) Quasiparticle excitation spectra along a linecut between the core of a vortex (intra-vortex) to the region between vortices (inter-vortex spectra). Bound quasiparticle states cause a zero-bias conduction peak to be observed for intra-vortex spectra near the vortex center [73, 74, 75, 76]. [Figure reproduced and adapted from Ref. [25].]

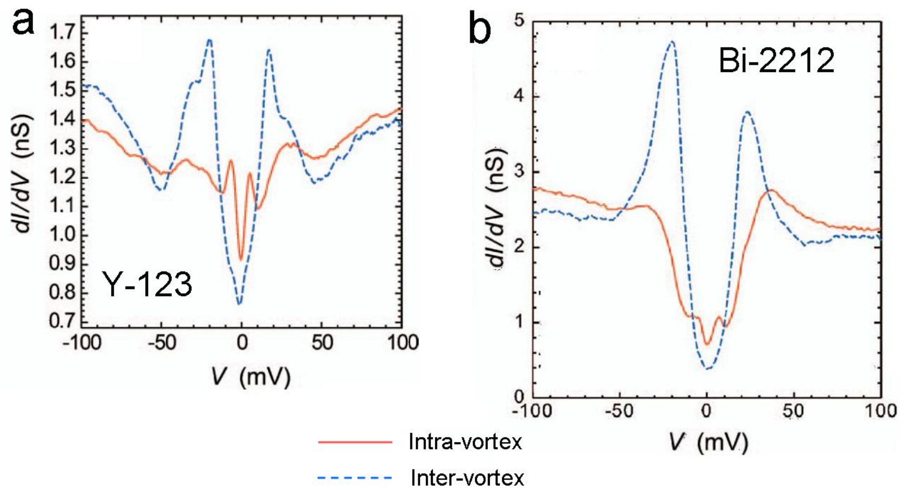

Figure 1.8: Unconventional vortex state quasiparticle excitation spectra in Y-123 and Bi-2212 revealing two gaps. One gap is larger than the superconducting gap for inter-vortex spectra and resembles the pseudogap spectra, while the other gap is smaller in energy than the inter-vortex gap and is referred to as the subgap energy: (a) Y-123, (b) Bi-2212. [Figures reproduced and adapted from Ref. [3] and references therein.]

because it is supposed that Cooper pairs begin to form at T*, the pseudogap temperature. The theoretical conjecture further assumes that the pairs do not exhibit global phase coherence for $T_C < T < T^*$. It is only for $T < T_C$ that the pairs condense and global phase coherence is observed in this viewpoint. Preformed pairs may then organize themselves into pair-density-waves in this scenario to account for the diffraction modes seen in FT-LDOS measurements [83, 84], and the subgap and pseudogap-like energies in quasiparticle spectra observed inside vortex cores are predicted to be due to disordered superconductivity alone [32, 3]. However, the preformed pair model cannot offer any explanation for the systematic variations in the wavevector of the pair-density wave with doping.

Another scenario to understand the unconventional and non-universal phenomena is to assume that superconductivity and competing orders are together responsible for the observed cuprate phenomena. We refer to this scenario as the "two-gap" model. This scenario supposes that the unconventional and non-universal phenomena in cuprates may be accounted for by including both Bogoliubov quasiparticles from superconductivity and collective excitations from competing orders to describe the complete set of low-energy excitations. Therefore, the unconventional excitations observed in cuprates are assumed to arise from a ground state of superconductivity and a competing order, and T* is assumed to be the competing order transition temperature, while T_C is the superconducting transition temperature. Many experimental results exhibit explicit "two-gap" behavior [6, 85, 60, 4], with one experimentally observed gap closing at T_C value and another gap persisting for $T_C < T < T^*$. Competing orders, such as pinned spin-density waves (SDW) [29, 86] and charge-density waves (CDW) [31, 87, 84], have also been proposed as possibilities to explain the energy-independent conductance modulations observed in FT-LDOS measurements on cuprates [21, 80, 81].

1.5 Overview of the thesis

Current experimental information and theoretical conjectures have not been able to sufficiently distinguish between the "one-gap" and "two-gap" models in cuprate superconductors, and it is possible that both scenarios find some applicability to the cuprates. In this thesis, we provide new investigations of the two models and the low-energy quasiparticle excitations by examining the temperature and magnetic-field evolution of low-energy quasiparticle excitations using spatially resolved scanning tunneling spectroscopy and bulk magnetization measurements in hole- and electron-type cuprates.

The theoretical background of quantum tunneling is reviewed briefly before proceeding to discuss various issues associated with the “one-gap” and “two-gap” models in Chapter 2. Instrumentation for the studies of spatially resolved scanning tunneling spectroscopy (STS) and bulk magnetization measurements are reviewed in Chapter 3. Experimental investigations of the quasiparticle excitations of the electron-type superconducting cuprate $La_{0.1}Sr_{0.9}CuO_2$ (La-112) and the hole-type superconducting cuprate $YBa_2Cu_3O_{7-\delta}$ (Y-123) as a function of magnetic field and temperature using spatially resolved scanning tunneling spectroscopy are presented in Chapters 4 and 5, respectively. We attempt to differentiate between a ground state of superconductivity alone and a ground state of superconductivity and competing orders from studying the low-energy quasiparticle excitations in zero and finite magnetic fields. By applying magnetic fields ($H \ll H_{C2}$) in La-112 and Y-123, we reveal vortices in both systems–notably for the first time in any electron-type cuprate. We discuss intra-vortex and inter-vortex quasiparticle spectra in both La-112 and Y-123, and we investigate the field evolution of the quasiparticle spectra to differentiate between the “one-gap” and “two-gap” viewpoints in both samples.

In addition, we experimentally manifest the effect of unconventional quasiparticle excitations on the bulk properties of cuprates by measuring the vortex phase diagrams of many different cuprates, which we present in Chapter 6. We find evidence for strong quantum phase fluctuations in all samples studied, and we discuss the implications. Finally, we develop a phenomenological framework to analyze the applicability of superconductivity coexisting with competing orders to explain the unconventional quasiparticle excitations among all cuprates in Chapter 7, and we analyze the feasibility of the phenomenology to account for the non-universal and unconventional phenomena among all cuprates before making our conclusions.

Appendices are included to describe additional processing of STS data (Appendix A), the complete set of energy dependent differential FT-LDOS in Y-123 (Appendix B), and the development of a cryogenic scanning tunneling/scanning electron microscope (STM/SEM) (Appendix C). The cryogenic STM/SEM was developed to expand experimental capabilities of STM and to enable larger scale, detailed investigations of materials with both STM and SEM capabilities. The STM/SEM instrumentation is not directly related to the results presented in the main text of this thesis. However, the STM/SEM instrumentation will provide vital new capabilities for future STM measurements on systems that would be difficult to study with STM alone.

Chapter 2

Physics of quasiparticle tunneling spectroscopy in superconductors

In this chapter the basic concepts of conventional quasiparticle tunneling spectroscopic studies of superconductors are reviewed. Additionally, how these analyses are extended to fitting the quasiparticle tunneling spectra of cuprate superconductors are discussed. It will become clear that the assumption of pure superconductivity in the ground state of cuprate superconductors fails to consistently account for a wide variety of quasiparticle tunneling spectra in the cuprates. These analyses together with overwhelming empirical evidences of competing orders in the cuprates therefore suggest that modifications to the conventional theory for quasiparticle tunneling spectroscopy in superconductors are necessary.

2.1 Physics of normal metal(N)-insulator(I)-superconductor(S) quasiparticle tunneling

To begin, we first consider a simple situation of quasiparticle tunneling from a normal metal to a superconductor. An intuitive way to model the tunneling of electrons between two materials separated by a tunneling barrier, such as an insulator, is to use the Bardeen transfer Hamiltonian formalism [88]. Bardeen first proposed this formalism to describe the quantum tunneling observed between a metal and a superconductor separated by a thin oxide layer, as observed experimentally by Giaever [89] and Nicol et al. [90]. In the experiments, the superconducting energy gap of lead was directly measured, and it was supposed that the measured quantum tunneling current was determined solely by the quasiparticle density of states of the superconductor. Bardeen confirmed this interpretation through his transfer Hamiltonian formalism.

The Bardeen formalism assumes that two systems, representing two materials, are separated by a tunneling barrier and that the quantum transmission through the barrier is small enough to treat the transmission as a perturbation. The formalism predicts the quantum mechanical transmission current through an insulating barrier from one system to another, and, for simplicity, we describe the formalism for the simple one-dimensional scenario shown in Fig. 2.1. The transmission is assumed to be small enough that the left- and right-hand systems may be treated as almost independent in Bardeen's approach. Specifically, the density of states on each side is considered approximately equivalent to the case where the systems are completely separate, and a small perturbation transfer Hamiltonian, H_T, is used in time-dependent perturbation theory to describe the transition probabilities for the left and right states to quantum mechanically tunnel through the barrier.

The Hamiltonian for the time-dependent treatment is given by

$$\begin{gathered} H = H_l + H_r + H_T = H_0 + H_T, \\ H_0\Psi_l = E_l\Psi_l, \\ H_0\Psi_r = E_r\Psi_r, \end{gathered} \tag{2.1}$$

where Ψ_l is the wavefunction of the left system, Ψ_r is the wavefunction of the right system, and H_T is the transfer Hamiltonian. The transfer probability for the left system from the initial state Ψ_l to the final state Ψ_r is calculated using the time-dependent Schröndinger equation:

$$H\Psi(t) = i\hbar\frac{d\Psi(t)}{dt}. \tag{2.2}$$

Using the *Ansatz*

$$\Psi(t) = c(t)\Psi_l e^{-iE_l t/\hbar} + d(t)\Psi_r e^{-iE_r t/\hbar} \tag{2.3}$$

in Eq. 2.2 the effective tunneling matrix becomes

$$M_{rl} = \int \Psi_r^*(H - E_l)\Psi_l dz = \int \Psi_r^* H_T \Psi_l dz. \tag{2.4}$$

The transmitted current is then given by using Fermi's golden rule

$$j_t = \frac{2\pi}{\hbar} \mid M_{rl} \mid^2 N_r, \tag{2.5}$$

where N_r is the density of states on the right system and M_{rl} is the tunneling matrix..

To fully describe the quantum tunneling current from left to right electrodes when a voltage bias (eV) is applied between the two systems separated by a tunneling barrier, as illustrated in Fig. 2.2, the Fermi function must be accounted for in Eq. 2.5. The transmitted current from left to right must be modified to account for the availability of density of states in the right system into which the electrons from the left system may tunnel, and the result is

$$j_t = \frac{2\pi}{\hbar} \mid M_{rl} \mid^2 N_r(1 - f_r), \tag{2.6}$$

where f_r is the Fermi function in the right system, $f_r = \frac{1}{e^{E/k_B T}+1}$, and $E = \epsilon - \epsilon_F$ is the energy, ϵ, measured relative to the Fermi level, ϵ_F. The total current from left to right with a voltage bias of eV is

$$j_{rl} \propto \int_{-\infty}^{\infty} \mid M \mid^2 N_l(E) N_r(E + eV) f_l(E)[1 - f_r(E + eV)] dE. \tag{2.7}$$

The transition of the right system from the initial state, Ψ_r, to the final state, Ψ_l, follows similarly, such that the net current is

$$j = j_{rl} - j_{lr} \propto \int_{-\infty}^{\infty} \mid M \mid^2 N_l(E) N_r(E + eV)[f_l(E) - f_r(E + eV)] dE. \tag{2.8}$$

For energy, E, near the Fermi level and at low temperatures, the value of the matrix element squared $\mid M \mid^2$ is assumed to be a constant that depends on the separation of the left and right

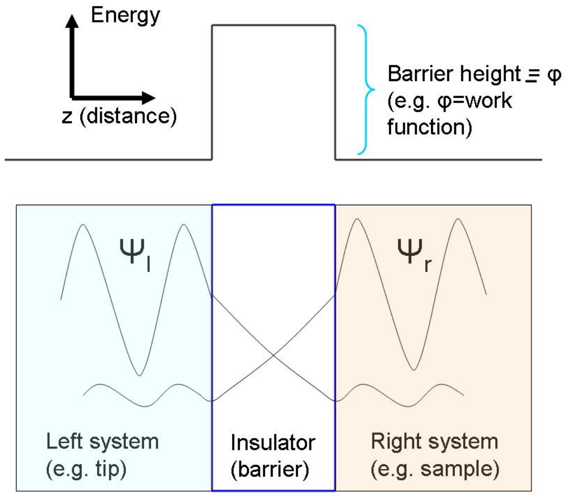

Figure 2.1: Simple schematic of quantum tunneling in one-dimension: The figure shows a simple one-dimensional rectangular potential for modeling quantum mechanical tunneling in one-dimension between two systems (left and right), using Bardeen's transfer Hamiltonian approach [88]. The approach is a time-dependent perturbation theoretical treatment to predict the quantum tunneling current that transfers between the left and right systems. The wavefunction of the left system, Ψ_l, and the wavefunction of the right system, Ψ_r, are labeled. For the left system, the formalism describes the transition rate from the initial state Ψ_l to the final state, Ψ_r, through interaction with the transfer Hamiltonian, H_T. The transition rate of the right-hand system is treated similarly.

systems. More concretely, the left and right systems may be considered to represent the tip (t) and sample (s) in an STM junction, separated by distance, z, and the tunneling matrix for a three-dimensional treatment is then given by

$$M_{ts} = -\frac{\hbar^2}{2m} \int d\mathbf{S} \cdot (\Psi_t^* \nabla \Psi_s - \Psi_s \nabla \Psi_t^*), \tag{2.9}$$

according to Ref. [88]. Here, $d\mathbf{S}$ is a surface integral over a surface within the tunneling barrier separating the tip and sample. Following the simple analysis of Refs. [91, 92], it is found that

$$\mid M \mid^2 \propto exp(-2\frac{\sqrt{2m\phi}}{\hbar}z), \tag{2.10}$$

where ϕ is the convoluted work function, or effective tunneling barrier, between the tip and the sample. The work function of simple metals, such as gold, are typically on the order of a few eV.

Assuming, in Eq. 2.8, that the tip is a simple metal with constant density of states and that

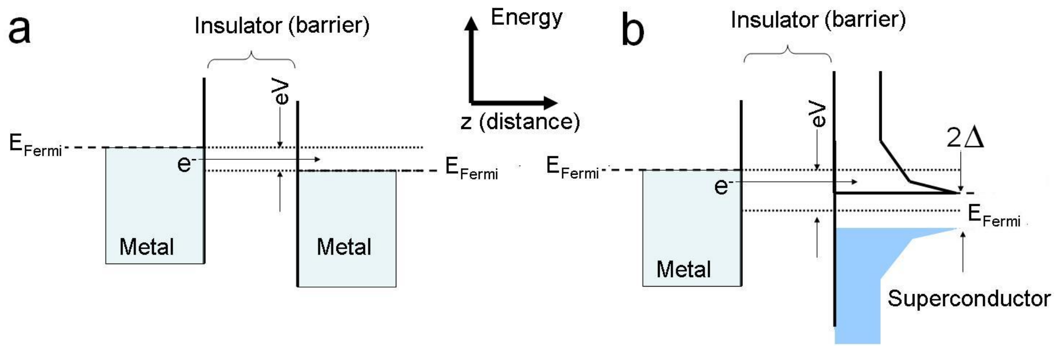

Figure 2.2: Bandstructure picture of quantum tunneling between two systems: (a) Schematic bandstructure picture of quantum tunneling between two metals at T = 0. The Fermi level is denoted E_F. Metals are expected to have a constant density of states that are filled to E_F at T = 0. (b) Schematic bandstructure picture of quantum tunneling between a metal and a superconductor at T = 0. The quasiparticle density of states for the superconductor is gapped by Δ, such that quantum tunneling cannot occur for $|eV| < \Delta$.

$|M|^2$ obeys Eq. 2.10, we may take $|M|^2$ and $N_t(E)$ outside of the integral in Eq. 2.8. The tunneling current at low temperature is then approximately given by

$$I \propto \int_{-\infty}^{\infty} N_s(E+eV)[\Theta(E+eV) - \Theta(E)]dE = \int_0^{eV} N_s(E+eV)dE, \qquad (2.11)$$

where $\Theta(x)$ is the heaviside function. The derivative of Eq. 2.11 for a superconductor is directly proportional to the quasiparticle density of states of the superconductor, $N_s(eV)$:

$$\frac{dI}{dV} \propto N_s(eV). \qquad (2.12)$$

To compute the density of states at finite temperatures, the Fermi functions must be retained in Eq. 2.8. The measured density of states is then approximately given by

$$dI/dV \simeq \int_{-\infty}^{\infty} \mid \frac{df(E+eV)}{dT} \mid \frac{dI}{dV}(E)dE. \qquad (2.13)$$

We measure the quasiparticle tunneling density of states in high-temperature cuprate superconductors for temperatures T ≪ T$_C$ to T > T$_C$. Based on Eqs. 2.12 and 2.13, we are then measuring the quasiparticle density of states of the superconductors.

2.2 Generalized Blonder-Tinkham-Klapwijk Tunneling Theory

While the transfer Hamiltonian formalism may be used to describe the quantum tunneling current between a normal metal and a superconductor (N-I-S tunneling), it does not completely account for all tunneling phenomena. Specifically, it does not account for Andreev reflection. Andreev reflection is an important effect in N-I-S quantum tunneling whereby an electron traveling toward the tunnel barrier from the normal metal side is reflected as a hole and a Cooper pair is transmitted to the superconducting side of the barrier. Andreev reflection occurs, for example, in the limit of point contact (N-S) tunneling for superconductors, but also may occur in N-I-S geometries for anisotropic superconductors, such as $d_{x^2-y^2}$-wave superconductors. Andreev reflection must be accounted for in order to understand the complete set of quasiparticle excitation spectra expected from a $d_{x^2-y^2}$-wave superconductor for tunneling along the {001}, {100}/{010}, and {110} directions. The formalism for describing N-I-S tunneling, by treating the problem as a scattering problem, is called the Blonder-Tinkham-Klapwijk (BTK) theory [93], and the generalization to anisotropic superconductors was described by Kashiwaya and Tanaka [94, 95, 96].

In Fig. 2.3, the four possible processes that arise when an electron from a normal metal travels at incident angle, θ_N, toward an insulating barrier and a superconductor are shown. The insulating barrier is modeled in the BTK theory as a delta function potential, $H\delta(x)$. The electron may either be reflected as a hole [a(E)], reflected as an electron in the normal side of the barrier at angle θ_N [b(E)], transmitted as an electron-like quasiparticle into the superconductor at angle θ_S [c(E)], or transmitted as a hole-like quasiparticle into the superconductor at angle θ_S [d(E)]. Here, a(E), b(E), c(E), and d(E) denote the coefficients for each process to occur, and probability conservation dictates that $\mid a(E) \mid^2 + \mid b(E) \mid^2 + \mid c(E) \mid^2 + \mid d(E) \mid^2 = 1$.

The net transmitted differential conductance of the junction obeys

$$dI/dV \propto \int_{-\infty}^{\infty} [f(E+eV) - f(E)][1 + \mid a(E) \mid^2 - \mid b(E) \mid^2] dE, \tag{2.14}$$

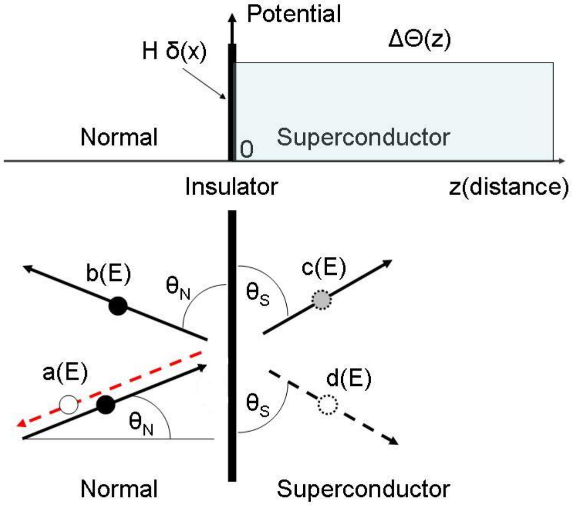

Figure 2.3: Top: The N-I-S junction is modeled as a normal metal (left) with pairing potential Δ=0. The insulating barrier (middle) is modeled as a delta-function barrier of potential, V=Hδ(x). The barrier height may be varied to model different insulating barriers or no barrier (H = 0). The pairing potential in the superconductor (right side) is modeled by $\Delta\Theta(x)$. Bottom: Possible BTK processes for N-I-S tunneling with an electron incident on the insulating barrier: [a(E)]: Andreev reflection and transmission of a Cooper pair into the superconductor from the surface. An incident electron transfers as a Cooper pair and a hole is reflected. [b(E)]: Specular electron reflection. [c(E)]: Transmission of the electron as a electron-like quasiparticle. [d(E)]: Transmission of the electron as a hole-like quasiparticle

which may be understood as the net transfer of electrons minus the reflection terms. Andreev reflection adds to the conductance because one electron approaches the boundary, and a pair travels through the boundary. Thus, the sign of the Andreev reflection term, $|\mathrm{a(E)}|^2$, is positive in Eq. 2.14 because it adds to the transmitted conductance. We may solve for a(E) and b(E) using the Bogoliubov-de-Gennes equations for spatially varying gap function and chemical potential [93, 94, 95]. The results, following Refs. [94, 95, 96], are given by

$$\begin{aligned} a(E) &= \frac{4\lambda\Gamma_{+}exp(-i\phi_{+})}{(1+\lambda)^2+4Z^2-[(1-\lambda)^2+4Z^2]\Gamma_{+}\Gamma_{-}exp(i\phi_{-}-i\phi_{+})} \\ b(E) &= \frac{-(1-\lambda^2-4iZ-4Z^2)[1-\Gamma_{+}\Gamma_{-}exp(i\phi_{-}-i\phi_{+})]}{(1+\lambda)^2+4Z^2-[(1-\lambda)^2+4Z^2]\Gamma_{+}\Gamma_{-}exp(i\phi_{-}-i\phi_{+})}. \end{aligned} \tag{2.15}$$

Here,

$$\begin{aligned} \Gamma_{\pm} &= \tfrac{E-\sqrt{E^2-\Delta_{\pm}^2}}{|\Delta_{\pm}|}, \\ \lambda &= \tfrac{k_{FS}cos(\theta_S)}{k_{FN}cos(\theta_N)}, \\ Z &= \tfrac{Z_0}{cos(\theta_N)}, \\ Z_0 &= \tfrac{mH}{\hbar^2 k_{FN}}, \\ \Delta_{\pm} &= \Delta(\pm\mathbf{k}_{FS}^{\pm}/k_{FS}) =\mid \Delta_{\pm} \mid \exp i\phi_{\pm}. \end{aligned} \tag{2.16}$$

The electron-like and hole-like quasiparticles wavevectors are given by $\mathbf{k}_{FS}^{+}$ and $-\mathbf{k}_{FS}^{-}$, respectively, and the two types of quasiparticles experience different pairing potentials, Δ_{+} and Δ_{-}, respectively.

Inputting Eq. 2.15 into the differential conductance in Eq. 2.14, (σ_S) across the N-I-S junction yields

$$\sigma_S = \sigma_N \frac{1 + \sigma_N \mid \Gamma_{+} \mid^2 + (\sigma_N - 1) \mid \Gamma_{+}\Gamma_{-} \mid^2}{\mid 1 + (\sigma_N - 1)\Gamma_{+}\Gamma_{-} \exp(i\phi_{-} - i\phi_{+}) \mid^2} dE, \tag{2.17}$$

with $\sigma_N = 4\lambda/[(1+\lambda)^2 + 4Z^2]$. If we assume $k_{FS}/k_{FN} \simeq 1$, then $\theta_N \simeq \theta_S \equiv \theta_{\mathbf{k}}$ may be assumed for simplicity. The differential conductance may then be modeled by

$$\frac{dI}{dV}(V) \propto \int d\theta_{\mathbf{k}} \left[1 + |a(E,\theta_{\mathbf{k}})|^2 - |b(E,\theta_{\mathbf{k}})|^2\right] e^{-\frac{\theta_{\mathbf{k}}^2}{\beta^2}}. \tag{2.18}$$

Here, the finite transverse momentum of the incident electrons arising in STM tunneling experiments is modeled using a tunneling cone defined by β. Equation 2.18 may then be used to model the expected quantum tunneling into a d$_{x^2-y^2}$-wave superconductor for the N-I-S geometry along the {001} direction (c-axis) or for tunneling into the CuO$_2$ planes (ab-plane tunneling) at any angle between the {100} and {010} directions. The expected differential conductances (dI/dV) for in-plane and c-axis tunneling are shown in Fig. 2.4 in the tunneling limit with $Z = 10$.

For tunneling momenta in-plane, or parallel to the CuO$_2$ planes, the d$_{x^2-y^2}$-wave order parameter is given by $\Delta(\theta_{\mathbf{k}}) = \Delta_0 cos(2\theta_{\mathbf{k}})$. The pairing potential experienced by the electron-like and hole-like quasiparticles are then

$$\begin{aligned} \Delta_{+} &= \Delta_0 \cos(2\theta_{\mathbf{k}} - 2\alpha) \\ \Delta_{-} &= \Delta_0 \cos(2\theta_{\mathbf{k}} + 2\alpha). \end{aligned} \tag{2.19}$$

Here, α is the angle between the normal vector of the interface and the {100} direction of the pairing potential, as illustrated in Fig. 2.5. For tunneling along $\alpha = 0$ or $\alpha = \pi/2$, the resulting dI/dV spectra in the tunneling limit resembles a "U" with coherence peaks at $\omega = \pm\Delta_0$ and no density of states below the coherence peaks. This case is shown in Fig. 2.4 and labeled as ab-plane tunneling when $\alpha = 0$. In contrast, tunneling along the {110} ($\alpha = \pi/4$) direction results in a zero-bias conduction peak when $\Delta_+ = -\Delta_-$. This case is shown in Fig. 2.4 and labeled as ab-plane tunneling when $\alpha = \pi/4$.

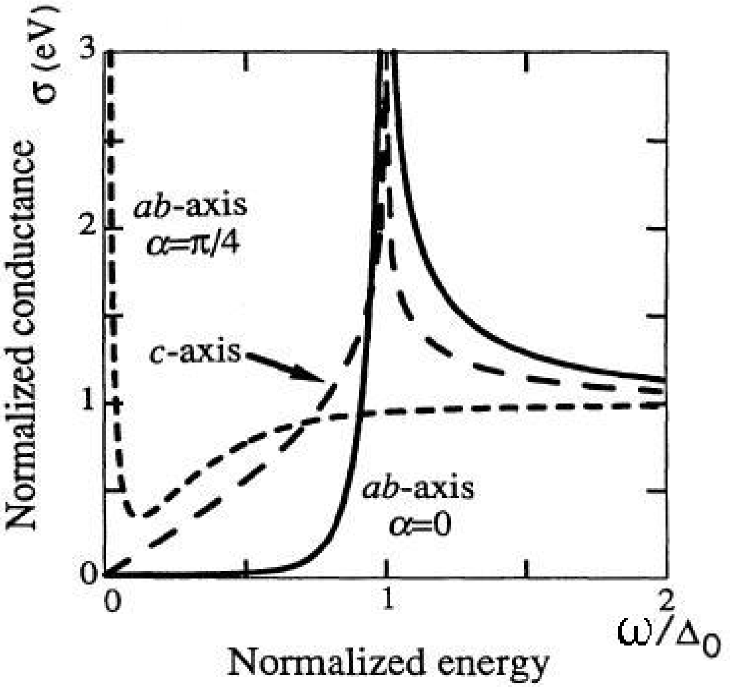

Figure 2.4: Figure reproduced from Ref. [96]. Directional dependence of tunneling into a $d_{x^2-y^2}$-wave superconductor: The expected results for tunneling experiments on $d_{x^2-y^2}$ superconductors for tunneling along the c-axis ({001} direction), into the ab-plane with $\alpha = 0$ ({100} direction), and into the ab-plane with $\alpha = \pi/4$ ({110}direction) are shown in the figure. For tunneling along the anti-nodal direction ({100} direction), the spectra resembles a "U". Peaks are located at $\omega = \pm\Delta_0$ in this scenario, and this scenario mimics the expected quasiparticle tunneling spectra for an s-wave superconductor with $\Delta_s = \Delta_0$. For tunneling along the c-axis, a V-shaped spectra is produced and has coherence peaks at $\omega = \pm\Delta_0$. Finally, tunneling along the nodal direction ({110}direction) produces a zero-bias ($\omega = 0$) tunneling peak. The peak arises from an Andreev bound state at the surface [95].

As $\sigma_N \rightarrow 0$, the normalized tunneling conductance reduces to the surface density of states, and the zero-bias conductance peak is associated with an Andreev bound state [95]. The energy of the surface Andreev bound state arises at the energy when the denominator of Eq. 2.17 equals zero. The equation for the denominator is given by

$$1 - \Gamma_{+}\Gamma_{-}e^{i(\phi_{-}-\phi_{+})} = 0 \tag{2.20}$$

as $\sigma_N \to 0$. Due to the fact that $\phi_{-} - \phi_{+} = \pi$ and $|\Delta_{+}| = |\Delta_{-}|$, the bound state energy occurs at $E = 0$.

For tunneling along the c-axis, a V-shaped spectrum is observed with peaks at $\omega = \pm\Delta_0$. This spectrum is observed because the tunneling cone flattens out for tunneling along this direction ($\beta \to \infty$) and all values of θ are sampled. This case is shown in Fig. 2.4c.

In this thesis, we measure hole-type $YBa_2Cu_3O_{7-\delta}$ (Y-123) with tunneling currents along the c-axis. We expect a V-shaped quasiparticle tunneling spectra because Y-123 has a (s+$d_{x^2-y^2}$)-wave superconducting order parameter [97, 35] with small s-wave component and dominant $d_{x^2-y^2}$-wave component. The s-wave component arises due to the orthorhombicity of Y-123. We also measure electron-type $La_{0.1}Sr_{0.9}CuO_2$ (La-112) along many randomly oriented grains. Our measurements in this thesis, as well as previous results from our group [39], find no evidence of a zero-bias conduction peak for any orientation of the grains in La-112 while the gap values determined from one half of the peak-to-peak energy separation also exhibit small variations. Although the zero-bias conductance peak (ZBCP) is a signature for superconductors with nodes, its presence is under the premise of the clean limit. Namely, the mean free path is much longer than the superconducting coherence length. In Y-123 the clean limit condition is indeed satisfied and the ZBCP has been clearly detected. On the other hand, in the event that the mean free path is comparable to or shorter than the superconducting coherence length, as in the case of La-112, it becomes difficult to assert the pairing symmetry solely based on the absence of the ZBCP. Moreover, based on other measurements on electron-type cuprate superconductors, the possibility of a $d_{x^2-y^2}$-wave superconductor coexisting with a competing order remains. We discuss the superconducting order parameters and the possible existence of competing orders that coexist with superconductivity more fully in La-112 and Y-123

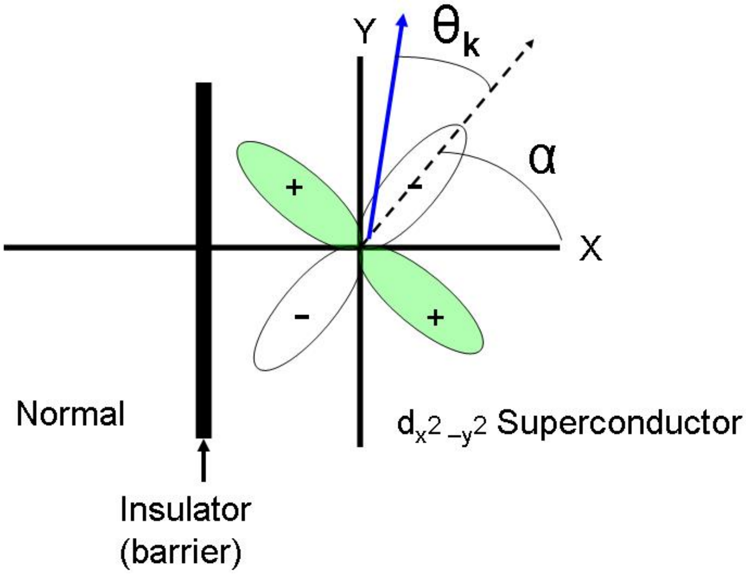

Figure 2.5: Definition of $\theta_{\mathbf{k}}$ and α for generalized BTK analysis of N-I-S tunneling: The normal (N) metal-insulator(I)-superconductor(S) geometry for ab-plane tunneling with the angles $\theta_{\mathbf{k}}$ and α defined relative to the anti-nodal direction ({100} direction)

in Chapters 4, 5, and 7.

Both the Bardeen transfer Hamiltonian formalism and the generalized BTK theory outlined above assume that the ground state of the superconductor consists of a single order parameter. Moreover, both formalisms assume infinite quasiparticle lifetime without considering quasiparticle scattering by either bosonic collective modes or impurities. Hence, these oversimplified formalisms cannot describe the vastly varying quasiparticle tunneling spectra among different cuprates of different families and doping levels. Incorporation of more than one order parameter in the ground state of the cuprates is an important step towards understanding the complexity of the low-energy excitations in the high-temperature superconductors.

2.3 "One-gap" versus "two-gap" phenomenological models of the quasiparticle excitations in cuprate superconductors

Among the unconventional and non-universal cuprate phenomena, the theoretical description of the spectral inhomogeneity observed in some hole-type cuprates and the Fermi arc phenomena in the hole-type cuprates have attracted much of the theoretical attention. The discussion of these phenomena in the context of the "one-gap" and "two-gap" models provides a useful assessment for the applicability of these theories in describing the physics of the high-temperature superconducting cuprates.

To predict the quasiparticle density of states, for comparison with tunneling experiments, and the quasiparticle spectral density function, for comparison with ARPES results, Green's function techniques may be employed. The Green's function may be calculated by specifying the Hamiltonian of the system to be described. For example, the low-energy effective superconducting Hamiltonian may be written as

$$\begin{aligned}\mathcal{H}_{SC} &= \textstyle\sum_{\mathbf{k},\sigma}\ \xi_{\mathbf{k}}\ c^{\dagger}_{\mathbf{k},\sigma}c_{\mathbf{k},\sigma} - \sum_{\mathbf{k}}\ \Delta_k\ \left(c^{\dagger}_{\mathbf{k},\uparrow}c^{\dagger}_{-\mathbf{k},\downarrow} + c_{-\mathbf{k},\downarrow}c_{\mathbf{k},\uparrow}\right) \\ &= \textstyle\sum_{\mathbf{k}}\ \left(c^{\dagger}_{\mathbf{k},\uparrow}\ c_{-\mathbf{k},\downarrow}\right)\begin{pmatrix}\xi_{\mathbf{k}} & -\Delta_k \\ -\Delta_k & -\xi_{\mathbf{k}}\end{pmatrix}\begin{pmatrix}c_{\mathbf{k},\uparrow} \\ c^{\dagger}_{-\mathbf{k},\downarrow}\end{pmatrix} \\ &\equiv \sum_{\mathbf{k}}\ \Psi^{\dagger}_{\mathbf{k}}\ H_{SC}\ \Psi_{\mathbf{k}},\end{aligned} \tag{2.21}$$

where $\xi_{\mathbf{k}}$ is the normal-state energy of particles of momentum $\mathbf{k}$ relative to the Fermi energy, σ is the spin index, $c^{\dagger}$ and c are the fermion creation and annihilation operators, and Δ_k denotes the superconducting energy gap. H_{SC} is the (2×2) matrix, and the adjoint of Ψ represents a (1×2) matrix $\Psi^{\dagger}_{\mathbf{k}} \equiv \left(c^{\dagger}_{\mathbf{k},\uparrow}\ c_{-\mathbf{k},\downarrow}\right)$. The mean-field superconducting Hamiltonian in Eq. (2.21) can

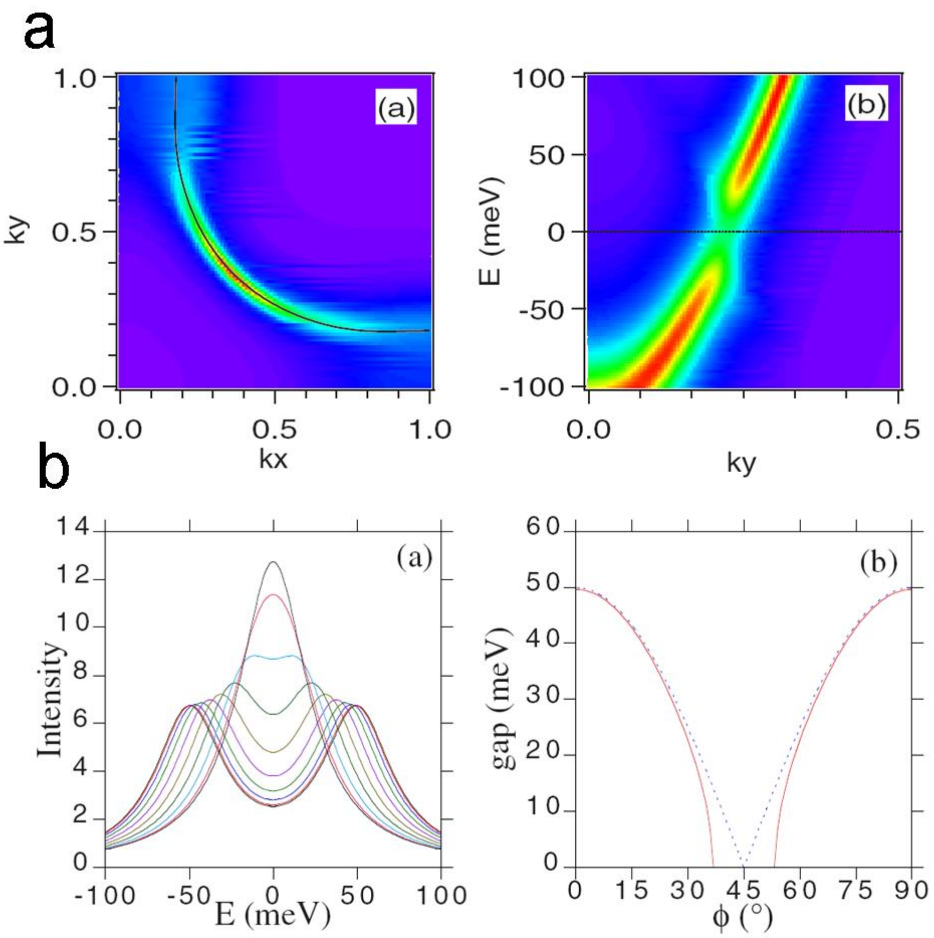

Figure 2.6: Generating the Fermi arc in a "one-gap" model treatment: (a) The spectral density functions as a function of **k**-space obtained by using a "one-gap" model. (b) The spectral density functions with fixed k$_x$ in **k**-space near $(\pi, 0)$ showing symmetric spectral density functions about the Fermi energy as a function of k$_y$. (c) Evolution of spectral density functions from the nodal to the anti-nodal direction. The nodal spectral density functions show peaks at $\omega = 0$, while the anti-nodal spectral density functions remain gapped above T$_C$. The spectral density functions are generated by assuming the persistence of disordered superconductivity for T$_C$ < T < T*. (d) The values of Δ_k-vs.-θ_k for finite Γ_k (red curve) and $\Gamma_k = 0$ (blue dashed curve). The case of finite Γ_k resembles a Fermi arc, while the case of $\Gamma_k = 0$ reproduces the expectation from a d-wave superconductor. [Figures reproduced from Ref. [8].]

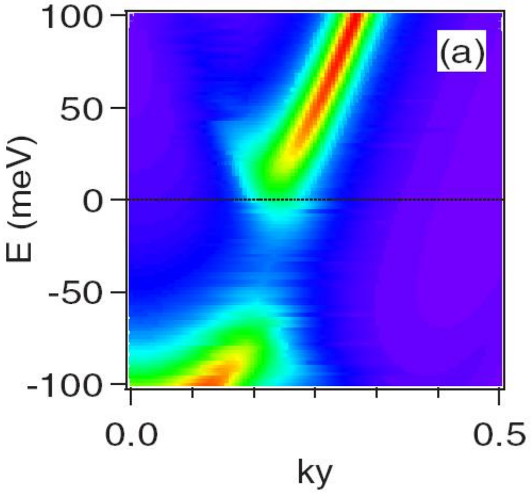

Figure 2.7: Energy dependence of points in **k**-space in a general “two-gap” model treatment: the spectral density functions at a fixed k_x point in **k**-space near $(\pi, 0)$ showing asymmetric spectral density functions about the Fermi energy. The results in the figure are based on two different approaches to model the “two-gap” scenario, and more details may be found in Ref. [8]. [Figure reproduced from Ref. [8].]

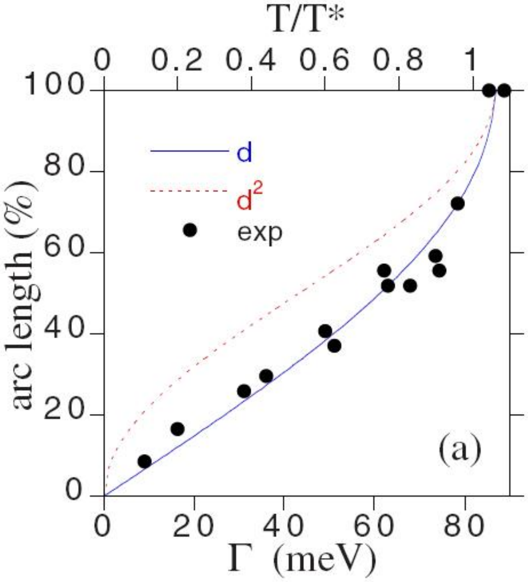

Figure 2.8: “One-gap” model fit of the temperature dependence of Γ_k for determination of Fermi arc percentages: The Fermi arc percentages-vs.-T/T* are fit to the “one-gap” model treatment in Ref. [8] to determine the expected temperature dependence of Γ_k in the model. The d^2 model shown is discussed more fully in Ref. [8] but does not directly relate to the discussion presented here. [Figure reproduced from Ref. [8].]

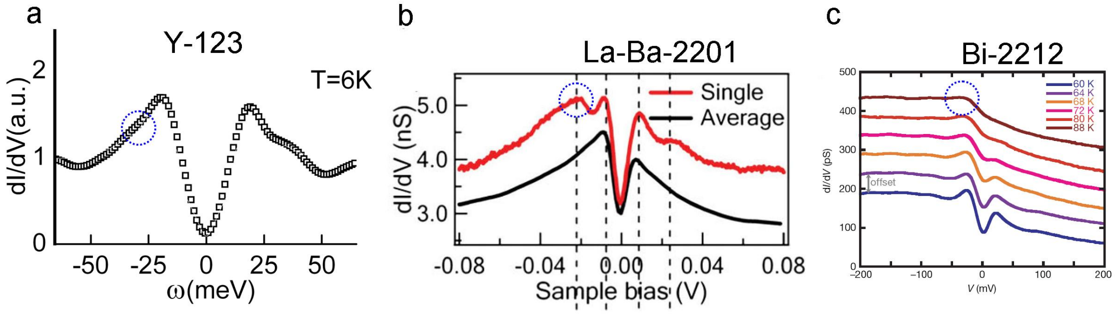

Figure 2.9: Evidence of van-Hove singularities in quasiparticle tunneling density of states measurements. The van-Hove singularities are circled in blue in the figures for: (a) our data in Y-123, to be presented more fully in Chapter 5, (b) data in La-Bi-2201 [70] [Figure reproduced from Ref. [70]], and (c) data in Bi-2212 [49] [Figure reproduced from Ref. [49]].

be exactly diagonalized so that the Green's function $G_0(\mathbf{k},\omega)$ is given by

$$G_0^{-1} = \omega I - H_{SC} = \begin{pmatrix} \omega - \xi_{\mathbf{k}} & \Delta_k \\ \Delta_k & \omega + \xi_{\mathbf{k}} \end{pmatrix}, \tag{2.22}$$

where I denotes the (2×2) unit matrix.

The Green's function will then yield the spectral density function according to

$$A(\mathbf{k},\omega) \equiv -\mathrm{Im}\left[G(\mathbf{k},\omega)\right]/\pi, \tag{2.23}$$

and the quasiparticle density of states according to

$$\mathcal{N}(\omega) \equiv \sum_{\mathbf{k}} A(\mathbf{k},\omega). \tag{2.24}$$

The value of $G_0^{-1}(\mathbf{k},\tilde{\omega})$ is given by

$$G_0^{-1}(\mathbf{k},\omega) = \omega - \xi_{\mathbf{k}} + i\Gamma_k - \frac{\Delta_k^2}{\omega + \xi_{\mathbf{k}} + i\Gamma_k}, \tag{2.25}$$

where Γ_k denotes the linewidth of the quasiparticles in this description and will obey $\Gamma_k \rightarrow 0$ in conventional superconductors. Using Eq. 2.25 to determine the spectral density function in Eq. 2.23,

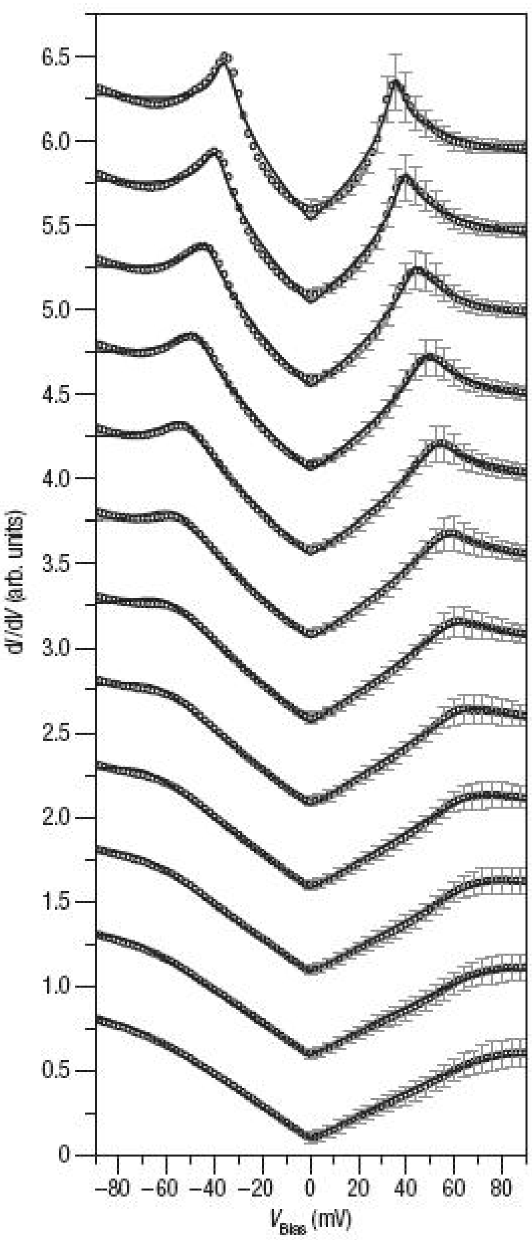

Δ_1 (meV)	Γ_2^* (meV)
38	1.2
43	2.2
48	3.7
53	5.2
57	7.3
62	10.4
67	13.7
72	17.1
77	19.5
82	21.7
87	25.4
92	30.0

Figure 2.10: Phenomenological fitting of spectral inhomogeneity using the "one-gap" viewpoint and Eq. 2.28: Various fits to the inhomogeneous spectra in Bi-2212 are shown [33]. [Figure reproduced from Ref. [33].]

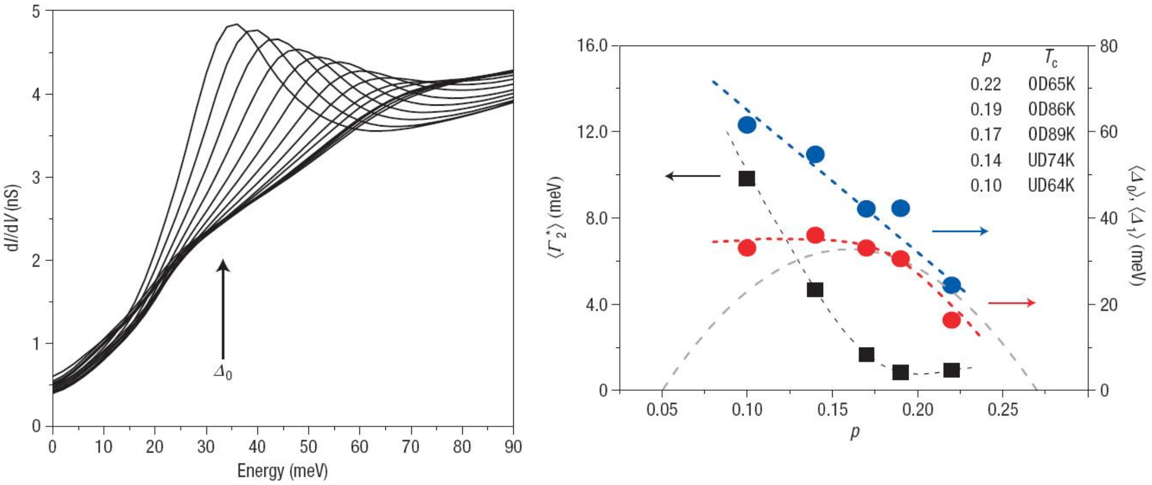

Figure 2.11: Inability of the the phenomenological fitting using the "one-gap" viewpoint to account for the "kink"-like feature in Bi-2212. Left panel: Experimental data in Bi-2212 zoomed in to show the "kink"-like feature more clearly. Right panel: The average "kink"-like feature ($< \Delta_0 >$, red circles), peak-to-peak feature ($< \Delta_1 >$, blue circles) and linewidth at Δ_1 ($< \Gamma_2^* >$, black squares) as a function of doping. [Figures reproduced from Ref. [33].]

while retaining the linewidth term, leads to:

$$A(\mathbf{k},\omega) = -\frac{1}{\pi}\frac{\Gamma_k(\omega^2-\xi_{\mathbf{k}}^2-\Delta_k^2-\Gamma_k^2)-2\Gamma_k\omega(\omega+\xi_{\mathbf{k}})}{(\omega^2-\xi_{\mathbf{k}}^2-\Delta_k^2-\Gamma_k^2)^2+4\Gamma_k^2\omega^2}. \tag{2.26}$$

With the definition of $A(\mathbf{k},\tilde{\omega})$ in Eq. 2.26, the spectral density functions in $\mathbf{k}$-space are defined so that the measurements by ARPES may be modeled. Further, by summing over the entire two-dimensional $\mathbf{k}$-space in the first Brillouin zone for c-axis tunneling experiments, the quasiparticle tunneling experiments can be modeled. As derived thus far, these models account for excitations from superconductivity alone in the ground state.

In Ref. [8], Eq. 2.26 is utilized to model the "one-gap" scenario of the Fermi arc phenomena in cuprates. In contrast to the expectation of a conventional superconductor, the value of Γ_k is assumed to be finite and constant as a function of $\mathbf{k}$. In Fig. 2.6a, the resulting spectral density functions based on the assumption of finite Γ_k for $\xi_{\mathbf{k}} = 0$ (the Fermi surface) using Eq. 2.26 in one quadrant of the Brillouin zone are shown. The result is a Fermi arc-like behavior. Furthermore, as stressed in Ref. [8], the gap in the spectral density function is symmetric about the Fermi energy in this scenario, as shown in Fig. 2.6b, and experimental ARPES and tunneling data is argued by the authors to be consistent with this behavior. Several individual spectra functions as well as a plot of Δ_k-vs.-θ_k along the Fermi surface are also shown in Figs. 2.6c and 2.6d. The spectral density functions are seen to be peaked near $\omega = 0$ near the nodal point ($\mathbf{k} = 0$), while the spectral density functions near the anti-nodal ($\mathbf{k} = (0, \pm\pi)/(\pm\pi, 0)$) points remain gapped. Overall the Δ_k-vs.-θ_k dependence qualitatively resembles the Fermi arc. Additionally, the values of Γ_k as a function of T/T* are modeled by fitting the Fermi arc lengths for superconducting cuprates [8] as a function of doping for $\mathrm{T}_C < \mathrm{T} < \mathrm{T}^*$ and are reproduced in Fig. 2.8. The question as to why Fermi arcs are not observed for $\mathrm{T} < \mathrm{T}_C$ arises from this analysis. Namely, it is shown in Fig. 2.6d that the Fermi arc disappears for $\Gamma_k = 0$ (blue-dashed line), but a finite Fermi arc is always present for finite values of Γ_k. Therefore, to explain the absence of the pseudogap for $\mathrm{T} < \mathrm{T}_C$, it must be assumed that Γ_k goes to zero upon crossing the superconducting transition temperature and rapidly increases to a finite value for $\mathrm{T}_C < \mathrm{T} < \mathrm{T}^*$. The validity of this assumption is questionable when comparison with empirical facts is made. In particular, for the Bi-2212 system on which the Fermi arc phenomena were based, strong spatial inhomogeneity was found in the tunneling spectra at $\mathrm{T} \ll \mathrm{T}_C$. This finding would imply a significant value of Γ_k, which is inconsistent with the assumption of $\Gamma_k = 0$ immediately below T_C.

In the analysis of Ref. [8], competing order models of the spectral density function are considered as well to explain ARPES data. However, it is argued that the spectral density functions at a given point in **k**-space are not in general centered about the Fermi energy for competing order models, as they are in the case of the “one-gap” consideration. Examples of the lack of centered energy for general competing orders models are shown in Figs. 2.7a and 2.7b. However, the assumption that a “two-gap” model in the cuprates must necessarily be asymmetric remains to be investigated. Namely, a more specific form of the “two-gap” model than is captured by the analysis of Ref. [8] may be necessary. For example, we consider the case of particle-hole pairs with equal magnitude of particle and hole energy to form charge- or spin-density wave in Chapter 7, and this assumption produces symmetric spectral density functions at a given point in **k**-space.

Interpretations of the symmetry of the pseudogap could also be examined in quasiparticle density of states spectra in order to differentiate between "one-gap" and "two-gap" models. However, the identification of symmetry from quasiparticle density of states data is further complicated by the observation of van-Hove singularity in the bandstructure of the cuprates (e.g., Ref. [98]) near the $(\pi, 0))$ points in **k**-space. Due to the fact that the quasiparticle density of states are enhanced near the van-Hove singularities, identification of symmetric or asymmetric pseudogap features or satellite features are expected to be obscured. Examples of van-Hove singularities affecting actual quasiparticle density of states, in the form of satellite features, are shown in Fig 2.9. Therefore, whether the "one-gap" or "two-gap" models are more relevant remains open to interpretation and requires further experiments and detailed analysis.

In addition to modeling the Fermi arc using "one-gap" analysis, the strongly inhomogeneous quasiparticle tunneling spectra in Bi-2212 [68, 99] has been modeled using "one-gap"-type analysis in Ref. [33]. The original functional form of the quasiparticle density of states for pure superconductors with a finite quasiparticle lifetime

$$N(\omega, \Gamma_k) = A \times Re\left(\frac{\omega + i\Gamma_1}{\sqrt{[\omega + \Gamma_1]^2 - \Delta_k^2}}\right) \tag{2.27}$$

is assumed to be extended to

$$N(\omega, \Gamma_k) = A \times Re\left(\frac{\omega + i\Gamma_2}{\sqrt{[\omega + \Gamma_2(\omega)]^2 - \Delta_k^2}} + B \times E\right) \tag{2.28}$$

in Ref. [33]. Here, Γ_1 is a constant linewidth term and is equivalent to Γ_k for the analysis of Ref. [8] discussed above. The extension of the functional form of the quasiparticle density of states assumes that Γ_2 may now be a function of energy, ω. Further, the term $B \times E$ is implemented to mimic the strong particle-hole asymmetry observed in the quasiparticle density of states of Bi-2212 [33, 99, 100, 68]. Additionally, the energy dependence of $\Gamma_2(\omega)$ is assumed to obey $\Gamma_2(\omega) = \alpha\omega$, with α being an empirically modeled parameter. The ad hoc assumption of linear dependence on ω in $\Gamma_2(\omega)$ is crucial to analysis of the quasiparticle observed in Bi-2212 because the zero energy

($\omega = 0$) density of states observed experimentally is equal to zero within experimental uncertainty for all spatially inhomogeneous spectra. Based on this assumption, the highly broadened peaks, at $\mid \omega \mid = \Delta_1$ for quasiparticle spectra with large peak-to-peak gap values, $\Delta_{pk-pk} = \Delta_1$, may be accounted for in addition to the zero energy ($\omega = 0$) density of states. Results of fitting to data using Eq. 2.28 are reproduced in Fig. 2.10 for comparison.

An important feature that the above analysis cannot account for is the homogeneous "kink"-like feature observed in the quasiparticle spectra in Bi-2212 [68]. To investigate the "kink"-like feature further, Ref. [33] computed the average "kink"-like feature values ($< \Delta_0 >$) as a function of position from spatially resolved maps and found that the feature was correlated with the superconducting dome. A plot of $< \Gamma_2^* >=< \Gamma_2(\Delta_1) >$, $< \Delta_1 >$, and $< \Delta_0 >$ as a function of doping in Bi-2212 is reproduced in Fig. 2.11 where Δ_1 is the gap associated with the rounded, dominant peaks in the spectra and Δ_0 is associated with the kink-like feature. While the apparent rise of Γ_2^* is interesting, it cannot be ascertained whether this "one-gap" model may better fit this observation than a "two-gap" model. Namely, it is unclear if the behavior of Γ_2^* is due to disordered superconductivity or competing orders interacting with superconductivity. Further, the fact that $< \Delta_0 >$ follows the values of T_C implies that this feature is highly important to superconductivity. Therefore, an equally valid assumption would be that $< \Delta_1 >$ is either due to a competing order or due to combined effects of superconductivity and a competing order in a "two-gap" model, while $< \Delta_0 >$ relates directly to the superconducting gap. Overall, the analysis of Ref. [33] in fact finds two energy scales in the process of "forcing" the validity of the "one-gap" model, which seems self contradictory. Moreover, the energy linewidth Γ_2 for the quasiparticle scattering rates at $\mathrm{T} \ll \mathrm{T}_C$ is unreasonably large, which also contradicts the assumption made for the "one-gap" Fermi arc model in Ref. [8] where Γ_k must be forced to 0 below T_C.

At this point, it seems natural to develop a more quantitative "two-gap" model to compare with ARPES and quasiparticle density of states data. In fact we have detailed such analysis using Green's function techniques, and the results are more fully discussed and presented in Chapter 7. Briefly, the modifications to the theory for the "two-gap" scenario may be summarized by substituting an effective gap, $\Delta_{eff}(k)$, into the above "one-gap" analysis for Δ_k. The effective gap is rigorously determined by the Green's function techniques to be $\Delta_{eff}^2 = \Delta_{SC}^2 + V_{CO}^2$, where the superconducting gap energy is denoted by Δ_{SC} and the competing order energy, for the density-wave orders considered in this work, is denoted by V_{CO}. This formula holds, for example, for spin- and charge-density waves. As a concrete example, the spectral density function at the mean-field level becomes

$$A(\mathbf{k}, \omega) = -\frac{1}{\pi} \frac{\Gamma_k(\omega^2 - \xi_{\mathbf{k}}^2 - \Delta_{eff}^2 - \Gamma_k^2) - 2\Gamma_k \omega(\omega + \xi_{\mathbf{k}})}{(\omega^2 - \xi_{\mathbf{k}}^2 - \Delta_{eff}^2 - \Gamma_k^2)^2 + 4\Gamma_k^2 \omega^2}. \tag{2.29}$$

The Fermi arcs may then be accounted for if V_{CO} persists above T$_C$ to the pseudogap temperature, T*. Further, the effective gap may be modeled to vary as a function of position in **k**-space according to the density-wave wavevector and the variations in the wavevector due to interactions with disorder, which are parameterized by $\mathbf{Q}_{CO}$ and $\delta\mathbf{Q}$, respectively. Based on empirical clues to pinpoint the type and location of competing orders relevant in cuprates, the satellite features and the superconducting coherence peaks unexplained by the "one-gap" model may then be fully accounted for using this "two-gap" model. Moreover, consistent modeling between tunneling spectra and ARPES data using our "two-gap" model also contrasts the inconsistency of "one-gap" models for two different types of experiments. We reserve further discussion for Chapter 7.

Chapter 3

Instrumentation

3.1 Scanning tunneling microscopy and spectroscopy

3.1.1 STM operation modes

The technique of scanning tunneling microscopy (STM) was invented in 1981 by Gerd Binnig and Heinrich Rohrer [101, 102] and has since been a vital tool for studying physics and material properties with atomic resolution. To perform STM experiments, a sharp tip is brought to within several angstroms of a sample surface to be examined, while a voltage bias is applied between the tip and sample. For a sufficiently small vacuum gap between tip and sample, a quantum mechanical tunneling current flows between the tip and sample, and the current depends on the electronic density of states of the tip and sample as well as the voltage bias, the tunneling barrier, and the distance between tip and sample. By using a metallic tip, with an essentially constant density of states (DOS) near the Fermi level, STM can provide information on the electronic density of states and the constant tunneling current topography of the sample. In this thesis, we utilize the scanning tunneling spectroscopy (STS) capability of STM to investigate the local quasiparticle DOS of the high-temperature cuprate superconductors $YBa_2Cu_3O_{7-\delta}$ (Y-123) and $La_{0.1}Sr_{0.9}CuO_2$ (La-112) with atomic level spatial resolution. Spatially resolved STS studies are vital when studying the cuprate superconductors because nanometer-scale variations in the electronic properties have been reported in some systems (e.g., Ref. [68]) and the nanometer-scale superconducting coherence lengths for cuprates(ξ_{SC} ~2–5nm, ξ_{SC}: superconducting coherence length) are susceptible to disor-

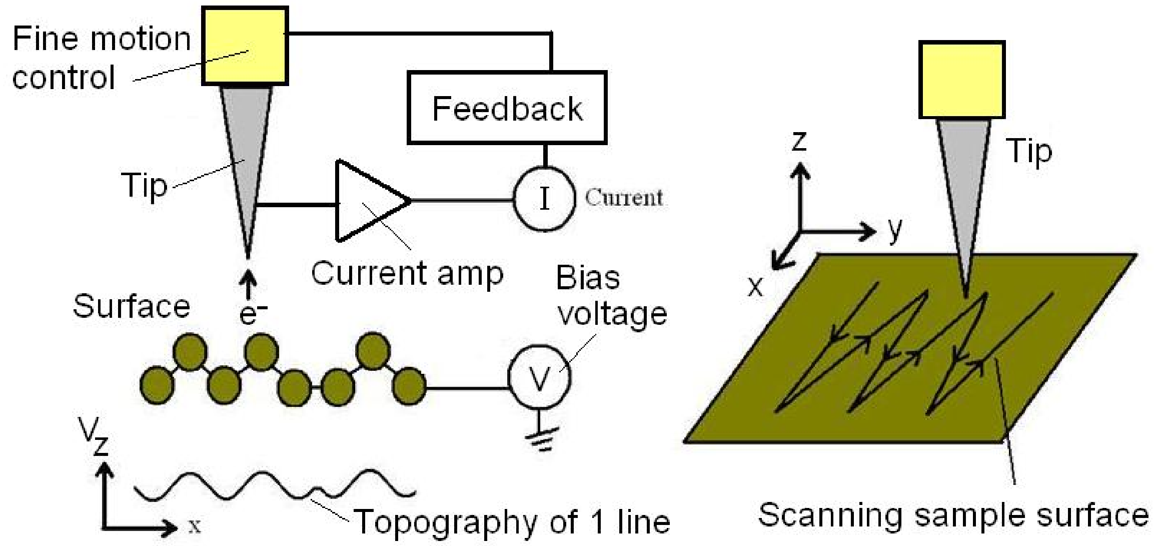

Figure 3.1: Basic illustration of a scanning tunneling microscope: A sharp tip is brought close enough toward the surface of a voltage-biased sample so that a detectable quantum mechanical tunneling current may be detected. In the constant-current topography mode of STM operation, the tip is scanned across the surface and a constant current is maintained by a feedback loop. The tip-sample separation necessary to maintain a constant current is controlled by a piezoelectric tube scanner, discussed in more detail in Fig. 3.3. The topographic signal is given by the z-piezo voltage of the tube scanner, V_z, needed for the feedback loop to maintain a constant-current as the tip is scanned.

der fluctuations. Furthermore, studies of the vortex-state of cuprate superconductors require spatial resolution better than ξ_{SC} to adequately characterize the intra-vortex and inter-vortex electronic DOS, or the quasiparticle excitation spectra.

In order to perform STM experiments with atomic resolution, the STM tip must be brought within several angstroms of the sample surface and must then be moved laterally with sub-angstrom control. In addition, the small quantum tunneling currents (1pA–100nA) must be detected with a large signal-to-noise ratio. To meet these requirements, piezoelectric elements are employed to achieve fine motion control, and the STM instrumentation must be designed to achieve sufficiently small acoustic, vibrational, and electronic noises to resolve the small STM signals. Piezoelectrics typically provide control on the order of 1nm/V, and the typical electronic noise for a well designed STM system is on the order of a few pA.

There are three modes of STM operation that we concern ourselves with here: the constant-current imaging, the constant-height imaging, and the constant tip-junction resistance spectroscopy modes. All three modes require sophisticated instrumentation to perform experiments, which we discuss more fully below. Briefly, the block diagram of the STM and the electronics associated with the operation are shown in Fig. 3.2. Coarse-motion stages (XY-stage and Z-stage) initially position the tip near the sample, and then fine motion control is achieved by a piezoelectric (piezo) tube scanner. The STM controller[1] controls the voltage bias between the tip and sample, measures the tunneling current after amplification, communicates with the feedback controller, and applies voltages to control the piezo tube scanner.

The constant-current imaging mode is an STM mode of operation that is used to measure the topography associated with a constant tunneling current between the tip and sample. This mode is commonly associated with the ability to resolve individuals atoms on a surface of interest, such as our measurements showing individual atoms on highly-oriented pyrolytic graphite (HOPG) shown in Fig. 3.4. A constant-current imaging scan is performed by engaging the STM controller feedback circuit, which maintains a constant tunneling current between the sample and the tip, and scanning the tip across the sample by changing the high-voltage outputs to the piezo tube scanner. Throughout this process a constant voltage bias is maintained between the tip and sample. The desired tunneling current for imaging may be selected by adjusting the set point current, I_{set}, of the feedback loop. The topography of the surface, $z(x, y)$, is determined by the voltage applied to the z-piezo of the piezo tube scanner, V_z, in order to maintain a constant current between the tip and sample and the conversion relation between V_z and $z(x, y)$. An illustration of scanning in the constant-current mode is shown in Fig. 3.1.

Ideally, each point in an image of the constant-current mode is obtained with a constant-current; however, the feedback loop does not respond instantly to changes in topography. Therefore, the gain and time-constant, τ, of the STM feedback control on the STM controller must be adjusted such that the tip can follow the contours of the surface as accurately and quickly as possible. Rough surfaces require the feedback loop to respond to changes in topography quick enough to avoid a "crash" between the tip and sample. The scanning speed and feedback parameters must be optimized in

---

[1] SPM 1000 Controller from RHK Technology

constant-current imaging mode in order to obtain useful images without tip changes arising from "crash" events. Moreover, the scan speed and feedback loop should be optimized due to the fact that the more time it takes to measure topography, the more susceptible the STM measurement is to low frequency noise contributions.

In contrast to constant-current imaging mode, constant-height imaging mode avoids many of the complications associated with the feedback loop of the STM. Constant-height imaging mode is obtained by turning off the feedback loop and measuring the resulting tunneling current as the tip is scanned across the sample. The tip may be scanned more quickly in constant-height mode because the feedback loop response time is no longer a factor. The scan speed is limited by the response time of the current pre-amplifier, and the upper limit of scan speed is determined by the lowest mechanical resonance of the STM head. An advantage of scanning faster in constant-height mode is the fact that the effects of low frequency noises, such as building vibrations ($f \sim 1 - 20 Hz$), on topography images are reduced. The topography, $z(x,y)$, in constant-height mode is obtained by assuming an exponential relation between the measured tunneling current and the distance between tip and sample, such as would be expected for Eqs. 2.10 and 2.11. However, the actual height between tip and sample requires knowledge of the local tunneling barrier height; thus the relative height is usually measured in constant-height topography mode. The surface must be relatively flat (nearly atomically flat) to avoid tip contact with the sample in constant-height mode and to maintain tunneling currents large enough to be measurable by the electronics.

Operation of the STM in constant tip-junction resistance spectroscopy mode allows measurements of the tunneling current-(I-)vs.-voltage bias (V_{bias}) or measurements of the tunneling differential conductance-(dI/dV-)vs.-V_{bias} to be made. The dI/dV-vs.-V_{bias} may also be computed numerically from I-vs.-V_{bias} measurements. As was discussed in Chapter 2, measurements of the tunneling differential conductance for superconducting samples provide a measurement of the quasiparticle excitation spectra. Initially constant tip-junction resistance spectroscopy is performed similar to the constant-current imaging mode of operation in that a constant voltage bias is applied to the sample while the feedback loop adjusts the tip height to maintain a constant tunneling current at each pixel. After establishing the desired tip-junction resistance at each pixel in a spectroscopy map, the feedback loop is disabled in order to perform spectroscopy. This mode is referred to as constant tip-junction resistance spectroscopy mode because the tip junction resistance is given by $R_{junction}$ =V$_{bias}$/I, and the tip-sample junction resistance is the same at each pixel of the spectroscopy map.

The surface topography of the sample is approximately eliminated from measurements of spatially resolved differential conductance maps in constant tip-junction resistance spectroscopy mode for a homogeneous surface. This fact arises for a homogeneous surface because constant tip-sample junction resistance ensures approximately constant tip-sample height separation at each pixel in this scenario. For the general case of examining cuprate superconductors, which are known to have varying local density of states on the order of a few nanometers in some cases [68], the voltage bias must be set to exceed the energy scale over which variations are observed to maintain an approximately constant height. For Y-123 and La-112 considered here, we do not observe such inhomogeneity in zero-field spectra, and variations in quasiparticle spectra in a finite magnetic field occur up to $\omega = \pm\Delta_{eff} =\sim \pm$40meV. Therefore, we apply V$_{bias}$ =-80meV and expect that constant-junction resistance spectroscopy mode eliminates surface topography roughness from measurements of spectroscopy to a first approximation in Y-123 and La-112. Additional electrical cross-talk between the high-voltages on the tube scanner and the signal at the tunneling tip are also minimized by our instrumentation to eliminate the effect of topography roughness on dI/dV-vs.-V$_{bias}$ maps in constant tip-junction resistance spectroscopy mode.

The majority of measurements performed in Chapters 4 and 5 are measurements of constant tip-junction resistance spectroscopy measurements. Typical resistances used were 1GΩ, with I$_{set}$=-80pA, V$_{bias}$=-80meV. At each pixel in a spatially resolved scanning tunneling spectroscopy (STS) map, an I-vs.-V$_{bias}$ curve was taken. The differential conductance, dI/dV, was then numerically computed from the I-vs.-V$_{bias}$ curves to determine the local quasiparticle DOS from dI/dV-vs.-V$_{bias}$. We now describe the instrumentation of our STM for performing these measurements.

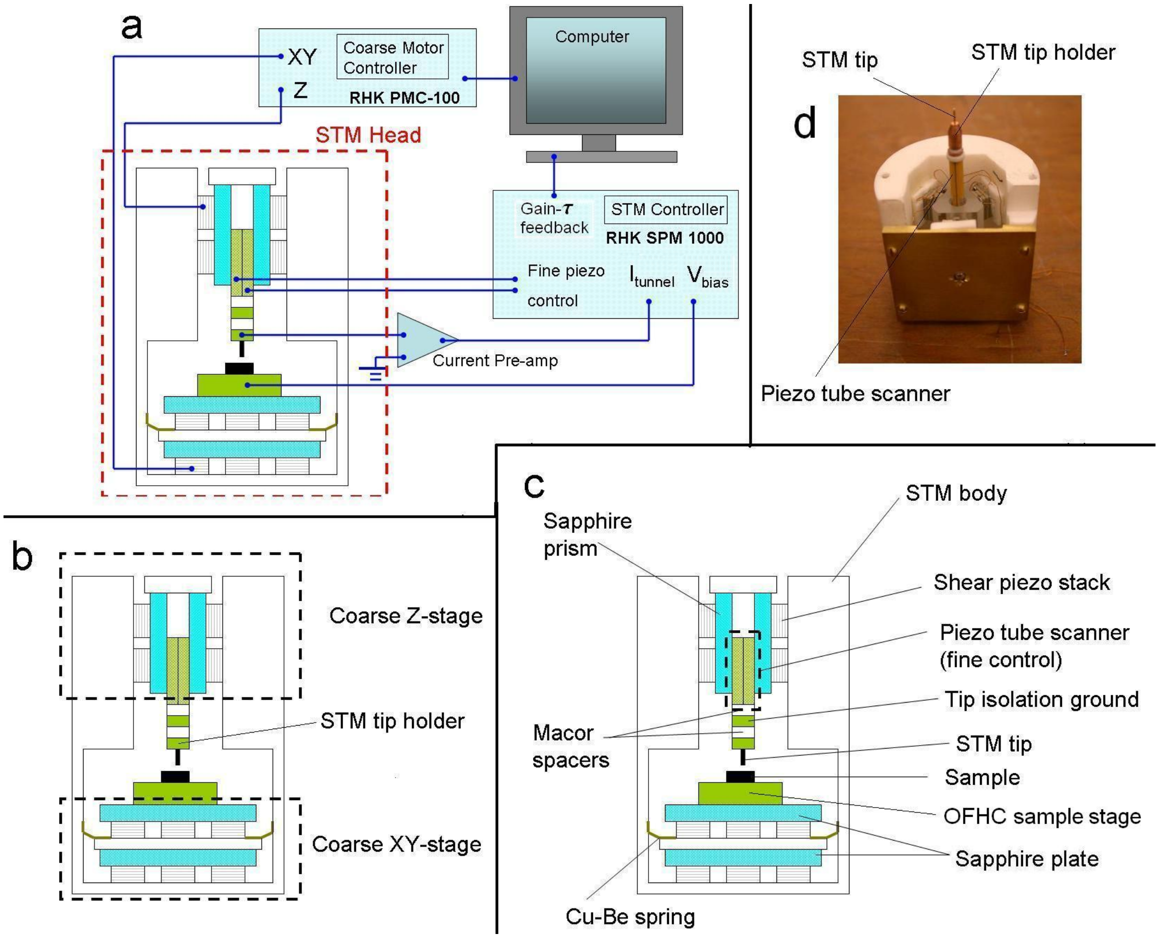

Figure 3.2: Overview illustration of the STM head. (a) Schematic drawing of the STM and the connections to the STM controller and the coarse approach motor controller. The STM controller controls the piezoelectric tube scanner movement, measures the quantum tunneling current, applies the voltage bias, V_{bias}, for imaging and spectroscopy, provides the feedback loop to control tip height, and records all data to the computer. Each of the voltages necessary to manipulate the piezoelectric tube scanner (V_z, V_x, V_y,V_{-x}, V_{-y}), which are shown in Fig. 3.3, can be varied from -215V to 215V to provide fine motion control. In addition, the coarse approach motor controller applies a high-voltage waveform (amplitude up to 300V), shown in Fig. 3.5e, to the piezoelectric shear stacks in order to move the XY- or Z-stages in coarse steps. The coarse step process is illustrated more fully in Fig. 3.5. (b) Schematic illustration of the location of the XY- and Z-coarse stages, as well as the tip holder. (c) A more detailed map of the STM head. The piezoelectric tube scanner is controlled by the STM to provide fine (atomic-resolution) motion. An electrically insulating Macor spacer attaches to the end of the tube scanner to prevent electrical shorts between the tip isolation ground and the tube scanner connections. (Macor is a machineable ceramic made by Corning, Inc.) The tip isolation ground helps to decouple the high voltage piezo tube scanner signals from the tunneling current detected at the STM tip. Another Macor space separates the tip isolation ground from the STM tip to prevent an electrical short between the two. The STM tip, oxygen-free high thermal conductivity (OFHC) copper sample stage, and the sample are shown in the figure. The shear piezoelectric (piezo) stacks, the sapphire plates, the sapphire prism, and the copper-beryllium (Cu-Be) springs that comprise the XY- and Z-stages for coarse motion are also shown. The Z-stage coarse motion parts are discussed in more detail in Fig. 3.5. A resistive heater is mounted directly to the top sapphire plate of the XY coarse-motion stage in order to raise the temperature of the STM above the temperature of the cryogenic bath. A Cernox temperature sensor (purchased from Lakeshore Cryotronics, Inc.) was located on the OFHC sample stage. (d) A picture of the actual STM head without the XY-stage attached. The design of the STM head combines elements of design from Refs. [103, 104].

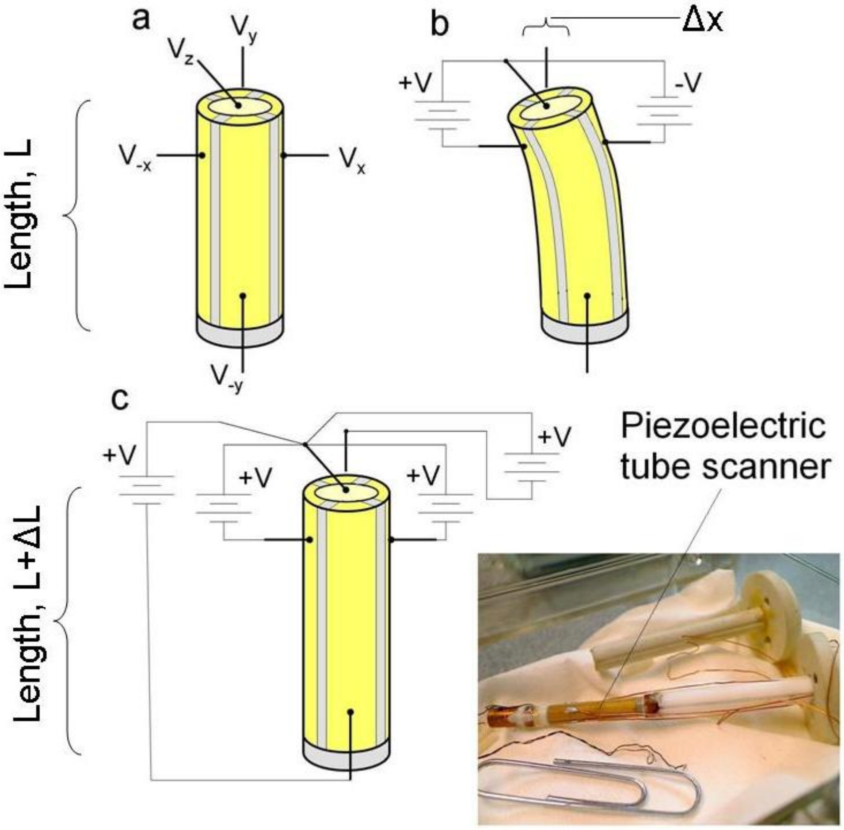

Figure 3.3: Schematic illustration of the functionality of the piezoelectric tube scanner: (a) Schematic illustration of the piezoelectric tube scanner. The tube scanner used was a hollow cylinder with dimensions of: O.D. = 0.125”, I.D = 0.085”, length = 0.600”. It is divided into four quadrants of shear piezos to provide scanning motion in the x- and y-directions. The piezoelectric tube scanner showing the connections to the four quadrants (V$_x$, V$_y$,V$_{-x}$,V$_{-y}$), as well as the shared connection to the inner surface of the piezoelectric tube (V$_z$), are shown in the figure. (b) By applying an equal positive and negative voltage to opposite quadrants relative to V$_z$, the piezoelectric tube scanner will shear oppositely on the two quadrants and provide a displacement for scanning. A representative displacement (Δx) along the x-direction is shown. The value of $\Delta x = \frac{0.9 d_{31} V L^2}{d_m t}$, where d_{31} is the shear piezo contast, V is the voltage applied, L is the length of the tube scanner, $d_m = (O.D.{+}I.D)/2$, and t is the wall thickness of the tube scanner. The value of d_{31} at T = 293K for an EBL#2 piezo is -0.173nm/V on average. However, the actual value is gained by calibrating each tube scanner. (c) If an equal voltage is applied to all four quadrants relative to V$_z$, the tube scanner will extend by an amount, $\Delta L = \frac{d_{31} V L}{t}$. For simplicity, it can be considered that the quadrant voltages, (V$_x$, V$_y$,V$_{-x}$,V$_{-y}$), control the motion in the x- and y-directions, while V$_z$ controls the height of the tube scanner. Other configurations to control motion are possible, but a full discussion is beyond the scope of this work. (d) A picture of an actual piezoelectric tube scanner. Actual tube scanners used in this work were calibrated on highly-oriented pyrolytic graphite (HOPG) to determine the calibrated voltage dependence of Δx, Δy, and ΔL. A representative calibration of a piezoelectric tube scanner on graphite showing atomic resolution topography, from the constant-current topography mode of STM operation, is shown in Fig. 3.4.

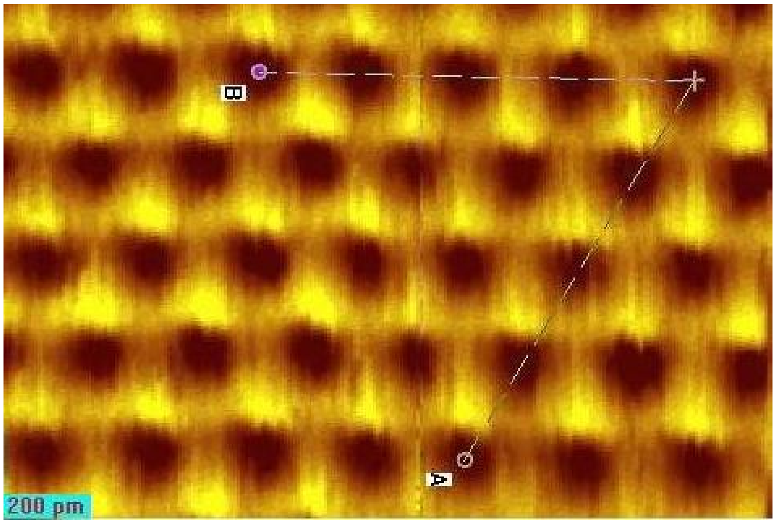

Figure 3.4: A representative topographic image measured on HOPG using a piezo tube scanner. The image shows atomic resolution topography obtained using the constant-current topography mode of STM operation. The image was used to calibrate the piezo tube scanner motion, and the carbon-carbon separations were found to be ~ 0.142nm upon proper calibration, as expected.

3.1.2 STM instrumentation

To perform reliable STM measurements on cuprate superconductors, sophisticated instrumentation is required to bring the STM tip close enough to the sample to perform scanning measurements, to cool the sample to cryogenic temperatures, to apply magnetic fields, to achieve ultra-high vacuum (UHV) at cryogenic temperatures, and to reduce electronic, vibrational, and acoustic noise from measurements. In addition, the sample surface for measurement and reliable STM tips that provide reproducible results must be prepared. The sample surface preparation for La-112 and Y-123 is discussed in Chapters 4 and 5, and the rest of the instrumentation is discussed below.

The preparation of the STM tip is crucial to achieving reproducible topography and spectroscopy from measurements on any surface. Two commonly used tip materials are tungsten (W) tips and platinum-iridium (Pt-Ir) tips. Our STM does not achieve UHV conditions until we reach cryogenic temperatures. Therefore, Pt-Ir tips are used because they are more inert and do not oxidize as quickly as W tips. Our tips are prepared following the methods of Ref. [105]. In brief, we mechanically cut our tips until they are optically sharp, as observed by an optical microscope at $\sim \times 25$ magnification. The cut tips are then electrochemically etched for approximately 10 seconds in a solution of $CaCl_2{\cdot}2H_2O$ (∼35 g), de-ionized water (∼200 mL), and acetone (∼10 ml) at 10–15V_{AC}. The mechanically cut tips are immersed into the solution to a depth of 1-3mm. Electrochemically etched tips were also purchased for use as STM tips[2]. We found that the purchased tips also required processing according to the methods of Ref. [105] to achieve atomic resolution topography on HOPG. Prepared STM tips were loaded into the STM head and held by the tip holder, as is shown schematically in Fig. 3.2b and in actuality in Fig. 3.2d.

Fine motion scanning of the STM tip was performed by the piezoelectric tube scanner. The tube scanner is shown schematically in Fig. 3.2b and in actuality in Fig. 3.2d. The piezoelectric tube scanners[3] used were cylindrical and divided into four quadrants of shear piezoelectrics. The operation of the tube scanner is illustrated in Fig. 3.3. The four quadrants are sheared simultaneously to move the tip toward the sample, while the x and -x or y and -y quadrants are sheared oppositely to scan the tip along the x or y directions respectively. Shearing occured when a voltage was applied between the inner surface of the tube scanner, on the z-piezo voltage connection (V_z), and any of the connections to the quadrants (V_x, V_{-x}, V_y, V_{-y}). By controlling all possible linear combinations of shearing motions using the STM controller, the tip may be scanned and the tip-sample separation controlled for all the modes of STM operation. At room temperature, the tube scanner could approximately scan an area given by $30\mu m \times 30\mu m$ with a vertical range of $\sim 15\mu m$. At liquid helium temperatures the xy-range reduced to $10\mu m \times 10\mu m$ and the vertical range to $\sim 4.5\mu m$.

With a reliable tip loaded into the STM, the tip must be positioned close enough to the sample so that the piezoelectric tube scanner can scan the sample for STM measurements; to achieve this feat, the coarse motion stages brought the tip close enough to the sample and adjusted the position of the sample under the tip. The principle for the XY- and Z-coarse motion stages are similar, and the principle of the Z-stage is illustrated in Fig. 3.5.

The motion of the coarse Z-stage is accomplished through the use of shear piezoelectric stacks[4]. The STM tip holder and piezoelectric tube scanner are held within a sapphire prism, as shown in

---

[2] Purchased from Agilent Technologies

[3] 0.020″ thick, 0.125″ OD, EBL #2 tube scanner purchased from EBL Products, Inc.

[4] Stacks of four 0.040” thick EBL #2 shear piezoelectrics. Individual shear piezos were purchased from EBL Products, Inc.

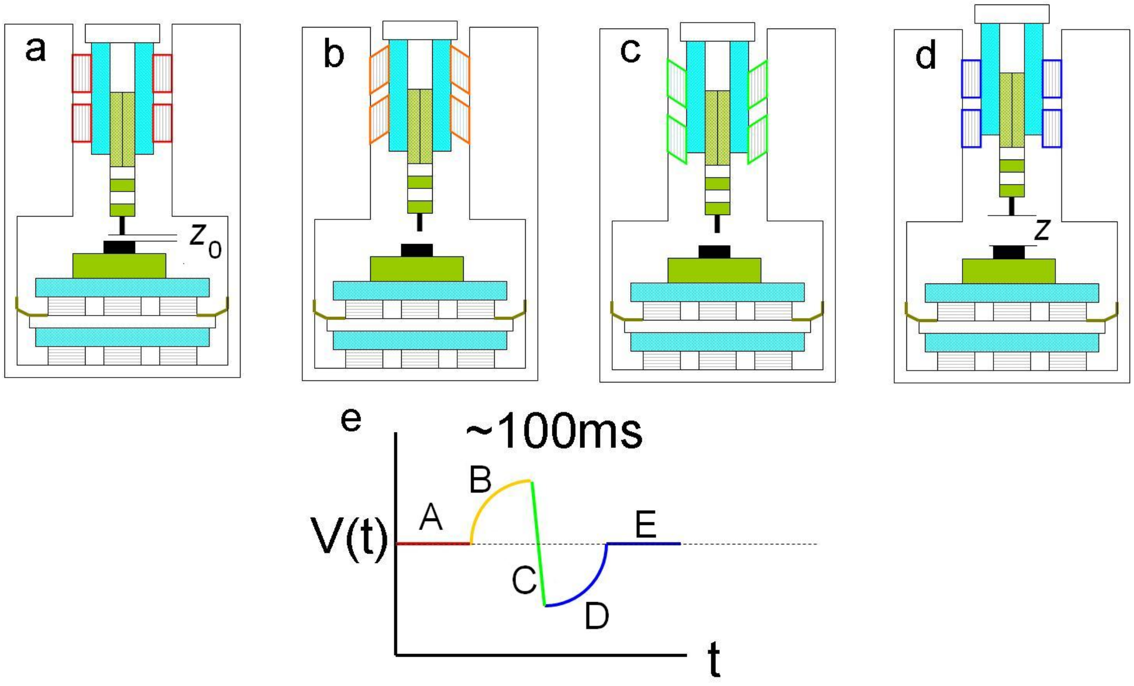

Figure 3.5: Schematic illustration of the operation of the Z-stage coarse motion: The parts of the Z-stage are labeled in Fig. 3.2. A top view of the Z-stage design and more detailed discussion of the design to adjust the shear stack frictional force on the sapphire prism is shown in Fig. 3.6. (a) The STM tip is held at an initial height, z_0, by six piezo stacks that hold up the sapphire prism via frictional forces. (b) To begin a coarse step, the voltage applied to all six piezo stacks is slowly increased such that frictional forces between the stacks and the sapphire prism cause the sapphire prism to move with the piezo stacks. (c) The voltage applied to the six piezo stacks rapidly switches polarity, such that the stacks slip and the sapphire prism maintains its height shown in (b). (d) Next, the piezo stack voltage is slowly lowered to zero, such that frictional forces cause the sapphire prism to follow the piezo stacks. The STM tip is now at height z. (e) The voltage waveform applied to the shear piezo stacks to take one coarse step. By reversing the polarity of the waveform, the direction of the coarse step may be reversed. The XY-stage works in a similar fashion [104], except that the XY-piezo stacks are electrically wired so that two shear piezos move in the x-direction and two shear piezos move in the y-direction. The Z-stage stacks are electrically wired so that four shear piezos move together.

Fig. 3.2c, and the sapphire prism is bounded by six shear piezoelectric stacks. A copper-beryllium (Cu-Be) spring adjusts how tightly the stacks hold the sapphire prism. The design to adjust the tightness of the shear piezo stacks is illustrated in Fig. 3.6. The shear stacks experience a waveform as shown in Fig. 3.5e to perform a coarse step. At stage A in the waveform, the tip is at position z_0. During the B stage, the stacks shear together slowly enough that the sapphire prism moves with the stacks due to frictional forces. In stage C, the voltage is rapidly changed such that the stacks slip along the sapphire prism. Finally, the stacks are translated slowly enough again in stage D to put the tip into a new vertical position, z, in stage E. After a coarse step, the piezoelectric tube scanner probes forward to see if the tip is within range to generate a measurable quantum tunneling current. If tunneling current is not detected, the coarse step is repeated.

Each coarse step takes approximately 3-4 seconds and moves approximately 0.8μm at room temperature for 300V applied across a shear stack. Similarly, the XY-stage may be used to position the sample under the tip in a desirable position, which is useful, for example, if the tip lands on a non-stoichiometric portion of the sample surface, or if different grains of a polycrystalline sample are to be investigated..

To achieve UHV and preserve the sample surface during measurements, the STM is loaded into a vacuum jacket equipped with a cryogenic charcoal pump. A schematic of the vacuum jacket with cryogenic charcoal pump is shown in Fig. 3.7. The cryogenic charcoal pump utilizes zeolite molecular sieve[5], which absorbs gases and reduces the pressure in the jacket space. The efficiency of adsorption of gases by the molecular sieve improves upon cooling to liquid helium temperatures, and we achieve pressures $< 10^{-9}$ torr at T = 6K in our system. The cryogenic pump is regenerated after each liquid helium measurement by heating the cryogenic charcoal pump in the vacuum jacket while pumping on the vacuum jacket.

Under UHV, the STM is cooled through the use of radiation baffles, copper mesh connections, and copper-berylium (Cu-Be) fingers. These features are illustrated in Fig. 3.7. The radiation baffles prevent the transmission of room temperature radiation down to the STM. The copper

---

[5] Leybold Zeolite Molecular Sieve, part no. Ag ZEG 854 10

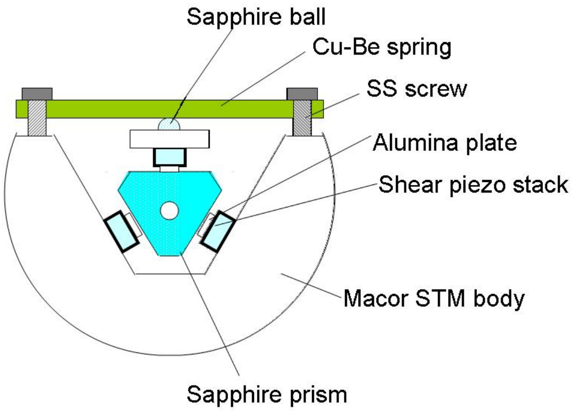

Figure 3.6: Top view design of the Z-stage for coarse motion: Six piezo stacks (three shown), capped by smooth alumina plates (0.020" thick Superstrates manufactured by Coors Ceramic Company), hold a sapphire prism in the Z-stage design. Voltages may be applied to the shear piezo stacks to move the sapphire prism, as described in Fig. 3.5. The STM tip holder, STM tip, and piezo tube scanner all connect to the sapphire prism so that when it moves, the STM tip and fine-motion piezo tube scanner move with it. To control the frictional forces so that the piezo stacks may properly translate the sapphire prism, the tension between the stacks may be adjusted by a copper-beryllium (Cu-Be) spring. The Cu-Be spring pushes on a sapphire ball that connects to the back of two of the shear piezo stacks. By adjusting the stainless steel (SS) screws, the tension may be adjusted such that vertical motion will occur when the waveform in Fig. 3.5e is applied to all six stacks.

mesh connections and Cu-Be fingers make contact to the jacket walls, which are in contact with the cryogenic bath (liquid nitrogen or liquid helium) in the STM dewar, to improve thermal conductivity. The base temperature for the system is T = 6K under UHV using these methods. The temperature of the STM is raised above the temperature of the cryogenic bath by applying a current through a resistive heater mounted directly to the top sapphire plate of the XY coarse-motion stage. A Cernox temperature sensor[6], mounted to the OFHC sample stage, is employed to measure the temperature of the STM.

The STM is inserted into an Oxford dewar that holds a 3" bore superconducting magnet to provide magnetic fields up to 7 Tesla, as shown in Fig. 3.7b. The Oxford dewar holds up to ~ 35 liters of liquid helium and boils off ~ 7 liters per day, allowing measurements to be performed for up to 5 days. The magnet field may be applied for ~ 3 days on a full dewar of liquid helium before the dewar must be refilled or the magnet turned off to prevent a magnet quench.

We employed several techniques to reduce electronic, vibrational, and acoustic noise affecting

---

[6] Purchased from Lakeshore Cryotronics, Inc.

our STM measurements. The elimination of these noise sources is vital to ensure that the tip does not contact the sample during our measurements and to provide sensitivity to the small currents (1pA–100nA) detectable by state of the art STM instruments.

The presence of an air handler outside the front door of our lab housing the STM and instrumentation contributed to large amounts of acoustic noise in the lab and affected our STM measurements. To eliminate this noise source and additional acoustic noises, we put acoustic absorbing foam[7] on the walls of our room, we setup vinyl curtains[8] to prevent transmission of noise from the air handler through the front door to our lab, we installed two bass traps[9], and we built two wooden boxes covered with acoustic absorbing foam around the STM inside the lab space. Carpets were also installed to prevent transmission of acoustic noise from a nearby metal grating that ran under our lab space. Measurements of the acoustic noise levels with the lids open and the lids closed on the two wooden acoustic shielding boxes are shown in Fig. 3.8a.

We employed measures to reduce RF frequency noises, to reduce cross-talk between electronic components, and to reduce ground loops for our STM. Ground loops in our measurements were carefully eliminated by ensuring single connections to ground among the various instruments, such as the temperature controller, the STM controller, and the computer. Further, we installed floating BNC feedthrough conflat flanges[10] to reduce ground loops between the grounds of the tunneling current connection, the voltage bias connection, and the metal STM dewar. All sensitive instruments were connected to a white power source installed in our lab for reducing common mode noise from the building ground connections. Finally, copper powder cryogenic RF filters were made using a mixture of 50% copper powder[11] and 50% epoxy[12] to reduce RF frequency pickup by our STM. Typical RF filters[13] removed frequency components for frequency > 2GHz, as shown in Fig. 3.8b.

The transmission of vibrations, such as building vibrations and vibrations due to the air-handler outside our lab, was reduced to the STM by mounting the STM dewar on a 3”-thick aluminum plate

---

[7] Uncoated Sound Absorbing Foam from McMaster-Carr

[8] Vinyl Reinforced Mass Loaded Barrier Curtain, 0.11” Thick, 54” W X 8′ H, from McMaster-Carr

[9] 16” OD tube trap purchased from Silent Source; Reinforced Hanging Sound Absorbing Cylinder 12” X 24” purchased from McMaster-Carr

[10] 1.33” conflat flanges with floating BNC feedthrough from Insulator Seal Inc.

[11] The powder used was -350 mesh copper powder purchased from Alfa Aesar.

[12] A mix of 50% 2850KT epoxy and 50% 1266 epoxy purchased from Emerson and Cuming

[13] More details about RF filters and their construction may be found in Ref. [106].

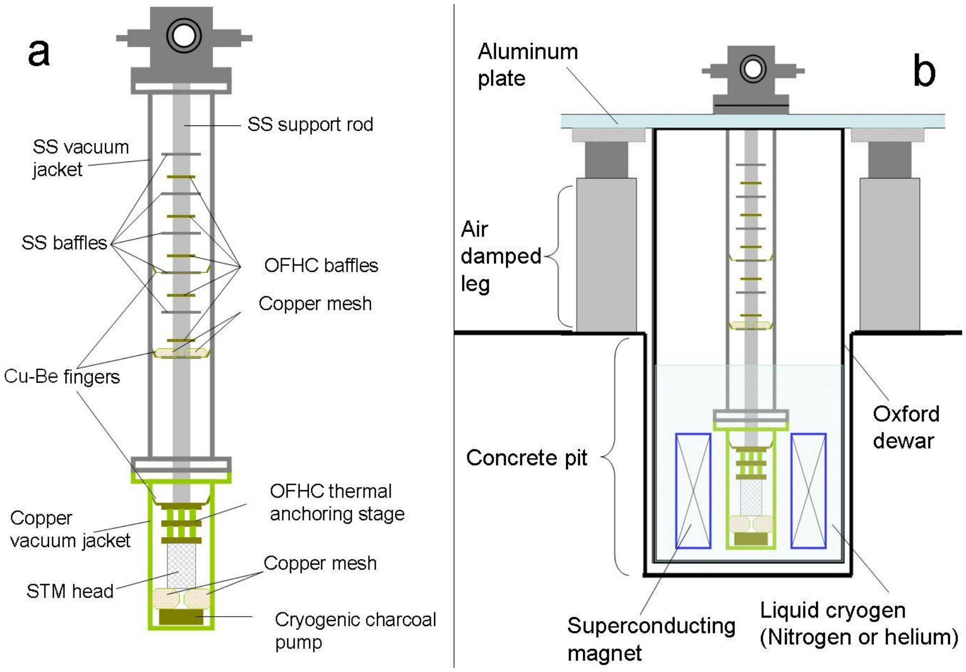

Figure 3.7: Schematic illustration of the STM dewar and vacuum jacket. (a). The STM vacuum jacket showing all the components used to reduce the heat load on the STM. Baffles reduce the transmission of thermal radiation to the STM. Cu-Be fingers and copper mesh provide thermal connections to the wall of the vacuum jacket near the bottom of the jacket, where the liquid helium or liquid nitrogen contact the vacuum jacket. In addition, the lower section of the vacuum jacket is constructed out of OFHC copper to improve thermal conductivity. Finally, a cryogenic charcoal pump is employed to pump to UHV conditions ($P < 10^{-9}$ torr for $T = 6K$) in the vacuum jacket. (b) Schematic illustration of the STM vacuum jacket mounted in the STM dewar. The vacuum jacket is mounted to a 3”-thick aluminum plate sitting on top of four air-damped pneumatic legs to reduce transmission of vibrations to the STM. (We refer to this setup as the air damped table.) The STM dewar sits in a concrete pit and has a superconducting magnet capable of applying magnetic fields up to $H = 7T$.

held up by 4 air-damped pneumatic legs[14] , as illustrated in Fig. 3.7b. The STM dewar was lowered into a concrete pit in order to make room for the setup and to reduce acoustic noise transmission. Lead bricks and lead shot were placed upon the aluminum plate to weigh it down and reduce the mechanical resonant frequency of the entire STM assembly. Additionally, vinyl skirts were lined around the edges of the aluminum plate to further weigh down the plate and reflect acoustic noise. The aluminum plate and air damped legs behaved like a low-pass filter. Vibration levels were significantly damped over the measured range of 0–250Hz, and the results with and without vinyl skirts and with the air damped legs deflated and inflated are compared in Figs. 3.8c and 3.8d.

The result of all our noise reduction methods is a baseline current noise level of ∼10pA peak-to-peak. Furthermore, the tip-sample vertical separation is constant to within 0.01nm when disabling the feedback loop at a fixed location. The methods are successful in producing a state-of-the-art cryogenic STM for characterization of materials and surfaces.

3.2 Bulk magnetization measurement techniques

In addition to measurements of the local density of states using STM, we utilize bulk magnetization measurements to characterize the vortex phase diagrams of cuprates in Chapter 6. In this section, we briefly describe the techniques to measure magnetization utilized in this work.

3.2.1 AC Susceptibility Measurements

A homemade AC susceptibility Hall probe magnetometer was utilized in order to investigate vortex dynamics in high-temperature cuprates. The probe allowed measurements to be performed on the fundamental harmonic response of a cuprate sample to a small AC excitation field, h_{AC}. Additionally, the probe could measure higher harmonic response to h_{AC} indicative of non-linear response of vortices. The onset temperature, T_{on}, of non-linear vortex response signalled the transition from reversible vortex behavior, for $\mathrm{T}_{on} < \mathrm{T} < \mathrm{T}_C$, to irreversible behavior, for $\mathrm{T} < \mathrm{T}_{on}$. In particular, we examined the magnitude of the third harmonic response, $| \chi_3 |$ to identify T_{on} empirically. We

---

[14] Air-damped legs available from Newport Scientific

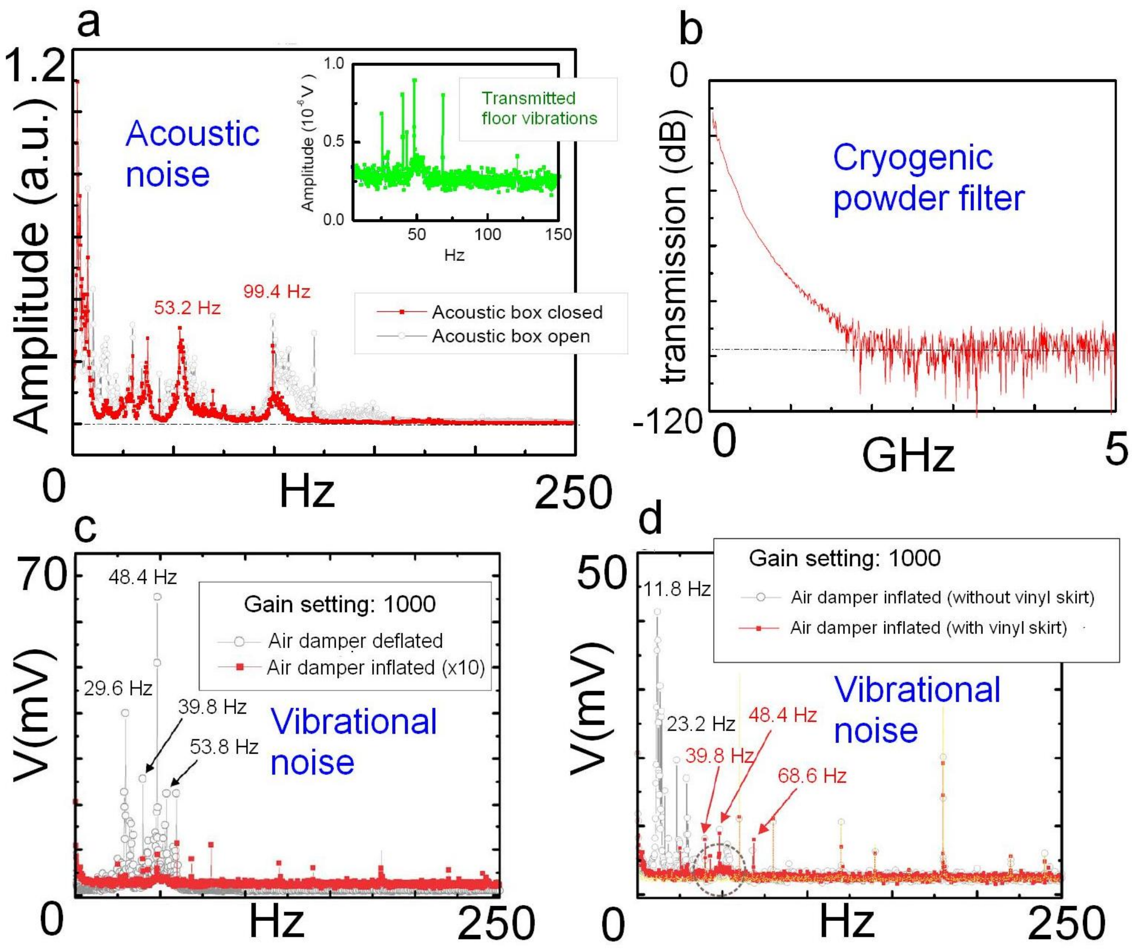

Figure 3.8: Figure adapted from Ref. [107]. Measurements of acoustic, vibrational, and electronic noise for our STM. (a) Main panel: Measurement of the acoustic noises affecting our STM. Measurements were performed with the acoustic shielding wooden boxes open and closed. Inset: Measurement of the transmitted floor vibrations. (b) Transmission of a cryogenic copper powder filter, showing suppression of transmitted RF frequencies greater than 2GHz. (c) Measurement of vibration levels associated with the STM experimental apparatus with the air damped table's legs deflated and with the air damped legs inflated. The case with the legs inflated significantly reduces the vibrations observed. The vibrations were measured using an accelerometer (ENTEK model 9200L accelerometer purchased from Rockwell Automation). The vibration levels were measured using a piezoelectric accelerometer. (Inside its casing, the accelerometer contains a load mass attached to a spring-like element. The mass and spring are loaded on top of a piezoelectric element inside the casing. When the accelerometer experienced vibrations, the changing force of the loaded mass on the piezoelectric element was converted into an electric signal for measurement through the piezoelectric effect. The piezoelectric signal was amplified inside the accelerometer to improve the signal-to-noise ratio.) (d) Measurement of vibrations associated with the STM experimental apparatus with the vinyl skirt on the air damped table versus the vibrations without the vinyl skirt. The case with the vinyl skirt attached shows significantly reduced vibrations. (Timothy Ward contributed to measurements in (c) and (d) during his SURF study at Caltech in the summer of 2004.)

identified the maximum value of T_{on} as being approximately equal to the in-plane (ab-plane) irreversibility temperature, T_{irr}^{ab}, for the polycrystalline samples examined in this work because $T_{irr}^{ab} > T_{irr}^{c}$, where T_{irr}^{c} is the c-axis irreversibility temperature.

A schematic of the experimental instrumentation for the AC susceptibility Hall probe is shown in Fig. 3.9a. Samples were loaded for measurements onto a Hall probe[15] using vacuum grease[16]. An AC excitation field was applied to the sample by running an AC current through the AC excitation coil. The AC current was generated by driving a resistor, $R_{load} \simeq 100\Omega$, in series with the AC excitation coil by using the voltage output of a lock-in amplifier[17]. Frequencies in the range from 1Hz to 1000Hz were used for h_{AC}, and h_{AC} was $\sim$ 1 Oe. The AC excitation coil was made of 0.002" diameter copper wire, with approximately 25 turns, radius of 0.2", and height of 0.2". A DC current source [18] provided DC current up to 5mA to the Hall probe for measurements, and the Hall voltage on the Hall probe was detected by the lock-in amplifier. The Hall voltage signal was carried on two BNC cables in order to perform a differential measurement on the lock-in amplifier to reject common mode noise. Measurements were performed in liquid helium cryostat, and our experimental setup allowed us to perform variable temperature measurements from T = 4.2K to T = 295K . Additionally, we could apply magnetic fields up to H = 9T via a 4" bore superconducting magnet[19] in the cryostat.

The technique of AC susceptibility has been used extensively in our research group to perform detailed scaling analysis of transitions in the high-temperature cuprates [108, 109, 110]. More details about AC susceptibility techniques may be found in Ref. [110]

3.2.2 DC SQUID magnetometer

A DC SQUID magnetometer[20] was utilized at the Beckman Institute at Caltech for sensitive DC magnetization measurements up to H = 5T. Samples to be examined were loaded into plastic straws

---

[15] Model Number THS118 Toshiba Hall Sensor from Toshiba

[16] Apiezon Type-N Vacuum Grease

[17] Model SR830 Lock-In from Standford Research Systems

[18] Keithley Model 220 Current Source

[19] Magnet from American Magnetics Inc.

[20] MPMS-XL SQUID purchased for the Materials and Molecular Research Center at the Beckman Institute from Quantum Design Inc.

using nylon string and gelatin capsules[21]. The straws, nylon string, and gelatin capsules are chosen for their low contribution to the magnetization compared to the sensitivity of the SQUID. For small sample signals, the effects of these materials must be calibrated away; however, typical signal levels for the high-temperature superconducting cuprates considered here ($\sim 10^{-5}$emu or greater) greatly exceed the signals due to the straw, nylon string, and gelatin capsules ($\sim 10^{-7}$emu).

Once the sample was loaded into a straw, the straw was then mounted on the end of a steel and copper rod for loading into the SQUID. The sample space and straw were purged of air using helium gas and loaded into the cryogenic section of the SQUID apparatus. A small magnetic field ($\sim$ 50 Oe) was then applied in order to perform a centering scan on the sample. This procedure was performed in order to align the sample in the center of a set of differential detection coils. Upon centering the sample, measurements were performed by translating the sample either 4 cm or 6 cm through the set of differential detection coils. The detection coils coupled through an inductive element to the SQUID for high sensitivity magnetization measurements of the induced signal. The response was measured and then modeled by the response of an ideal magnetic dipole to determine the magnetic moment of the sample at each temperature and magnetic field via the software accompanying the SQUID[22]. Magnetization(M(T,H)-)-vs.-T measurements, for zero-field cooled-vs.-field cooled measurements, and M-vs.-H measurements, for magnetization hysteresis loops, could be performed from T = 2K up to T = 400K and in fields up to H = 5T to characterize samples. A schematic of the DC SQUID magnetometer is shown in Fig. 3.9b.

3.2.3 DC magnetization with metal cantilevers

A DC cantilever magnetometer was constructed[23] to measure DC magnetization in high-temperature superconducting cuprate samples. The technique allowed measurement of the magnetization, M(T,H), as a function of magnetic field for determination of the in-plane (ab-plane) irreversibility field, H_{irr}^{ab}. Measurements were performed at the National High Magnetic Field Laboratory (NHMFL) in Tallahassee in magnetic fields up to H = 33T. Cryostats for ^{3}He or ^{4}He were utilized to perform

---

[21] Available for purchase from Quantum Design Inc.

[22] MPMS Multivu from Quantum Design Inc.

[23] Constructed by Cameron Hughes and the author of this thesis

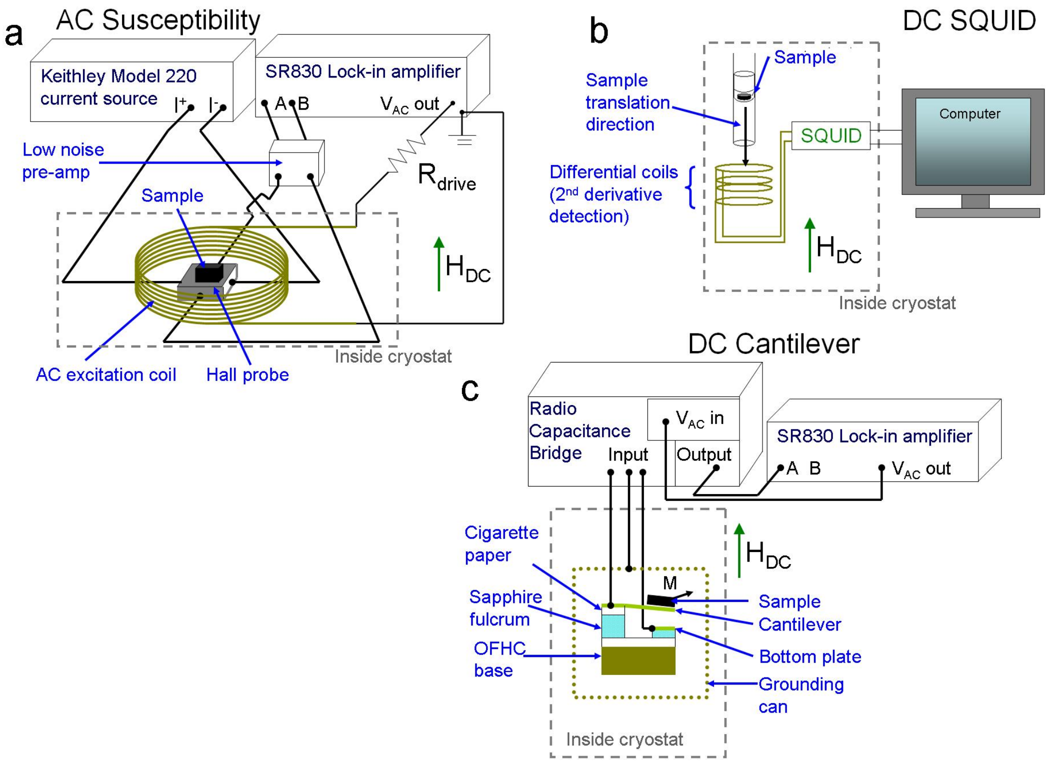

Figure 3.9: Schematic illustrations of bulk magnetization measurement techniques. (a) Schematic of the AC susceptibility Hall probe magnetometer used for measuring the magnitude of third harmonic response, $| \chi_3 |$-vs.-T for determination of the onset temperature of non-linear vortex response, T_{on}. (b) Schematic of the DC SQUID magnetometer for measuring M(T,H)-vs.-T and M(T,H)-vs.-H in bulk superconducting cuprate samples. (c) Schematic of the DC cantilever magnetometery technique for measuring M(T,H)-vs.-H in bulk superconducting cuprate samples

measurements from T$\simeq 2K$ up to T$\simeq 150K$. The technique exploited the fact that a sample with an anisotropic magnetic moment experiences a torque and a force in an applied magnetic field. Therefore, by loading the sample onto a metal cantilever, the deflection of the cantilever due to the force and torque could be employed as a measure of the magnetization as a function of temperature and magnetic field, M(T,H). The values of the in-plane (ab-plane) irreversibility field, H_{irr}^{ab}, could be determined from M(T,H)-vs.-H hysteresis loops.

A schematic of the experimental apparatus is shown in Fig. 3.9c. We used a metallic cantilever as one plate of a capacitor and utilized an AC capacitance bridge technique [111, 112] in order to measure the deflection of the cantilever due to the magnetic moment of the sample. The cantilevers were Cu-Be cantilevers of 0.0005" thickness, and the opposite plate (bottom plate in Fig. 3.9c) of the capacitor was a metal plate, which was made out of OFHC copper. Additionally, a grounding can, made of OFHC copper, surrounded the cantilever capacitor as part of a 3-terminal capacitor. The entire probe was loaded onto an OFHC copper block in order to reduce thermal gradients in the apparatus. The components of the cantilever were electrically isolated, in order to prevent electrical shorting, by using sapphire pieces and cigarette paper. An AC excitation of 5 V_{rms} at 5kHz was input to a 1616 General Radio Capacitance Bridge to provide a signal for the capacitance bridge, which had one arm of the bridge connected to the 3-terminal capacitance of the DC cantilever apparatus. The bridge was balanced prior to sweeping the magnetic field. A lock-in amplifier was utilized to measure the difference signal that resulted as the bridge became unbalanced due to the changing values of magnetization upon sweeping the magnetic field from H = 0 to H = 33T (and then back down to H = 0). The lowest magnetic field at which reversibility was observed in the M(T,H)-vs.-H hysteresis loops served as the empirical identification of H_{irr}^{ab}.

Chapter 4

Scanning tunneling spectroscopic studies of the electron-type cuprate $La_{0.1}Sr_{0.9}CuO_2$

To date, the ground state of cuprate superconductors is a subject of intense research and theoretical debate. In this chapter, we report our findings from spatially resolved studies of the quasiparticle tunneling spectra of the infinite-layer electron-doped cuprate $La_{0.1}Sr_{0.9}CuO_2$ (La-112). We examined La-112 using scanning tunneling spectroscopy (STS) as a function of magnetic field, H, and temperature, T to infer information about the ground state of La-112 and electron-type cuprates. First, we found that the excitation spectra observed in zero magnetic field was homogeneous over the entire spatial region examined and independent of tunneling momentum. Secondly, all the zero-field dI/dV-vs.-ω tunneling spectra measured showed only one set of peaks in dI/dV, no satellite features, and excess sub-gap states unaccountable by pure d-wave or pure s-wave superconductivity. Under applied magnetic fields, we demonstrated, for the first time, spatially resolved identification of vortices in an electron-type cuprate superconductor. The spectra inside the core of vortices revealed a hidden pseudogap-like spectrum, characterized by a pseudogap energy, $V_{PG}=(8.5 \pm 0.6)$meV. Overall, the evolution of the quasiparticle spectra as a function of magnetic field and temperature were unconventional when compared with Bogoliubov quasiparticles. The results presented here suggest that the ground state of high-T_C superconductors are inconsistent with a ground state of pure superconductivity alone.

4.1 Introduction

In this introduction, we review the unconventional spin- and charge-excitations seen in electron doped cuprates. We also discuss the expected field-induced effect on quasiparticle spectra in conventional type-II superconductors in order to put the unconventional behavior we observe for La-112 in perspective.

Superconductivity in the cuprates arises by doping antiferromagnetic Mott insulators with electrons or holes. The doped compounds become superconducting only over a range of doping concentrations, whether doping with holes or electrons. In fact, various ground state phases besides superconductivity may emerge from doping antiferromagnetic Mott insulators [26]. Consequently the ground state of cuprates may consist of coexisting competing orders and superconductivity, thereby displaying unconventional quasiparticle properties because of a mixed ground state.

As mentioned previously, two of the most widely discussed unconventional phenomena in hole-type cuprates are the pseudogap and Fermi arcs above the superconducting transition of the underdoped and optimally doped samples. In contrast, both features are absent in the quasiparticle DOS and ARPES data of all electron-type cuprates. As examples, scanning tunneling spectroscopy on $\mathrm{Pr_{0.88}LaCe_{0.12}CuO_4}$ (PLCCO) [63], planar junction spectroscopy on $\mathrm{Pr_{0.89}LaCe_{0.11}CuO_4}$ (PLCCO) [62], grain-boundary tunneling spectroscopy on $\mathrm{Pr_{1.85}Ce_{0.15}CuO_{4-y}}$ (PCCO) and $\mathrm{Nd_{1.85}Ce_{0.15}CuO_{4-y}}$ (NCCO) [61], and doping dependent grain-boundary tunneling (GBT) spectroscopy on $\mathrm{La_{2-x}Ce_xCuO_{4-y}}$ (LCCO) and PCCO [17] all find no evidence for a pseudogap in the quasiparticle density of states (DOS) of the one-layer electron-doped cuprates for $\mathrm{T>T_C}$. Similarly, we do not find a pseudogap above $\mathrm{T_C}$ in the infinite-layer electron-doped La-112 data presented later in this chapter. Further, ARPES measurements on optimally doped NCCO [64] and underdoped PLCCO [41] show no Fermi arcs above $\mathrm{T_C}$, revealing a full Fermi surface. The pseudogap and Fermi arcs are considered highly unconventional quasiparticle excitation behavior in hole-doped cuprates, but they are absent in electron-doped cuprates. Therefore, electron-doped cuprates appear to have quasiparticle excitation spectra different from hole-doped cuprates for $\mathrm{T>T_C}$.

While Fermi arcs were not revealed in the ARPES measurements of electron-type cuprates at

$T > T_C$, an unconventional, non-monotonic d-wave gap was observed, for example, in the ARPES data of electron-doped PLCCO at $T \ll T_C$ [41]. The observed non-monotonic d-wave gap showed a maximum gap at 25^o off the anti-nodal direction of the Brillouin zone, instead of showing a maximum gap along the anti-nodal direction. Doping dependent ARPES studies on NCCO revealed that the Fermi surface of the electron-doped cuprate grew from a "Fermi patch" into a few separated "Fermi patches" and then into a full Fermi surface as doping increased from heavily underdoped to optimally doped [64]. ARPES measurements revealed that the high-energy pseudogap in NCCO arose from regions of the Fermi surface between the nodal and anti-nodal directions [113]. Interestingly, the non-monotonic d-wave gap, which is a low-energy feature, and the anomalous properties associated with the high-energy pseudogap both occurred when the Fermi surfaces of the electron-doped cuprates intersected the antiferromagnetic Brillouin zone at the so-called antiferromagnetic "hot spots." [41] These findings seem to suggest that the ground state excitations of electron-doped cuprates may arise from superconductivity and a derivative phase of antiferromagnetism or that quasiparticles are less developed near the hot spots. The "hot spots" and "Fermi patches" are illustrated for clarity in Fig. 4.1.

The unconventional Fermi surface and d-wave gap anomalies are possibly related to a "hidden pseudogap"-type phenomena observed in electron-doped cuprates [17], just as pseudogap and Fermi arcs are related in hole-doped cuprates [6]. The so-called "hidden pseudogap" was revealed in doping dependent studies of GBT spectroscopy on one-layer electron-doped LCCO and PCCO as a function of temperature and magnetic field. [17] Pseudogap-like spectra were seen in these studies for $T \ll T_C$ by tuning the samples into the normal state using magnetic fields such that $H > H_{C2}$, where H_{C2} is the upper critical field of the type-II cuprate superconductor. For $T \ll T_C$, the "hidden pseudogap" persisted to the highest fields attainable experimentally. The pseudogap temperature, T^*, was then determined by applying a field $H \gg H_{C2}$ and raising temperature until the pseudogap-like spectra disappeared. It was found that $T^* < T_C$ for all samples of different doping levels. It is feasible to conjecture that a hidden pseudogap state conspires with d-wave superconductivity to produce the non-monotonic d-wave gap observed in the ARPES and GBT quasiparticle spectra of electron-type

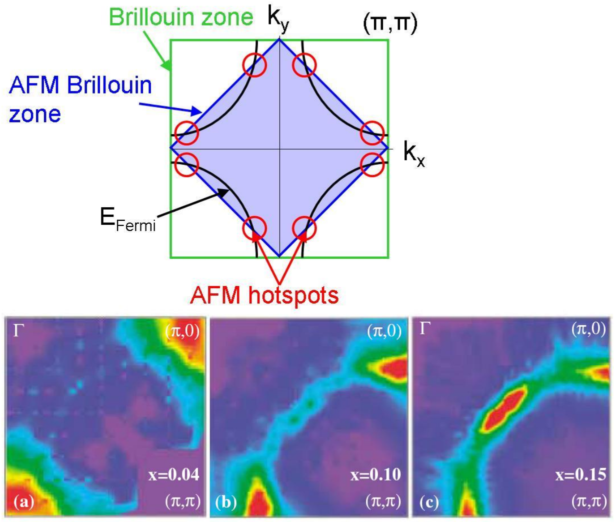

Figure 4.1: Schematic illustration of the antiferromagnetic "hot-spots": Top: The antiferromagnetic "hot spots" occur at the intersection of the antiferromagnetic (AFM) Brillouin zone with the Fermi surface ($\xi_{\mathbf{k}}$) determined by the electronic bandstructure. The Γ point is at the center of the first Brillouin zone shown by the green square. The AFM Brillouin zone is illustrated by the shaded area. Bottom: Spectral density functions measured by ARPES integrated from -40meV to 20meV in $\mathrm{Nd}_{2-x}\mathrm{Ce}_x\mathrm{CuO}_{4-y}$: (a) x=0.04, (b) = 0.10, (c) x = 0.15. One quadrant of the Brillouin zone is shown for the bottom images. The "Fermi patches" are evident as high-intensity (red) regions in these images. [Bottom figures reproduced from Ref. [64]. High intensity is indicated by a red color, while low intensity is indicated by purple. The exact colorbar was not available in Ref. [64].]

cuprate superconductors at $T \ll T_C$.

Finally, neutron scattering experiments also reveal unconventional behavior of spin correlations in electron-doped cuprates that differs from the findings in hole-type cuprates. Neutron scattering experiments on hole-doped $\mathrm{La}_{2-x}\mathrm{Sr}_x\mathrm{CuO}_{4-y}$ observed incommensurate spin correlations in the superconducting state, with a temperature independent spin gap above and below T_C [13, 14, 15]. In contrast, spin correlations were commensurate in the electron-doped cuprate $\mathrm{Nd}_{2-x}\mathrm{Ce}_x\mathrm{CuO}_{4-y}$ (NCCO), and the spin gap was a maximum of 4meV as $T \rightarrow 0$ and disappeared as $T \rightarrow T_C$ [9]. Curiously, the spin gap seems to mirror the behavior of the pseudogap in both hole- and electron-doped cuprates. Additionally, a static, commensurate magnetic order was seen to be enhanced by application of a magnetic field up to 9T in underdoped electron-doped PLCCO [10], and a commensurate "quasi-2D spin-density wave" was enhanced by magnetic field equal to 5T in another underdoped PLCCO measurement [11]. Comparison of the hidden pseudogap and the neutron scattering data of electron-type cuprates suggest a link between these two types of observations: The static orders observed in neutron scattering could be competing orders other than superconductivity, and the observed spin gap could be associated with the quasiparticle spin excitation spectra of the competing order. In finite magnetic fields, this spin gap may be manifested by a "hidden pseudogap" associated with the quasiparticle charge excitations in electron-doped cuprates.

However, the connection between the hidden pseudogap and a competing order appears to be inconclusive in the one-layer electron-type cuprates: Other groups caution that secondary material phases may appear during the oxygen reduction process necessary to achieve superconductivity in the one-layer electron-doped cuprates, paramagnetism of Nd^{3+} or Pr^{3+}, and whether or not holes are the actual carriers in the nominal one-layer electron-doped cuprates should be considered [65, 66]. On the other hand, the aforementioned concerns do not arise in infinite layer electron-doped La-112 because oxygen reduction is not required to achieve optimal doping, La-112 is free from magnetic ions, and thermopower measurements are consistent with electrons as the relevant carriers[67].

A feasible empirical approach to investigate the "hidden pseudogap" features in more detail would be to perform spatially resolved vortex-state quasiparticle tunneling spectroscopy. For conventional type-II superconductors, an applied magnetic field smaller than the upper critical field, $H < H_{C2}$, will induce periodic vortices, thereby giving rise to periodic regions of suppressed local superconducting order inside the vortices [72]. Continuous bound states [114] inside the regions of suppressed superconducting order would lead to a zero-bias conduction peak at the Fermi level inside vortices [24]. If another competing order coexists with superconductivity in the ground state and is gapped, the competing order could contribute to pseudogap-like spectra inside vortices upon suppression of superconductivity. This finding would be in contrast to the zero-bias conduction peak expected near the center of vortex cores had superconductivity been the sole ground-state order parameter. A "hidden pseudogap" would then be seen for $H<H_{C2}$. In hole-doped cuprates, it is well known that quasiparticle spectra inside vortices remains gapped [69, 115]. Prior to the work presented here, vortices had not been imaged or located in electron-doped cuprates with spatially resolved spectroscopy to study the modification of their excitation spectra inside vortices.

In this chapter, we use spatially resolved STS as a function of magnetic field and temperature to collect data on optimally doped, infinite-layer, electron-type La-112. We first examine the zero field properties of La-112 and present a spatially resolved map of zero-field single quasiparticle spectra. A histogram of the peak-to-peak gaps, Δ_{pk-pk}, observed in the map reveals homogeneous spectra over the area examined with $\Delta_{pk-pk} = (12.2 \pm 0.8)$meV. We further examine the temperature evolution of the zero-field spectra and find no pseudogap or satellite features above T_C. We then apply a magnetic field $H \ll H_{C2}$ and search for vortices. We find significant field induced modulations in maps of the differential conductivity that may be used to locate vortices. Moreover, we observe pseudogap-like spectra inside the core of vortices and the pseudogap gap energy V_{PG} is less than the zero-field gap Δ_{pk-pk}. There is no evidence for a zero-bias conduction peak inside vortices, which would have been expected for a purely superconducting ground state.

4.2 Experimental preparation and material considerations in $La_{0.1}Sr_{0.9}CuO_2$

The infinite-layer cuprates, $Ln_xSr_{1-x}CuO_2$ (Ln = La, Gd, Sm), have the simplest structure among all cuprates, as illustrated in Figure 4.2. However, single-phase bulk samples with nearly 100% superconducting volume are difficult to produce [116, 117, 118]. Fortunately, progress has been made in recent years [119] to synthesize samples using high-pressure (4 GPa) and high-temperature (950 C°). The process is able to achieve single-phase polycrystalline samples of $La_{0.1}Sr_{0.9}CuO_2$ with nearly 100% superconducting volume and sharp superconducting transition temperatures ($T_c = 43$ K). The samples used for the studies presented in this chapter were prepared with the high-pressure, high-temperature method by our collaborator, Professor Sung-Ik Lee. Samples prepared in this way provide reliable quasiparticle spectroscopy for studying spatial spectral homogeneity in zero-field as well as spectral modification due to vortices in a magnetic field.

Two samples of high-density granular $La_{0.1}Sr_{0.9}CuO_2$(La-112) were studied in this work. The samples were single phase, as measured by X-ray diffraction (XRD) measurements [120]. Scanning electron microscopy (SEM) and X-ray photoemission spectroscopy (XPS) both observed random

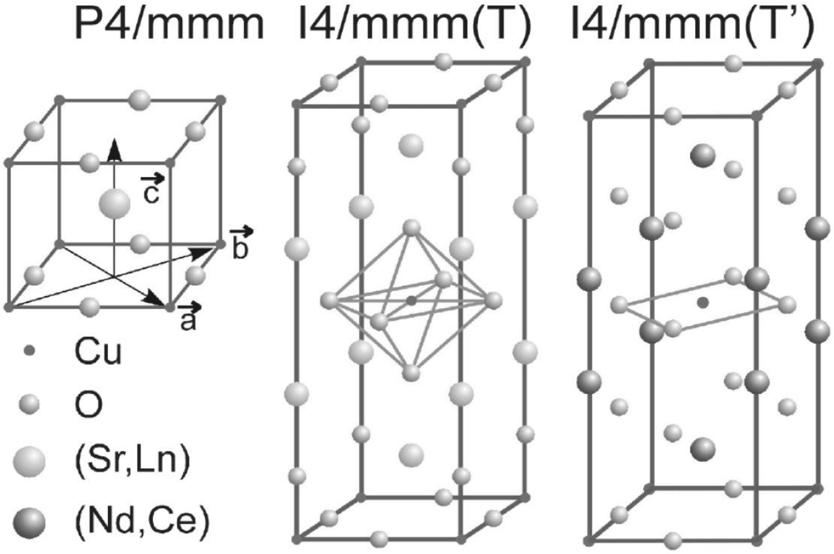

Figure 4.2: Figure taken from Ref. [39]. The infinite-layer system $\mathrm{Sr_{1-x}Ln_xCuO_2}$, (Ln = La, Gd, Sm) (left). One-layer hole-doped, T-phase. (middle). One-layer electron-doped, T′-phase (right)

grain orientations and typical grain diameter sizes on the order of a few micrometers [119, 120]. Magnetization measurements showed nearly 100% superconducting volume for the samples, $T_c = 43$ K, and $\Delta T_c \leq 1.0$ K. The system was also homogeneous in stoichiometry based on XPS measurements [120].

The sample surface for STS studies was prepared by chemical etching with 0.5–2% bromine in absolute ethanol for 1–4 minutes [120], rinsing in pure ethanol to remove bromides, and drying by blowing cold-trap-filtered helium gas onto the sample. The sample was then mounted on the STM sample stage while blowing cold-trap-filtered helium gas over the sample. Bromine etching reveals a nearly stoichiometric surface, as seen by X-ray photoemission spectroscopy (XPS) [120].

The etched surface of La-112 does not permit sufficient topographical sensitivity to reveal individual atoms in the STM constant-current topographic imaging mode. However, the STM can still measure STS spectra and the etched surface topography with atomic-level spatial resolution. We further note that this behavior has been observed in other cuprates, such as $\mathrm{YBa_2Cu_3O_{7-\delta}}$ [3]. Atomic-level resolution merely relies on our ability to control the piezoelectric tube scanner movement down to sub-angstrom displacements, which we have demonstrated for T=6K to T=300K on highly oriented pyrolytic graphite. The fact that we cannot see the individual atoms in topography is due to the etched surface and the nature of the wavefunctions on the surface of La-112. That is, the overlap of the STM tip with the electronic wave functions on the La-112 surface does not exhibit sufficient variations along the vertical direction to yield detectable changes in the tunneling current if the vertical position of the STM tip does not displace more than the atomic scale.

We perform spatially resolved STS studies in the constant tip-junction resistance mode using $1\text{G}\Omega$ tunnel junction resistance at each pixel on the sample surface. In the constant tip-junction resistance STS mode, the surface topography roughness is eliminated from spatially resolved quasiparticle tunneling density of states maps to lowest order, as discussed in Chapter 3.

The structure of La-112 differs from most other cuprates because no excess charge reservoir block is found between CuO_2 planes. Only a layer of La or Sr ions is found between CuO_2 planes, as shown in Fig. 4.2. The oxygen distribution in La-112 is perfectly stoichiometric and lacks oxygen vacancies in the CuO_2 planes and excess interstitial oxygen [116]. The c-axis superconducting coherence length ($\xi_c = 0.53$ nm) is longer than the c-axis lattice constant ($c_0 = 0.347$ nm) [121], unlike other cuprate superconductors that exhibit $\xi_c \ll c_0$ and are quasi-two-dimensional in character. The ab-plane superconducting coherence length is 4.9nm, and the in-plane lattice constant is 0.395nm. The superconducting properties of the infinite-layer system should be the most three-dimensional among all the cuprates.

As was shown in Ref. [39], the pairing symmetry of La-112 seems to be consistent with s-wave. This conclusion was based on the observation of momentum-independent quasiparticle tunneling spectroscopy, lack of a zero-bias conduction peak due to Andreev reflection along the nodal direction, and the stronger suppression of superconductivity when La-112 is doped with magnetic impurities, such as Ni, than when doped with non-magnetic impurities, such as Zn. We confirmed momentum-independent quasiparticle tunneling spectroscopy and lack of a zero-bias conduction peak over the hundreds of areas studied in this work. We also found the same general quasiparticle tunneling spectra at $H = 0$ as Ref. [39]. While the pairing symmetry of electron-doped cuprates is a source of contention [40, 36, 37, 122, 123, 124, 125, 126, 127, 128, 129], we leave further discussion of the pairing symmetry of La-112 until the Discussion section of this chapter.

4.3 Zero-field (H= 0), spatially resolved STS in $La_{0.1}Sr_{0.9}CuO_2$

In this section, we present data obtained at zero magnetic field that characterizes zero field single quasiparticle spectra. We observe peaks in the spectra and identify the peak-to-peak separation as $2\Delta_{pk-pk}$. We present representative quasiparticle spectra, average Δ_{pk-pk} value observed, topography, and the spatial homogeneity and histogram of Δ_{pk-pk} over a representative 64 x 64 nm^2 area. Further, we present the temperature dependence of Δ_{pk-pk} obtained from the quasiparticle spectra on La-112. The spatially resolved differential tunneling conductance vs. energy (ω) spectra presented here were acquired with our homemade cryogenic STM described in Chapter 3.

First, we show the constant current topography obtained via STM at zero field over a 64 x 64 nm^2 area in Fig. 4.3. The topography shown is representative of typical topography obtained on the surface of a single grain of etched La-112. The surface is flat to within 1nm.

We show in Fig. 4.3a a typical differential conductance (dI/dV) vs. voltage (V) tunneling spectrum (open circles) obtained over the area shown in Fig. 4.3a at $T = 6$ K and H = 0. The spectrum is normalized to its high-voltage background according to the methods described in Ref. [39]. Solid lines in the figure will be discussed in more detail in the Discussion section of this chapter. We notice no satellite features in the representative spectra or in any quasiparticle spectra in the spatially resolved map. A spatial map of the values of Δ_{pk-pk} over a 64nm x 64nm area and a histogram of the values are shown in Fig. 4.4b,c. We find an average value of $\Delta_{pk-pk} = 12.2$meV and a linewidth from a Lorentzian fitting of the histogram of 0.8meV.

Averaged quasiparticle spectra versus temperature taken over spatial areas of 64 x 64 nm^2 are shown in Fig. 4.5. For $T > T_C$, we find no evidence of suppressed density of states that would indicate pseudogap behavior, and this finding is consistent with the lack of pseudogap in all other electron-doped cuprates. The inset of Fig. 4.5 shows the measured Δ_{pk-pk} vs. temperature, which appears to follow a BCS-like temperature dependence (shown as a solid line).

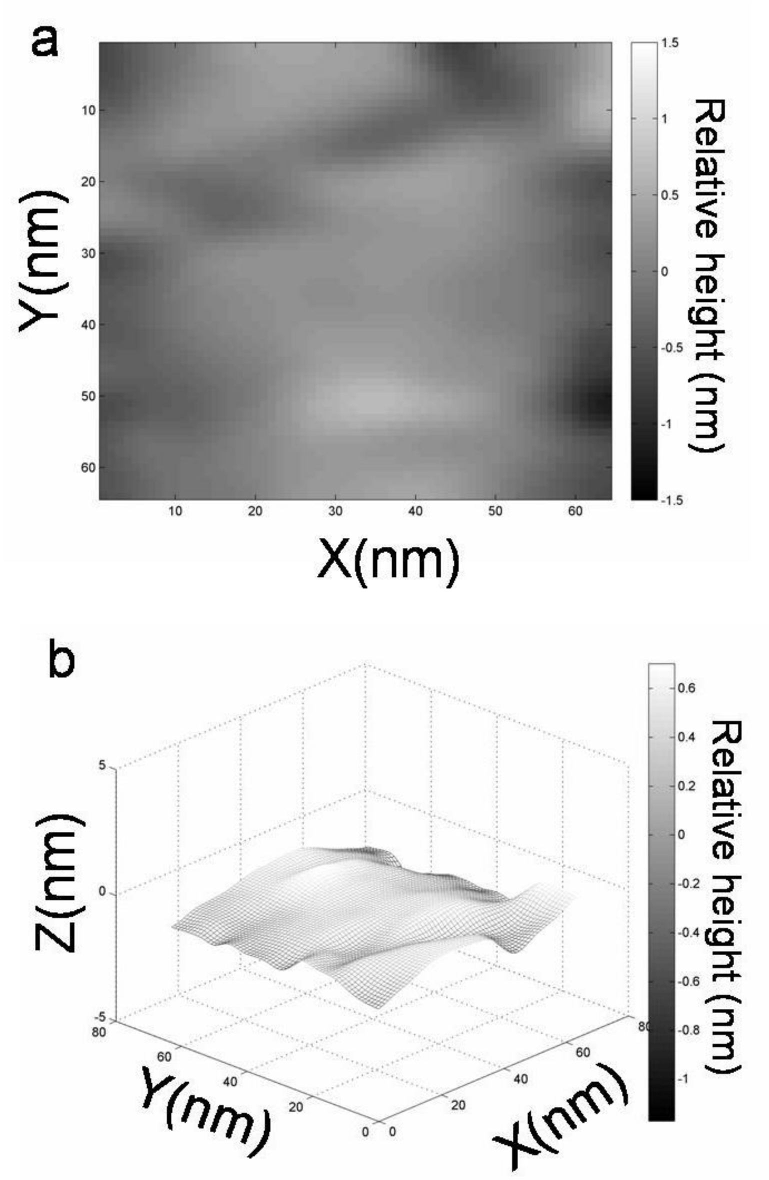

Figure 4.3: The relative height of $La_{0.1}Sr_{0.9}CuO_2$ as measured at H=0, T=6K from constant current topography using STM. The representative area is flat to within 1nm. The set current and bias voltage to obtain the constant current topography was I_{set}=-80nA, V_{bias}=-80meV.

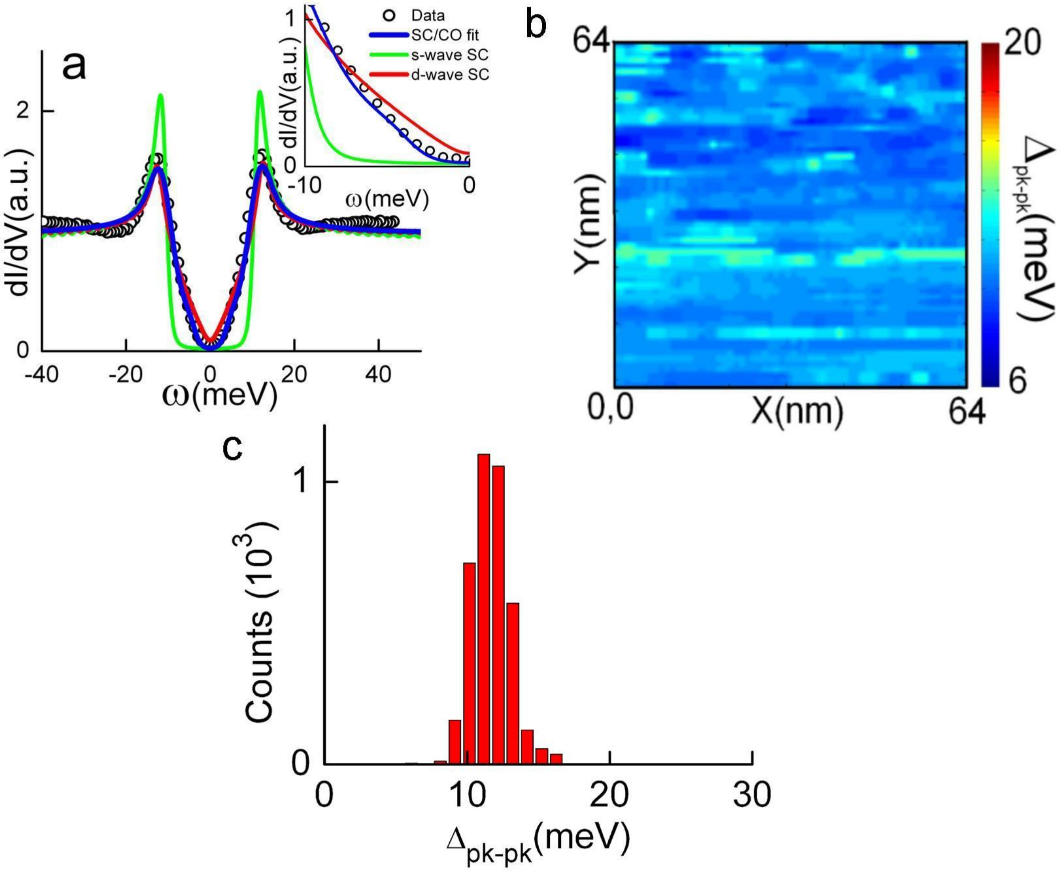

Figure 4.4: (a)Main panel: A representative normalized dI/dV spectra (open cirlces) taken at H= 0 and T= 6K on $La_{0.1}Sr_{0.9}CuO_2$ over the 64nm x 64nm area in Fig. 4.3. The value of Δ_{pk-pk} is labeled in the figure. We show comparisons of an attempt to fit the data using BCS superconductivity alone as solid-lines for pure s-wave (green) and pure d-wave (red) pairing symmetry. We also show an attempt to fit the data using a model of coexisting superconductivity and a competing order (SC/CO) as another solid-line (blue) on top of the data. The attempts to fit the data all use Δ_{SC}=12.0meV. The competing order model assumes a gapped spin-density wave for the competing order and uses values of V_{CO}=V_{PG}=8.0meV and density-wave vector $\mathbf{Q}=(\pi,\pi)$ to generate the fit (more details are available in Chapter 7). We find that neither fitting that assumes pure superconductivity can sufficiently account for the gapped spectra and the sub-gap states, while the fitting of superconductivity and a gapped spin-density wave more closely models the data. Inset: A closer view of the sub-gap quasiparticle tunneling spectra that better shows the inability of d-wave and s-wave BCS spectra to fit the data, while the SC/CO fit better accounts for the sub-gap states. (b) A map of Δ_{pk-pk} values over a 64nm x 64nm area. (c) A histogram of Δ_{pk-pk} values from (b)

4.4 Finite magnetic field (H> 0), spatially resolved STS in $La_{0.1}Sr_{0.9}CuO_2$

In this section, we present spatially resolved STS as a function of magnetic field at low temperatures ($T \ll T_C$) in La-112. To locate vortices in La-112, we needed the vortices to remain stationary for a sufficiently long time to be imaged by STM. The irreversibility field determined the threshold temperature and magnetic field of vortex motion during a measurement, and the irreversibility field of La-112 has been thoroughly characterized in Ref. [130] and also detailed in Chapter 6. The c-axis irreversibility field is found to be about 8-10T as $T \rightarrow 0$ [130]. Our measurements occurred over the region of parameter space shown in Fig. 4.6 so that we did not expect vortices to move during our measurement time of three to five days.

The size of vortex cores for superconductors are determined by the relevant coherence lengths and, in anisotropic superconductors, such as the cuprates, depend on the crystalline plane examined. For tunneling currents parallel to the c-axis, or {001} surface, vortices will be circular in shape and have a core radius given by the ab-plane coherence length, ξ_{ab}. For tunneling currents perpendicular to the c-axis, vortices will be ellipsoidal with the semimajor axis length given by ξ_{ab} and the semiminor axis length given by ξ_c. For the areas studied in this chapter at finite magnetic field, we find circular vortices with radius, r, consistent with $r \sim \xi_{ab}$ and $H \parallel \hat{c}$. Hence, we conclude that the tunneling current is parallel to the c-axis for the remainder of this section. Additionally, we expect vortices to be separated by the Abrikosov vortex lattice constant, $a_B = 1.075(\Phi_0/B)^{1/2}$.

A final concern was that prior to the work presented here, vortices had not been imaged in any electron-doped cuprate. Therefore, we were initially unsure of the quasiparticle tunneling spectra to be expected inside and outside of vortices in La-112 and how to achieve contrasting images of vortices. If gapped spectra persists inside vortex cores, a useful method to produce contrast between the spectra inside and outside of vortex cores is to use a differential conductance power ratio, r_G,

$$r_G = \frac{\left(\frac{dI}{dV}\right)^2_{\omega=\Delta_{pk-pk}(0)}}{\left(\frac{dI}{dV}\right)^2_{\omega=0}}. \tag{4.1}$$

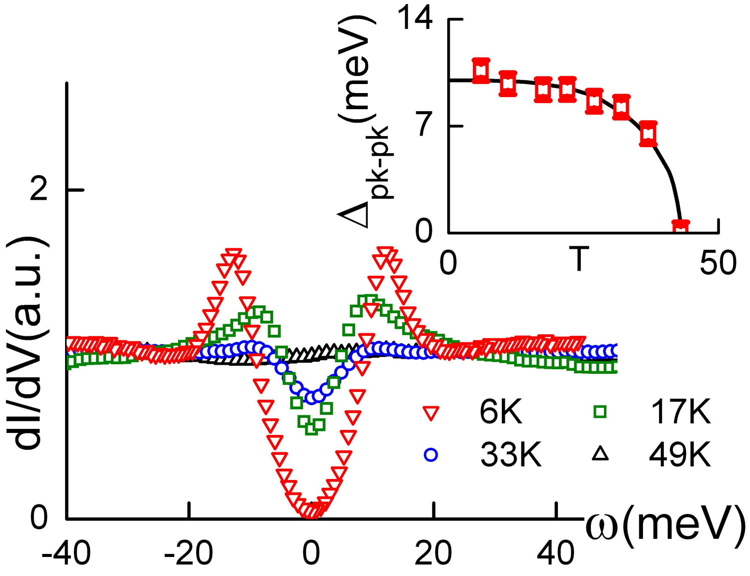

Figure 4.5: Main panel: Average differential conductance-(dI/dV-)-vs.-ω(meV) as temperature was varied in optimally doped $\mathrm{La}_{0.1}\mathrm{Sr}_{0.9}\mathrm{Cu}O_2$. The experimental quasiparticle spectra are shown as open symbols. It can be seen that there is no pseudogap above the superconducting transition temperature. Inset: The peak-to-peak gap value, Δ_{pk-pk} measured as a function of temperature. The Δ_{pk-pk} values vs. T follow the expectations of BCS theory, shown as a solid line.

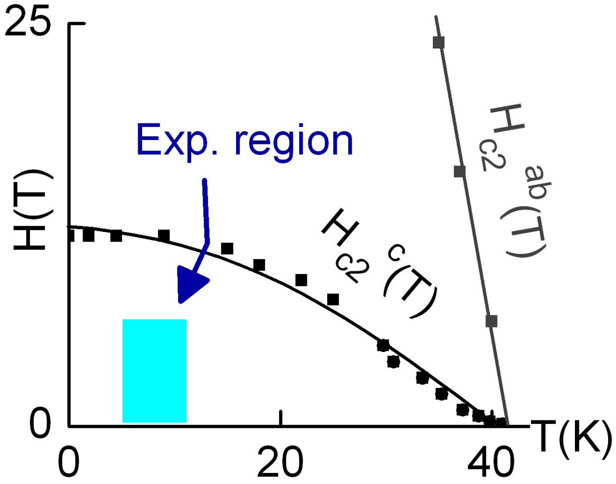

Figure 4.6: The experimental (H, T) region (shaded light blue) used in the $\mathrm{H}_{C2} > \mathrm{H} \geq 0$ and $\mathrm{T} \ll \mathrm{T}_C$ data presented here is compared to the measured upper critical field H_{c2}^{ab} for $H \perp \hat{c}$ and H_{c2}^{c} for $H \parallel \hat{c}$ of $\mathrm{La}_{0.1}\mathrm{Sr}_{0.9}\mathrm{CuO}_2$ [130].

Equation 4.1 provides contrast for regions inside and outside vortex cores for H>0 when superconductivity is fully or partially suppressed. We expect the zero bias conduction to increase in value inside vortices when H > 0 because more low-energy, sub-gap quasiparticles will be available for tunneling to the STM tip when superconductivity is suppressed inside vortex cores. Because of the conservation of spectral weight, the increase of the low-energy quasiparticles must be accompanied by a decreasing spectral weight of the coherence peak in the H = 0 spectra. Hence, we expect the differential conductance at $\omega = \Delta_{pk-pk}(H = 0)$ will decrease inside vortex cores. Using Eq. 4.1 to achieve contrast for inside and outside vortex cores, we expect regions with low values of r_G to be associated with vortices, while regions with higher values of r_G may be attributed to those outside vortices. We can use r_G to achieve contrast for vortices even if the quasiparticle spectra remains gapped inside vortex cores.

In Fig. 4.7a, we present a spatial map of r_G over a large, flat region of the sample of size 160 x 152 nm^2 at H= 0 in Fig. 4.7a and the same area at H= $1.5T$ in Fig. 4.7b. Both images are comprised of 128 x 128 pixels. Using the same contrast and color scale in both figures, we find that the map of r_G is relatively homogeneous for H=0, as shown in Fig. 4.7a. In contrast, there are 18 to 19 regions of low r_G value in Fig. 4.7b for H=1.5T. The total flux expected for this sized area based on an Abrikosov lattice of vortices [72] is consistent with the presence of 18–19 vortices. The image in Fig. 4.7b implies disordered vortices, which is expected in cuprates with random pinning sites.

While all the spectra in Fig. 4.7 are gapped, the spatial resolution of Fig. 4.7 is not sufficient to confirm the spatial evolution of the vortices to insure that we have not missed a zero bias conduction peak inside the vortex cores. To achieve high spatial resolution, it is necessary to perform STS measurements zoomed in on a few vortices at different fields to better characterize the spatial evolution of the quasiparticle tunneling spectral characteristics inside and outside of vortices. In Fig. 4.8a, we present a spatial map of r_G over the same 64nm x 64nm area examined in Figs. 4.3 and 4.4 at H=1T. In Fig. 4.9a, we present a r_G map over a 65nm x 50nm area at H = 2T. Zero-bias conduction peaks have not been not observed anywhere in either map, even in vortex cores.

To illustrate the lack of a zero-bias conduction peak and to better characterize the spectral evolution, we present a spatial linecut through two vortices at H=1T in Fig. 4.8b. The spatial linecut for H=1T is indicated by a black dashed line in Fig. 4.8a. Similarly, we examine the quasiparticle spectra along a linecut through three vortices for H=2T in Fig. 4.9b, with the spatial linecut for

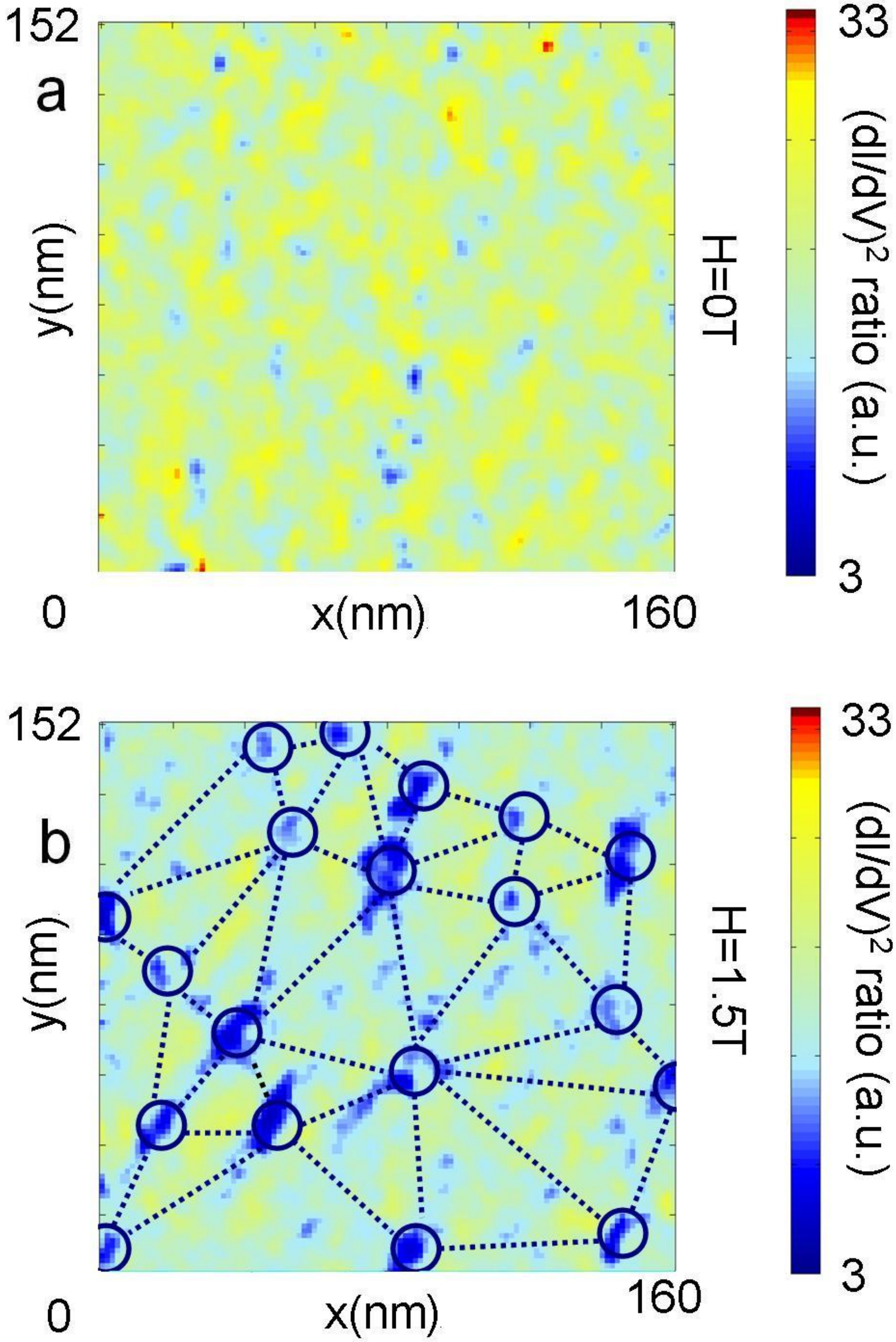

Figure 4.7: (a) A spatial map of the conductance power ratio (on a log scale) taken at H= 0 over a large 160 x 152 nm^2 area. [The conductance power ratio is defined as the ratio of (dI/dV)^2 at $\omega = \Delta_{pk-pk}(H = 0)$ and that at $\omega = 0$, as in Eq. 4.1.] We find a homogeneous map of the conductance ratio. (b) In contrast, the spatial map of the conductance power ratio (in log scale) taken over the same 160 x 152 nm^2 area as in (a) with H = 1.5 T, shows disordered vortices. The average vortex lattice constant a$_B$ = 42 nm is consistent with Arbikosov lattice of vortices and flux is conserved.

H=2T indicated by a black dashed line in Fig. 4.9a. We find that the value of Δ_{pk-pk} is lower inside vortices than that outside vortices. The value of Δ_{pk-pk} equals ∼8meV inside vortex cores for both fields, while the average, outside vortex core Δ_{pk-pk} =11meV for H=1T and Δ_{pk-pk} =10.5meV for H=2T.

The spatial linecuts at H = 1T and H= 2T also reveal the modulations induced in the quasiparticle spectra by vortices in La-112. Specifically, we find significant modulations in the zero-bias conductance ($\omega = 0$) and less severe modulations in the peak-to-peak energy gap ($\omega = \Delta_{pk-pk}$). The modulations track the periodicity of a_B, as expected. The zero-bias conductance is maximum inside vortices, while the $\omega = \Delta_{pk-pk}$ conductance is a minimum inside vortices.

To fully account for the statistics of the spectral evolution with increasing fields, we performed detailed spectral analysis over an extended spatial area and examined the resulting Δ_{pk-pk} histograms to track changes in the average Δ_{pk-pk} value for each spatial map as a function of field. We performed this analysis at magnetic fields of H = 0, 1, 2, 3, 3.5, 4.5 and 6T, and the results are summarized in Fig. 4.10. The histograms were generated from all spectra taken over spatial maps varying in size from (50×50) nm^2 to (100×100) nm^2. The vast majority of the observed Δ_{pk-pk} values appeared above $\Delta_{pk-pk} = (8.5 \pm 0.6)$ meV for all histograms, as illustrated by the pale blue wall in Fig. 4.10. Hence, we refer to $\Delta_{pk-pk} = (8.5 \pm 0.6)$ meV as the low-energy cutoff.

For H > 2T we find that the contrast of vortices in the r_G map diminishes quickly. The average Δ_{pk-pk} gap value associated with spectra outside vortices decreases in energy as field increases, while the intra-vortex spectra still has a Δ_{pk-pk} gap value of ∼8meV. Additionally, the average inter-vortex spectra for H>2T rapidly fills in at zero bias. These two combined effects make clear identification of vortices from the r_G maps more difficult, although vortices may still be found by inspecting the two-dimensional r_G maps and the spatial linecuts together.

In Fig. 4.11(a)–(d), we present a comparison of inter- and intra-vortex spectra for H = 1, 2, 3.5, and 6T. As H increases, the spectra inside vortices stays gapped at ∼8meV. The coherence peaks of spectra outside vortices gradually broadens and the zero-bias conduction fills in. The coherence peaks inside vortex cores remain sharp at lower fields and become significantly rounded

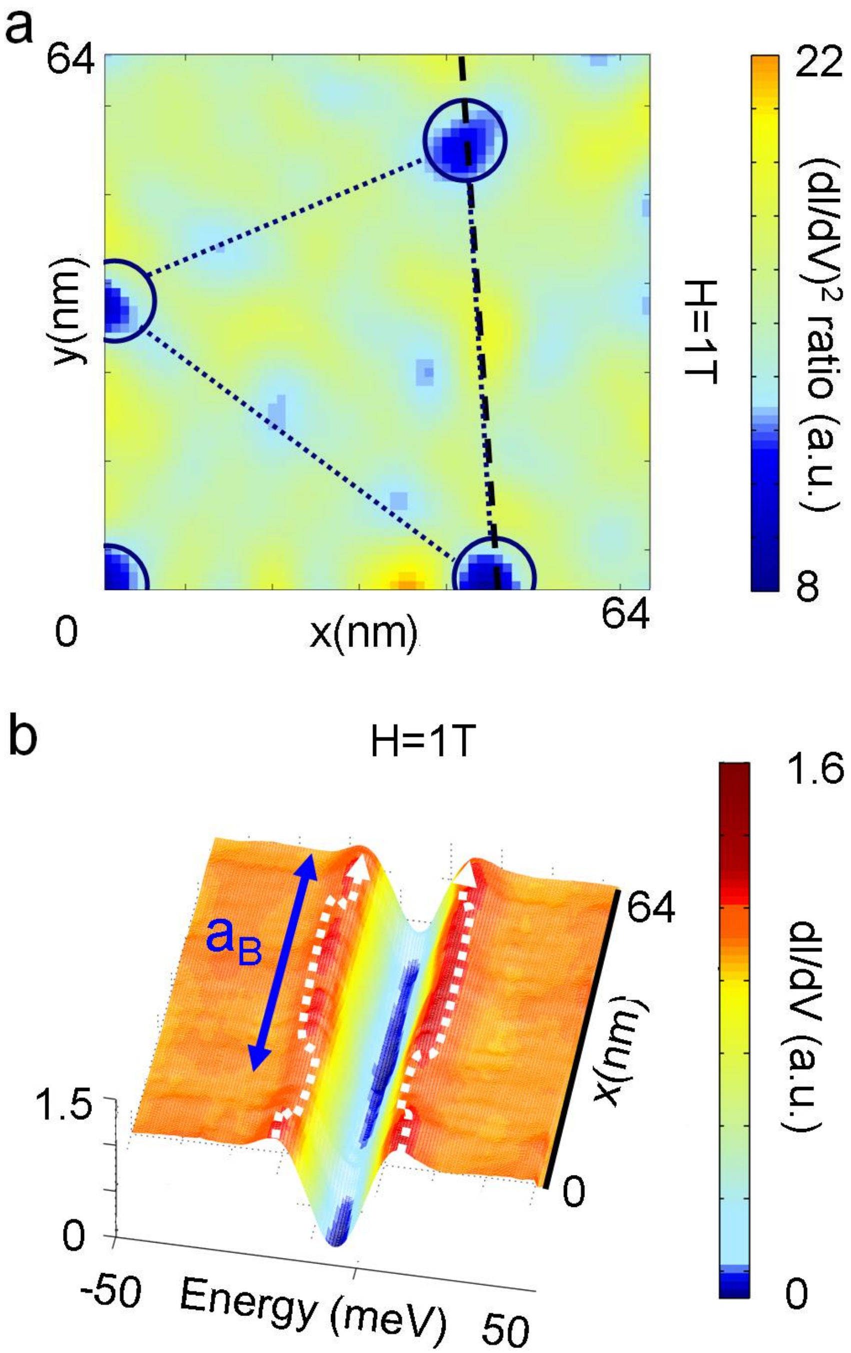

Figure 4.8: (a) A spatial map of the conductance power ratio (on a log scale) taken over the same 64nm x 64nm area shown in Figs. 4.3 and 4.4 with H = 1 T. The image shows a zoomed-in view of vortices separated by an average vortex lattice constant a_B = 52 nm, comparable to the expected value of 49 nm. The average radius of the vortices (indicated by solid circles) is (4.7 $\pm$ 0.7) nm. We expect a radius equal to the ab-plane coherence length, ξ_{ab} = 4.9 nm. (b) Spatial evolution of the quasiparticle tunneling spectra along the black dashed line cutting through two vortices in (a). We find significant modulations in the zero-bias conductance ($\omega = 0$) and slight modulations in the peak-to-peak energy gap ($\omega = \Delta_{pk-pk}$). The modulations track the periodicity of a_B. The zero-bias conductance is maximum inside vortices, while the $\omega = \Delta_{pk-pk}$ conductance is a minimum inside vortices.

as H increases. The H = 6T spectra inside vortices resembles the pseudogap spectra commonly seen in hole-doped cuprates for T>T_C most notably, as both types of spectra exhibit a lack of coherence peaks.

To date, the work presented here is the first direct observation of vortices in any electron-type cuprate superconductor. The difficulty in achieving this feat to date likely arises because of the pseudogap feature inside vortex cores with an energy scale smaller than the superconducting energy, as exemplified for all spectra in Fig. 4.11(a)–(d). Since the superconducting gaps are smaller in the one-layer electron-doped cuprates, it is expected to be even more difficult to observe vortices in the one-layer systems than in La-112. This fact probably explains the lack of vortex identification in electron-doped cuprates prior to this work.

4.5 Discussion

4.5.1 Quasiparticle excitation spectra and ground state hypotheses in $La_{0.1}Sr_{0.9}CuO_2$ for H=0

The goal of the study presented here was to infer information about the ground state of La-112 by studying the quasiparticle excitation spectra and to use our findings to better understand the general properties of excitations in electron-doped cuprates. A useful starting point to understand the excitation spectra observed is to model the H=0 spectra by assuming the ground state is a pure BCS-like superconducting state. Although there is clear evidence that cuprates exhibit unconventional, or non-BCS-like quasiparticle excitations in general, an attempt to fit the data using BCS superconductivity will at least be a useful measure of how far the ground state excitations deviate from conventional superconductivity.

For a representative quasiparticle excitation spectra shown in Fig. 4.4a, we attempt to fit the data by assuming either pure s-wave or pure $d_{x^2-y^2}$-wave superconductivity (d-wave). As mentioned, we use simple BCS-like s-wave or d-wave superconductivity to model the data. Since we observed no zero bias conduction peak in the particular spectra in question, we may model the d-wave pairing

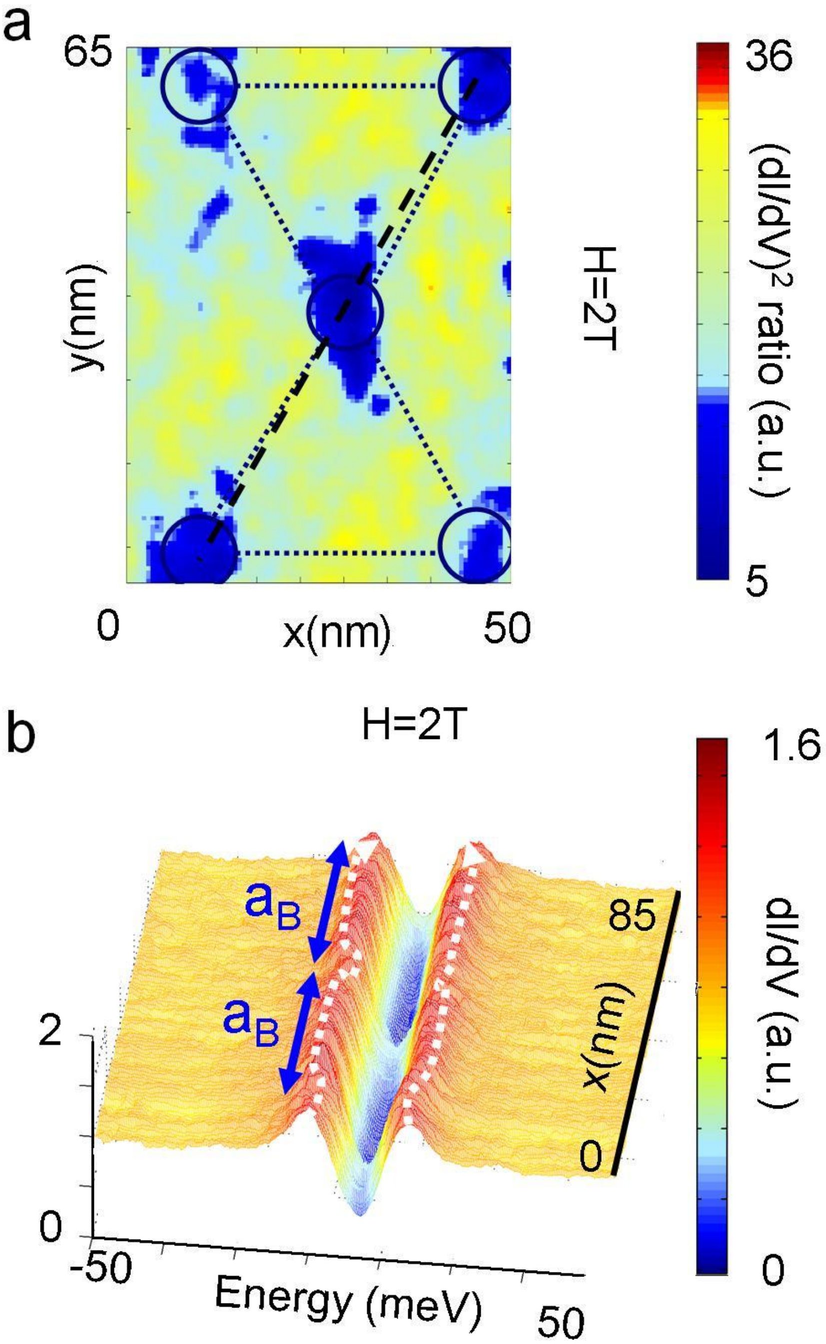

Figure 4.9: (a) A spatial map of the conductance power ratio (on a log scale) taken over a 65nm x 50nm area with H = 2 T. The image shows a zoomed-in view of vortices separated by an average vortex lattice constant a$_B$ = 35 nm, which is equal to the expected theoretical separation value. The average radius of the vortices (indicated by solid circles) is (5.0 $\pm$ 1.3) nm. Again, this value is close to the ab-plane coherence length, ξ_{ab} = 4.9 nm. (b) Spatial evolution of the quasiparticle tunneling spectra along the black dashed line cutting through three vortices in (a). We find significant modulations in the zero-bias conductance ($\omega = 0$) and slight modulations in the peak-to-peak energy gap ($\omega = \Delta_{pk-pk}$). The modulations track the periodicity of a$_B$. The zero-bias conductance is maximum inside vortices, while the $\omega = \Delta_{pk-pk}$ conductance is a minimum inside vortices.

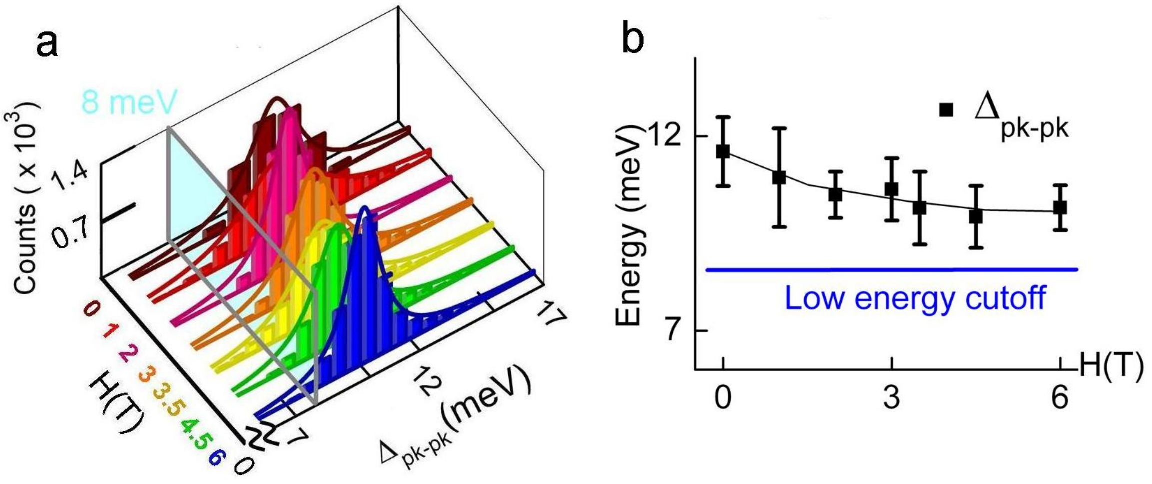

Figure 4.10: (a)Histograms of Δ_{pk-pk} in La-112 determined from quasiparticle tunneling spectra over spatial maps of size ranging from (50×50) nm^2 to (100×100) nm^2 reveal the spectral evolution for H$\geq$ 0. The value of Δ_{pk-pk} decreases as we increase field, but never seems to drop below $\Delta_{pk-pk} = (8.5\pm0.6)$ meV, the low-energy cutoff. Each histogram is fit by a Lorenztian form, shown as solid lines on top of the histograms in the figure. (b)Δ_{pk-pk} vs. H obtained from Lorentzian fits. Solid symbols indicate the peak location of histograms and error bars denote the linewidth of each fitting. The low energy cutoff is shown as a solid blue line.

symmetry by assuming quasiparticle tunneling along the {001} direction. Moreover, given that our measurements are in the tunneling regime of Blonder-Tinkham-Klapwijk (BTK) analysis [97, 93], the differential conductance, dI/dV, should simply be proportional to the single quasiparticle density of states. We can then use Green's function techniques detailed in Chapter 7 to model the quasiparticle excitation spectra expected for both cases. The fitting results are shown as lines over the data in Fig. 4.4a. The data are shown as open circles, while the s-wave fit is shown as a green solid line and the d-wave fit is a red solid line. We have used the superconducting gap value of Δ_{SC} = 12.0meV for the s-wave fitting and Δ_0 = 12.0meV for the d-wave fitting with $\Delta_{SC}(\mathbf{k})=\Delta_0\cdot\cos(2\theta_{\mathbf{k}})$. Here, $\theta_{\mathbf{k}}$ defines the angle in the Brillouin zone relative to the anti-bonding direction.

Close examination of the two fits suggest that the BCS s-wave fitting is far different from the observed excitation spectra at H=0 in La-112. The d-wave fitting is closer to the observed spectra, but we notice the sub-gap states exhibit systematic deviation from the model of pure d-wave superconductivity, as illustrated in the inset of Fig. 4.4a.

Experimentally, it is difficult to understand how simple d-wave superconductivity can come so close to explaining the gathered data in totality. As we have mentioned, a zero-bias conduction peak from tunneling into hundreds of randomly oriented grains and thousands of spectra has never been seen, all dI/dV spectra are independent of momentum within experimental resolution, and the spectral and bulk response to quantum impurities behaves like conventional, fully gapped s-wave superconductivity in La-112 [39]. All the findings mentioned above point to a lack of nodes in the pairing state of superconductivity in La-112, but d$_{x^2-y^2}$-wave superconductivity exhibits nodes oriented 45^o degrees from the Cu-O bonding direction in cuprates. Consequently, pure d$_{x^2-y^2}$-wave superconductivity cannot explain experimental observation.

As an aside, we point out that attempts to fit the spectra using the Dynes model [131] with extra quasiparticle lifetime-broadening leads to a substantial increase in the zero-energy quasiparticle spectra, inconsistent with the empirical observation of vanishing zero-field spectra at $\omega \sim 0$.

At this point, it is clear that a single pairing state of superconductivity cannot explain the observed tunneling spectra. The next logical step to interpret the quasiparticle spectra would be to consider, for example, a mixed pairing state of superconductivity or anisotropic s-wave superconductivity to model the ground state of La-112. In fact, Ref. [132] has considered both cases in detail and found no basis for interpreting the data in either case. Briefly, Ref. [132] found essentially isotropic tunneling spectra, with less than 8% anisotropy, and we expect continued inability of slightly anisotropic s-wave superconductivity to fit the sub-gap states observed in La-112. Further, Ref. [132] explained that a mixed state of (d$_{x^2-y^2}$+s)-wave pairing symmetry is also expected to have nodal quasiparticles, and the expected spectral and bulk response of a (d$_{x^2-y^2}$+s)-wave superconductor to quantum impurities in the CuO_2 planes cannot explain the observed response seen experimentally in La-112.

We may conclude to this point that any known type of ground state containing only superconductivity, whether a single pairing state or a more exotic and unconventional pairing state, cannot explain the observed data for H=0, T=6K in La-112 satisfactorily. Considering the totality of data at H=0, the most obvious signature of something lacking in our description of the ground state is the inability of any of our pure superconductivity models to correctly account for the sub-gap

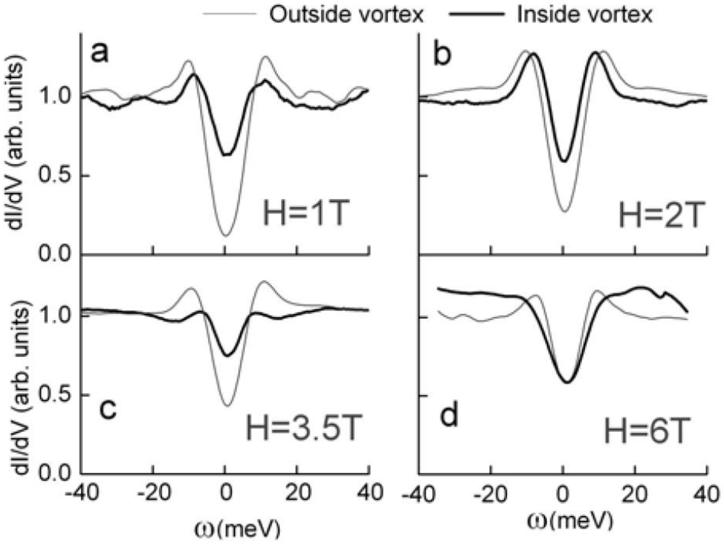

Figure 4.11: Evolution of inside and outside vortex quasiparticle tunneling spectra vs. H in La-112 for (a) $H = 1$ T and $T = 6$ K, (b) $H = 2$ T and $T = 6$ K, (c) $H = 3.5$ T and $T = 6$ K, (d) $H = 6$ T and $T = 11$ K. We find pseudogap-like spectra in the vortex cores, shown as thick lines. The spectra inside vortices for $H = 6$ T appears especially pseudogap-like, with no apparent coherence peaks. Spectra well outside of vortices are are shown as thin lines. The peak features around ($\omega = \pm\Delta_{pk-pk}$) broaden as H increases. The zero-bias conductance of the spectra outside vortices increases with H.

($\mid \omega \mid < \Delta_{pk-pk}(H = 0)$) quasiparticle states observed.

In Chapter 7, we consider the possibility that competing orders coexist with superconductivity in the ground state. We may generate the expected quasiparticle excitation spectra of a ground state of superconductivity and a gapped competing order by using the Green's function techniques of Chapter 7, and a comparison with the experimental observation in La-112 at H = 0 may then be made. Using the techniques of Chapter 7, we produce the theoretically expected quasiparticle excitation spectra from the assumption of superconductivity coexisting with a gapped spin-density wave and show the fit as a blue curve on top of the data in the main panel and inset of Fig. 4.4a. The theoretical fit of superconductivity and a competing order more closely models the data than either the theoretical fit of pure s-wave superconductivity or pure d-wave superconductivity, and as shown in the inset of Fig. 4.4a, reveals a more systematic fit of the sub-gap states observed in data than either model of pure superconductivity. Thus, it is plausible that a ground state of coexisting superconductivity and a competing order may explain the observed quasiparticle excitation spectra

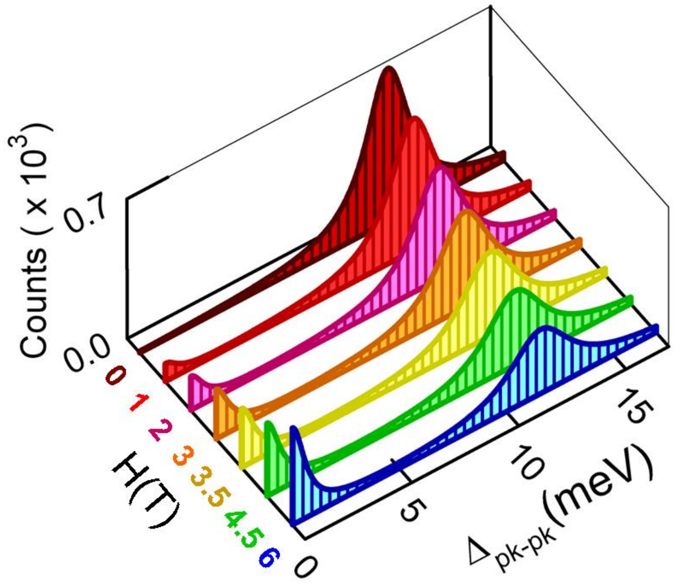

Figure 4.12: Schematic illustration of quasiparticle Δ_{pk-pk} histograms in a conventional type-II superconductor for $T \ll T_c$ and $H \ll H_{c2}$. As H increases, the quasiparticles in the vortex state of a conventional type-II superconductor shift to lower energy and a peak at $\omega = 0$ appears. The downshifted spectral weight is approximated by the ratio of the vortex core area relative to the Abrikosov vortex unit cell, $(\pi\xi_{ab}^2/2)/(\sqrt{3}a_B^2/4)$.

in La-112.

4.5.2 Pseudogap-like spectra inside vortices for H$_{C2}$ >H>0 in La$_{0.1}$Sr$_{0.9}$CuO$_2$

The complete absence of a zero bias conductance peak in the vortex-state quasiparticle spectra, shown in Figs. 4.8, 4.9, and 4.11, and the existence of the low-energy cutoff, shown in Fig. 4.10, further corroborate the notion that a pure superconducting ground state cannot explain the observed properties in La-112 for H>0. To clarify, a conventional type-II superconductor in a magnetic field would be expected to show the field evolution of histograms shown in Fig. 4.12 if superconductivity is the sole ground state order parameter. We would expect for $H < H_{C2}$ and $T \ll T_c$ that a fraction of quasiparticles equal to $(\pi\xi_{ab}^2/2)/(\sqrt{3}a_B^2/4)$ in the H=0 histogram would downshift to energies $\omega < \Delta_{pk-pk}(H = 0)$ due to the suppression of superconductivity inside vortices. The redistributed quasiparticles would create a peak in the histogram at $\omega = 0$, as depicted in Fig. 4.12. The number of quasiparticles redistributed to lower energies would be linearly proportional to H and easily seen in our experiments, with an estimated value of $\sim 25\%$ of the total spatial area considered for H=6T.

Another proposed hypothesis to consider here would be the case of superconductivity and one or more competing orders coexisting in La-112. We find that the results could be consistent with this scenario *if* the competing order or orders are not suppressed by a magnetic field. As was discussed in section 4.1, commensurate static orders [10, 11] were seen to be enhanced or at least unaffected by a magnetic field from neutron scattering measurements on one-layer electron-doped cuprates, and commensurate spin excitations with a spin gap smaller than the superconducting were also observed [9].

It is possible we are observing the combined gap of quasiparticles in our STS quasiparticle spectra due to superconductivity and a competing order, and we cannot resolve the competing order gap until we apply a magnetic field to suppress the superconducting gap inside vortex cores. Neutron scattering has not been performed on La-112 because of a lack of large single crystals for measurements, so that we cannot be certain about whether static and spin gapped correlations are present in La-112. Regardless, the competing order scenario maintains plausibility in La-112, and we will consider quantitative models of this scenario later in Chapter 7.

As an interesting note, we will see in Chapter 5 that STS spectra from optimally doped, hole-doped $YBa_2Cu_3O_{7-\delta}$ (Y-123) also reveal pseudogap-like features inside vortices, except that the pseudogap energy exceeds $\Delta_{pk-pk}(H = 0)$. Further, we *do* observe satellite features in Y-123 at low temperatures, and the situation in Y-123 can also be interpreted as arising from a ground state of competing orders and superconductivity when the competing order gap energy exceeds the superconducting gap energy. We will discuss these findings in more detail in Chapter 5.

There is another scenario worth discussing to explain our observations. In s-wave superconductors, bound single quasiparticle states inside vortex cores give rise to a zero-bias conductance peak for finite thermal smearing and low momentum (l=0) states, but for bound states of high angular momenta and small thermal smearing, the DOS inside the vortex core may acquire a dip-like feature in the conductance. [73] Therefore, high angular momentum states can display dips rather than a peak at zero bias, which could explain our data if low momentum states are absent and we have s-wave superconductivity. However, the dip widths can never exceed the superconducting energy, so this result is inconsistent with a pure superconducting ground state if we consider both experimental results from Y-123 and La-112. Additionally, theory for the vortex-state quasiparticle spectra of s-wave superconductivity predicts continuously varying energy dips at $0 < \omega < \Delta_{\rm SC}$ for $0 < r < \xi_{\rm ab}$ and $T \ll T_c$ [73], where r is the radius measured from a vortex core center. Our data reveals a nearly constant energy (8.5 ± 0.6) meV throughout the vortex core, with $(0.5 \times 0.5)\rm{nm}^2$ spatial resolution in a vortex core of radius $\sim$ 5 nm. Consequently, our data is inconsistent with high-angular-momentum bound states in an s-wave superconductor.

Finally, we note that our results are consistent with the finding of the hidden pseudogap in grain boundary tunneling experiments on LCCO and PCCO, where a spatially averaged, field-induced pseudogap was found with a gap smaller than the superconducting gap. [17] Both our results and the one-layer electron doped results suggest that the pseudogap energy is less than the superconducting energy and the pseudogap vanishes at temperature $T^* < T_C$. Both cases could be the result of superconductivity and competing orders in the ground state of electron-doped cuprates.

4.6 Summary

In conclusion, we present the spatially resolved scanning tunneling spectroscopy of single quasiparticle density of states in infinite-layer, electron-doped La-112 as a function of magnetic field and temperature. We find that the zero field spectra is consistent with a ground state showing a lack of pseudogap for $T > T_C$ and no satellite features for $T \ll T_C$. Upon application of a magnetic field $H_{C2} > H > 0$, vortices are introduced in La-112, and they can be identified by the contrast maps of the conductance power ratio, r_G. Moreover, all vortex-state spectra observed remain gapped and a hidden pseudogap energy of ∼8.5meV is revealed inside the vortex core. The energy histograms for the spatial statistics of Δ_{pk-pk} show that Δ_{pk-pk} never drops below the low energy cutoff of (8.5 ± 0.6) meV for all magnetic fields up to 6T. These results suggest that a pseudogap is hidden in the H=0 spectra because the pseudogap energy is less than the superconducting gap energy and that the observed quasiparticle excitation spectra for both $H = 0$ and $H > 0$ could be due to a ground state of coexisting competing orders and superconductivity. This issue will be investigated with more details in Chapter 7.

Chapter 5

Scanning tunneling spectroscopic studies of the hole-type cuprate $YBa_2Cu_3O_{7-\delta}$

Building on our results and conclusions in electron-type $La_{0.1}Sr_{0.9}CuO_2$ (La-112), we study quasiparticle excitation spectra in hole-type $YBa_2Cu_3O_{7-\delta}$ (Y-123) for comparison between electron- and hole-type cuprates in this chapter. Our goal is to study the low-energy excitations of Y-123 through detailed spatial studies of the quasiparticle tunneling spectra in zero and finite-magnetic field. Again, we investigate the quasiparticle spectra of Y-123 with spatially resolved scanning tunneling spectroscopy (STS) as a function of magnetic field and temperature in this chapter.

We find a plethora of evidence demonstrating that the quasiparticle excitations of Y-123 also exhibit unconventional behavior compared to conventional type-II superconductors. In zero-magnetic field and at T =6K, we observe a characteristic energy in the tunneling spectra with an average peak location given by the superconducting energy, $\Delta_{SC} = (20.0 \pm 1.0)$meV, and the presence of satellite features at a characteristic energy given by the effective gap energy, $\Delta_{eff} = (37.8 \pm 2.0)$meV. Under applied magnetic fields, the intra-vortex spectra of Y-123 reveal a pseudogap energy (V_{PG}) and a subgap energy (Δ') such that $V_{PG} > \Delta_{SC}$ and $\Delta' < \Delta_{SC}$, and the inter-vortex spectra show a rounded set of peaks at $\pm\Delta_{SC}$. As magnetic field is increased, a rapid shift of quasiparticle spectral weight from the superconducting energy, Δ_{SC}, to V_{PG} and Δ' occurs. In addition to observing Δ_{SC}, V_{PG}, and Δ' in inter-vortex and intra-vortex quasiparticle spectra, high-spatial-resolution STS studies as a function of magnetic field reveal energy-independent spatial conductance modulations along the Cu-O bonding direction and the nodal direction. Two conductance modulations are observed along the Cu-O bonding direction with periodicity of 3.6 and 7.1 lattice constants; further, a conductance modulation with periodicity of 9.5 lattice constants is observed along the nodal direction. Upon Fourier-transforming the local density of states (LDOS), we characterize the energy symmetry of the conductance modulations and find evidence of a pair-density wave (PDW), a charge-density wave (CDW), and a spin-density wave (SDW).

In this chapter, we briefly review the “one gap” and “two gap” theoretical models of the ground state excitations of cuprates and the experimental progress to date aimed at discerning between the two scenarios. Subsequently, we detail our experimental methods to perform spatially resolved STS on Y-123 as a function of temperature and magnetic field. We then present our experimental data and discuss the results in the context of the two models. The totality of results in Y123 suggest that a ground state of superconductivity alone is unable to account for all the unconventional behavior observed.

5.1 Introduction

Hole-type cuprates in contrast to electron-type cuprates exhibit a higher maximum superconducting transition temperature ($T_{C,max}$ = 138K under ambient pressure and $T_{C.max}$ = 165K under high pressure) and more readily reveal unconventional quasiparticle excitation phenomena. For example, temperature evolution studies of underdoped and optimally doped $Bi_2Sr_2CaCu_2O_x$ (Bi-2212) excitation spectra display pseudogap phenomena above T_C without need of a magnetic field to suppress superconductivity [2]. A debate continues today over the relevant ground state and the origin of the pseudogap phenomenology and unconventional quasiparticle behavior in hole-type cuprates [26, 3]. However, a complete theoretical description, consistent with all experimental results, has been lacking and little effort has been exerted to link the hole- and electron-type cuprates.

As we have discussed in Chapters 1 and 2, the debate over the relevant ground state to account for hole-type quasiparticle phenomena may generally be divided into two viewpoints. One viewpoint, which we refer to as the “one-gap” scenario, supposes that the ground state of cuprates contains superconductivity alone and that the onset of Cooper pair formation occurs at the pseudogap temperature, T^*, which is greater than T_C [26, 133, 134, 135, 98, 8]. For $T^* > T > T_C$, these preformed pairs exhibit no global phase coherence; therefore, macroscopic superconductivity is not observed in bulk measurements. Further, the "one-gap" scenario asserts that for $T < T_C$ preformed pairs condense and then cuprates exhibit macroscopic superconductivity and global phase coherence. Consequently, this scenario asserts that the pseudogap and the $T \leq T_C$ superconducting gap share a common origin.

In contrast, a second general viewpoint supposes that the ground state of cuprates consists of coexisting superconductivity and competing orders. We discussed this scenario, which we refer to as the "two-gap" scenario, more fully in the previous chapter detailing measurements on La-112. In addition to the findings in electron-type cuprates, experimental observations in hole-type cuprates appear to favor a "two-gap" model [6, 85, 60, 4]. The "two-gap" scenario asserts that the pseudogap is due to competing orders other than superconductivity and that the source of unconventional temperature and magnetic-field dependent quasiparticle excitations arise from interplay of superconductivity and competing orders [136, 31, 137, 86]. In the "two-gap" scenario, T^* indicates the transition temperature of a competing order, and T_C is the superconducting transition temperature.

The pseudogap excitation spectra may be investigated by varying temperature above T_C and characterizing the quasiparticle spectra in hole-type cuprates; however, pseudogap-like spectra may also be investigated by applying a magnetic field and examining the quasiparticle spectra inside vortex cores using the same technique we used in studying the electron-type La-112 in the last chapter. Similar to the experimental situation we observed in La-112, pseudogap-like quasiparticle excitation spectra also appear inside vortices in hole-type cuprates; however, two energy scales other than the superconducting gap emerge in the vortex cores of the hole-type cuprates. Specifically, an energy gap similar to the pseudogap energy and a subgap energy smaller than the superconducting gap have been observed in the vortex cores of Y-123 [69, 138] and Bi-2212 [20] previously. Doping dependent studies show that the subgap energy decreases as doping increases and demonstrates a linear relationship with the average peak-to-peak gap, Δ_{pk-pk}, seen in zero-field for $T \ll T_C$ in

Bi-2212 and optimally doped Y-123 [19, 3]. Further, the subgap and pseudogap energies appear independent of magnetic field in Bi-2212 [20], while the magnetic field dependence of the vortex core quasiparticle spectra in Y-123 remain unexplored prior to the work presented here.

In addition to the linear relationship between the T $\ll$ T$_C$ peak-to-peak gap, Δ_{pk-pk}, and Δ', a linear relationship between the pseudogap energy, V$_{PG}$, observed above T$_C$ and Δ_{pk-pk} are also found in Bi-2212 as a function of doping [3, 139]; however, questions arise over the validity of any inferred relation between V$_{PG}$ and Δ' and the peak-to-peak gap in Bi-2212. Namely, the quasiparticle spectra and values of Δ_{pk-pk} in Bi-2212 are known to exhibit significant inhomogeneity over lengths scales of approximately 5nm [68]. Therefore, any inferences [115, 33] drawn by the linear relationship between the peak-to-peak gap and the V$_{PG}$ energy require careful consideration of the origin of the peak-to-peak gap in zero-magnetic field, especially in underdoped Bi-2212. As we pointed out in Chapters 1 and 2, the average Δ_{pk-pk} values of underdoped Bi-2212 do not follow the same doping behavior as the bulk superconducting T$_C$ values [33, 68]. Furthermore, careful inspection of the vortex state spectra of hole-type cuprates reveals pseudogap-like behavior at energies that differ up to ~30meV from the values of Δ_{pk-pk} observed in zero-magnetic field [115, 69]. Due to the fact that the pseudogap and superconducting gap are similar in energy and that there is experimental evidence of two gaps coexisting in hole-type cuprates, detailed measurements of the zero-field and vortex-state gap energies in cuprates other than Bi-2212 are required to draw further conclusions. We perform such detailed spatial measurements on Y-123 in the work presented here.

Adding to the complexity of the vortex core spectra and zero-field spectra in hole-type cuprates, measurements in Bi-2212 at H=5T revealed an energy independent checkerboard-like conductance modulation with $4a_0 \times 4a_0$ lattice constant periodicity inside vortex cores [21] in addition to energy-dependent quasiparticle scattering interferences [68]. Here a_0=0.385nm is the planar lattice constant of Bi-2212. The energy-independent $4a_0 \times 4a_0$ conductance modulations could not be accounted for by modeling quasiparticle scattering interference in Bi-2212 [78, 79]. Various competing order models purport to explain the modulations by invoking pair-density waves (PDW) [83, 84], pinned spin-density waves (SDW) [29, 86], and charge-density waves (CDW) [31, 87], and it is supposed

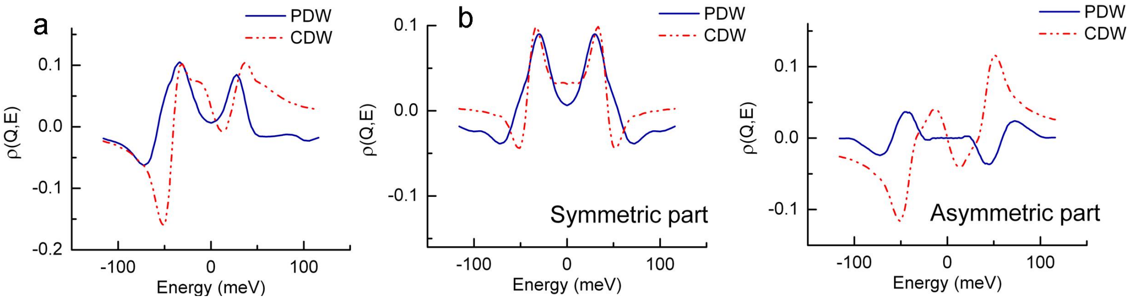

Figure 5.1: Energy symmetry of the amplitude of FT-LDOS to discern a pair-density wave (PDW) and a charge-density wave (CDW). (a) Theoretical energy dependence of the amplitude of FT-LDOS for CDW and PDW using realistic bandstructures for the cuprates. Figure adapted from Ref. [84]. (b) The results of decomposing the theoretical model for CDW and PDW in (a) into symmetric and anti-symmetric components. Left panel: Symmetric components from (a). Right panel: Anti-symmetric components from (a).

that the spatial ordering of these competing orders is more readily revealed in vortices where superconductivity is suppressed.

Fundamentally, PDWs differ from CDWs and SDWs because PDWs are particle-particle excitations with a finite momentum, whereas SDWs and CDWs are particle-hole excitations. Empirically, it is expected that the spatial conductance contrast of a PDW will remain the same when switching from positive to negative energy, while the spatial conductance contrast for CDW or SDW excitations is expected to reverse. Furthermore, a theoretical model to differentiate PDW from CDW and SDW excitations along these same lines exists [84]. The theory predicts the amplitude of diffraction modes observed in Fourier transformed local density of states (FT-LDOS) measurements will be symmetric in energy for PDW and antisymmetric in energy for CDW and SDW [84]. However, the insertion of realistic bandstructures for cuprates into the theory leads to mixing of symmetric and anti-symmetric energy dependence in the FT-LDOS for PDW, CDW, and SDW. The authors in Ref. [84] conclude, in this case, that a PDW is expected to show stronger symmetric components than anti-symmetric components, whereas a CDW or SDW will show show stronger anti-symmetric or equal symmetric/anti-symmetric components. We illustrate the theoretical scenario for realistic bandstructures in Fig. 5.1 for further clarity.

Following the observation of conductance modulations near vortices in Bi-2212, subsequent spatially resolved STS experiments performed in zero-magnetic field in Bi-2212 also revealed a $4a_0$ ×

$4a_0$ lattice constant modulation and found approximately symmetric energy dependence of the amplitude of the FT-LDOS [80]. The finding of symmetric energy-dependent FT-LDOS suggested a PDW as the origin of the checkerboard modulations. Furthermore, the authors of Ref. [80] pointed out that other energy independent diffractions appeared faintly visible in the FT-LDOS; however, the confluence of strong spectral inhomogeneity and the presence of supermodulations in Bi-2212 obscured definitive identification of any other periodicity. Curiously, inspection of the FT-LDOS data revealing checkerboard-modulations in Bi-2212 at H=5T [21] shows a set of seemingly energy-independent diffraction modes along the nodal direction; however, all spots along the nodal direction in the paper are attributed to supermodulations. In the context of our results in Y-123 to be presented, we point out that Y-123 does not exhibit periodicity due to supermodulation because of the absence of the BiO layers, but a set of nodal energy-independent diffraction modes is eminently observed. Therefore, it is possible that at least one other conductance modulation periodicity has been observed in Bi-2212 but overlooked. To date, experiments investigating the FT-LDOS and magnetic field dependence of the quasiparticle spectra in Y-123 have not been explored, except for the work we present here.

In this chapter, we explore the FT-LDOS of Y-123 using spatially resolved STS as a function of magnetic field. Additionally, we characterize the evolution of the Δ_{SC}, Δ_{eff}, V_{PG}, and Δ' energy scales as a function of magnetic field using spatially resolved STS and explore the implications of all our results in Y-123.

5.2 Sample preparation

The sample examined in this work is an optimally doped, untwinned Y-123 single crystal with $T_C=(92.9 \pm 0.5)$K grown by Dr. A. I. Rykov and provided by our collaborator Professor S. Tajima for the investigations performed here. The sample is a high-quality $YBa_2Cu_3O_{7-\delta}$ single crystal grown by a top-seeded pulling technique and oxygenated under uniaxial pressure in order to obtain the orthorhombic twin-free samples. The crystal has a volume of approximately 10 mm^3 with a transition width ΔT_C <0.2K [140] The crystal structure of Y-123 has two CuO_2 planes per unit cell and additional Cu-O chain layers in the unit cell.

Unlike Bi-2212, the surfaces of Y-123 cannot be easily cleaved without causing structural damages to the surface. Vacuum cleaved surfaces of Y-123 terminate at either the Cu-O chains that are prone to loss of oxygen or at the BaO layers that are prone to the development of surface states [141, 142, 143, 144, 145, 146]. In Bi-2212, cleaving occurs at the BiO layer due to the the fact that the double BiO layers are only bonded with van der Waal forces, and this layer protects the underlying CuO_2 planes from loss of oxygen and allows observation of reproducible quasiparticle tunneling spectra [2, 22]. Similarly, bromine etching of Y-123 surfaces leads to reproducible quasiparticle tunneling spectra and terminates at the CuO_2 planes according to XPS studies [142, 147]. Therefore, the structural integrity is retained and the loss of oxygen is largely prevented if the etched sample is immediately transferred into UHV and low-temperature environment. The top CuO_2 layer is found to be metallic with a well defined Fermi edge, and this metallic layer contributes to a constant conductance offset in the quasiparticle spectra. In Appendix A, we describe the procedure to account for the surface metallic contributions to the quasiparticle spectra so that the generic spectra of the superconducting states are deconvolved from our measurements.

We prepared the Y-123 surfaces for investigation with the STM by performing a bromine etch of the surface using the same procedure that was described in Chapter 4 for La-112. X-ray photoemission spectroscopy (XPS) reveals that bromine etching terminates the Y-123 surface at the CuO_2 planes and chemically passivates the surface while retaining the bulk spectra of the constituent elements [141, 142]. The etched surface of Y-123 does not permit sufficient topographical sensitivity to reveal individual atoms in the STM constant-current topographic imaging mode, and the origin of this effect is the same as that in La-112, described in the previous chapter. Furthermore, this behavior has been previously observed in Y-123 [3]. However, the STM can still measure quasiparticle spectra and the etched surface topography with atomic-level spatial resolution.

Characterization of the c-axis irreversibility field, H^c_{irr}, for H||c indicates that H^c_{irr} greatly exceeds H=6T in optimally doped Y-123 [148]. Furthermore, stationary vortices have been observed for c-axis tunneling experiments on optimally doped Y-123 samples at T=4.2K and H=6T [69]. Our experiments observe stationary vortices over the time scale of 3–5 days for experiments in fields up to 6T, in agreement with these results.

5.3 Experimental results

5.3.1 Zero magnetic field characterization of Y-123

We present in Fig. 5.2 representative normalized quasiparticle tunneling spectra (open symbols) measured on our optimally doped Y-123 single crystal at T =6K, 77K, and 102K. The quasiparticle spectra at T = 6K exhibits clear coherence peaks at the superconducting energy, $\Delta_{SC} \simeq \pm 20$meV, and rounded shoulder-like satellite features at the effective gap, $\Delta_{eff} \simeq \pm 38$meV. At T = 77K < T_C, only one set of rounded peak features remains in the quasiparticle spectra, and any remaining peaks vanish within experimental resolution for T = 102K > T_C. We identify the coherence peaks observed at T = 6K as the superconducting energy gap, Δ_{SC}, based on the fact that the coherence peaks for $T \ll T_C$ in Y-123 follow the same trend in doping as the bulk T_C values, as is discussed more fully in Chapter 7.

The $\omega = \pm\Delta_{SC}$ coherence peaks and subgap density of states in optimally doped Y-123 may be fit by assuming d-wave superconductivity alone with remarkable success [35]; however, further modeling is necessary to account for the satellite features associated with Δ_{eff}. Following the analysis in Chapter 7, we may model Δ_{SC} and Δ_{eff} in the T = 6K spectra by assuming coexisting d-wave or (d+s)-wave superconductivity (SC) and competing orders (CO) and using Green's function techniques (all fits to the data using SC/CO are shown as solid lines in Fig. 5.2). Specifically, we may model the competing order as a CDW specified by an energy scale, $V_{CO} = 32$meV, and a density-wave periodicity, $|\mathbf{Q}_{CO}| = (0.25 \pm 0.03)\pi$ (which is along the Cu-O bonding direction for the T = 6K spectra). The effective gap is determined by $\Delta^2_{eff} = \Delta^2_{SC} + V^2_{CO}$, while Δ_{SC} may be put directly into the model. Furthermore, we can fit the T=77K quasiparticle spectra using the same SC/CO assumption, but we must use thermal Green's function to model the data. We find that thermal broadening smears the identification of the Δ_{SC} and Δ_{eff} features in the T=77K data. A

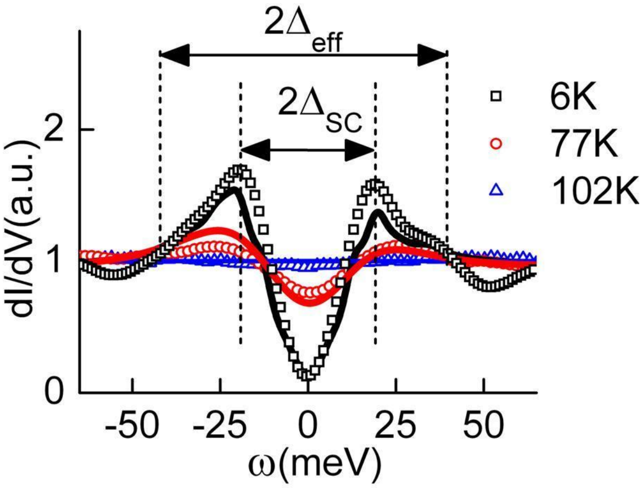

Figure 5.2: Representative quasiparticle spectra at zero magnetic field in Y-123. In this figure, we show experimental quasiparticle spectra normalized to the high energy background for T = 6K, 77K, and 102K in Y-123 (open symbols). The superconducting gap, Δ_{SC}, and the effective gap, Δ_{eff}, are indicated in the figure. Background normalization procedures are discussed in Appendix A. Solid lines are fits to the data by assuming a model of coexisting superconductivity and competing orders (SC/CO). A CDW order with a competing order energy and a wavevector along the Cu-O bonding direction given by V_{CO}=32meV and $|\mathbf{Q}_{CO}|=0.25\pm0.03\pi$ was used to fit the T = 6K data. More details of the theoretical fitting model using Green's functions techniques are presented in Chapter 7. The SC/CO model reproduces the features at Δ_{SC} and Δ_{eff} for T = 6K. Additionally, thermal Green's function modeling of SC/CO reproduces the quasiparticle spectra observed at T = 77K.

model assuming pure superconductivity in the ground states of cuprates does not present a natural means of generating both Δ_{SC} and Δ_{eff} at low temperatures.

To characterize the spatial evolution of Δ_{SC} and Δ_{eff} in the quasiparticle tunneling spectra more thoroughly for T = 6K, we generated spatial maps of Δ_{SC} and Δ_{eff} from quasiparticle spectra taken over a (95 × 95) nm^2 area using (128 × 128) pixels. The resulting spatial maps of Δ_{SC} and Δ_{eff} are shown in Fig. 5.3a and 5.3b, and histograms of the observed values are shown in Figs. 5.3c and 5.3d. We observe long range homogeneity in Δ_{SC} from the spatial map and the histogram of Δ_{SC} shown in Figs. 5.3a and 5.3c, and obtain a value of Δ_{SC}=(20±1.0)meV from a Gaussian fit of the Δ_{SC} histogram. The spatial map and histogram of Δ_{eff} are shown in Figs. 5.3b and 5.3d, and we observe less homogeneity in Δ_{eff} than in Δ_{SC} and obtain a value Δ_{eff}=(37.8±2.0)meV. We remark that the coherence peaks seen in Y-123 do not reproduce the strong spectral inhomogeneity seen in the coherence peaks in Bi-2212 [68]. In fact, the shoulder-like satellite features at Δ_{eff} display stronger inhomogeneity than the coherence peaks in Y-123 and compare more favorably with the

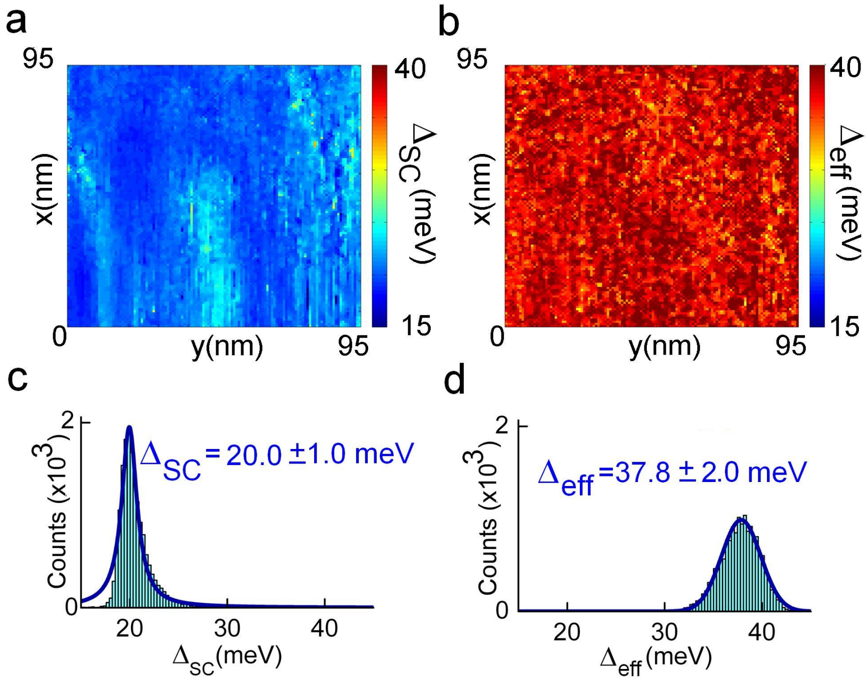

Figure 5.3: Spatial statistics of Δ_{SC} and Δ_{eff} at zero magnetic field in Y-123. (a) Spatial map of experimentally measured values of Δ_{SC} over an area of (95 × 95)nm^2 using (128 × 128) pixels. (b) Spatial map of experimentally measured values of Δ_{eff} over an area of (95 × 95)nm^2 using (128 × 128) pixels. (c) Histogram of Δ_{SC} obtained from the spatial map in (a). The histogram is fit using a Gaussian function, which yields Δ_{SC}=(20.0±1.0)meV. (d) (c) Histogram of Δ_{eff} obtained from the spatial map in (a). The histogram is fit using a Gaussian function, which yields Δ_{eff}=(37.8±2.0)meV.

inhomogeneity observed Δ_{pk-pk} in Bi-2212, although the Δ_{pk-pk} maps in Bi-2212 are still far more inhomogeneous than the Δ_{eff} map in Y-123.

5.3.2 Spectral evolution of Y-123 in an applied magnetic field

To further characterize Y-123, we examined the effect of magnetic field on the quasiparticle spectra for H = 2T, 4.5T, and 6T at T = 6K. Similar to our measurements in La-112, we utilized the conductance power ratio, r_G, defined in Eq. 4.1, to achieve spatial resolution of vortices in Y-123. In the definition of r_G in Y-123, the value of $\Delta_{pk-pk}(H = 0)$ may be identified with the superconducting gap, Δ_{SC}.

In Figs. 5.4a and 5.4b, we present representative spatial maps of r_G over approximately (40 × 75) nm^2 areas that display vortices for H = 2T and 4.5T. Figure 5.4h shows a representative map of r_G

values at H = 0 for comparison with r_G maps in magnetic fields. Vortices manifest as local minima in the value of r_G because of a loss of quasiparticle spectral weight at $\omega = \pm\Delta_{SC}$ and increase of $\omega = 0$ quasiparticle spectral weight in vortex cores due to the suppression of superconductivity.

In Figs. 5.4(a) – (d), significant modulations are observed in the quasiparticle spectra due to the application of a magnetic field, and we attribute the areas of low r_G value to vortices in Figs. 5.4a and 5.4b. We observe disordered vortices in Y-123, which is expected for doped cuprates with random pinning sites and is similar to what we observed in La-112. The total flux over the areas in Fig. 5.4a and 5.4b is conserved, and we find averaged vortex lattice constants of a_B=33.2nm and a_B=23.5nm for H = 2T and H = 4.5T. The empirical vortex lattice constants compare favorably with the expected values of a_B=35.0nm and a_B=23.3nm for H = 2T and H = 4.5T.

The size of vortices for tunneling along the c-axis are expected to have a radius equal to the ab-plane coherence length, $\xi_{ab} \simeq$2nm, in Y-123. The vortices identified in Fig. 5.4a and 5.4b are larger than ξ_{ab} and appear to have a halo of low r_G values around the vortex cores. Empirically, the halo radii are ξ_{halo}=(7.7±0.3)nm, ξ_{halo}=(6.4±0.6)nm, and ξ_{halo}=(5.0±0.7)nm for H = 2T, H = 4.5, and H = 6T, respectively.

Following the identification of vortices, we examine spatial linecuts through vortices seen in Fig. 5.4a and 5.4b. Figure 5.4c displays a spatial linecut at H = 2T through two vortices, where the white dashed line in Fig. 5.4a indicates the location of the linecut examined. Similarly, we present a spatial linecut through three vortices in Fig. 5.4d following the white dashed line shown in Fig. 5.4b. As expected, we find significant spectral modulations induced by vortices at zero energy (ω=0) and at the peak energy, $\omega = \pm\Delta_{pk-pk}$. The modulations follow the periodicity expected by an Abrikosov vortex lattice, following the value of a_B (the magnetic field-dependent vortex lattice spacing).

We find that the spectra inside vortex cores remains gapped and displays a pseudogap-like energy, V_{PG}, and a subgap energy, Δ', while the spectra between vortex cores displays peaks at the superconducting gap energy, $\omega \simeq \pm\Delta_{SC}$. Representative intra-vortex and inter-vortex spectra for H = 2T, 4.5T, and 6T are shown in Figs. 5.4(e)–(g), with Δ', Δ_{SC}, and V_{PG} identified.

To fully characterize the values of Δ', Δ_{SC}, and V_{PG} and the spectral evolution as magnetic

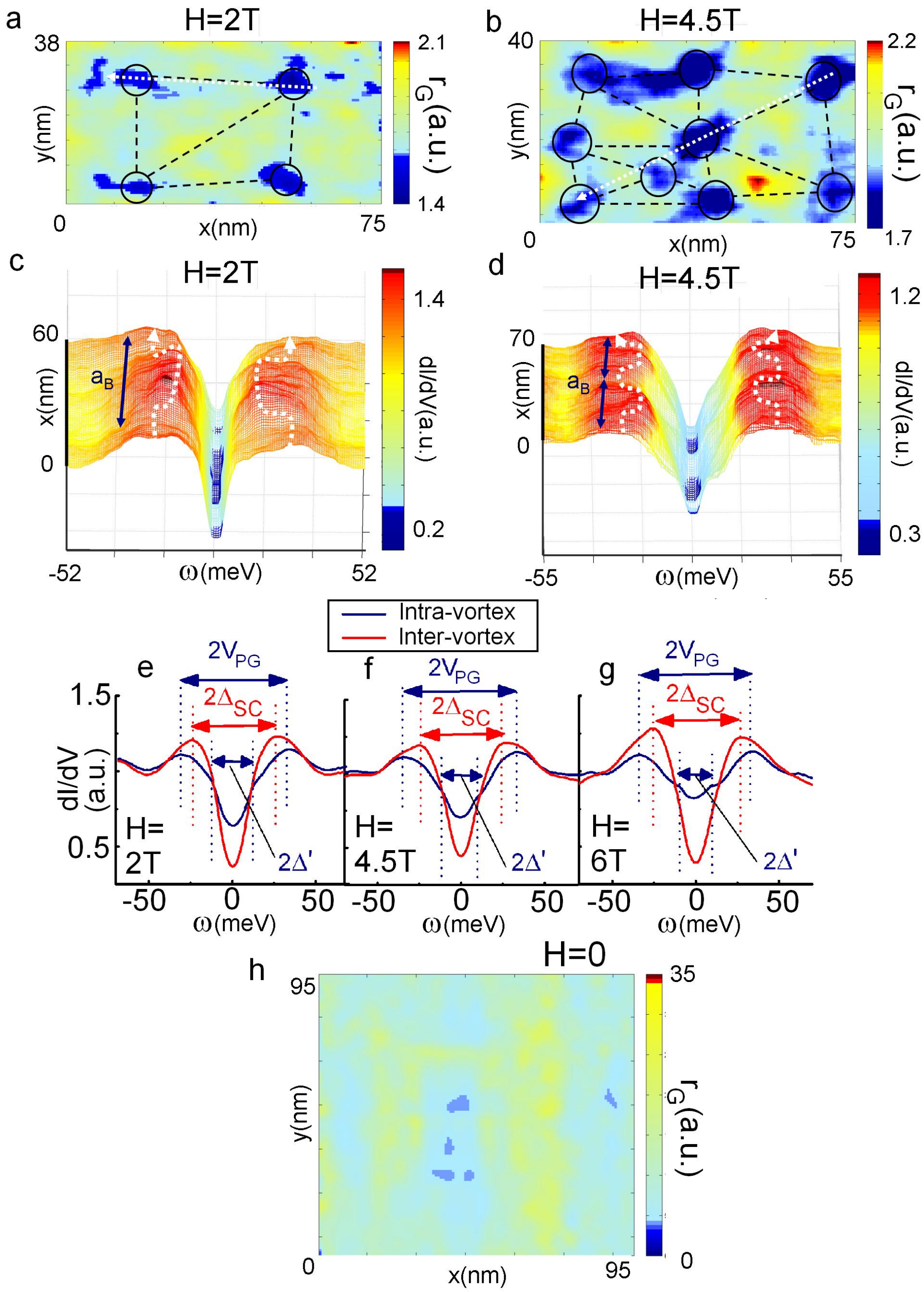

Figure 5.4: Vortex-state conductance maps at T = 6 K in Y-123: (a) Conductance power ratio r_G map over a (75 × 38) nm^2 area for H = 2 T, showing disordered vortices with an average a_B = 33.2nm. (b) The r_G map over a (75×40) nm^2 area for H = 4.5 T, showing a_B = 23.5 nm. (c) Conductance spectra along the white line in (a), showing SC peaks at $\omega = \pm\Delta_{SC}$ outside vortices and PG features at $\omega = \pm V_{PG}$ inside vortices. (d) Conductance spectra along the dashed line indicated in (b). Spatially averaged intra- and inter-vortex spectra for (e) H = 2 T, (f) H = 4.5 T and (g) H = 6 T. (h) The r_G map over the (95 × 95)nm^2 area in Fig. 5.3 at H = 0 for comparison with (a) and (b).

field is varied, we derived histograms from spatial maps of the peak-to-peak gap values, Δ_{pk-pk}, in Y-123 for H =0, 2T, 4.5T, and 6T, and the results are shown in Fig. 5.5a. Our algorithm for determining Δ_{pk-pk} chooses the smallest Δ_{pk-pk} value with clear peaks in each quasiparticle spectra at every pixel in the entire map. Some of the spatially resolved quasiparticle spectra around vortex cores show clear sets of peaks at $\omega = \pm\Delta'$, while other spectra displayed a gap width equal to $2\Delta'$ without clear peaks at $\omega = \pm\Delta'$. Therefore, for the spectra around vortex cores, the algorithm identified some of the quasiparticle spectra with Δ_{pk-pk}=Δ' and some of the quasiparticle spectra with Δ_{pk-pk}=V_{PG}.

To more fully characterize the histograms, we fit the histograms by using Gaussian fits, and the fits are shown as solid lines on top of the histograms in Fig. 5.5a. For the H = 2T, 4.5T, and 6T histograms, we fit the data by using a sum of two Gaussian functions. For H = 0, we fit the histogram by using one Gaussian function.

The parameters used to fit the histograms in Fig. 5.5a are shown in Fig. 5.5c. The central values of the two Gaussians in a finite magnetic field characterize the location of the intra-vortex pseudogap V_{PG} (PG) and the inter-vortex superconducting gap Δ_{SC} (SC), with $V_{PG} > \Delta_{SC}$. The central value of the histogram for H = 0 characterizes the location of the zero-field superconducting gap Δ_{SC}. Examining from the top panel to the bottom panel, Fig. 5.5c shows the values of Δ_{SC} and V_{PG} determined from the central value(s) of the histograms, the number of counts used in the Gaussian fit(s) at the central value(s), and the linewidth of the Gaussian fit(s), respectively.

From the Gaussian fits of finite field data, V_{PG}=(31.5±2)meV and Δ_{SC}=(22±2)meV. The value of V_{PG} from the Gaussian fits is equal, within uncertainty, to the value of V_{CO}=32meV used to fit the zero-field spectra in Fig. 5.2 for T = 6K, lending further credence to the assertion that the ground state of Y-123 contains superconductivity and competing orders. As a side note, the value of 32meV agrees favorably with the observed spin-gap energy for optimally doped Y-123 from neutron scattering studies [16].

In the middle panel of Fig. 5.5c, it is shown that the number of counts associated with the V_{PG} and Δ' energy scales increases with increasing magnetic field, while that associated with the Δ_{SC}

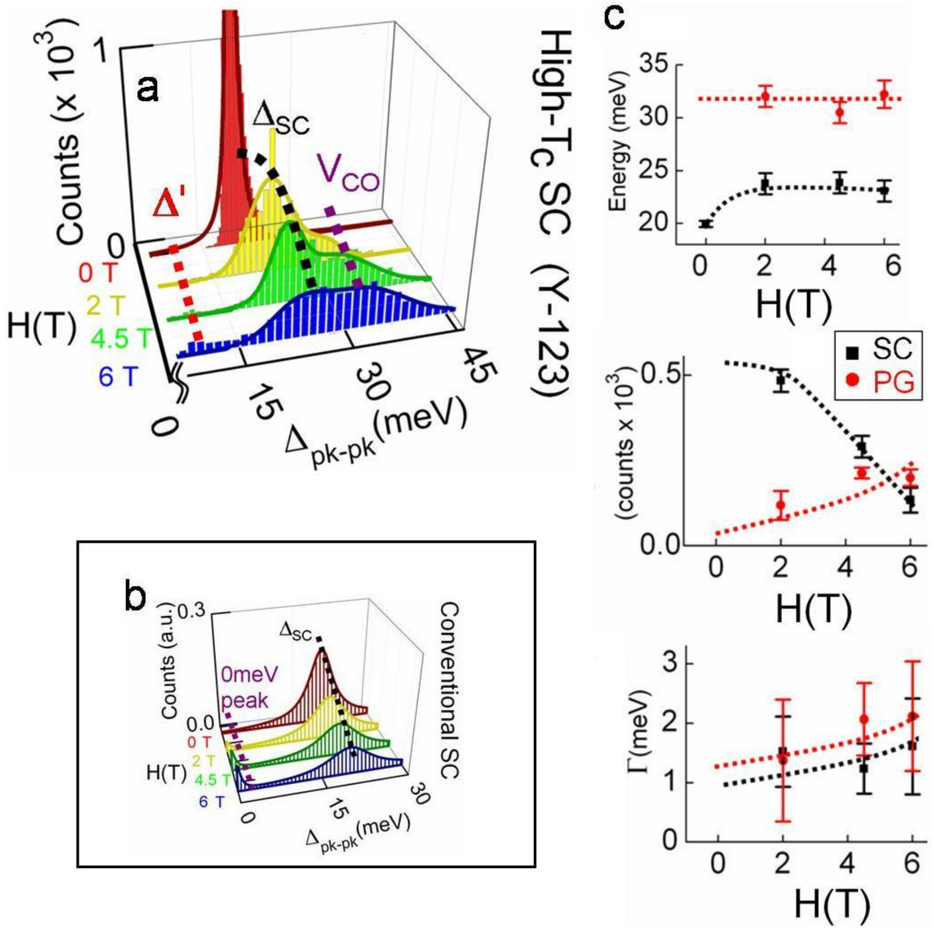

Figure 5.5: Field-dependent spectral evolution at T = 6 K in Y-123: (a) Energy histograms derived from STS data for H = 0, 2, 4.5, and 6 T, showing a spectral shift from Δ_{SC} to V_{PG} and Δ' with increasing H. (b) Schematic of the histograms for a conventional type-II superconductor in the limit of $T \ll T_C$ and $H \ll H_{C2}$. (c) Gaussian fitting parameters from the histograms in (a) reveals nearly field-independent Δ_{SC} and V_{PG} (top panel), decreasing Δ_{SC} and increasing V_{PG} spectral weight with increasing H (center panel), and increasing Δ_{SC} and V_{PG} linewidths with increasing H (bottom panel).

energy decreases. The bottom panel of Fig. 5.5c presents the standard deviation of the Gaussian functions, which we identify as an effective linewidth, Γ. We observe that the Γ values increase with increasing magnetic field.

The spectral shift of Δ_{pk-pk} from Δ_{SC} to V_{PG} and Δ' as magnetic field is increased is notable in several regards. First, the spectral shift from Δ_{SC} to V_{PG} and Δ' produces no zero-bias peak inside the core of vortices, as would be expected for a conventional type-II superconductor. As was discussed more fully in Section 4.5.2, a fraction of quasiparticles equal to $(\pi\xi_{SC}^2/2)/(\sqrt{3}a_B^2/4)$, which would increase linearly with H, are expected to shift to a peak located at $\omega = 0$ for conventional type-

II superconductors. For this scenario, we would have observed histograms similar to the schematic histograms illustrated in Fig. 5.5b. Second, the fraction of quasiparticles shifted to the zero-bias peak would be expected to be ∼25% at H = 6T for a conventional superconductor. We observe a shift of ∼50% for H = 6T to V_{PG}. Third, the spectral shift from Δ_{SC} led to the observation of two different gap energies, V_{PG} and Δ', around vortex cores. Finally, $V_{PG} > \Delta_{pk-pk}(H = 0)$ in Y-123, while $V_{PG} < \Delta_{pk-pk}(H = 0)$ in La-112. All of these findings are difficult to reconcile with the expected behavior from a ground state of pure superconductivity.

In addition to the characterization of Δ_{SC}, Δ_{eff}, Δ', and V_{PG} in Y-123 as a function of magnetic field, we performed high-spatial resolution quasiparticle spectra maps in Y-123 to investigate the possibility of spatial ordering in the quasiparticle spectra of Y-123. We performed spatially resolved STS over an area of size (22 × 29) nm^2 using 0.234nm spatial resolution in Y-123 at H = 0 and H = 5T, with the sample rotated $\sim 45^o$ from the scan directions of the tube-scanner. Our effective resolution along the 45^o direction was 0.166nm; therefore, our spatial sampling frequency $f_x \sim 6$ samples/nm exceeded the Nyquist sampling frequency criteria for observing the lattice constant ($f_{x,lattice,1}$= $1/a_1$=1/0.383nm$\simeq$ 2.61 samples/nm; $f_{x,lattice,2} = 1/a_2$ = 1/0.388nm $\simeq$ 2.58 samples/nm. Y-123 is orthorhombic, and the ab-plane lattice constants are a_1=0.383nm and a_2=0.388nm). The quasiparticle spectra were taken in constant tip-junction resistance STS mode of the STM, using I_{set}=-80pA and V_{bias}=-80mV, and the spatial maps for H = 0, 5T were taken over the same spatial area of (22 × 29) nm^2 so differential FT-LDOS could be performed.

The resulting spatial maps of dI/dV at H = 5T for $|\omega| \simeq \Delta'$, Δ_{SC}, and V_{PG}, as well as $|\omega| > V_{PG}$ are shown in Fig. 5.6. Vortices are observed and indicated by dashed blue circles. Conductance modulations are clearly visible throughout the $\mid \omega \mid \leq V_{PG}$ images but are most noticeable near the vortex cores. Conductance modulations remain for ω=-53meV but vortex halos are nearly invisible at this energy.

From the high-spatial resolution quasiparticle spectral maps of Y-123, we calculated differential Fourier transformed local density of states (FT-LDOS) in order to minimize common mode noise in FT-LDOS maps. The common mode noise may be removed by subtracting the FT-LDOS of the

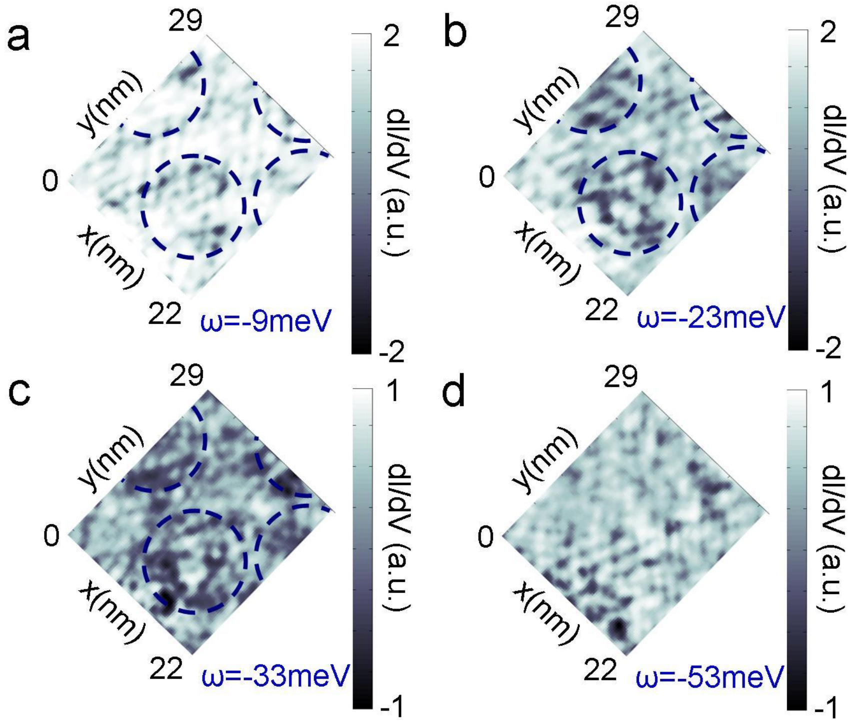

Figure 5.6: The local density of states (LDOS) modulations of Y-123 at H = 5T and T = 6 K over a (22 × 29) nm^2 area. The spatial dependence of the LDOS reveals modulations associated with density-waves and vortices (dashed circles) for ω = (a) -9meV$\sim -\Delta'$, (b) -23meV$\sim -\Delta_{SC}$, (c) -33meV$\sim$-V$_{PG}$ and (d) -53meV. The vortex contrast is most visible for $|\omega|\sim|\Delta_{SC}|$ and least visible for $|\omega|>$V$_{PG}$.

H = 0 from the H = 5T spatial maps. The differential FT-LDOS provided the best initial maps for identifying diffraction modes in FT-LDOS maps. The differential FT-LDOS, $\tilde{F}(\mathbf{k}$, ω, H), was calculated according to:

$$\tilde{F}(\mathbf{k},\omega,H) \equiv |\sum_j e^{i\mathbf{k}\cdot\mathbf{R}_j}(dI/dV(\mathbf{R}_j,\omega,H) - dI/dV(\mathbf{R}_j,\omega,0))|, \tag{5.1}$$

where dI/dV is the differential conductance, $\mathbf{R}_j$ denotes the coordinate of the j-th pixel, and the sum is taken over all pixels of the two-dimensional spatial maps. (Both FT-LDOS and differential FT-LDOS maps required corrections to be made for the surface topography of Y-123 using the methods described in Appendix A [Section A.2]).

Using Eq. 5.1, we produced differential FT-LDOS maps, $\tilde{F}(\mathbf{k}$, ω, H = 5T), over the energy range ω=-7meV to ω=-47meV and studied the energy dependence (all differential FT-LDOS maps at different energies are shown in Appendix B [Figs. B.1– B.43]). From systematic analysis of the differential FT-LDOS data, we observed energy-independent diffraction modes and energy-dependent diffraction modes. The energy dependent diffraction modes were highly dispersive and were similar to those observed in Bi-2212 [68]. These diffraction modes are understood to arise from elastic quasiparticle scattering interferences [79]. In addition to the energy-dependent modes, we also observed three sets of energy-independent diffraction modes in Y-123, with two sets of diffraction modes along the Cu-O bonding direction and one set of diffraction modes along the nodal direction. To better illustrate the energy-independent diffraction modes observed, we summed $\tilde{F}(\mathbf{k},\omega,\mathrm{H}=5\mathrm{T})$ from ω=-30meV to ω=-7meV, and the result is shown in Fig. 5.7. The energy-independent diffraction modes are circled in red, purple, and green, along with the diffraction modes due to the lattice periodicity circled in white.

We initially label the diffraction modes in Fig. 5.7 as $\mathbf{Q}_{PDW}$, $\mathbf{Q}_{CDW}$, and $\mathbf{Q}_{SDW}$ and describe our rationale for doing so more fully while describing the results. The location of the diffraction modes along the Cu-O bonding direction (Γ to $(2\pi,0)/(0,2\pi)$) direction are: $\mathbf{Q}_{PDW} = [\pm(0.56\pm0.06)\pi/\mathrm{a}_1,0]$ and $[0,\pm(0.56\pm0.06)\pi/\mathrm{a}_2]$; $\mathbf{Q}_{CDW} = [\pm(0.28\pm0.02)\pi/\mathrm{a}_1,0]$ and $[0,\pm(0.28\pm0.02)\pi/\mathrm{a}_2]$, and the location of the diffraction modes along the nodal direction ((Γ to (π,π)) are given by $\mathbf{Q}_{SDW} = [\pm(0.15\pm0.01)\pi/\mathrm{a}_1,\pm(0.15\pm0.01)\pi/\mathrm{a}_2]$. The $\mathbf{Q}_{PDW}$ diffraction modes correspond to checkerboard conductance modulations of $(3.6\pm0.4)\mathrm{a}_{1,2}$ lattice constants and are comparable to the $4\mathrm{a}_0 \times 4\mathrm{a}_0$ lattice constant conduction modulations observed in Bi-2212 [21, 80], which appeared to show PDW-like behavior in zero-field [80]. The location of the Q_{CDW} diffraction modes approximately agree with our fit to the T = 6K Y-123 data in Fig. 5.2, where we use a model of coexisting CDW and SC to generate the fit. We denote the diffraction modes along the nodal direction as $\mathbf{Q}_{SDW}$ due to the expected unequal population of spin-up and spin-down quasiparticles along the nodal direction in a magnetic field and due to the lack of pairing amplitude along the nodal direction for d-wave superconductivity.

Representative intensity plots of $\tilde{F}(\mathbf{k},\omega,\mathrm{H}=5\mathrm{T})$-vs.-$\mathbf{k}$ from Γ to $(0,2\pi)/(2\pi,0)$ and from Γ to (π,π) are shown in Fig. 5.8 to illustrate the spectral weight of different modes as a function of energy. The

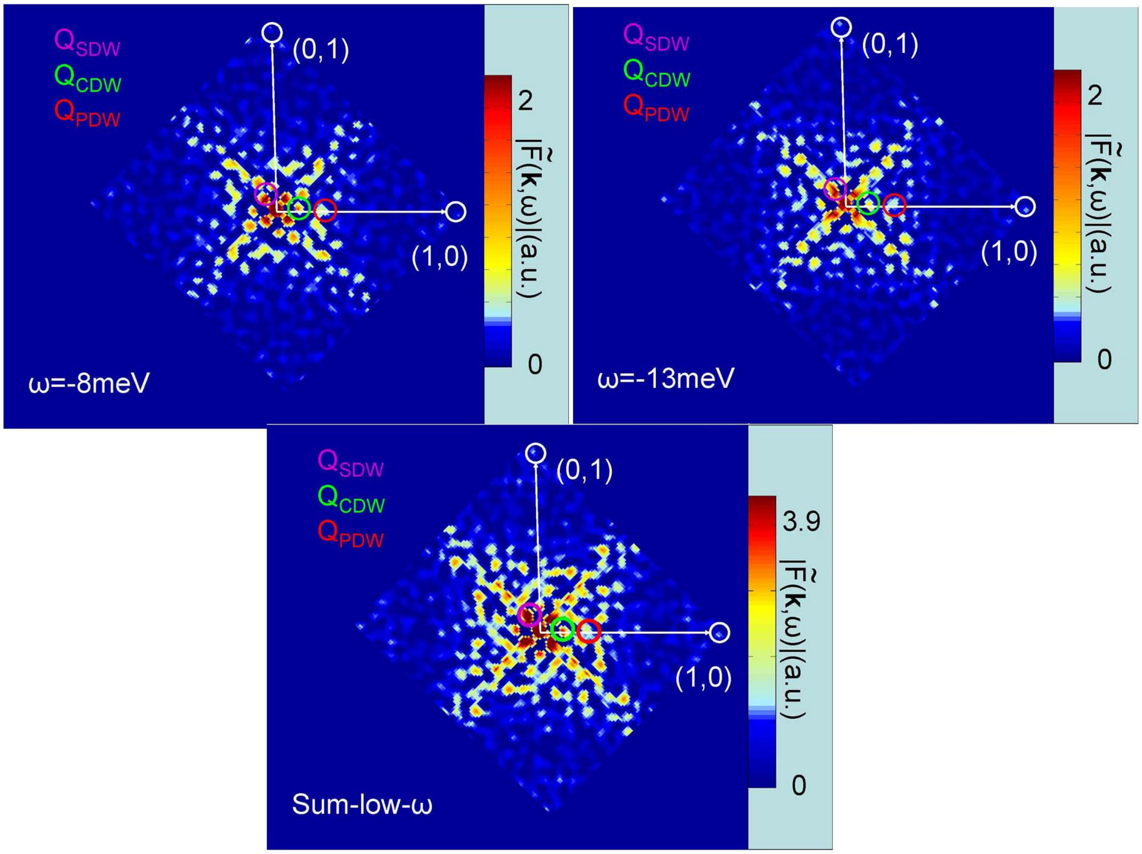

Figure 5.7: Differential FT-LDOS, $\tilde{F}(\mathbf{k},\omega,\text{H=5T})$, in Y-123. Top left: Differential FT-LDOS, $\tilde{F}(\mathbf{k},\omega\text{=-8meV,H=5T})$, in Y-123. Top right: Differential FT-LDOS, $\tilde{F}(\mathbf{k},\omega\text{=-13meV,H=5T})$, in Y-123. Bottom: Here, we show the summed differential FT-LDOS, $\sum_{\omega}\tilde{F}(\mathbf{k},\omega,\text{H=5T})$, calculated using Eq. 5.1 and summing from ω=-7meV to ω=-30meV. Three energy-independent modes are circled and labeled by $\mathbf{Q}_{PDW}$, $\mathbf{Q}_{CDW}$, and $\mathbf{Q}_{SDW}$. In addition, the lattice constant diffraction spots are circled in white. The values of the energy-independent spots correspond to $\mathbf{Q}_{PDW}=[\pm(0.56\pm0.06)\pi/\mathrm{a}_1,0]$ and $[0,\pm(0.56\pm0.06)\pi/\mathrm{a}_2]$, $\mathbf{Q}_{CDW}=[\pm(0.28\pm0.02)\pi/\mathrm{a}_1,0]$ and $[0,\pm(0.28\pm0.02)\pi/\mathrm{a}_2]$, and $\mathbf{Q}_{SDW}=[\pm(0.15\pm0.01)\pi/\mathrm{a}_1,\pm(0.15\pm0.01)\pi/\mathrm{a}_2]$. Notation: PDW — pair-density-wave, CDW — charge-density-wave, SDW — spin-density wave

three energy-independent modes are indicated in Fig. 5.8, as well as a dispersive spot, $\mathbf{q}_7$, along the Γ to (π,π) direction. In this work, we use the notation for the dispersive diffraction modes adopted in Ref. [99]. The resulting energy independence of $\mathbf{Q}_{PDW}$, $\mathbf{Q}_{CDW}$, and $\mathbf{Q}_{SDW}$, along with the energy dependence of $\mathbf{q}_7$, obtained from $\tilde{F}(\mathbf{k}, \omega, \text{H=5T})$-vs.-$\mathbf{k}$ plots, along with uncertainties, are shown in Fig. 5.9.

After identifying diffraction modes in $\tilde{F}(\mathbf{k}, \omega, \text{H=5T})$-vs.-$\mathbf{k}$, we may examine how the location of diffraction modes, both energy independent and energy dependent, depend on magnetic field by studying FT-LDOS alone, instead of differential FT-LDOS. The FT-LDOS maps may be calculated using

$$F(\mathbf{k}, \omega, H) \equiv |\sum_j e^{i\mathbf{k}\cdot\mathbf{R}_j} dI/dV(\mathbf{R}_j, \omega, H)|. \tag{5.2}$$

Representative FT-LDOS maps at ω=-12meV for H = 0 and H = 5T are shown in Fig. 5.10, with circles indicating the location of the lattice constants and $\mathbf{Q}_{PDW}$, $\mathbf{Q}_{CDW}$, and $\mathbf{Q}_{SDW}$. The scan direction is indicated by a yellow arrow in both panels of Fig. 5.10, and the FT-LDOS intensity is slightly higher along the scan direction, from approximately (-π,π) to (π, -π), than in other locations in the FT-LDOS maps. This finding is an experimental artifact correlated with scanning of the STM tip; however, it does not prevent us from identifying diffraction modes in FT-LDOS data.

To more accurately characterize the intensity and location of diffraction modes as magnetic field is varied, we then generate plots of the intensity of FT-LDOS, $|F(\mathbf{k},\omega,\text{H})|$-vs.-(k,$\omega$), along the Cu-O bonding direction and the nodal direction. The results of $|F(\mathbf{k},\omega,\text{H})|$-vs.-(k,$\omega$) for H = 0 and H = 5T along the Cu-O bonding direction are shown in Fig. 5.11, while the results along the nodal direction are shown in Fig. 5.12. In both figures, the spectral intensity is represented by the color bar and is shown on a two-dimensional plane of (k,ω), where k is the magnitude of the momentum along the specified direction. Therefore, the energy independent modes are represented by vertical straight lines, and are indicated by thick dashed lines. Additionally, the energy-dependent quasiparticle interference (QPI) diffraction modes are indicated by thin dotted lines, and the energy-dependent QPI modes modulated by reciprocal lattice vectors are indicated by thinner dotted lines. The fact that we detected the QPI diffraction modes modulated by reciprocal lattice vectors indicates that $\mathbf{k}$

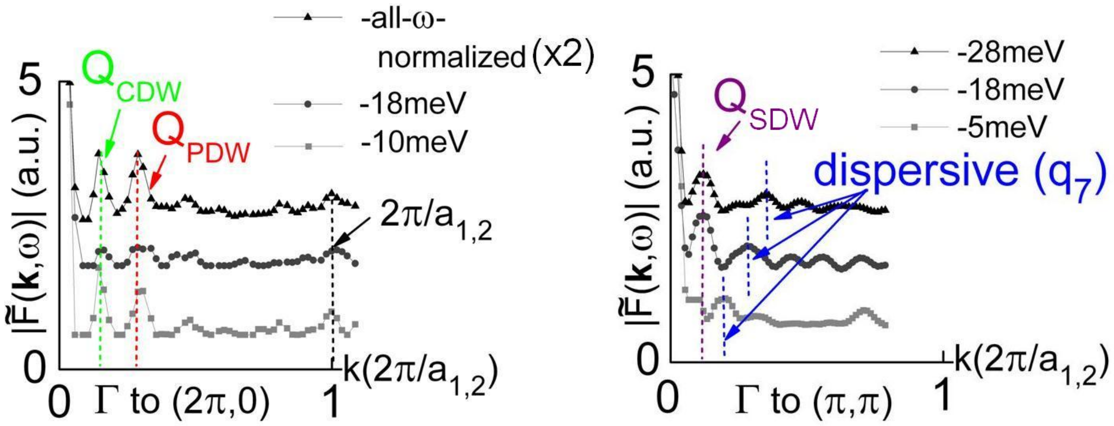

Figure 5.8: $\tilde{F}(\mathbf{k},\omega,\mathrm{H}{=}5\mathrm{T})$-vs.-$\mathbf{k}$ from Γ to $(0,2\pi)/(2\pi,0)$ and Γ to (π,π). Left panel: Representative plots of $\tilde{F}(\mathbf{k},\omega,\mathrm{H}{=}5\mathrm{T})$-vs.-$\mathbf{k}$ from Γ to $(0,2\pi)/(2\pi,0)$ for ω=-10meV and -18meV, along with the plot obtained from summing the differential FT-LDOS from ω=-1meV to ω=-30meV. The energy independent spots $\mathbf{Q}_{PDW}$ and $\mathbf{Q}_{CDW}$ are indicated in the figure along with the lattice constant diffraction modes. Right panel: Representative plots of $\tilde{F}(\mathbf{k},\omega,\mathrm{H}{=}5\mathrm{T})$-vs.-$\mathbf{k}$ from Γ to (π,π) for ω=-5meV, -18meV, and -28meV. The energy independent spot $\mathbf{Q}_{SDW}$, as well as an energy dependent spot ($|\mathbf{q}_7|$) are identified. The energy dependent spot may be understood as arising from elastic quasiparticle scattering interference [79], and has been seen in Bi-2212 as well [99]. The notation for $|\mathbf{q}_7|$ follows the convention of Ref. [99].

is a good quantum number on the Y-123 area examined.

From the plots of Figs. 5.11 and 5.12, we find that the energy-independent diffraction modes of $\mathbf{Q}_{PDW}$, $\mathbf{Q}_{CDW}$, and $\mathbf{Q}_{SDW}$ varied in intensity as magnetic field was changed but remained at the same location in $\mathbf{k}$-space. The energy-dependent modes also varied in intensity as magnetic field changed but had the same dispersion for H = 0, 5T. The representative dispersion relations of $\mathbf{q}_1$, $\mathbf{q}_2$, $\mathbf{q}_3$, $\mathbf{q}_6$, and $\mathbf{q}_7$ valid for both H = 0, 5T are shown in Fig. 5.13a for completeness. The notation used for these energy-dependent modes follows the convention of Ref. [99]. We find that the dispersion relations of these energy-dependent modes are in good agreement with the theoretical predictions for elastic quasiparticle scattering interferences. Schematic illustrations of these QPI modes in reference to the Fermi surface of the cuprates are shown in Fig. 5.13b, along with the notation convention of Ref. [99].

To characterize possible competing orders associated with $\mathbf{Q}_{PDW}$, $\mathbf{Q}_{CDW}$, and $\mathbf{Q}_{SDW}$, we analyzed the symmetry of the real part of the FT-LDOS for each set of energy-independent modes using the formalism developed in Ref. [84] and discussed in the introduction of this chapter. To

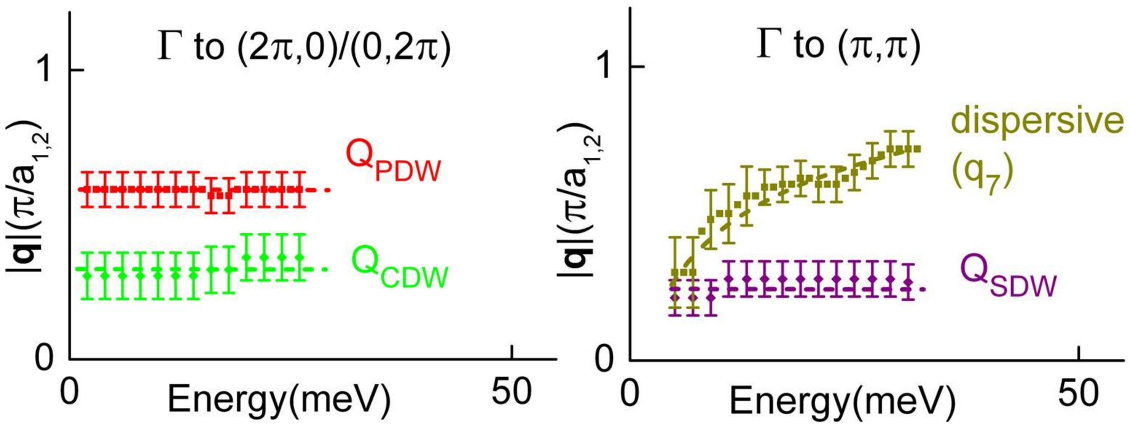

Figure 5.9: Energy dependence of $\mathbf{Q}_{PDW}$, $\mathbf{Q}_{CDW}$,$\mathbf{Q}_{SDW}$ and $|\mathbf{q}_7|$ in Y-123 with uncertainties generated from plots of $\tilde{F}$($\mathbf{k}$,ω,H=5T)-vs.-$\mathbf{k}$ along the nodal direction and the bonding direction. Left panel: The length of Q_{PDW} (red data points) and Q_{CDW} (green data points) diffraction modes along the Cu-O bonding direction in Y-123 with uncertainties. [$\mathbf{Q}_{PDW}$=[±(0.56±0.06)π/a$_1$,0] and [0,±(0.56±0.06)π/a$_2$]; $\mathbf{Q}_{CDW}$=[±(0.28±0.02)π/a$_1$,0] and [0,±(0.28±0.02)π/a$_2$]] Right panel: The length of Q_{SDW} (red data points) diffraction modes along the nodal direction in Y-123 with uncertainties. [$\mathbf{Q}_{SDW}$=[±(0.15±0.01)π/a$_1$,±(0.15±0.01)π/a$_2$]] Example plots of differential FT-LDOS-vs.-$\mathbf{k}$ for H = 5T are shown in Fig. 5.8.

perform this analysis, the real part of the spectral weight of each set of energy-independent modes was measured as a function of energy and then broken down into the symmetric and anti-symmetric components, as was illustrated for the theoretical expectations for the PDW and CDW modes in Fig. 5.1. The spectral weight of each mode is averaged over the momentum spot sizes of the $\mathbf{Q}_{PDW}$, $\mathbf{Q}_{CDW}$, and $\mathbf{Q}_{SDW}$, with the spot sizes being determined by the full-width at half maximum of the intensity of the summed FT-LDOS.

Based on our observation that $\mathbf{Q}_{PDW}$, $\mathbf{Q}_{CDW}$, and $\mathbf{Q}_{SDW}$ did not vary substantially in location in $\mathbf{k}$-space as magnetic field was varied from H = 0 to H = 5 T, we performed an additional spatially resolved STS map over an area of (56 × 56)nm^2 at H = 3T with spatial resolution of 0.492nm. By examining the (56 × 56)nm^2 area with lower spatial resolution for H = 3T compared to the H = 0, 5T data, we effectively increased the resolution in momentum space relative to the two-dimensional diffraction patterns shown in Figs. 5.7 and 5.10, resulting in more pixels associated with the energy-independent modes at H = 3T. The corresponding FT-LDOS for H = 3 T and summed from ω = -1 meV to - 30 meV is shown in Fig. 5.14.

The final results of energy-dependent spectral weight analysis of $\mathbf{Q}_{PDW}$, $\mathbf{Q}_{CDW}$, and $\mathbf{Q}_{SDW}$ for H = 0, 3T, and 5T are shown in Fig. 5.15, and similar analysis for the differential FT-LDOS, $\tilde{F}(\mathbf{k},\omega,\mathrm{H{=}5T})$, is shown in Fig. 5.16. From the data in Figs. 5.15 and 5.16, we observe the evolution of $\mathbf{Q}_{PDW}$, $\mathbf{Q}_{CDW}$, and $\mathbf{Q}_{SDW}$ as magnetic field is varied and find that the data contains both symmetric and anti-symmetric components at each set of modes, as expected [84]. Further, the symmetric component associated with each energy-independent mode appears to increase with magnetic field, while the anti-symmetric components shift to lower energies and decrease in magnitude as magnetic field increased. The plots of FT-LDOS amplitudes-vs.-energy for H = 0 in Fig. 5.16 indicate that the $\mathbf{Q}_{PDW}$ modes is largely symmetric in energy and may therefore be associated with a PDW. The mode at $\mathbf{Q}_{SDW}$ is largely anti-symmetric for H = 0, so that our initial assignment of these diffraction modes to a SDW is reasonable. Finally, the diffraction modes at $\mathbf{Q}_{CDW}$, which agree with $\mathbf{Q}_{CO}$ from our Green's function fitting of the T = 6K quasiparticle spectra in Fig. 5.2 using coexisting superconductivity and a CDW, show equal symmetric and anti-symmetric components in different ranges of energy and may be associated with a CDW.

5.4 Discussion

5.4.1 Relevant low-energy excitations in Y-123

An important objective of the work considered here was to distinguish between the "one-gap" and "two-gap" models of the origin of the pseudogap and the unconventional quasiparticle excitations in hole-type cuprates. The STS results of Y-123 presented here indicate that the quasiparticle excitations in Y-123 are complex and appear to involve a ground state that displays excitation phenomena of both fermionic quasiparticle excitations and bosonic collective modes. Specifically, the "one-gap" model asserting simple Bogoliubov quasiparticle excitations cannot account for all phenomena, such as the energy-independent collective modes and additional energy scales besides Δ_{SC}. Hence, multiple orders are needed, which is consistent with the spirit of the "two-gap" model. Interestingly, we note that a PDW alone may be reconciled with the "one-gap" model

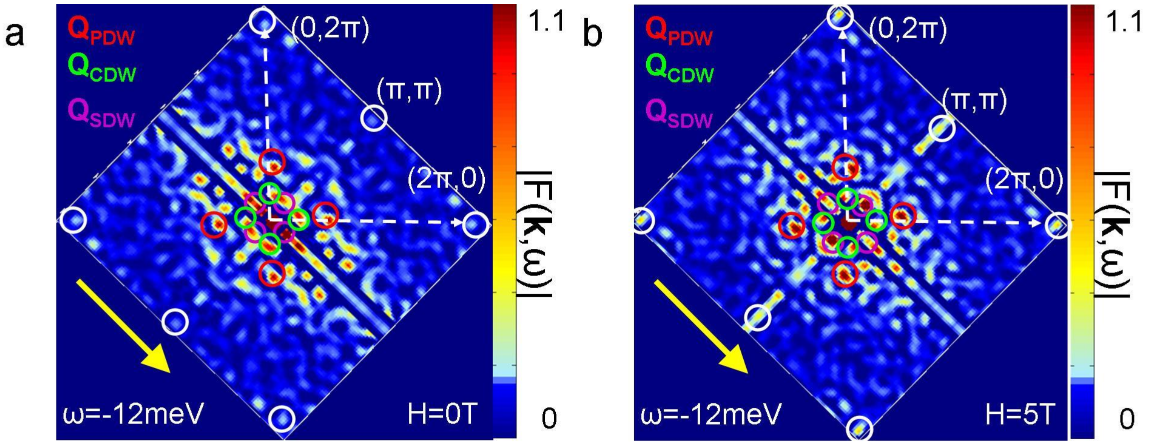

Figure 5.10: FT-LDOS maps at H = 0,5T in Y-123. Left panel: FT-LDOS in Y-123 for H = 0 at ω=-12meV with $\mathbf{Q}_{PDW}$, $\mathbf{Q}_{CDW}$,$\mathbf{Q}_{SDW}$ indicated by circles. Additionally, the lattice constant diffraction modes are circled in white, as well as diffraction modes that appear at (π, π). The scan direction of the STM tube scanner is indicated by a yellow arrow. Right panel: FT-LDOS in Y-123 for H = 5T at ω=-12meV with $\mathbf{Q}_{PDW}$, $\mathbf{Q}_{CDW}$, and $\mathbf{Q}_{SDW}$ indicated by circles. Additionally, the lattice constant diffraction spots are circled in white, as well as diffraction modes that appear at (π, π). The scan direction of the STM tube scanner is indicated by a yellow arrow.

because it supposes that Cooper pairs exist in the PDW mode but they no longer acquire a global superconducting phase [84]. Instead of a global phase, the disordered Cooper pairs in the PDW mode exhibit a spatially varying phase characterized by an ordering wavevector $\mathbf{Q}_{PDW}$. In contrast, the presence of either CDW or SDW collective excitations is a manifestation of the "two-gap" model because both modes are particle-hole collective excitations that exhibit energy scales differing from the superconducting gap (V_{CO} and/or Δ') and ordering wavevectors, given by $\mathbf{Q}_{CDW}$ and $\mathbf{Q}_{SDW}$.

As further evidence of the complexity of the excitations in Y-123, the data in Figs. 5.15 and 5.16 show significant contributions to FT-LDOS that may be attributed to PDW, CDW, and SDW, but the relative symmetric and anti-symmetric amplitudes vary as functions of energy and magnetic field. The symmetric components of $\mathbf{Q}_{PDW}$, $\mathbf{Q}_{CDW}$, and $\mathbf{Q}_{SDW}$ appear to increase with magnetic field.

Additionally, while the PDW, CDW, and SDW cannot be explained by conventional superconductivity, the quasiparticle excitations energies and spectral shifts among the PDW, SDW, and CDW excitations as a function of energy and magnetic field further indicate a complex ground state in Y-123. Close inspection of Figs. 5.11 and 5.12 reveal that all modes exhibit significant spectral

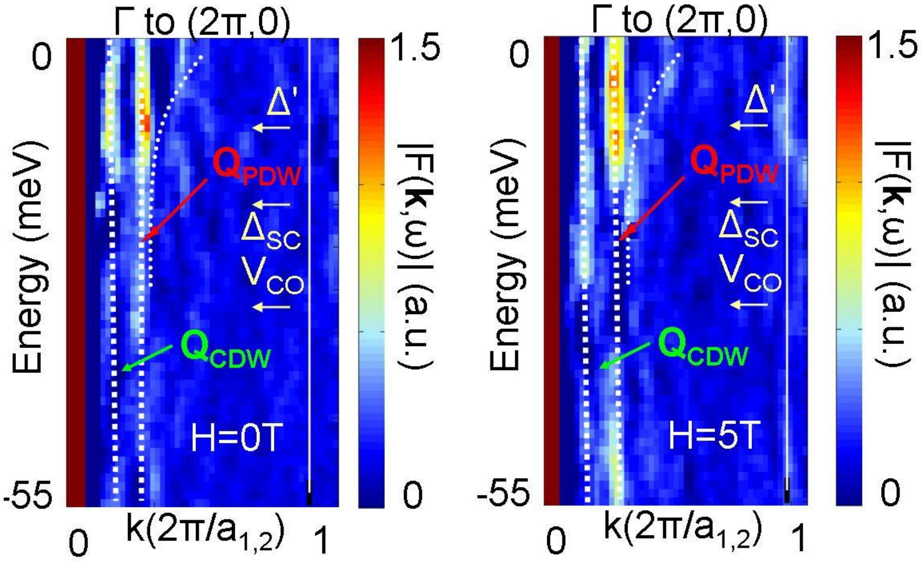

Figure 5.11: Intensity plots of FT-LDOS-vs.-**k** along the bonding direction in Y-123 at H = 0, 5T. Left panel: Intensity plot of FT-LDOS-vs.-**k** along the bonding direction for H = 0 in Y-123. The energy-independent diffraction modes, $\mathbf{Q}_{PDW}$ and $\mathbf{Q}_{CDW}$, are indicated by thick dashed lines. A dispersive energy-dependent mode is shown as a thin dotted line. Right panel: Intensity plot of FT-LDOS-vs.-**k** along the bonding direction for H = 5T in Y-123. The energy-independent diffraction modes, $\mathbf{Q}_{PDW}$ and $\mathbf{Q}_{CDW}$, are indicated by thick dashed lines. A dispersive energy-dependent diffraction spot is shown as a thin dotted line.

intensity around Δ_{SC}, Δ' and V_{PG} at H = 0, but the spectral intensity also varies with energy as magnetic field increases to H = 5T. For H = 5T, the Q_{PDW} mode loses its intensity above Δ_{SC}, which could be attributed to the fact that superconducting pairing is absent above Δ_{SC}. In addition, longitudinal optical phonon modes associated with the Cu-O bond can also contribute to overdamping of the collective modes along the $(\pi, 0)/(0, \pi)$ direction at higher energies due to inelastic scattering of the collective modes. Specifically, longitudinal optical phonon modes arise in the energy range between 45–55meV in cuprates [149] and can be expected to damp the $\mathbf{Q}_{PDW}$ and $\mathbf{Q}_{CDW}$ collective excitations along the Cu-O bonding direction. Empirically, for $|\omega| > 40$meV, the mode with ordering wavevector of $\mathbf{Q}_{SDW}$ maintain its intensity over the entire energy range, whereas the intensity of $\mathbf{Q}_{PDW}$ and $\mathbf{Q}_{CDW}$ fades for $|\omega| > 40$meV. This observation lends credence to the interplay of phonons and the collective excitations. Therefore, it appears that PDWs, CDWs, SDWs, and phonons all contribute to the low-energy excitations in hole-type Y-123.

Based on the fact that we observe diffraction modes at $\mathbf{Q}_{PDW}$, $\mathbf{Q}_{CDW}$, and $\mathbf{Q}_{SDW}$ in Y-123, the

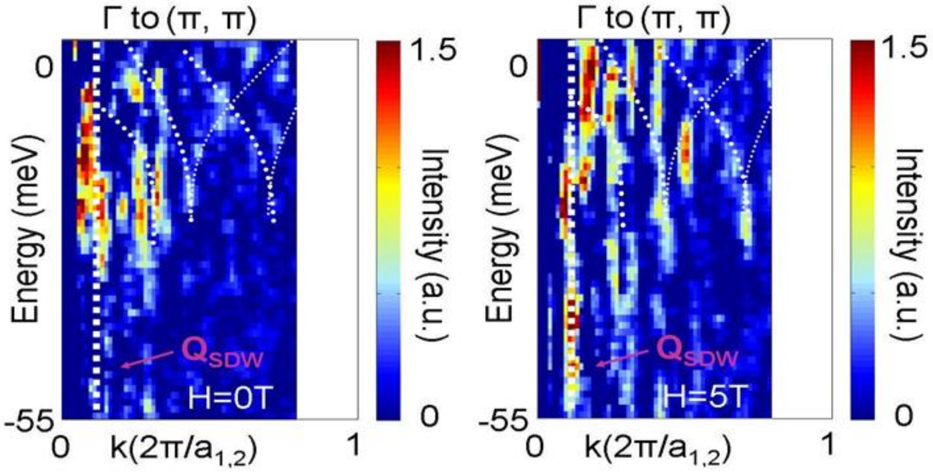

Figure 5.12: Intensity plots of FT-LDOS-vs.-**k** along the nodal direction in Y-123 at H = 0, 5T. Left panel: Intensity plot of FT-LDOS-vs.-**k** along the nodal direction for H = 0 in Y-123. The energy-independent diffraction spot, $\mathbf{Q}_{SDW}$, is indicated by a thick dashed line. Energy-dependent modes are shown as a thin dotted lines, while the dispersive energy-dependent modes modulated by reciprocal lattice vectors are shown as thinner dotted lines. The fact that we observe the energy-dependent diffraction patterns modulated by the reciprocal lattice vectors indicates that our sample surface is clean and **k** is a good quantum number. Right panel: Intensity plot of FT-LDOS-vs.-**k** along the nodal direction for H = 5T in Y-123. The energy-independent mode, $\mathbf{Q}_{SDW}$, is indicated by a thick dashed line. Energy-dependent patterns are shown as a thin dotted lines, while the dispersive energy-dependent diffraction modes modulated by reciprocal lattice vectors are shown as thinner dotted lines.

ground state of Y-123 appears inconsistent with notion that “one-gap”, due to superconductivity alone, can account for all the excitations observed. In fact, we observe both disordered pairs, in the form of PDWs, and competing orders, in the form of CDWs and SDWs, as relevant excitations of the ground state of Y-123.

5.4.2 The origin of the pseudogap and subgap energies in vortex cores of hole-type cuprates

In addition to the analysis of energy-dependent spectral evolution of the Q_{PDW}, Q_{CDW}, and Q_{SDW} modes, we may argue against the scenario of one superconducting gap as the origin of the pseudogap and subgap energies in the vortex cores of the cuprates based on the totality of our data in hole-type Y-123 along with those in electron-type La-112. The average peak-to-peak gap observed in cuprates at $\mathrm{T} \ll \mathrm{T}_C$ has been argued to scale with the pseudogap energy as a function of doping [3, 139], and the pseudogap-like spectra observed in vortex cores in Bi-2212 has been argued to follow this same doping trend [18, 3]. We find that these arguments do not agree with our results in La-112 and Y-123 presented in this work, and the arguments appear to be skewed toward the experimentally realized scenario in Bi-2212.

Concerning the first argument, it has been asserted that the $T \ll T_C$ peak-to-peak gap scales linearly as a function of doping with the pseudogap observed above T_C in data on Bi-2212, Bi-2201, and Y-123 and that the peak-to-peak gap is the superconducting gap [3, 139], which would indicate the pseudogap is due to disordered pairing above T_C. The data in Y-123 for supporting this argument are in fact only one doping level at optimal doping [150], and the analysis in Ref. [150] suggests that a single superconducting gap, which does not change in energy, may be used to account for the observed quasiparticle tunneling spectra up to T_C in Y-123. This point is made because the gap width does not appear to change much in Y-123 until above T_C, when the gapped quasiparticle spectra disappears. We observe this same behavior in our Y-123 data as shown in Fig. 5.2; however, our model of coexisting superconductivity and competing orders (SC/CO) can quantitatively account for the observed behavior as temperature increases in Y-123, such that the observed gap does not appear to change much with increasing temperature because of the presence of a larger competing energy gap above T_C. In addtion, our SC/CO model accounts for the observed satellite features in Y-123 for $T \ll T_C$, while the hand-waving assertion of one superconducting gap [150] fails to account for either the presence of the satellite features or the quantitative temperature-dependent evolution of both the coherence peaks and the satellite features.

Furthermore, conclusions made regarding the scaling between the pseudogap for $T > T_C$ and the peak-to-peak gap, Δ_{pk-pk} for $T \ll T_C$ in Bi-2212 and Bi-2201 must be brought to question because, unlike Y-123, Δ_{pk-pk} is highly inhomogeneous in Bi-2212 and is not necessarily associated with the superconducting gap, as is shown more fully in Chapter 7. Additionally, the Δ_{pk-pk} gap maps in Bi-2212 [99] and $(Bi_{1-y}Pb_y)_2Sr_2CuO_{6+x}$ [(BiPb)-2201] [4] show nanoscale variations on the order of 10meV or greater. The large variations are generally associated with rounded pseudogap like features, in sharp contrast to the highly homogeneous coherence peaks observed in Y-123, as illustrated in Fig. 5.3. The issue of questionable identification of the superconducting gap simply

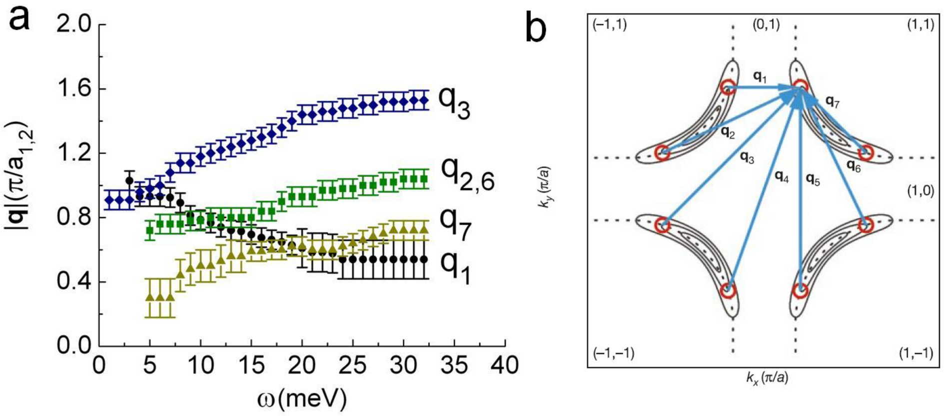

Figure 5.13: Energy dispersion relations of energy dependent diffraction modes in Y-123. (a) The energy dispersion relations and uncertainties of $|\mathbf{q}_1|$, $|\mathbf{q}_2|$, $|\mathbf{q}_3|$, $|\mathbf{q}_6|$, and $|\mathbf{q}_7|$ obtained in Y-123 are shown. We use the notation convention from Ref. [99]. (b) Visual representation of the notation from Ref. [99]. [Figure in (b) reproduced from Ref. [99].]

by the peak-to-peak features in Bi-2212 is further corroborated by recent studies of the (BiPb)-2201 spectra [4]. In (BiPb)-2201, the authors of Ref. [4] showed that the average Δ_{pk-pk} $\simeq$16meV observed in (BiPb)-2201 for T $\ll$ T$_C$ evolved into the pseudogap spectra, with gap of $\sim$16meV above T$_C$. However, further analysis revealed a spectrum with coherence peaks at a smaller energy Δ_N $\simeq$6.7meV well below T$_C$ by normalizing away the pseudogap background spectra found above T$_C$. It was further found that with increasing temperature, the smaller energy gap in the normalized spectra did close at T$_C$. In agreement with these findings, our analysis from Chapter 7 indicates that the average quasiparticle spectra for T $\ll$ T$_C$ in Bi-2212 may be modeled using coexisting SC/CO such that the rounded pseudogap-like features are in fact associated with the effective gap $\Delta_{eff} = \Delta_{pk-pk}$ for T $\ll$ T$_C$, and are due to contributions from both superconductivity and disorder-pinned competing orders. Our model assumes that the competing order persists above T$_C$ to T*, that the competing order energy, V$_{CO}$, exceeds Δ_{SC}, and that disorder in Bi-2212 contributes to an increase in spectral weight for the effective gap features. For heavily underdoped Bi-2212, V$_{CO}$ $\gg$ Δ_{SC} leading to Δ_{eff} $\sim$V$_{CO}$, which naturally leads to an empirical observation of a linear relationship between $\Delta_{eff} = \Delta_{pk-pk}$ and the pseudogap as a function of doping because the competing order energy, V$_{CO}$, is the cause of the pseudogap.

The second argument that the pseudogap arises from a ground state of superconductivity alone is based on the notion that the pseudogap spectra in vortex cores in Bi-2212 resembles the T > T_C spectra in Bi-2212 and that this relationship follows the same linear doping dependence with Δ_{pk-pk} as described above [18, 3]. However, our analysis of V_{PG}, Δ', Δ_{SC}, and Δ_{eff} in Y-123 and V_{PG} and Δ_{eff} in La-112 does not agree with this conclusion. In contrast to the results obtained in Bi-2212, our detailed results characterizing the spatially resolved energy scales in Y-123 indicate a marked difference between $\Delta_{SC} = \Delta_{pk-pk} \simeq$20meV and $V_{PG} \simeq$32meV observed for zero field and intra-vortex spectra, as shown in Figs. 5.3 and 5.5, respectively, and indicate $V_{PG} > \Delta_{SC} = \Delta_{pk-pk}$. In contrast, we observe intra-vortex pseudogap energies V_{PG} that obey $V_{PG} < \Delta_{eff} = \Delta_{pk-pk}$ in La-112. In fact, we find in Chapter 7 that the differences in La-112 and Y-123 can be accounted for by using a coexisting SC/CO model if $V_{CO} > \Delta_{SC}$ in Y-123 and $V_{CO} < \Delta_{SC}$ in La-112, but there is no natural explanation for the differences in the shift of the quasiparticle energies in La-112 and Y-123 based on a ground state of pure superconductivity alone. In fact, we find the empirical value $V_{PG} \simeq$32meV in vortex cores in Y-123 agrees with the competing order energy V_{CO} = 32meV derived from our SC/CO fitting of the satellite features in the T=6K zero field quasiparticle spectra of Fig. 5.2. Specifically, the fitting yields a competing order of a CDW with V_{CO}=32meV and $|\mathbf{Q}|_{CO}=(0.25\pm0.03)\pi$ along the Cu-O bonding direction, and the competing order wavevector is in further agreement with the Q_{CDW} value observed in the FT-LDOS.

Finally, the subgap energy observed in the vortex cores of hole-type cuprates has also been attributed to arising from superconductivity alone in a phenomenological model [32] to explain the apparent linear relationship between Δ' and Δ_{pk-pk} observed in Bi-2212 and in one measurement on optimally doped Y-123 [19, 3]. While the subgap energy can essentially arise from disordered pairs, possibly in the form of a PDW, we find that the assumed equivalence between V_{PG} and Δ_{SC} is not consistent with our histograms of spatially resolved Δ_{pk-pk} values in Y-123. As we have seen from our Δ_{pk-pk} histograms as a function of magnetic field, the energy scales of V_{PG} and Δ_{SC} differ by $\sim$7$-$12meV in Y-123, and this "one-gap" model cannot account for the presence of these two distinctly different energy scales at T $\ll$ T_C. Furthermore, the linear relationship between Δ' and Δ_{pk-pk} observed in Bi-2212 may imply that the Δ' and V_{PG} have a similar origin since

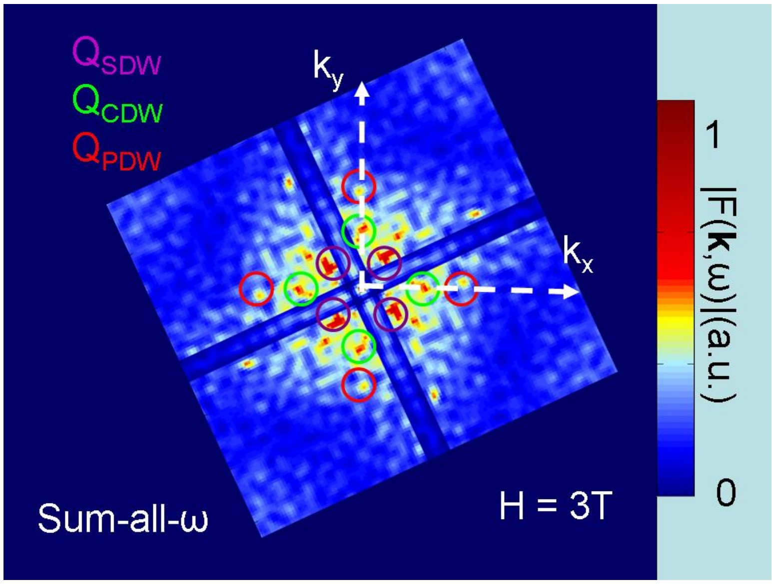

Figure 5.14: Low energy summed FT-LDOS at H = 3T in Y-123. The FT-LDOS, |F(**k**,ω,H=3T)|, shown in Y-123 is summed from ω=-1meV to ω=-30meV. The energy independent spots $\mathbf{Q}_{PDW}$, $\mathbf{Q}_{CDW}$, and $\mathbf{Q}_{SDW}$ at H = 3T in Y-123 are indicated by circles in the figure.

$\Delta_{eff} = \Delta_{pk-pk} \sim$V$_{PG}$ for underdoped Bi-2212, as pointed out in the discussion above. However, the assertion of the “one-gap” model that both features can be explained by superconductivity alone does not seem applicable to Y-123 based on our analysis of the energy scales of Δ_{SC}, Δ_{eff}, Δ', and V$_{PG}$.

5.5 Summary

In this chapter, we examined the spatially resolved quasiparticle tunneling spectra in hole-type Y-123 as a function of magnetic field and temperature. We observed a spatially homogeneous superconducting energy gap, $\Delta_{SC} = (20.0 \pm 1.0)$meV, and greater inhomogeneity in the shoulder-like satellite features at the effective gap, $\Delta_{eff} = (37.8 \pm 2.0)$meV. Upon introduction of vortices, we observed significant spectral weight shifts from Δ_{SC} to two other energy scales, the pseudogap energy, V$_{PG} \simeq 32$meV, and the subgap energy, $\Delta' \sim 7-12$meV. This finding could not be accounted for by conventional superconductivity alone. The two energy scales, V$_{PG}$ and Δ', were observed in intra-vortex spectra, while a gap approximately equal to Δ_{SC} was observed for inter-vortex spectra. The intra-vortex gap value of V$_{PG}$ was consistent with the competing order energy, V$_{CO}$, derived

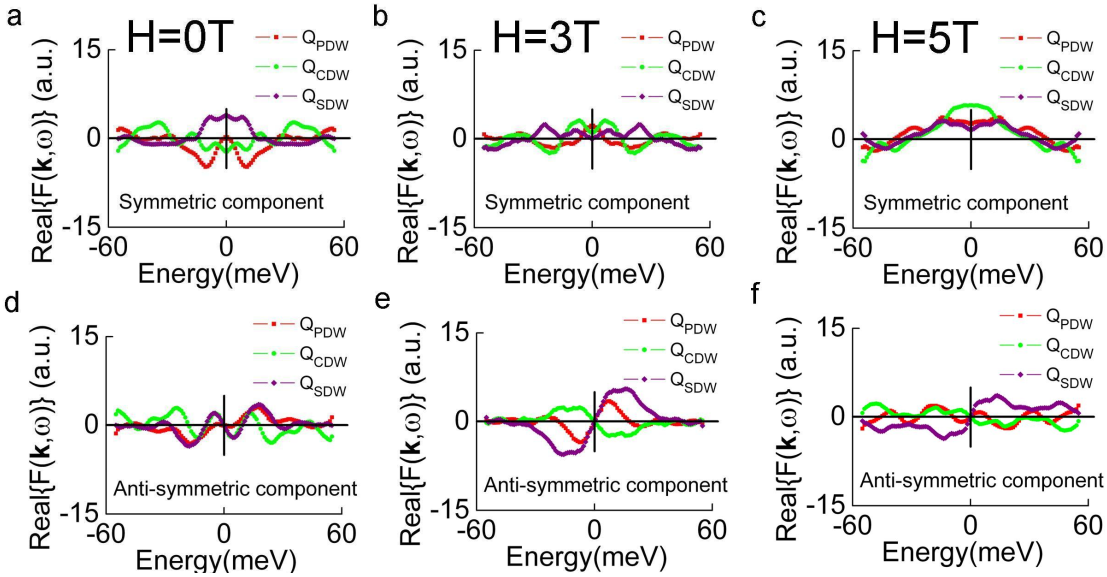

Figure 5.15: Energy dependence of the FT-LDOS amplitudes of the diffraction modes $\mathbf{Q}_{PDW}$, $\mathbf{Q}_{CDW}$, and $\mathbf{Q}_{SDW}$ in Y-123 for H = 0, 3T, and 5T. Top panels: The symmetric components of the FT-LDOS amplitudes for H = 0, 3T, and 5T respectively. Bottom panels: The anti-symmetric components of the FT-LDOS amplitudes for H = 0, 3T, and 5T respectively. We label $\mathbf{Q}_{PDW}$ as a PDW because it shows a strongly symmetric amplitude component of the FT-LDOS for H = 0. In contrast, $\mathbf{Q}_{SDW}$ shows an anti-symmetric amplitude component of the FT-LDOS for H = 0. We expect unequal populations of spin-up and spin-down quasiparticles in a magnetic field, so we associate this point with an SDW. Finally, $\mathbf{Q}_{CDW}$ shows mixed symmetric and anti-symmetric amplitude components of FT-LDOS. The value of $\mid \mathbf{Q}_{CDW} \mid \sim 0.28\pi$ approximately agrees with $\mid \mathbf{Q}_{CO} \mid \sim 0.25\pi$ used in our model of a CDW coexisting with superconductivity to fit the T = 6K spectra in Y-123 in Fig. 5.2.

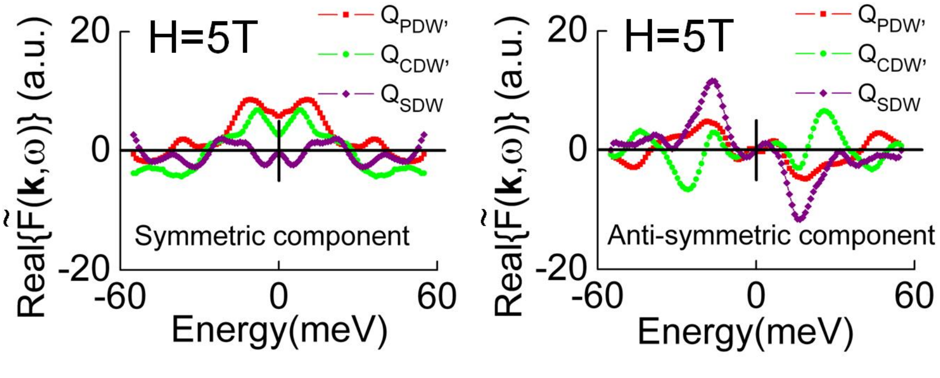

Figure 5.16: Energy dependence of the differential FT-LDOS amplitudes of $\mathbf{Q}_{PDW}$, $\mathbf{Q}_{CDW}$, and $\mathbf{Q}_{SDW}$ in Y-123 for H = 5T. Left panel: The symmetric components of the differential FT-LDOS amplitude for H = 5T. Right panel: The anti-symmetric components of the differential FT-LDOS amplitude for H = 5T.

from the SC/CO fitting of the $T \ll T_C$ spectra in zero magnetic field and compared favorably with the spin-gap energy observed in neutron scattering measurements of optimally doped Y-123 [16].

Fourier-transformation of local density of states (FT-LDOS) measurements revealed three sets of energy independent modes, which could be labeled $\mathbf{Q}_{PDW}$, $\mathbf{Q}_{CDW}$, and $\mathbf{Q}_{SDW}$ and located at $\mathbf{Q}_{PDW} = [\pm(0.56\pm0.06)\pi/a_1,0]$ and $[0,\pm(0.56\pm0.06)\pi/a_2]$; $\mathbf{Q}_{CDW} = [\pm(0.28\pm0.02)\pi/a_1,0]$ and $[0,\pm(0.28\pm0.02)\pi/a_2]$; and $\mathbf{Q}_{SDW} = [\pm(0.15\pm0.01)\pi/a_1,\pm(0.15\pm0.01)\pi/a_2]$. Analysis of the FT-LDOS amplitudes of each set of energy independent modes revealed that the real part of the amplitude at $\mathbf{q} = \mathbf{Q}_{PDW}$ was predominantly symmetric. In contrast, the real part of the amplitude at $\mathbf{q} = \mathbf{Q}_{SDW}$ was predominantly anti-symmetric in energy, whereas that at $\mathbf{q} = \mathbf{Q}_{CDW}$ revealed mixed symmetric and anti-symmetric components. Based on these results, the energy-independent wavevector $\mathbf{Q}_{PDW}$ was identified as a pair-density wave (PDW) and $\mathbf{Q}_{SDW}$ was identified as a spin-density wave (SDW). The value of $\mathbf{Q}_{CDW}$ could be attributed to a charge-density wave (CDW) based on its agreement with the value of $\mathbf{Q}_{CO}$ derived from fitting of the $T \ll T_C$ quasiparticle tunneling data using the coexisting SC/CO model.

In conclusion, the totality of results in Y-123 cannot be explained by assuming a ground state of superconductivity alone, and the unconventional behavior observed suggests that a model of coexisting competing orders and superconductivity can better account for the data. In addition, a model of coexisting competing orders and superconductivity can also explain the differences in the unconventional phenomena between hole- and electron-type cuprate superconductors, which is further elaborated in Chapter 7.

Chapter 6

Characterization of the macroscopic quantum fluctuations in cuprate superconductors with magnetization measurements

To date, our theoretical understanding of the macroscopic vortex dynamics of high-temperature cuprate superconductors remains at a phenomenological level. Although empirically it is well known that the vortex state of cuprate superconductors exhibits strong quantum, thermal and disorder fluctuations, the microscopic mechanism leading to these strong fluctuation effects has not been established. In this chapter, magnetization measurement techniques are used to characterize the macroscopic vortex phase diagrams of a wide variety of cuprate superconductors. Subsequently, the field-induced quantum fluctuations exhibited by many different superconducting cuprates with different microscopic parameters are quantified by the empirically determined vortex diagrams. Specifically, vortex phase diagrams are measured with magnetic field applied parallel to the CuO_2 planes, also known as the ab-planes, in all samples, and the irreversibility fields, $H_{irr}^{ab}(T)$, and upper critical fields, $H_{C2}^{ab}(T)$, are determined as functions of temperature, yielding the magnetic field (H)-vs.-temperature (T) vortex phase diagrams. By applying in-plane magnetic fields and taking the limit of $T \rightarrow 0$, the effects of disorder and thermal fluctuations may be minimized, leaving quantum fluctuations as the primary source that suppresses H_{irr}^{ab} relative to H_{c2}^{ab} and the paramagnetic field H_p as $T \rightarrow 0$. Strong field-induced quantum phase fluctuations are observed in the vortex phase diagrams of all samples examined and are quantified by comparing the suppression of H_{irr}^{ab} relative to H_p as $T \rightarrow 0$. The microscopic parameters affecting each cuprate are defined by a characteristic material parameter, α, and a consistent trend between field-induced quantum fluctuations and α for all samples is observed. The observed trend suggests close proximity to quantum criticality in all cuprate superconductors, which may be attributed to a ground state of superconductivity and competing orders in cuprate superconductors.

6.1 Introduction

The high-temperature cuprate superconductors are extreme type-II superconductors with $\xi << \lambda$, where ξ is the superconducting coherence length and λ the magnetic penetration depth. As a result of the extreme type-II behavior and susceptibility to thermal and disorder fluctuations, vortex liquid states exist over a large portion of the vortex phase diagrams of cuprate superconductors, which is in contrast to the absence of vortex liquid states in most conventional type-II superconductors. Additional novel vortex states, such as the vortex glass and Bragg glass, are found in cuprate superconductors [151, 152, 153, 154, 155, 156, 157, 130, 158]. Schematic illustrations for the differences in the vortex phase diagrams of conventional type-II superconductors and cuprate superconductors are shown in Fig. 6.1.

Although various phenomenological models can qualitatively account for the empirical H-vs.-T vortex phase diagrams and the experimental observation associated with different vortex phases in cuprate superconductors by incorporating strong fluctuation effects [159, 152, 153, 154, 155, 157]. However, a deeper understanding of the extreme type-II behavior and the physical origin of strong fluctuations remains to be developed.

A simple starting point to elucidate the vortex dynamics in the cuprates is to empirically measure the transition from the vortex liquid state to the vortex solid states, as this transition signals the onset of macroscopic superconducting phase coherence. For the purposes of the discussion here, we broadly define a vortex solid as a state where the superconductor maintains its global phase coherence. Transitions from the vortex liquid state to the vortex solid state occur at a characteristic field called the irreversibility field, H$_{irr}$. The irreversibility field, H$_{irr}$(T), may be measured experimentally, and is determined by the degree of thermal, disorder, and quantum fluctuations, which vary depending on the material parameters and temperature, T. When a superconductor is in the vortex liquid state, the phase of the superconducting order parameter is incoherent so that coherent macroscopic properties, such as the presence of supercurrents, are lost. Despite the loss of superconducting coherence in the vortex liquid state, the amplitude of the superconducting order parameter persists up to the maximum upper critical field, H$_{C2}$. Therefore, the threshold of superconductivity under a finite magnetic field is determined by H$_{C2}$(T), whereas the onset of macroscopic superconducting phase coherence is determined by H$_{irr}$.

Cuprate superconductors are anisotropic superconductors and, thus, have different irreversibility fields, H$^{ab}_{irr}$ and H$^{c}_{irr}$, and upper critical fields, H$^{ab}_{C2}$ and H$^{c}_{C2}$, for magnetic field applied along the c-axis direction (H$\|$c) and in-plane (H$\|$ab), respectively. The in-plane upper critical field and irreversible field are larger than the c-axis upper critical field and irreversible field, and one may therefore conclude that the maximum upper critical field, H$_{C2}$, would be given by H$^{ab}_{C2}$. However, the paramagnetic field, H$_p \equiv \Delta_{SC}/(\sqrt{2}\mu_B) \simeq 4.5k_BT_C/(\sqrt{2}\mu_B)$, which is defined as the field above which Cooper pairing is destroyed because the Zeeman energy exceeds the superconducting gap energy, may also determine a characteristic field that limits superconductivity. In the definition of H$_p$, Δ_{SC} is the superconducting gap, k_B is the Boltzmann constant, and μ_B is the Bohr magneton. Once a magnetic field equal to H$_p$ is applied in cuprates, the macroscopic superconducting order parameter is lost as the electrons in Cooper pairs break up and become paramagnetically aligned. For most cuprates, H$^{ab}_{C2} > H_p$. Therefore, the maximum critical field for cuprate superconductivity is typically H$_p$. We generally find H$^{ab}_{C2} > H_p$ to be true for the measurements considered here, so that we may define the onset of superconductivity as H$_p$. Measurements of H$^{ab}_{C2}$(T) are still relevant for calculating the electronic anisotropy, $\gamma \equiv \xi_{ab}/\xi_c =H^{ab}_{C2}$/H$^{c}_{C2}$.

Under certain experimental circumstances, we may minimize the effects of thermal and disorder fluctuations, leaving quantum fluctuations to be the dominant factor in determining the vortex phase diagram. For instance, theoretically thermal fluctuations, may be eliminated by reducing the

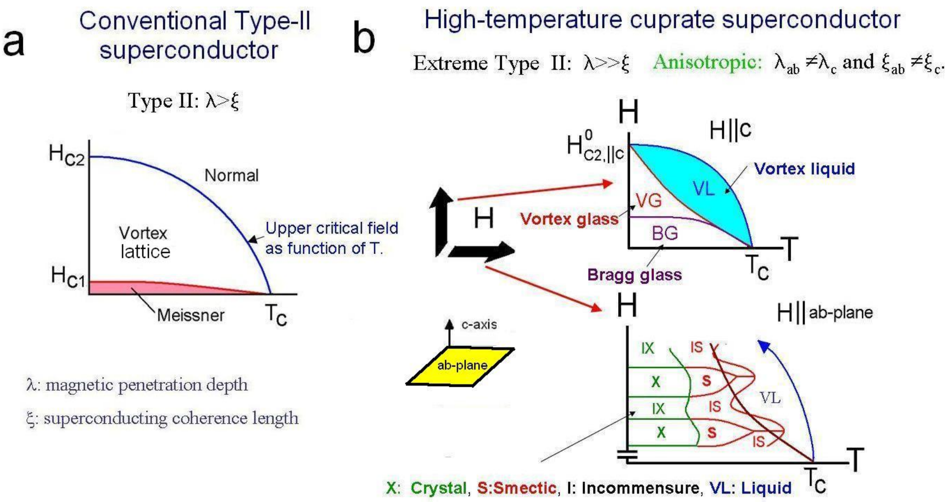

Figure 6.1: Schematic comparison of the vortex diagrams of type-II and high-T_C superconductors:(a) For conventional type-II superconductors, the vortex lattice phase inhabits the vast majority of the H-vs.-T vortex phase diagram compared to the vortex liquid state. We do not show the vortex liquid state in (a) because it exists over such a narrow range of [H,T] values that it would not easily be observed on the entire H-vs.-T phase diagram for conventional type-II superconductors. (b) In contrast, vortex liquid states exist over large portions of H-vs.-T vortex phase diagram in cuprates. Smectic and crystalline vortex phases, both commensurate and incommensurate with the CuO_2 lattice spacing, are predicted to be observed for in-plane magnetic fields due to the intrinsic pinning between CuO_2 planes [154]. Vortex glass and Bragg glass phases are predicted to exist for c-axis magnetic field measurements and arise from an interplay between point disorder and vortices [159, 155, 157]. For the schematic illustration shown here, we have neglected quantum fluctuations, which would have reduced the irreversibility fields, H_{irr}^{ab} and H_{irr}^{c}, below the upper critical fields, H_{C2}^{ab} and H_{C2}^{c}, as T→0. We find strong quantum fluctuations *are* present in all cuprates examined in this work.

temperature to zero. Experimentally, we may extrapolate the upper critical fields and irreversible fields measured at low temperature to T = 0. The extrapolated characteristic fields are effectively free of thermal fluctuations. To eliminate disorder fluctuations, we must consider what occurs in the vortex state when in-plane magnetic fields versus c-axis aligned magnetic fields are applied.

For magnetic field applied along the c-axis of cuprate superconductors (H||c), random point disorder and variations in disorder from sample to sample significantly affect the extent of vortex phases [159, 155, 157] observed in vortex phase diagrams. Therefore, the irreversibility will depend on the amount of disorder at finite temperatures and as T→0, which will obscure any attempts to isolate the effect of quantum fluctuations by extrapolating H_{irr}^{c} to T = 0 due to the added presence of disorder fluctuations.

For in-plane magnetic fields, the intrinsic pinning effect of layers in between CuO_2 planes generally dominates over that of random point disorder. For H$\|$ab, vortex smectic and vortex solid phases are predicted to arise when random point disorder and intrinsic pinning cooperate to pin vortices [154]. In the absence of quantum fluctuations, the vortex smectic and vortex solid states are expected to persist to the maximum critical field as T→0 [154]. Thus, if quantum fluctuations are absent, we expect that $H_{irr}^{ab} \rightarrow H_p$ as T→0. On the other hand, the presence of quantum fluctuations are expected to suppress the in-plane irreversibility field, leading to $H_{irr}^{ab} < H_p$. The specific deviation of H_{irr}^{ab} from H_p will depend on the actual strength of quantum fluctuations. Therefore, measurements with the configuration of in-plane magnetic fields can minimize the disorder fluctuations because intrinsic pinning suppresses the fluctuation effects associated with the random point disorder. In this context, we may measure H_{irr}^{ab} as a function of the temperature, and then extrapolate $H_{irr}^{ab}(T\rightarrow 0)$ to characterize the effects of quantum fluctuations alone. For the remainder of this chapter, we will concern ourselves with in-plane vortex phase diagrams so that we can determine the effect of field-induced quantum fluctuations.

To consider possible sources of quantum fluctuations in the cuprates, we note that a natural conjecture would be the coexistence of superconductivity and magnetic field enhanced competing orders in the ground state. Specifically, the loss of superfluid density, n_s, to a competing order as magnetic field is increased would increase the superconducting phase fluctuations so that macroscopic phase coherence was lost at an irreversibility filed $H_{irr}^{ab}(T\rightarrow 0)$ suppressed below H_p. This conjecture may be corroborated by our scanning tunneling spectroscopic studies of the electron-type $La_{0.1}Sr_{0.9}CuO_2$ (La-112) and hole-type $YBa_2Cu_3O_{7-\delta}$ (Y-123). Unconventional quasiparticle spectra in both La-112 and Y-123 may be explained by coexisting superconductivity and competing orders. Further, the energy histograms reveal significant redistribution from the superconducting gap to the pseudogap energy, V_{PG}, as magnetic field increased in both La-112 and Y-123 and can be interpreted as a strong spectral redistribution from superconductivity to a competing order as magnetic field is increased, lending credence to our conjecture of competing orders as the source of quantum fluctuations.

The susceptibility to quantum fluctuations in the cuprates may also imply that cuprates are in close proximity to quantum criticality [29, 30, 160]. For a scenario of quantum criticality due to coexisting competing orders and superconductivity, we expect the degree of quantum fluctuations to vary with respect to microscopic parameters of the cuprates [29]. The relevant microscopic parameters would include electronic anisotropy (γ), nominal doping (δ), number of CuO_2 planes (n), and charge imbalance (δ_o/δ_i) between the doping of inner layers (δ_i) and the doping of outer layers (δ_o) in multi-layer ($n \geq 3$) [161, 162] cuprates.

In this chapter, we present results of macroscopic magnetization measurements of the in-plane irreversibility field, and upper critical field in several different hole- and electron-doped cuprate superconductors. Our results provide evidence of strong field-induced quantum fluctuations in all cuprates examined. We present methods to quantify field-induced quantum fluctuations and the dependence of field-induced quantum fluctuations on microscopic variables. Our measurements are performed on optimally doped $HgBa_2Ca_2Cu_3O_x$ (Hg-1223, T_C=133K), $HgBa_2Ca_3Cu_4O_x$ (Hg-1234, T_C=125K), $HgBa_2Ca_4Cu_5O_x$ (Hg-1245, T_C=108K), and $La_{0.1}Sr_{0.9}CuO_2$ (La-112, T_C=43K). We also compare our results with published data on optimally doped $Nd_{1.85}Ce_{0.15}CuO_4$ (NCCO, T_C=23K) [163], underdoped $YBa_2Cu_3O_{7-\delta}$ (Y-123, T_C=87K) [164], and overdoped $Bi_2Sr_2CaCu_2O_x$ (Bi-2212, T_C=60K) [165]. We observe a trend in the measured field-induced quantum fluctuations as a function of microscopic variables, which is suggestive of the proximity of all cuprates to quantum criticality.

6.2 Methods

To investigate the role of unconventional quasiparticle excitations in field-induced quantum fluctuations, we developed a method to quantify field-induced quantum fluctuations in all our samples. As discussed in the previous section, in the limit of T→0 and with in-plane magnetic fields, thermal and disorder fluctuations become negligible. Consequently, quantum fluctuations become the sole factor that determines the deviation of H_{irr}^{ab} from the paramagnetic field, H_p, in this experimental situation. We may define two characteristic fields, $H^* \equiv H_{irr}^{ab}(T \rightarrow 0)$ and $h^* \equiv H^*/H_p$, and use the value of h^* as a measure of the field-induced quantum fluctuations in a superconducting cuprate.

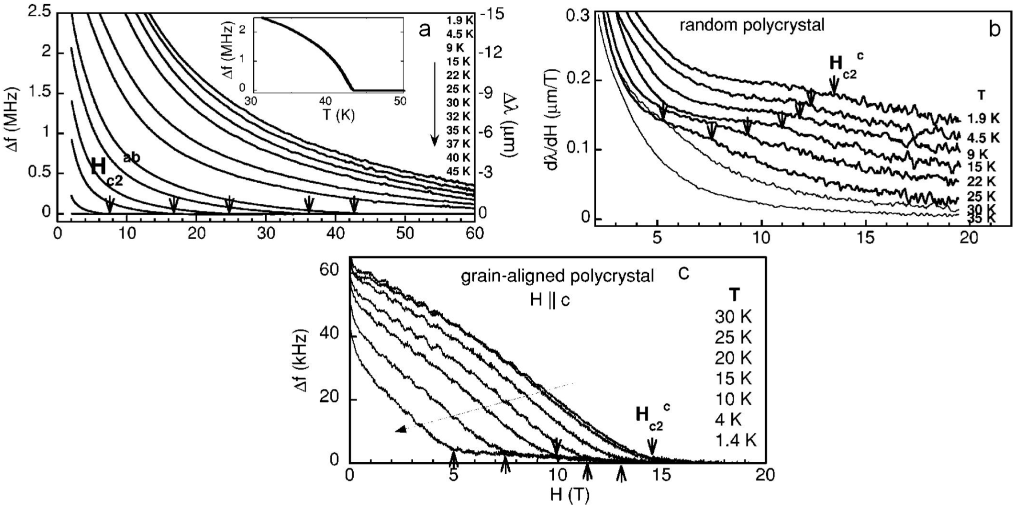

Figure 6.2: Measurements of the change in resonant frequency, Δf(H), vs. magnetic field, H, of a tunnel diode oscillator (TDO) tank circuit containing polycrystalline and grain-aligned $La_{0.1}Sr_{0.9}CuO_2$ (La-112). Changes in Δf(H) are measured relative to the normal state resonant frequency, f_0, measured for T=45K. The left axis shows the change in resonant frequency, and the corresponding change in penetration depth, $\Delta\lambda$(H), is indicated on the right axis. Inset: Δf(H) vs. T for H=0, showing $\Delta f \rightarrow 0$ at T_C=43 K. (b) Plots of dλ/dH vs. H, determined from the data in (a), as temperature was varied. Arrows indicate a kink, which identifies H_{C2}^C. (c) H_{C2}^C identified using the TDO technique for c-axis-aligned $La_{0.1}Sr_{0.9}CuO_2$ with H$\|$c and at different temperatures. We note that the values of H_{C2}^C determined from (b) and (c) are consistent. (Figure reproduced from Ref. [130], of which the author of this work was a coauthor.)

More specifically, a value of $h^* \rightarrow 1$ implies a negligible amount of field-induced quantum fluctuations, and a value of $h^* \rightarrow 0$ implies strong field-induced quantum fluctuations.

In addition to h^*, we seek a single parameter to characterize the role of all microscopic material parameters so that the effect of microscopic parameters on h^*, our measure of quantum fluctuations, may be determined. Specifically, we need to establish an intrinsic material parameter α that incorporates combined effects of the following microscopic parameters: doping level (δ), electronic anisotropy (γ), number of CuO_2 planes per unit cell (n), and charge imbalance (δ_o/δ_i) between the doping of inner CuO_2 planes (δ_i) and outer planes (δ_o) for n$\geq$3 [161, 162].

To better understand a reasonable method to define α, we consider the physical situation that determines the transition from an irreversible macroscopic superconducting state to a reversible macroscopic superconducting state. Magnetic irreversibility for $H \parallel ab$ and for $T \ll T_C$ and $H < H_{C2}^{ab}$ is maintained when a supercurrent flows along the c-axis direction and in the CuO_2 planes.

Strong thermal fluctuations or quantum fluctuations disrupt the supercurrent flow by reducing the phase coherence and depleting superfluid density, n_s, along the c-axis or the in-plane direction. The c-axis supercurrent is the most susceptible supercurrent direction to strong fluctuations. For T→0, we expect either the decoupling of $\mathrm{CuO_2}$ planes or the loss of c-axis phase coherence due to field-enhanced competing orders will determine h*.

For either scenario, we expect that quantum fluctuations will increase with increasing electronic anisotropy (γ) and charge imbalance (δ_o/δ_i) and decrease as doping (δ) increases, so that the simplest form for α is given by:

$$\alpha \equiv \gamma^{-1}\delta(\delta_o/\delta_i)^{-(n-2)}, \qquad (n \geq 3); \tag{6.1}$$

$$\alpha \equiv \gamma^{-1}\delta, \qquad (n \leq 2). \tag{6.2}$$

If strong quantum fluctuations arise because of proximity to a quantum critical point (QCP), we may define the QCP as α_c [29]. In this scenario, cuprates exhibit quantum criticality due to the proximity to a QCP, and we expect h*(α) to depend on $|\alpha - \alpha_c|$ [29]. Therefore, we will examine h*-vs.-α subsequent to measuring the vortex phase diagrams for all cuprates studied in this work and revisit the scenario that cuprates exhibit quantum fluctuations due to proximity to a QCP.

6.3 Results of macroscopic magnetization measurements on cuprate superconductors

To characterize the in-plane vortex phase diagrams and h* values for the cuprates in this chapter, it is essential to acquire data of the in-plane upper critical field H_{C2}^{ab}(T) and irreversibility field H_{irr}^{ab}(T) at low temperatures. We obtain H^* by extrapolating H_{irr}^{ab}(T→0) and subsequently divide H^* by the value of the paramagnetically limited field, H_p, to determine h^*. The values of H_{C2}^{ab}(T) are used to present a complete empirical determination of the in-plane H-vs.T vortex phase diagrams of each

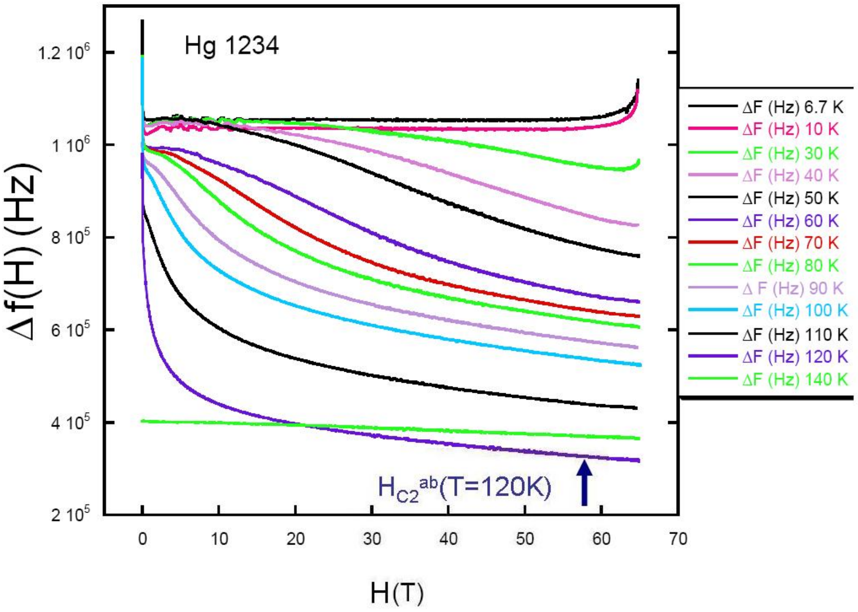

Figure 6.3: Measurements of Δf(H)-vs.-H of a tunnel diode oscillator (TDO) tank circuit containing polycrystalline $HgBa_2Ca_3Cu_4O_x$ (Hg-1234). The normal state resonant frequency, f_0 was measured for T=140K. All curves are offset for clarity. The T= 120K curve is offset below the T=140K curve, while the other curves are offset above the T=140K curve because we could not identify H_{C2}^{ab} at those temperatures. The upper critical field was measured to be H= 58±4T at T=120K.

cuprate. We may also use estimated values of $H_{C2}^{ab}(T\rightarrow 0)$, when available, to verify that H_p is indeed the maximum critical field. Furthermore, if we measure both $H_{C2}^{ab}(T\rightarrow 0)$ and $H_{C2}^{c}(T\rightarrow 0)$, we may determine the electronic anisotropy, $\gamma = H_{C2}^{ab}(0)/H_{C2}^{c}(0)$, for input to the parameter α.

In the next two sections, we present our magnetization measurements of the upper critical fields and in-plane irreversibility field in bulk samples of optimally doped Hg-1223 (polycrystalline and grain-aligned), Hg-1234 (polycrystalline), Hg-1245 (grain-aligned), and La-112 (polycrystalline and grain-aligned) superconducting cuprates.

We investigated the superconducting cuprates in grain-aligned or polycrystalline forms as noted above. The maximum upper critical field and irreversibility field for polycrystalline samples are empirically determined by H_{C2}^{ab}(T) and H_{irr}^{ab}(T), respectively, because the magnetic irreversibility and upper critical fields of polycrystalline samples are dominated by the maximum upper critical field, H_{C2}^{ab}(T), and maximum irreversibility field, $H_{irr}^{ab}(T)$, among different grains.

The sample quality of each sample investigated here has been verified with x-ray diffraction and magnetization measurements to ensure that the samples are single phased with nearly 100% volume superconductivity [166, 167].

6.3.1 Measurements of $\mathbf{H}_{C2}^{ab}$(T)

We experimentally determined the upper critical fields, H_{C2}^{ab}(T) and H_{C2}^{c}(T), of the cuprate superconducting samples by measuring changes in the magnetic penetration depth of samples in pulsed magnetic fields up to 60T. The pulsed field magnetization measurements were performed at the National High Magnetic Field Laboratory (NHMFL) in Los Alamos, NM, in a ^{3}He refrigerator with pulsed fields up to 60T. A tunnel diode oscillator resonant tank circuit was utilized to measure the penetration depth of samples by placing one of the cuprate superconducting samples into an inductor component of the tank circuit and measuring the frequency shift, Δf(H), as magnetic field was pulsed from H = 0 to H = 60T.

To determine Δf(H), the normal state resonant frequency, f_0, was established for the tank circuit containing a sample by pulsing the magnetic field to H = 60T at T>T_C, and f_0 was found to be independent of H. The value of Δf(H) was then determined at temperature T < T_C, by Δf(H)=(f(H)-f_0), with f(H) denoting the resonant frequency as a function of magnetic field, H. Changes in the resonant frequency relative to the normal state resonant frequency, due to changes in penetration depth between the normal and superconducting states, signaled the transition between normal and superconducting states and empirically determined the upper critical field, at temperature, T. Polycrystalline samples exhibited an upper critical field equal to H_{C2}^{ab}(T), while H_{C2}^{ab}(T) or H_{C2}^{c}(T) could be determined from grain-aligned samples depending on alignment of the magnetic field.

In Fig. 6.2, we present pulsed field measurements of Δf(H) and magnetic penetration depth change, $\Delta\lambda$(H), as temperature was varied for determining H_{C2}^{ab}(T) and H_{C2}^{c}(T) in La-112. In Fig. 6.2a we display arrows to indicate the identification of H_{C2}^{ab}(T) from data of Δf(H) on polycrystalline La-112. Verification of the value of T_C from measurements of $\Delta f(0)$ versus temperature is also shown in the inset of Fig. 6.2a, indicating a value of T_C=43K.

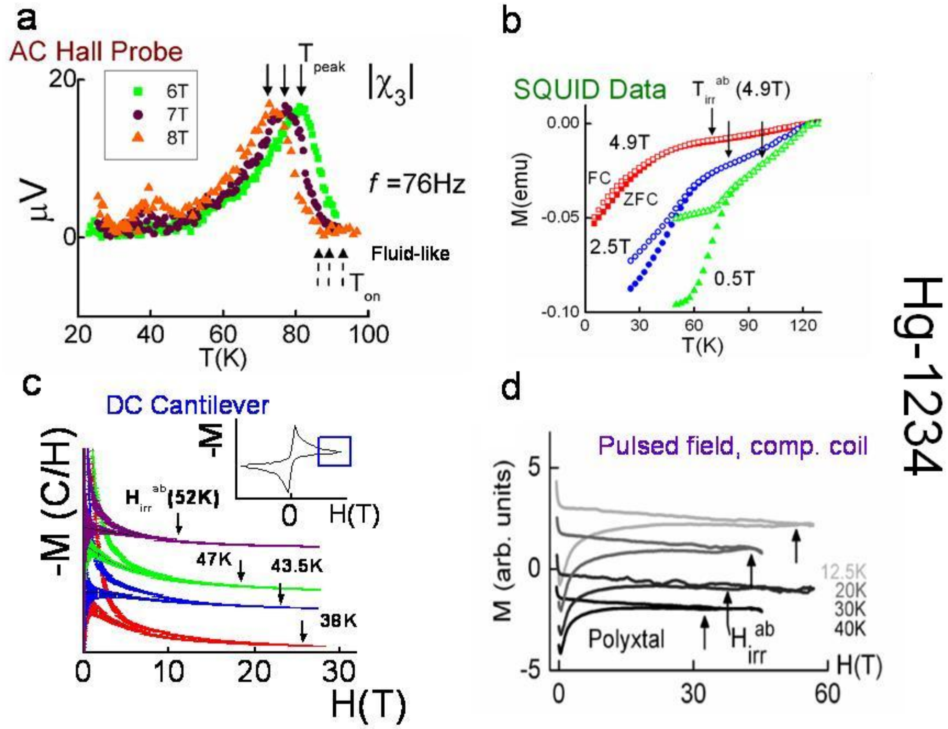

Figure 6.4: DC magnetization and AC susceptibility measurements of H_{irr}^{ab} in Hg-1234:(a) Magnitude of third harmonic response, $|\chi_3|$-vs.-T. The onset of a $|\chi_3|$ signal at high temperatures,for $T < T_C$, signals the transition from reversible to irreversible behavior of vortices. We identify T_{irr}^{ab} by T_{on}, the onset temperature of a $|\chi_3|$ signal for $T < T_{on}$. (b) SQUID M(T,H)-vs.-T measurements. Zero-field-cooled (ZFC) and field-cooled (FC) measurements were performed for various magnetic fields. When the ZFC and FC curves overlap, we identify the point as T_{irr}^{ab} as indicated by arrows in (b). (c) Measurements of M(T,H)-vs.-H as temperature is varied to determine H_{irr}^{ab} using DC cantilever techniques. The value of H_{irr}^{ab} is indicated by arrows in the figure. (d) Measurements of M(T,H)-vs.-H as temperature is varied to identify H_{irr}^{ab} using the compensated coil technique and pulsed magnetic fields up to H = 60T. The value of H_{irr}^{ab} is indicated by arrows in the figure.

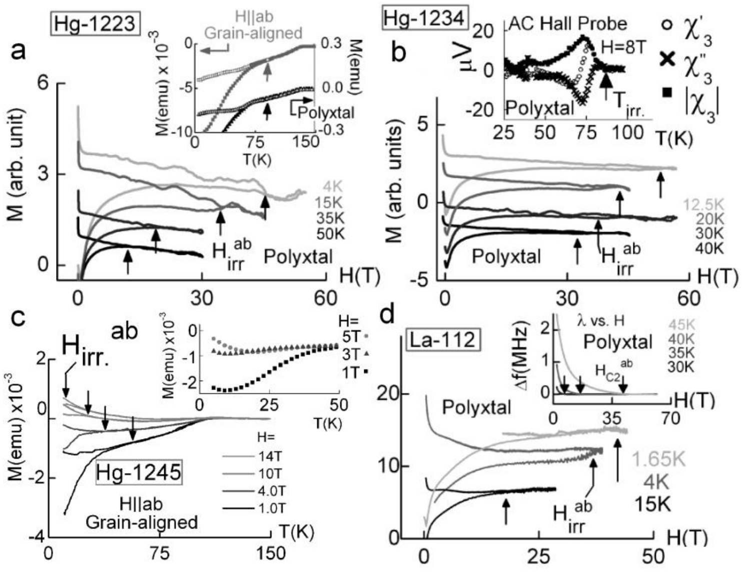

Figure 6.5: Representative measurements of the in-plane irreversibility fields $H_{irr}^{ab}(T)$ from measurements of M(T,H) in three cuprate superconductors. Main panels (a) Hg-1223 (polycrystalline and grain-aligned), (b) Hg-1234 (c) Hg-1245 (grain-aligned), and (d) La-112 (polycrystalline). Insets: (a) Demonstration of consistent $T_{irr}^{ab}(H)$ obtained from irreversibility of polycrystalline Hg-1223 and from irreversibility of a grain-aligned sample of Hg-1223 with $H \parallel ab$. (b) $|\chi_3|$-vs.-T in Hg-1234 reproduced from Fig. 6.4b.(c) Representative M-vs.-T curves showing an anomalous increase in magnetization for T < $\tilde{T}$. (d) H_{C2}^{ab}(T) measured in La-112 reproduced from Fig. 6.2a.

The values of Δf(H) approximately relate to $\Delta\lambda$(H) by $\Delta\lambda = -[(R^2/r_s)(\Delta f/f_0)]$, where R is the radius of the coil and r_s is the radius of the sample [168]. Here, $R \sim r_s$=0.7 mm, and the value of $f_0 \simeq 60$ MHz. Therefore, $\Delta f \sim (0.16\mathrm{MHz}/\mu m)\Delta\lambda$. Approximate values of $\Delta\lambda$ are illustrated on the right axis of Fig. 6.2a, determined from the values of Δf shown on the left axis of Fig. 6.2a.

In Fig. 6.2b, the numerical derivative, $d\lambda/dH$, computed from the data on polycrystalline La-112 in Fig. 6.2a, is shown, and a kink indicates the location of H_{C2}^{c}(T). Subsequently, we verified the identification of the kink location as being due to H_{C2}^{c}(T) by performing pulsed field TDO measurements on grain-aligned La-112 with H$\|$c, and the results confirming the consistent identification are shown in Fig. 6.2c.

In Fig. 6.3, we present Δf(H)-vs.-H data taken on polycrystalline Hg-1234 using the TDO technique. Only H_{C2}^{ab} at T=120K was identifiable, indicating that $\mathrm{H}_{C2}^{ab} > 60$T for T < 120K.

6.3.2 Measurements of $\mathbf{H}_{irr}^{ab}$(T)

We experimentally determined the magnetic irreversibility field, $H_{irr}^{ab}(T)$, of the samples considered here from AC and DC magnetization techniques. Measurements of the DC magnetization as a function of T and H, M(T,H), were performed with the use of a SQUID magnetometer at the Beckman Institute and our homemade Hall probe magnetometer for magnetic fields up to 9 Tesla in our lab. The onset of non-linear vortex response to an external AC field in the low-excitation limit was also employed to identify $H_{irr}^{ab}(T)$ in our lab by means of AC measurements of the third harmonic magnetic susceptibility (χ_3) [108] as a function of temperature in a constant field. To further characterize the in-plane irreversibility field at lower temperatures, we conducted measurements in much higher fields at the NHMFL in Los Alamos and the NHMFL in Tallahassee. At the NHMFL in Los Alamos, we used a DC magnetometer for fields up to 14 Tesla and a compensated coil setup for magnetization measurements in pulsed fields up to 65 Tesla pulsed fields in a ^{3}He refrigerator to measure M(T,H). At the NHMFL in Tallahassee we used a cantilever magnetometer in fields up to 33 Tesla in ^{3}He or ^{4}He refrigerators to determine M(T,H). The techniques mentioned above were described in more detail in Chapter 3.

Representative measurements of $H_{irr}^{ab}(T)$ in Hg-1234 using AC third harmonic, DC SQUID, DC cantilever, and compensated coil techniques are shown in Fig. 6.4(a)–(d). The consistency of the $H_{irr}^{ab}(T)$ results measured by different techniques is verified. The consistency is also summarized in the H-vs.-T vortex phase diagram for ($H \parallel ab$) of Hg-1234 shown in Fig. 6.6b. We find similar consistency among techniques for data on all cuprates presented here.

In the main panel of Fig. 6.5a, we present representative determinations of $H_{irr}^{ab}(T)$ from M(T,H) measurements on Hg-1223 in pulsed fields using the compensated-coil magnetization measurement technique. Additionally, we show verification that $H_{irr}^{ab}(T)$ measured in polycrystalline samples is consistent with $H_{irr}^{ab}(T)$ measured in grain-aligned samples with magnetic field applied along the CuO_2 planes (H$\|$ab) in the inset of Fig. 6.5a. The measurements shown were verified from SQUID measurements on polycrystalline Hg-1223 and for grain aligned Hg-1223 with H$\|$ab.

Representative measurements of the in-plane irreversibility fields for Hg-1234, Hg-1245, and La-

112 from measurements of M(T,H) are shown in Figs. 6.5(b)–(c). Below a temperature, $\tilde{T}$, the magnetization of Hg-1245 exhibits an anomalous increase which is labeled in the inset of Fig. 6.5c. The increasing magnetization may be attributed to increasing magnetic ordering in the inner CuO_2 layers of the multi-layer cuprates with $n \geq 3$, according to muon spin resonance experiments and NMR measurements [169, 170].

6.3.3 Vortex phase diagrams

The H-vs.-T vortex phase diagrams for Hg-1223, Hg-1234, Hg-1245 and La-112 based on the magnetization measurements described earlier are shown in Fig. 6.6(a)–(d). The vortex phase diagrams display the values of $H_{irr}^{ab}(T)$ determined from all techniques considered in this work and demonstrate consistency in the identification of $H_{irr}^{ab}(T)$ among techniques.

We may compare the vortex phase diagrams of different cuprates on a reduced field, h, versus reduced temperature, t, plot by normalizing all magnetic fields to the paramagnetic field, H_p, and all temperatures to the transition temperature, T_C, such that $h \equiv H/H_p$ and $t \equiv T/T_C$. We also consider published results of in-plane irreversibility field $H_{irr}^{ab}(T)$ identified in single crystals for underdoped $YBa_2Cu_3O_{7-\delta}$ (Y-123, $T_c = 87$ K), [164] optimally doped $Nd_{1.85}Ce_{0.15}CuO_4$ (NCCO, $T_c = 23$ K) [163] and overdoped $Bi_2Sr_2CaCu_2O_x$ (Bi-2212, $T_c = 60$ K) [165] for comparison with our results. The results for all cuprate superconductors considered here are shown together in the reduced field versus reduced temperature phase diagram in Fig. 6.7, and the necessary parameters are tabulated in Table 6.1.

In h-vs.-t vortex phase diagrams, the irreversibility field $H_{irr}^{ab}(T)$ becomes $h_{irr}^{ab}(t) \equiv H_{irr}^{ab}(T/T_C)/H_p$. We may then determine the value of h* by simply extrapolating $h_{irr}^{ab}(t)$ to zero temperature, because $h^* = h_{irr}^{ab}(t \rightarrow 0)$. Clearly, all samples shown in Fig. 6.7 show strong suppression of $h_{irr}^{ab}(t \rightarrow 0)$ and small values of h* due to field-induced quantum fluctuations. The values of h* obtained give a measure of the field-induced quantum fluctuations in each case, with $h^* \rightarrow 1$ implying weak field-induced quantum fluctuations and $h^* \rightarrow 0$ implying strong field-induced quantum fluctuations. Among all the samples considered, the value of h* for Y-123 is the largest value ($h^* = 0.88$), while Hg-1245 shows

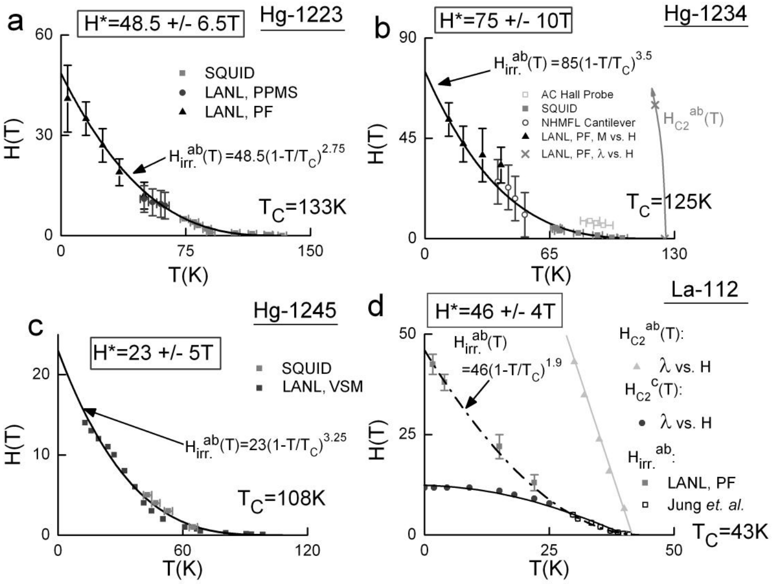

Figure 6.6: Vortex phase diagrams for extrapolating H_{irr}^{ab}(T→0) using various magnetization measurement techniques: (a) Hg-1223, (b) Hg-1234, (c) Hg-1245, and (d) La-112. We find consistency among the values of H_{irr}^{ab} obtained from different techniques. We additionally show identified values of the upper critical field $H_{C2}^{ab}(T)$ in (b) and (d) and the upper critical field $H_{C2}^{c}(T)$ in (d) for completeness.

the smallest value (h*=0.08).

To determine the effect of microscopic parameters on h* we compute α using Eqs. 6.2 and the microscopic parameters in Table 6.1. Additionally, Table 6.1 presents the calculated values of α and includes the uncertainties in all parameters.

6.3.4 Examining trends of field-induced quantum fluctuations with microscopic parameters

If the conjecture that strong field-induced quantum fluctuations in cuprate superconductors arise due to proximity to a QCP is correct, the values of h* will be a function of $|\alpha - \alpha_c|$ [29]. To investigate this scenario, we plot values of h*-vs.-α taken from Table 6.1 in Fig. 6.8a and 6.8b. We observe a trend in the experimental h*-vs.-α values, and consider two models to explain the data in Fig. 6.8a and 6.8b, which we discuss below.

The formalism of a scenario of coexisting spin-density waves and superconductivity in cuprate was discussed in Ref. [29] and it was shown that h^* follows the relation

$$h^*(\alpha) \propto |\alpha - \alpha_c|/(\ln|\alpha - \alpha_c|). \tag{6.3}$$

Furthermore, the value of α_c is non-universal among different cuprates and $h^*(\alpha)$ will approach zero as $\alpha \rightarrow \alpha_c$[29]. Theoretical fits using Eq. 6.3 are shown with data in Fig. 6.8a using three different values of α_c (0, 10^{-4}, 2 x 10^{-4}) for comparison. For ease of comparison, the main panel of Fig. 6.8a shows the data and theoretical fits on log-log axes and the inset shows the data on linear-linear axes.

As an alternative formalism to Eq. 6.3 we could use a simple scaling argument, which would predict a power-law dependence for the QCP scenario that would obey:

$$h^*(\alpha) \propto |\alpha - \alpha_c|^a, \tag{6.4}$$

with a = 0.5. In Fig. 6.8b, we present our data with three power-law curves generated using Eq. 6.4. The three fits use the same values of α_c that were used for the field-induced SDW theoretical curves in Fig. 6.8a. The power-law fits appear to agree better with the data than the field-induced SDW curves given by Eq. 6.3. However, we cannot further distinguish between the three values of α_c based on the data to conclude the actual value of α_c.

The smallest value of h^* measured was in Hg-1245, so we may attempt to unravel more information about α_c by examining the data in Hg-1245 more closely, especially in the context of our observation of field-induced reentry of a magnetic order in M(T,H) measurements. The reentry of magnetic ordering in Hg-1245 suggests the vortex phase diagram of Hg-1245 incorporates superconductivity and a competing order that is magnetic in origin. We can associate a characteristic magnetic field, $\tilde{H}$, with the values of $\tilde{T}$ determined at each magnetic field in Hg-1245 and produce the vortex phase diagram shown in Fig. 6.9.

In the phase diagram of Hg-1245 of Fig. 6.9, we suggest that the region below both H_{irr}^{ab} and $\tilde{H}$ is a coherent superconducting state (c-SC). The region bounded by H_{irr}^{ab} and $\tilde{H}$ is a coexisting phase

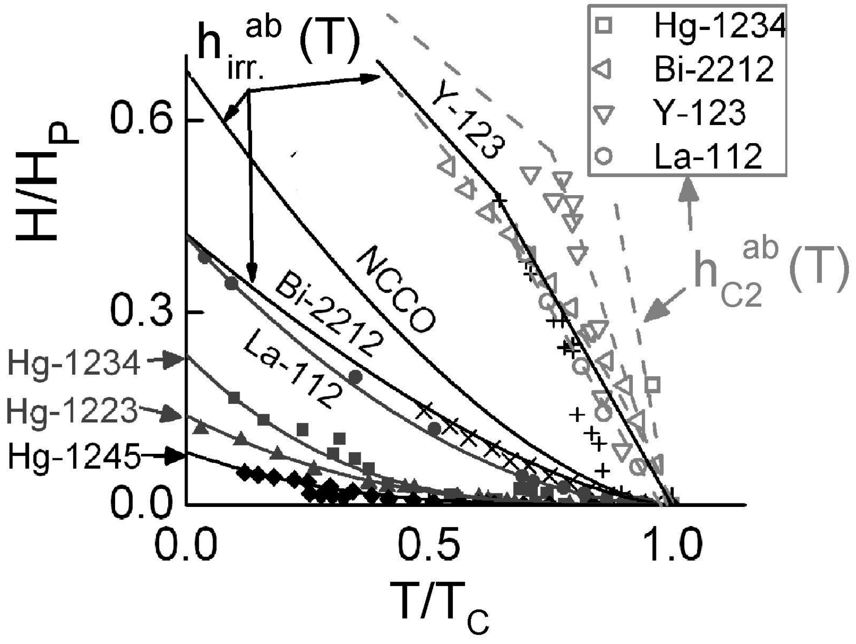

Figure 6.7: The reduced field, h≡H/H$_p$, vs. reduced temperature, t≡T/T$_C$ phase diagram of Hg-1245, Hg-1223, Hg-1234, La-112, Bi-2212, NCCO, and Y-123. The reduced in-plane irreversibility fields, h$^{ab}_{irr}(T) \equiv H^{ab}_{irr}(T)/H_p$, and reduced in-plane upper critical fields, h$^{ab}_{C2}(T) \equiv H^{ab}_{C2}(T)/H_p$, are shown. The values of h* are determined by h*=h$^{ab}_{irr}(T \to 0) \equiv H^*/H_p$ and are listed in Table 6.1. All samples show strong suppression of h$^{ab}_{irr}$(T→0), indicating strong field-induced quantum fluctuations.

of coherent superconductivity and a magnetic competing order(c-SC/CO), while the region above H$^{ab}_{irr}$ is an incoherent superconducting phase (i-SC and i-SC/CO) with strong fluctuations.

Therefore, the source of strong field-induced quantum fluctuations and quantum criticality in cuprates would be the field-induced competing order and proximity to the quantum critical point, α_c, associated with the competing order. In the context of the other Hg-based cuprates we considered here, the scenario for Hg-1245 shown in Fig. 6.9 may explain our observation of strong field-induced quantum fluctuations in all cuprates. Namely, Hg-1223, Hg-1234, and Hg-1245 have some of the highest values of T$_C$ but some of the lowest values of h* and α of all cuprates, as summarized in Table 6.1,. The small values of α may be conjectured to arise from the large electronic anisotropy [166, 171] and significant charge imbalance in the Hg-based cuprates. The lower doping in the inner layers may lead to the presence of competing orders in the inner layers [161, 162], which will lead to strong quantum fluctuations. Therefore, we would expect the strength of the competing order to increase with further charge imbalance so that Hg-1245 would exhibit more quantum

Table 6.1: Parameters to determine h* and α in: Hg-1245, Hg-1223, Hg-1234, La-112, Bi-2212, NCCO, and Y-123. All fields are in tesla. σ denotes a parameter's uncertainty.

	δ	δ_o	δ_i	γ	σ_γ	$\alpha(10^{-2})$	$\sigma_\alpha(10^{-3})$	H^*	σ_{H^*}	$H^{ab}_{C2}[H_P]$	σ_{H_P}	h^*	σ_{h^*}
Hg-1245	0.15	1.30	0.80	55[172]	25	0.06	0.3	23.0	5.0	−[278]	40	0.08	0.02
Hg-1223	0.15	1.04	0.92	52[173]	18	0.26	0.9	48.5	6.5	−[347]	50	0.14	0.02
Hg-1234	0.15	1.20	0.80	52[173]	10	0.13	0.2	75.0	10.0	−[320]	46	0.23	0.02
La-112	0.10	1.00	1.00	13[130]	4.0	0.77	2.4	46.0	4.0	160[110]	10	0.42	0.04
Bi-2212	0.225	1.00	1.00	11[165]	8.0	2.05	15	65.0	10	100[155]	22	0.42	0.06
NCCO	0.15	1.00	1.00	13[163]	5.0	1.15	4.4	40.0	5.0	77[59]	8.0	0.68	0.12
Y-123	0.13	1.00	1.00	7.0[173]	2.0	1.86	5.3	210	50	600[239]	25	0.88	0.10

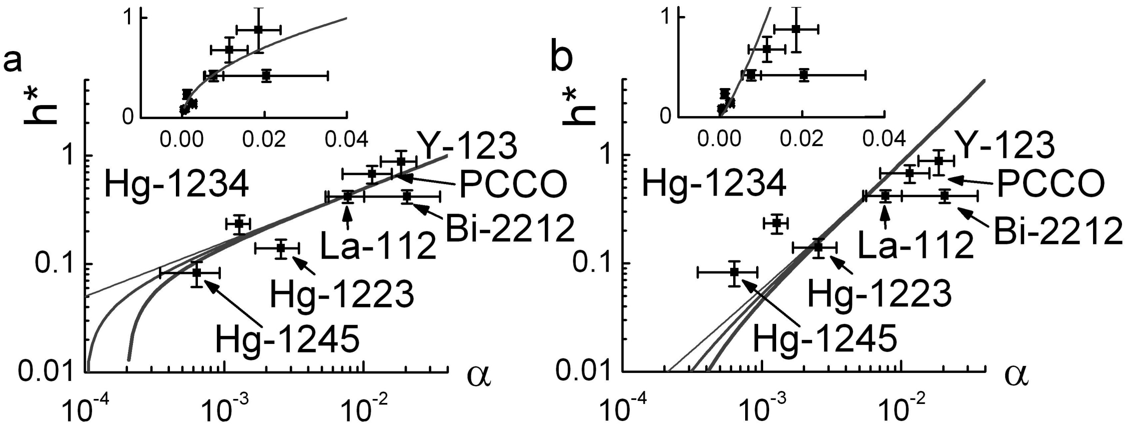

Figure 6.8: Comparison of field-induced quantum fluctuations (h*) and microscopic parameters (α) in cuprates.(a) Main panel: h* vs α data (solid symbols) from Table 6.1 plotted on logarithmic axes. The lines are fits to the field-induced SDW theoretical model [29] described by Eq. 6.3 using α_c=0, 10^{-4}, and 2 x 10^{-4} from left to right. The actual functional form used is $-400|\alpha - \alpha_c|/(\ln|\alpha - \alpha_c|)$. Inset: The same plot as the main panel in (a) on linear axes. (b)Main panel: h* vs α data (solid symbols) from Table 6.1 plotted on logarithmic axes. The lines are fits to the power law dependence described by Eq. 6.4 using α_c=0, 10^{-4}, and 2 x 10^{-4} from left to right. The actual functional form used is $5|\alpha - \alpha_c|^{1/2}$. Inset: The same plot as the main panel in (b) on linear axes.

fluctuations than Hg-1234 and Hg-1223. However, it is difficult to separate the roles of electronic anisotropy and charge imbalance in the determination of h* from the data presented. Namely, it is difficult to conclude whether quantum criticality arises merely from decoupling of the CuO_2 planes or from competing orders. On the other hand, the existence of a magnetic competing order in Hg-1245 suggests that competing orders play an important role. Further measurements of h* and γ in other cuprates, especially multi-layer cuprates with varying charge imbalance, are needed to confirm the exact role of competing orders in the observation of strong field-induced quantum fluctuations.

6.4 Summary

In conclusion, we performed magnetization measurements to characterize the vortex phase diagrams in Hg-1223, Hg-1234, Hg-1245, and La-112, and we compared our measured vortex phase diagrams with published vortex phase diagrams of Y-123, NCCO, and Bi-2212. We found strong field-induced quantum fluctuations in all cuprates examined, as evidence by the values of $h^* < 1$. Furthermore, we observed a trend between microscopic parameters, characterized by the material parameter, α, and a measure of quantum fluctuations, h^*. The observed trend among all cuprates suggests that cuprate superconductors exhibit strong field-induced quantum fluctuations due to their proximity to quantum criticality. We conjectured that the quantum criticality derives from the nearby presence of competing orders to superconductivity. Additionally, we observed evidence for a field enhanced competing order and the smallest value of h^* in Hg-1245, indicating strongest field-induced quantum fluctuations among all the samples in this work. Similarly, all three Hg-based multi-layer cuprates exhibited small values of h^*, while having the three highest values of T_C. These results therefore suggest that competing orders play an important role in the occurrence of field-induced quantum fluctuations and give rise to the unconventional vortex-state quasiparticle excitations in cuprates.

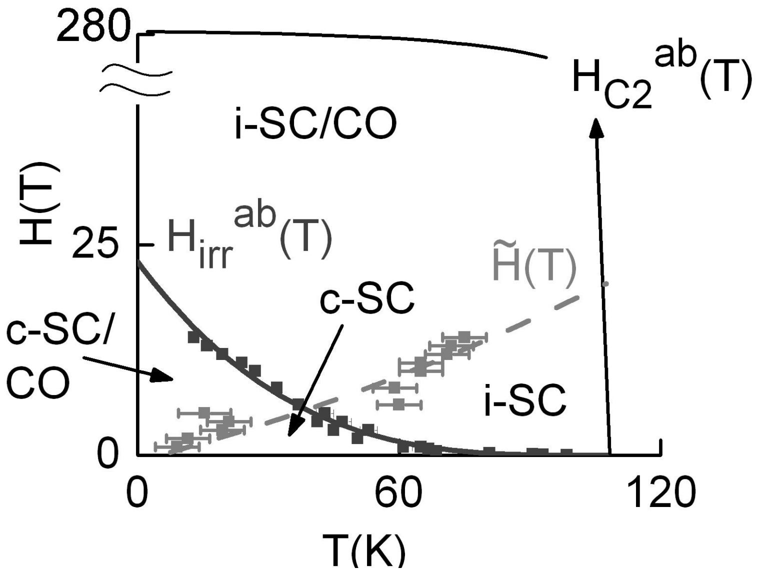

Figure 6.9: The conjectured H-vs.T phase diagram for $HgBa_2Ca_4Cu_5O_x$ (Hg-1245) showing incoherent superconductivity (i-SC), coherent superconductivity (c-SC), and a magnetic field enhanced competing order(CO). Coherent superconductivity occurs for H $< H^{ab}_{irr}(T)$ and incoherent superconductivity occurs for $H^{ab}_{C2}(T) >$ H $> H^{ab}_{irr}(T)$. The competing order is stabilized for H $> \tilde{H}$. Regions of overlap are shown, such as the overlap region of coherent superconductivity and the presence of a competing order (c-SC/CO) defined by $\tilde{H}$ <H $< H^{ab}_{irr}(T)$ near T = 0. The presence of a field-induced competing order suggests that strong field-induced quantum fluctuations and quantum criticality arise due to coexistence of the competing order and superconductivity. The coexistence of a competing order and superconductivity leads to the significant suppression of H* due to field-induced quantum fluctuations between superconductivity and the competing order.

Chapter 7

Modeling low-energy excitations in cuprate superconductors using Green's function techniques

In this chapter, we investigate the possibility that the quasiparticle excitations observed in high-temperature cuprate superconductors arise from a ground state of coexisting superconductivity (SC) and a competing order (CO), and we model the spectral density function and resulting quasiparticle excitation spectra for comparison with empirical observations. Specifically, we consider charge-density waves, spin-density waves, and d-density waves as possible CO's and use Green's function techniques to generate the theoretical quasiparticle spectral density function and quasiparticle density of states assuming the CO's coexist with SC. We find that five uniquely determined parameters are needed to model quasiparticle behavior in the SC/CO scenario: the superconducting gap energy(Δ_{SC}), the competing order energy (V_{CO}), the COs density-wave wavevector ($\mathbf{Q}_{CO}$), the disorder of the density-wave wavevector ($\delta\mathbf{Q}$), and the strength of quantum phase fluctuations between SC and the CO (η). Using the SC/CO model, we may fit angle resolved photoemission spectroscopy (ARPES) data and quasiparticle excitation spectra, typically from tunneling spectroscopy techniques, to obtain values for the five parameters. From this analysis, we find that experimental spectroscopic data in electron-(hole-)type cuprates may be fit with commensurate(incommensurate) density-wave orders with $\mathbf{Q}_{CO}$ parallel to the nodal (anti-nodal) direction. In addition, we find that the five parameters in our model needed to fit ARPES data are consistent with the parameters needed to fit quasiparticle tunneling spectra. Furthermore, the Δ_{SC}-vs.doping (δ) evolution, determined from fitting of the doping dependent experimental data, exhibits the same non-monotonic doping (δ) dependence as the bulk T_C values-vs.-δ. Finally, the presence(absence) of satellite features and the above T_C pseudogap in the hole-(electron-)type cuprates can be accounted for if the conditions $V_{CO} > \Delta_{SC}$ ($V_{CO} < \Delta_{SC}$) and $T^* > T_C$ ($T^* < T_C$) are satisfied, respectively.

Additionally, we solve two self-consistent equations to determine the temperature dependence of Δ_{SC} and V_{CO} by assuming the phonon-mediated mechanism as the microscopic origin for coexisting s-wave SC and charge-density wave (CDW) in the ground state. We find, for hole-type cuprates, that the temperature evolution of Δ_{SC} and V_{CO} determined by the phonon-mediated coexisting s-wave SC/CDW agrees qualitatively with the temperature evolution of Δ_{SC} and V_{CO} from ARPES on Bi-2212. However, the assumption of phonon-mediated pairing requires unreasonable physical parameters to reproduce the temperature evolution of Δ_{SC} and V_{CO}. Moreover, the assumption of s-wave SC is also inconsistent with the strong dependence of ARPES and tunneling spectra on the quasiparticle momentum. Therefore, if SC and CO arise from the same microscopic origin, electron-phonon interaction does not appear to be the viable microscopic mechanism that accounts for the occurrence of both phases simultaneously.

7.1 Methods

The starting point for our phenomenological model is to consider a Hamiltonian with coexisting superconductivity (SC) and competing orders (CO) that may be used to fit the quasiparticle spectral density function and quasiparticle density of states (DOS) at $T = 0$. We consider density-wave orders for the competing orders in our Hamiltonian, and here, we limit ourselves to consideration of charge-density waves (CDW), spin-density waves (SDW), and d-density waves (DDW), based on empirical observation and theoretical conjectures of CDWs, SDWs, and DDW's in cuprates [28, 31, 30, 174, 29, 26, 175, 82, 70, 5].

For each CO we consider, we may specify the CO energy by V_{CO}, the competing order wavevector by $\mathbf{Q}_{CO}$, and the disorder of the CO wavevector by $\delta\mathbf{Q}$. There are two types of SDWs that we consider. One type is a direct commensurate SDW (V_{CO}=V_{SDW}), with $\mathbf{Q}_{CO}$= (π, π) [176], and the other type is a disorder pinned SDW (V_{CO}=$g^2\mathrm{V}_{SDW}$) [86]. The value of g is the coupling strength between SDW and disorder. For CDW and DDW, we use V_{CO} =V_{CDW} and $|\mathrm{V}_{CO}|$=V_{DDW}, respectively.

For a CDW, $\mathbf{Q}_{CO}$ is parallel to the Cu-O bonding directions, and we assume $|\mathbf{Q}_{CO}| \sim 2k_F$ near $(0,\pi)/(\pi,0)$ based on empirical observations [4, 7, 70]. Here, k_F denotes the separation of the Fermi surface near the anti-nodes ($(0,\pi)/(\pi,0)$). In addition, $\mathbf{Q}_{CO}$ for the disorder-pinned SDW also is expected to be parallel to the Cu-O bonds, and the wavevector $\mathbf{Q}_{CO}$ of the charge modulations caused by the disorder-pinned SDW is expected to be half that of the CDW theoretically [86]. An example of $\mathbf{Q}_{CO}$ for the case of a CDW is shown in Fig. 7.1a for clarity. We may determine $\mathbf{Q}_{CO}$ by fitting ARPES experimental data, which provides momentum-dependent information in $\mathbf{k}$-space, or we may infer $\mathbf{Q}_{CO}$ from quasiparticle density of states data, although the latter is less direct than the former identification from ARPES.

Using the aforementioned fitting parameters to characterize the CO, we may consider a model that treats both SC and CO's exactly in the ground state by including both contributions in the mean-field Hamiltonian. For example, the mean-field Hamiltonian for a disorder pinned SDW or CDW is given by:

$$
\begin{aligned}
\mathcal{H}_{MF} &= \mathcal{H}_{SC} + \mathcal{H}_{CO} \\
&= \textstyle\sum_{\mathbf{k},\sigma} \xi_{\mathbf{k}}\, c^{\dagger}_{\mathbf{k},\sigma} c_{\mathbf{k},\sigma} - \sum_{\mathbf{k}} \Delta_k \left(c^{\dagger}_{\mathbf{k},\uparrow} c^{\dagger}_{-\mathbf{k},\downarrow} + c_{-\mathbf{k},\downarrow} c_{\mathbf{k},\uparrow} \right) \\
&\quad + \textstyle\sum_{\mathbf{k},\sigma} V_{CO} \left(c^{\dagger}_{\mathbf{k},\sigma} c_{\mathbf{k}+\mathbf{Q},\sigma} + c^{\dagger}_{\mathbf{k}+\mathbf{Q},\sigma} c_{\mathbf{k},\sigma} \right) \\
&= \textstyle\sum_{\mathbf{k}} \left(c^{\dagger}_{\mathbf{k},\uparrow}\; c_{-\mathbf{k},\downarrow}\; c^{\dagger}_{\mathbf{k}+\mathbf{Q},\uparrow}\; c_{-(\mathbf{k}+\mathbf{Q}),\downarrow} \right)
\begin{pmatrix}
\xi_{\mathbf{k}} & -\Delta_k & -V_{CO} & 0 \\
-\Delta_k & -\xi_{\mathbf{k}} & 0 & V_{CO} \\
-V_{CO} & 0 & \xi_{\mathbf{k}+\mathbf{Q}} & -\Delta_k \\
0 & V_{CO} & -\Delta_k & -\xi_{\mathbf{k}+\mathbf{Q}}
\end{pmatrix}
\begin{pmatrix}
c_{\mathbf{k},\uparrow} \\
c^{\dagger}_{-\mathbf{k},\downarrow} \\
c_{\mathbf{k}+\mathbf{Q},\uparrow} \\
c^{\dagger}_{-(\mathbf{k}+\mathbf{Q}),\downarrow}
\end{pmatrix} \\
&\equiv \textstyle\sum_{\mathbf{k}} \Psi^{\dagger}_{\mathbf{k},\mathbf{Q}}\, H_0\, \Psi_{\mathbf{k},\mathbf{Q}},
\end{aligned}
$$

Here $\xi_{\mathbf{k}}$ is the normal-state energy of particles of momentum $\mathbf{k}$ relative to the Fermi energy, σ is the spin index, $c^\dagger$ and c are the fermion creation and annihilation operators, $\mathbf{Q}$ is the wave vector of the CO for a quasiparticle of momentum, $\mathbf{k}$, Δ_k denotes the SC energy gap and is dependent on the pairing symmetry, and V_{CO} denotes the CO energy scale. H_0 is the (4×4) matrix shown above, and the adjoint of Ψ represents a (1×4) matrix $\Psi^\dagger_{\mathbf{k},\mathbf{Q}} \equiv \left(c^\dagger_{\mathbf{k},\uparrow}\ c_{-\mathbf{k},\downarrow}\ c^\dagger_{\mathbf{k}+\mathbf{Q},\uparrow}\ c_{-(\mathbf{k}+\mathbf{Q}),\downarrow} \right)$. We model superconductivity as $\Delta_{SC}\ (\mathrm{k}) = \Delta_s$ for s-wave SC and $\Delta_{SC}\ (\mathbf{k}) = \Delta_0 \cos(2\theta_k)$ for d-wave SC, with θ_k being the angle between $\mathbf{k}$ and the anti-node of the pairing potential in reciprocal space ($\mathbf{k}$-space). In the case of $\mathrm{YBa_2Cu_3O_{7-\delta}}$, the pairing symmetry is (d+s) so that we have $\Delta_{SC}(k) = \Delta_0 cos(2\theta_k) + \Delta_s$, and $\Delta_s \ll \Delta_0$ in the optimal doping limit. We further remark that our approach of treating both SC and CO on equal footing and using realistic bandstructures is the first attempt to make such exact analysis in the high-temperature superconductivity field. All theoretical fittings by others to date have either taken CO as perturbation to SC or ignored CO altogether.

The density-wave orders considered are particle-hole excitations; therefore, the condition $\xi_{\mathbf{k}}\xi_{(\mathbf{k}+\mathbf{Q})} < 0$ must be employed in our numerical model to ensure particle-hole pairing. Additionally, we restrict the CO excitations to obey $\mid \xi_{\mathbf{k}} \mid \simeq \mid \xi_{\mathbf{k}+\mathbf{Q}} \mid$, and we expect this condition to be an accurate expression for modeling the low-energy excitations near the Fermi surface. The values of $\xi_{\mathbf{k}}$ are determined by the bandstructure of each cuprate modeled, and we use realistic bandstructures based on results from the literature for all fittings[177, 178, 179]. Using H_{MF}, the bare Green's function $G_0(\mathbf{k},\omega)$ is given by

$$G_0^{-1} = \omega I - H_0 = \begin{pmatrix} \omega - \xi_{\mathbf{k}} + i\Gamma_k & \Delta_k & V_{CO} & 0 \\ \Delta_k & \omega + \xi_{\mathbf{k}} + i\Gamma_k & 0 & -V_{CO} \\ V_{CO} & 0 & \omega - \xi_{\mathbf{k}+\mathbf{Q}} + i\Gamma_k & \Delta_k \\ 0 & -V_{CO} & \Delta_k & \omega + \xi_{\mathbf{k}+\mathbf{Q}} + i\Gamma_k \end{pmatrix}, \qquad (7.1)$$

where I denotes the (4×4) unit matrix and $\Gamma_k \simeq \Gamma_{|\mathbf{k}+\mathbf{Q}} \mid$ is the linewidth of the spectral density function due to finite quasiparticle lifetimes. The linewidth may depend on disorder and the interactions of quasiparticles with bosonic modes, and therefore is a function of angle θ_k in general. The bare Green's function may be used to calculate the mean-field spectral density function

$A(\mathbf{k},\omega) \equiv -\mathrm{Im}\left[G_0(\mathbf{k},\omega)\right]/\pi$ and the DOS, $\mathcal{N}(\omega) \equiv \sum_{\mathbf{k}} A(\mathbf{k},\omega)$. The former may be directly compared with ARPES data, and the latter with quasiparticle tunneling spectra.

In addition to modeling mean-field behavior using the bare Green's function, we may also model the quantum fluctuations between SC and CO by incorporating phase fluctuations in the SC order parameter $\Delta(\mathbf{r}) = |\Delta(\mathbf{r})|\, e^{i\theta(\mathbf{r})}$. In order to calculate the modified spectral density function and quasiparticle DOS, we need to develop the low-energy effective theory to describe this scenario and deduce the full Green's function. To begin, we utilize the formalism of Ref. [180] to couple the quasiparticles to the phase field, $\theta(\mathbf{r})$, and gauge transform the fermion operators according to $c_\sigma(\mathbf{r}) \rightarrow c_\sigma(\mathbf{r})e^{i\theta(\mathbf{r})/2}$. We then integrate out the degrees of freedom with momentum larger than ξ_{SC}^{-1}, where ξ_{SC} is the superconducting coherence length, so that we are left with the low-energy effective theory [181]. The low-energy effective theory incorporates the mean-field theory of coexisting SC and CO, the Gaussian theory of the phase fluctuations, and the coupling between the two orders [180]:

$$\begin{aligned} \mathcal{H}_{eff} &= \mathcal{H}_0 + \mathcal{H}_I, \\ \mathcal{H}_0 &= \mathcal{H}_{MF} + \tfrac{1}{2}\textstyle\sum_{\mathbf{q}} \frac{n_f}{4m}\mathbf{q}^2\theta(\mathbf{q})\theta(-\mathbf{q}), \\ \mathcal{H}_I &= \textstyle\sum_{\mathbf{k},\mathbf{q},\sigma} m\mathbf{v}(\mathbf{k})\cdot\mathbf{v}_s(\mathbf{q})c^\dagger_{\mathbf{k}+\mathbf{q},\sigma}c_{\mathbf{k},\sigma}. \end{aligned} \tag{7.2}$$

Here m is the free electron mass, $\mathbf{v}(\mathbf{k}) = \nabla_{\mathbf{k}}\xi_{\mathbf{k}}/\hbar$ is the normal-state group velocity, and $\mathbf{v}_s = \int d^2re^{-i\mathbf{q}\cdot\mathbf{r}}\nabla\theta(\mathbf{r})/2m$ is the superfluid velocity. We may express the interacting Hamiltonian in the basis, Ψ, using $\mathcal{H}_I = \sum_{\mathbf{k},\mathbf{q}} \Psi^{\dagger}_{\mathbf{k},\mathbf{Q}}\, H_I(\mathbf{k},\mathbf{q})\, \Psi_{\mathbf{k},\mathbf{Q}}$ with

$$\begin{aligned} H_I &\propto \begin{pmatrix} i\theta_{\mathbf{q}}\, \mathbf{q}\cdot\nabla_{\mathbf{k}}\xi_{\mathbf{k}} & 0 & 0 & 0 \\ 0 & i\theta_{\mathbf{q}}\, \mathbf{q}\cdot\nabla_{\mathbf{k}}\xi_{\mathbf{k}} & 0 & 0 \\ 0 & 0 & i\theta_{\mathbf{q}}\, \mathbf{q}\cdot\nabla_{\mathbf{k}}\xi_{\mathbf{k}+\mathbf{Q}} & 0 \\ 0 & 0 & 0 & i\theta_{\mathbf{q}}\, \mathbf{q}\cdot\nabla_{\mathbf{k}}\xi_{\mathbf{k}+\mathbf{Q}} \end{pmatrix} \\ &\approx i\theta_{\mathbf{q}}\, \mathbf{q}\cdot\nabla_{\mathbf{k}}\xi_{\mathbf{k}} \begin{pmatrix} 1 & 0 & 0 & 0 \\ 0 & 1 & 0 & 0 \\ 0 & 0 & -1 & 0 \\ 0 & 0 & 0 & -1 \end{pmatrix}. \end{aligned} \tag{7.3}$$

We have explicitly used the condition $|\,\xi_{\mathbf{k}}\,|=|\,\xi_{\mathbf{k}+\mathbf{Q}}\,|$ to simplify Eq. 7.3.

The proper self-energy from Eq. 7.3 is:

$$\begin{aligned} \Sigma^*(\mathbf{k}) &= \textstyle\sum_{\mathbf{q}} H_I(\mathbf{k},\mathbf{q}) G(\mathbf{k}+\mathbf{q},\omega) H_I(\mathbf{k}+\mathbf{q},-\mathbf{q}) \\ &= \textstyle\sum_{\mathbf{q}} \frac{1}{16}\, \langle\theta_{\mathbf{q}}\theta_{-\mathbf{q}}\rangle\, (\mathbf{q}\cdot\nabla_{\mathbf{k}}\xi_{\mathbf{k}})(\mathbf{q}\cdot\nabla_{\mathbf{k}}\xi_{\mathbf{k}+\mathbf{q}}) \begin{pmatrix} G_{11}(\mathbf{k}+\mathbf{q},\omega) & -G_{12}(\mathbf{k}+\mathbf{q},\omega) \\ -G_{21}(\mathbf{k}+\mathbf{q},\omega) & G_{22}(\mathbf{k}+\mathbf{q},\omega) \end{pmatrix}, \end{aligned} \tag{7.4}$$

where $G_{ij}(\mathbf{k},\omega)$'s are the (2×2) matrices composing the full Green's function

$$G(\mathbf{k},\omega) = \begin{pmatrix} G_{11}(\mathbf{k},\omega) & -G_{12}(\mathbf{k},\omega) \\ -G_{21}(\mathbf{k},\omega) & G_{22}(\mathbf{k},\omega), \end{pmatrix}.$$

For the scenario of T = 0 and H = 0, we include the longitudinal phase fluctuations and ignore the transverse phase fluctuations in the phenomenological SC/CO model because transverse phase fluctuations are completely suppressed at T = 0. Following the technique of Ref. [182], the sum over an infinite series of ring diagrams determines the phase field correlation function $\langle\theta_{\mathbf{q}}\theta_{-\mathbf{q}}\rangle$ in Eq. 7.4, and the result is given by

$$\langle\theta_{\mathbf{q}}\theta_{-\mathbf{q}}\rangle \approx \frac{4m\,\omega_p}{\hbar\, n_s^{2D}\,\Omega}\,\frac{1}{q^2}, \tag{7.5}$$

where n_s^{2D} the two-dimensional superfluid density, ω_p the plasma frequency, and Ω the sample volume.

After determining the proper self-energy by using Eq. 7.5 in Eq. 7.4, we may incorporate the bare Green's function and the proper self-energy together in Dyson's equation to self-consistently determine the full Green's function, $G(\mathbf{k},\omega)$. Using Dyson's equation, the full Green's function is:

$$\begin{aligned} G^{-1}(\mathbf{k},\tilde{\omega}) &= G_0^{-1}(\mathbf{k},\omega) - \Sigma^* \\ &= G_0^{-1}(\mathbf{k},\omega) - \eta \textstyle\sum_{\mathbf{q}} \frac{1}{q^2} \left(\mathbf{q}\cdot\nabla_{\mathbf{k}}\xi_{\mathbf{k}}\right)\left(\mathbf{q}\cdot\nabla_{\mathbf{k}}\xi_{\mathbf{k+q}}\right) \begin{pmatrix} G_{11}(\mathbf{k+q},\tilde{\omega}) & -G_{12}(\mathbf{k+q},\tilde{\omega}) \\ -G_{21}(\mathbf{k+q},\tilde{\omega}) & G_{22}(\mathbf{k+q},\tilde{\omega}) \end{pmatrix} \\ &= \begin{pmatrix} \tilde{\omega}-\tilde{\xi}_{\mathbf{k}}+i\tilde{\Gamma}_k & \tilde{\Delta}_k & \tilde{V}_{CO} & 0 \\ \tilde{\Delta}_k & \tilde{\omega}+\tilde{\xi}_{\mathbf{k}}+i\tilde{\Gamma}_k & 0 & -\tilde{V}_{CO} \\ \tilde{V}_{CO} & 0 & \tilde{\omega}-\tilde{\xi}_{\mathbf{k+Q}}+i\tilde{\Gamma}_k & \tilde{\Delta}_k \\ 0 & -\tilde{V}_{CO} & \tilde{\Delta}_k & \tilde{\omega}+\tilde{\xi}_{\mathbf{k+Q}}+i\tilde{\Gamma}_k \end{pmatrix}. \end{aligned} \tag{7.6}$$

The parameters $\tilde{\omega}$, $\tilde{\Delta}_k$, $\tilde{V}_{CO}$, $\tilde{\xi}_{\mathbf{k}}$, and $\tilde{\Gamma}_k$ denote the quasiparticle energy, the superconducting gap energy, the competing order energy, the normal-state energy, and the linewidth renormalized by the phase fluctuations, respectively. The parameter $\eta \equiv m\omega_p/4\hbar n_s^{2D}\Omega q^2$ in Eq. 7.6 indicates the strength of quantum phase fluctuations between SC and CO. The renormalized parameters $\tilde{\omega}$, $\tilde{\Delta}_k$, $\tilde{V}_{CO}$, $\tilde{\xi}_{\mathbf{k}}$, and $\tilde{\Gamma}_k$ are solved self-consistently, and we utilize an iterative method to determine the solutions.

If we diagonalize the Hamiltonian prior to insertion into the Green's function formula, then Dyson's equation may be put into a simple self-consistent format. The problem encountered by diagonalizing the Hamiltonian is that the renormalization of $\tilde{\omega}$, $\tilde{\Delta}_k$, $\tilde{V}_{CO}$, $\tilde{\xi}_{\mathbf{k}}$, and $\tilde{\Gamma}_k$ by phase fluctuations becomes difficult to investigate in a simple analytical form for numerical simulations. A method to preserve simple self-consistent formulas for the renormalized parameters and to make the Dyson's equation self-consistent among the parameters is to add a linewidth term to each parameter in the Green's function, such that the inverse Green's function, $\mathrm{G}(\mathbf{k},\omega)^{-1}$, becomes

$$G(\mathbf{k},\omega)^{-1} \equiv \begin{pmatrix} \tilde{\omega}+i\tilde{\Gamma}_k-\tilde{\xi}_{\mathbf{k}}-i\tilde{\xi}'_{\mathbf{k}} & \tilde{\Delta}_k+i\tilde{\Delta}'_k & \tilde{V}_{CO}+i\tilde{V}'_{CO} & 0 \\ \tilde{\Delta}_k+i\tilde{\Delta}'_k & \tilde{\omega}+i\tilde{\Gamma}_k+\tilde{\xi}_{\mathbf{k}}+i\tilde{\xi}'_{\mathbf{k}} & 0 & -\tilde{V}_{CO}-i\tilde{V}'_{CO} \\ \tilde{V}_{CO}+i\tilde{V}'_{CO} & 0 & \tilde{\omega}+i\tilde{\Gamma}_k+\tilde{\xi}_{\mathbf{k}}+i\tilde{\xi}'_{\mathbf{k}} & \tilde{\Delta}_k+i\tilde{\Delta}'_k \\ 0 & -\tilde{V}_{CO}-i\tilde{V}'_{CO} & \tilde{\Delta}_k+i\tilde{\Delta}'_k & \tilde{\omega}+i\tilde{\Gamma}_k-\tilde{\xi}_{\mathbf{k}}-i\tilde{\xi}'_{\mathbf{k}} \end{pmatrix}, \tag{7.7}$$

where a prime denotes the linewidth of a given parameter, and we have explicitly used the conditions $\xi_{\mathbf{k}}\xi_{(\mathbf{k+Q})} < 0$ and $\mid \xi_{\mathbf{k}} \mid = \mid \xi_{\mathbf{k+Q}} \mid$, as well as $\Delta_{|\mathbf{k+Q}|} = \Delta_k$ (valid for CDW or pinned SDW in the example Green's function treatment considered here), to simplify Eq. 7.7. Using this notation, we may obtain G_0^{-1} for a self-consistent solution of Eq. 7.6 by substituting the parameter $\tilde{x}$ with the bare parameter x in Eq. 7.7 (e.g. $\tilde{\omega} \rightarrow \omega$).

To simplify the entire set of self-consistent equations that result from using $\mathrm{G}(\mathbf{k},\omega)^{-1}$ and $\mathrm{G}(\mathbf{k},\omega)_0^{-1}$ in Eq. 7.6, we define some simplifying functions and notation. First, we define the entire set of parameters in $\mathrm{G}(\mathbf{k},\omega)_0^{-1}$ as $p_k = (\omega, \Gamma_k, \xi_{\mathbf{k}}, \xi'_{\mathbf{k}}, \Delta_k, \Delta'_k, V_{CO}, V'_{CO})$ and the parameters in $\mathrm{G}(\mathbf{k},\omega)^{-1}$ as $\tilde{p}_k = (\tilde{\omega}, \tilde{\Gamma}_k, \tilde{\xi}_{\mathbf{k}}, \tilde{\xi}'_{\mathbf{k}}, \tilde{\Delta}_k, \tilde{\Delta}'_k, \tilde{V}_{CO}, \tilde{V}'_{CO})$. Then, the first simplifying function we define is

$$n_1(p_k) = \omega^2 - \xi_{\mathbf{k}}^2 - \Delta_k^2 - V_{CO}^2 + \xi'^2_{\mathbf{k}} + \Delta'^2_k + V'^2_{CO} - \Gamma_k^2 \tag{7.8}$$

The second simplifying function is

$$n_2(p_k) = \Delta_k\Delta'_k + V_{CO}V'_{CO} + \xi_{\mathbf{k}}\xi'_{\mathbf{k}} - \Gamma_k\omega. \tag{7.9}$$

Using Eqs. 7.8 and 7.9 and the simplified notation, we may write the self-consistent solutions for the parameters by

$$\tilde{x} = x \pm \eta \sum_{\mathbf{q}} \frac{1}{q^2} \left(\mathbf{q}\cdot\nabla_{\mathbf{k}}\xi_{\mathbf{k}}\right)\left(\mathbf{q}\cdot\nabla_{\mathbf{k}}\xi_{\mathbf{k+q}}\right) \frac{\tilde{x}n_1(\tilde{p}_{k+q}) - 2\tilde{x}'n_2(\tilde{p}_{k+q})}{n_1(\tilde{p}_{k+q})^2 + 4n_2(\tilde{p}_{k+q})^2}, \tag{7.10}$$

and

$$\tilde{x}' = x' \pm \eta \sum_{\mathbf{q}} \frac{1}{q^2} \left(\mathbf{q} \cdot \nabla_{\mathbf{k}} \xi_{\mathbf{k}}\right) \left(\mathbf{q} \cdot \nabla_{\mathbf{k}} \xi_{\mathbf{k+q}}\right) \frac{\tilde{x}' n_1(\tilde{p}_{k+q}) + 2\tilde{x} n_2(\tilde{p}_{k+q})}{n_1(\tilde{p}_{k+q})^2 + 4n_2(\tilde{p}_{k+q})^2}. \tag{7.11}$$

Here, the variable $\tilde{x} = (\tilde{\omega}, \tilde{\Delta}_k, \tilde{\xi}_{\mathbf{k}}, \tilde{V}_{CO})$ applies to the unprimed parameters in $\tilde{p}_k$, while $\tilde{x}'$ applies to the primed parameters defined in $\tilde{p}_k$, and $\tilde{\omega}' = \tilde{\Gamma}_k$. The positive sign in Eq. 7.10 applies to $\tilde{x} = \tilde{\xi}_{\mathbf{k}}, \tilde{\Delta}_k$, and the negative sign applies to $\tilde{x} = \tilde{\omega}, \tilde{V}_{CO}$. Similarly, the positive sign in Eq. 7.11 applies to $\tilde{x}' = \tilde{\xi}'_{\mathbf{k}}, \tilde{\Delta}'_k$, and the negative sign applies to $\tilde{x}' = \tilde{\Gamma}'_k, \tilde{V}'_{CO}$. We use a bare value when $x' = \Gamma_k$ in Eq. 7.11, but we set $x' = 0$ otherwise. Using Eqs. 7.10 and 7.11, we solve for the set of parameters, $\tilde{p}_k$, using an iterative method.

For example, the equation for $\tilde{\omega}$ is given by:

$$\tilde{\omega} = \omega - \eta \sum_{\mathbf{q}} \frac{1}{q^2} \left(\mathbf{q} \cdot \nabla_{\mathbf{k}} \xi_{\mathbf{k}}\right) \left(\mathbf{q} \cdot \nabla_{\mathbf{k}} \xi_{\mathbf{k+q}}\right) \frac{\tilde{\omega} n_1(\tilde{p}_{k+q}) - 2\tilde{\Gamma}_k n_2(\tilde{p}_{k+q})}{n_1(\tilde{p}_{k+q})^2 + 4n_2(\tilde{p}_{k+q})^2}, \tag{7.12}$$

and we iteratively solve this equation using the following recurrence relation:

$$\tilde{\omega}_{m+1} = \omega - \eta \sum_{\mathbf{q}} \frac{1}{q^2} \left(\mathbf{q} \cdot \nabla_{\mathbf{k}} \xi_{\mathbf{k}}\right) \left(\mathbf{q} \cdot \nabla_{\mathbf{k}} \xi_{\mathbf{k+q}}\right) \frac{\tilde{\omega}_m n_1([\tilde{p}_{k+q}]_m) - 2(\tilde{\Gamma}_k)_m n_2([\tilde{p}_{k+q}]_m)}{n_1([\tilde{p}_{k+q}]_m)^2 + 4n_2([\tilde{p}_{k+q}]_m)^2}, \tag{7.13}$$

with $\omega_0 = \omega$ and m specifying the value of the m-th iteration. Numerically, the $\tilde{\omega}$ values are considered converged to their final value when $\mid \tilde{x}_{m+1} - \tilde{x}_m \mid < x_{crit}$, where x_{crit} is the criteria level for a general parameter, $\tilde{x}$. We required convergence such that $x_{crit} = 0.005$meV and $x'_{crit} = 0.005$meV.

Once we have determined all the renormalized parameters, we are left with the full Green's function and may use it to obtain the resulting spectral density function $A(\mathbf{k}, \tilde{\omega}) \equiv -\mathrm{Im}\left[G(\mathbf{k}, \tilde{\omega})\right]/\pi$ and the DOS $\mathcal{N}(\tilde{\omega}) \equiv \sum_{\mathbf{k}} A(\mathbf{k}, \tilde{\omega})$ that incorporate quantum phase fluctuations.

We find

$$\mid A(\mathbf{k}, \tilde{\omega}) \mid \equiv \frac{1}{\pi} \mid \frac{2(\tilde{\omega} + \tilde{\xi}_{\mathbf{k}}) n_2(\tilde{p}_k) + (\xi'_{\mathbf{k}} + \tilde{\Gamma}_k) n_1(\tilde{p}_k)}{n_1(\tilde{p}_k)^2 + 4n_2(\tilde{p}_k)^2} \mid . \tag{7.14}$$

With the spectral density function defined according to Eq. 7.14, quantum fluctuations are introduced into our numerical simulations by setting $\eta > 0$. The spectral weight using Eq. 7.14 is conserved, and we may use Eqs. 7.10 and 7.11 to investigate the evolution of $p_k \rightarrow \tilde{p}_k$ as quantum

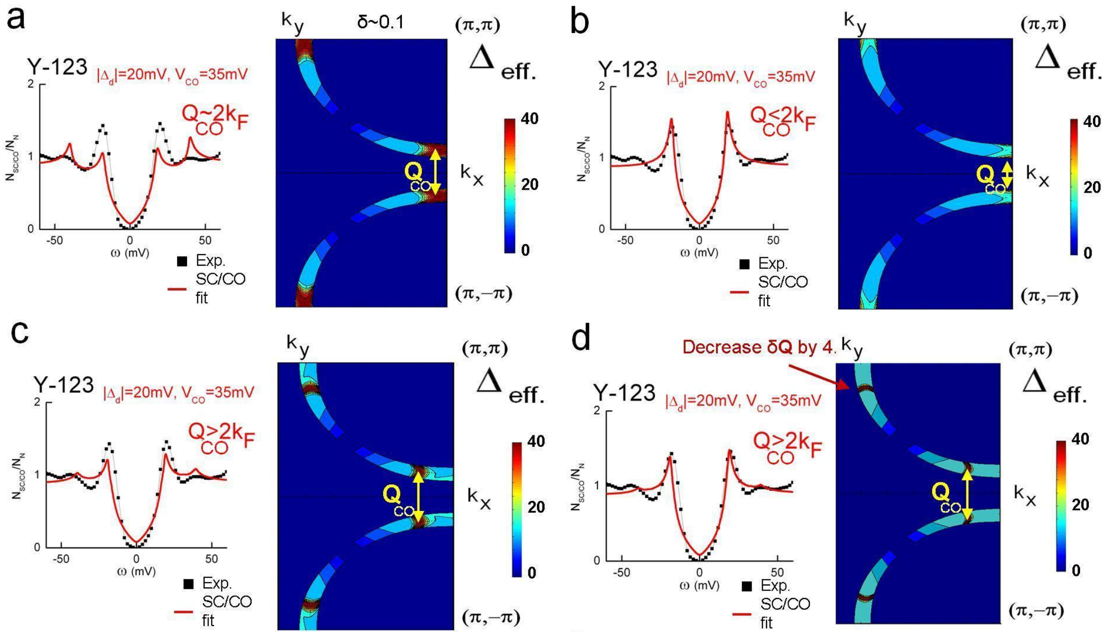

Figure 7.1: Schematic illustration of the effect of $\mathbf{Q}_{CO}$ and $\delta\mathbf{Q}$ on the coexisting SC/CO model. Left panels: Quasiparticle density of states spectra modeled by $\Delta_{SC} = \Delta_0 cos(2\theta_k)$ (Δ_0 = 20meV), V$_{CO,max}$=35meV (solid red lines). A representative quasiparticle density of states spectrum in Y-123 (symbols) from Ref. [35] is shown for comparison. Right panels: Plots of Δ_{eff}-vs.-$\mathbf{k}$ for the k$_x$ > 0 portion of the Brillouin zone in window of 100meV around the Fermi energy ($|\ \xi_{\mathbf{k}}\ |$<100meV). Values of $\mathbf{Q}_{CO}$ and $\delta\mathbf{Q}$ shown are: (a) $\mathbf{Q}_{CO} \sim 2k_F$, $\delta\mathbf{Q}$=0.2π, (b) $\mathbf{Q}_{CO} < 2k_F$, $\delta\mathbf{Q}$=0.2π, (c) $\mathbf{Q}_{CO} > 2k_F$, $\delta\mathbf{Q}$=0.2π, (d) $\mathbf{Q}_{CO} > 2k_F$, $\delta\mathbf{Q}$=0.05π.

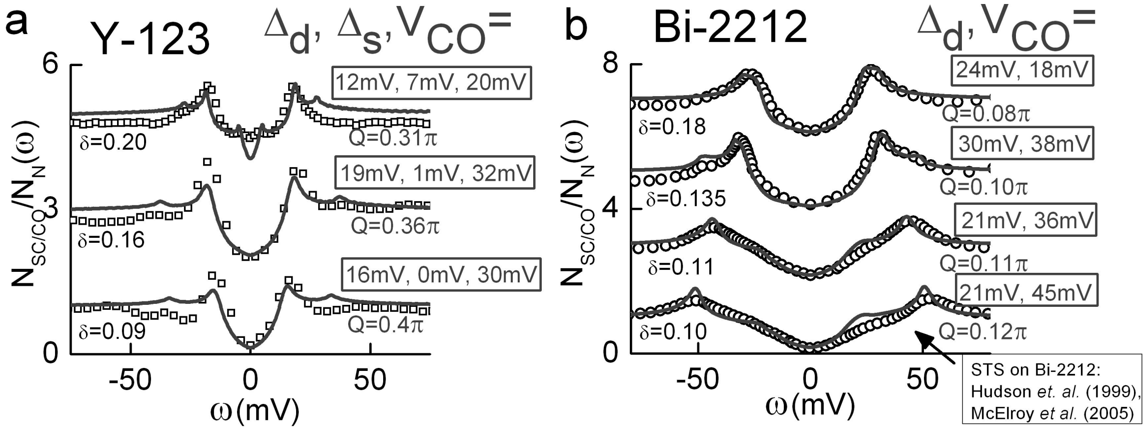

Figure 7.2: (a) Normalized c-axis quasiparticle tunneling spectra on Y-123 for different doping levels [35, 97] (symbols) with phenomenological fits using the SC/CO model (solid lines). The quasiparticle spectra for different doping levels are slightly offset for clarity. The fitting parameters of V$_{CO}$ and Δ_{SC} are nearly independent of fitting $\mathbf{Q}_{CO} \sim 2k_F$ to the bonding or anti-bonding bands. The $\mathbf{Q}_{CO}$-values shown approximately match the Fermi level of the bonding band. (b) Spatially averaged c-axis quasiparticle tunneling spectra on Bi-2212 (symbols) from Refs. [68, 100]) with phenomenological fits using the SC/CO model (solid lines). The $\mathbf{Q}_{CO}$-values shown match the Fermi level of the anti-bonding band. The doping levels listed here are determined by the bulk T$_C$ values from Ref. [68].

phase fluctuations increase in a straight-forward manner. The quasiparticle DOS is then obtained by plugging Eq. 7.14 into

$$N(\omega) = \sum_{\mathbf{k}} A(\mathbf{k}, \omega). \tag{7.15}$$

7.2 Results

For a given superconducting cuprate and the set of experimental ARPES and quasiparticle DOS data that we model using Eq. 7.14 and 7.15, we wish to obtain the parameters of the SC energy gap, Δ_{SC}, the CO energy, V$_{CO}$, the CO wavevector ($\mathbf{Q}_{CO}$), and the disorder of the wavevector ($\delta\mathbf{Q}$) to characterize the two coexisting orders. To perform a fit, we must determine the location and extent of the CO in reciprocal space within the first Brillouin zone to determine the region of coexistence with SC, and the relevant parameters are $\mathbf{Q}_{CO}$ and $\delta\mathbf{Q}$. These two parameters couple with the electronic bandstructure, $\xi_{\mathbf{k}}$, and the conditions $\xi_{\mathbf{k}}\xi_{\mathbf{k+Q}} < 0$ and $\mid \xi_{\mathbf{k}} \mid \simeq \mid \xi_{\mathbf{k+Q}} \mid$ to specify the region associated with the CO. Empirically, $\mathbf{Q}_{CO}$ and $\delta\mathbf{Q}$ also determine the location of the diffraction modes observed in FT-LDOS data and the size of the diffraction modes respectively. We model $\mathbf{Q}_{CO}$ and $\delta\mathbf{Q}$ using a Gaussian distribution for simplicity, so that $\mathbf{Q}_{CO}$ is the mean-value and $\delta\mathbf{Q}$ is the standard deviation according to

$$V_{CO}(\mathbf{k}) = V_{CO} \exp\left(-\frac{(\mathbf{Q}-\mathbf{Q}_{CO})^2}{2\delta\mathbf{Q}^2}\right). \tag{7.16}$$

The region where SC and COs coexist exhibits an effective gap, given by $\Delta_{eff}^2(\mathbf{k}) = \Delta_{SC}^2(\mathbf{k})+\mathrm{V}_{CO}(\mathbf{k})^2$. For $\mathrm{V}_{CO} > \Delta_{SC}$, we expect to observe two features in quasiparticle DOS spectra because these two energies are the poles of the Green's function. We expect a gap determined by $\Delta_{SC}(\mathbf{k})$, from regions in reciprocal space where $\mathrm{V}_{CO} \sim 0$, and a gap determined by $\Delta_{eff}(\mathbf{k}) > \Delta_{SC}$, in regions of reciprocal space where $\mathrm{V}_{CO}(\mathbf{k}) \sim \mathrm{V}_{CO}$. For the case $\mathrm{V}_{CO} < \Delta_{SC}$, we expect to find a single gap in DOS measurements determined by $\Delta_{eff}(k)$ since $\Delta_{eff} \simeq \Delta_{SC}$ throughout reciprocal space. We may, however, still distinguish Δ_{SC} from V_{CO} from ARPES measurements by fitting Δ_{eff} as a function of $\mathbf{k}$ or θ_k. An illustration of the effects of varying $\mathbf{Q}_{CO}$ and $\delta\mathbf{Q}$ is shown in Fig. 7.1.

In addition to affecting the size of the diffraction modes in FT-LDOS maps, the value of $\delta\mathbf{Q}$ will affect the length of the Fermi arcs if the CO persists above T_C. We assume that the relevant transition temperature for the CO is given by the pseudogap temperature T* and that the CO develops a correlation length, ξ_{CO} below T*, similar to the development of a superconducting coherence length, ξ_{SC} below T_C. We find that $\delta\mathbf{Q}$ is finite below T*, and we attribute this observation to the fact that CO's interact with disorder such that $\mathbf{Q}_{CO}$ is broadened for $\mathrm{T} < \mathrm{T}_C$. For a second order phase transition at T*, we expect $\delta\mathbf{Q}(\mathrm{T}) = \delta\mathbf{Q}(0)(1\text{-}T/T^*)^{\nu}$, where ν is a critical exponent. The fact that $\delta\mathbf{Q}(\mathrm{T})$ decreases as T increases implies a weakened disorder pinning potential for the CO as T increases.

We may characterize the relevant types of COs needed to fit experimental data on hole-and electron-type cuprates. We use the values of $\mathbf{Q}_{CO}$ for CDWs, DDWs, and SDWs that are valid from empirical observations to deduce the relevant COs. For the hole-type cuprates, the dichotomy of quasiparticle lifetimes [7, 183, 184] and the presence of an enhanced gap [6] near the anti-nodal, or

(0,$\pm\pi$)/($\pm\pi$,0) regions of the Brillouin zone suggest that a CO exists near this region of reciprocal space. Further, neutron scattering indicates the presence of incommensurate spin correlations along the Cu-O bonding direction in hole-type cuprates [13, 14, 15]. Therefore, we do not expect the value of $\mathbf{Q}_{CO}$ to be commensurate with the lattice structure, and we expect $\mathbf{Q}_{CO}$ will be along the bonding direction in hole-type cuprates. In contrast, the presence of a non-monotonic gap in momentum [41], reaching maximum between the anti-nodal and nodal regions of the reciprocal space, in the one-layer electron-type cuprate $Pr_{0.89}LaCe_{0.11}CuO_4$ (PLCCO) [41] suggests the existence of a CO with a momentum dependence of the energy gap differing from that of the $d_{x^2-y^2}$-wave SC gap . Additionally, neutron scattering has observed commensurate spin excitations in the one-layer electron-type cuprates [9, 12] so that we may expect that $\mathbf{Q}_{CO}$ will be commensurate with the lattice structure in electron-type cuprates and resemble the wavevector of spin excitations in PLCCO.

To differentiate among the possible COs quantitatively, we first examine the quasiparticle excitation spectra in the hole-type cuprates Bi-2212 and Y-123. The hole-type cuprates Bi-2212 and Y-123 exhibit satellite features in the $T \ll T_C$ experimental quasiparticle DOS most notably in underdoped and optimally doped data. Representative Bi-2212 [68, 100] and Y-123 [35, 97] quasiparticle tunneling data for $T \ll T_C$ displaying satellite features are shown in Fig. 7.2, along with fits to the data using the SC/CO model to be discussed more fully below. The fact that satellite features are observed in Y-123 implies that $V_{CO} > \Delta_{SC}$ because we observe features in the tunneling spectra at both $\omega = \pm\Delta_{SC}$ and $\omega = \pm\Delta_{eff} = \pm\sqrt{\Delta_{SC}^2 + V_{CO}^2}$. Additionally, the underdoped Bi-2212 data show rounded pseudogap-like peaks at high energies and kink-like structure at low energies, and, as we will discuss later, the kink-like features may be attributed to Δ_{SC}, while the rounded peaks arise from Δ_{eff}.

We now consider which COs may exhibit significant gapped quasiparticle spectra to account for the features in the hole-type cuprates. For direct SDW and DDW, the value of the CO wavevector is given by $\mathbf{Q}_{CO} = (\pm\pi, \pm\pi)$. In contrast, disorder pinned SDW and CDW exhibit incommensurate values of $\mathbf{Q}_{CO}$ along the Cu-O bonding direction with $\mid Q_{CO} \mid\sim 2k_F$. Due to the fact that an enhanced gap is observed near the anti-node in hole-type cuprates, we select $\mathbf{Q}_{CO}$ for CDW of

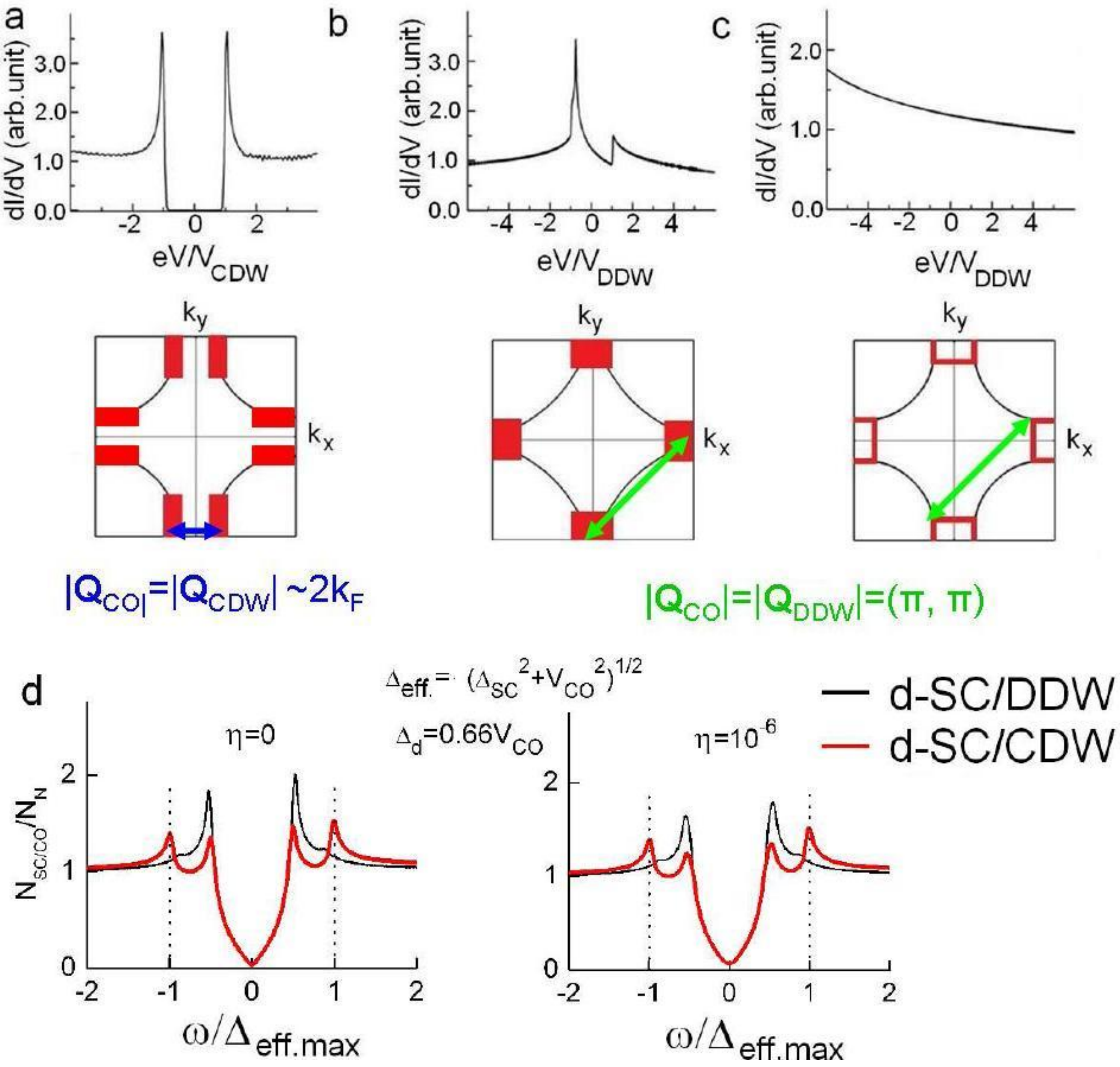

Figure 7.3: Comparison of the expected contribution to the quasiparticle excitation spectra of CDW and DDW in hole-type cuprates using a one-band approximation: (a) Quasiparticle excitation spectra expected from CDW alone in an optimally doped hole-type cuprate. The reciprocal phase space associated with the CDW in the first Brillouin zone is shown (red bars) in the lower panel. Additionally, $\mathbf{Q}_{CO} \sim 2k_F$ is shown in the lower panel is representative of $\mathbf{Q}_{CO}$ for disorder pinned SDW or CDW. (b) Quasiparticle excitation spectra expected from DDW alone under a nearly nested condition [185]. The reciprocal phase space associated with DDW in the first Brillouin zone is shown (red rectangles) in the lower panel. The nearly nested condition does not constitute a realistic bandstructure for doped cuprates. Additionally, $\mathbf{Q}_{CO} = (\pi, \pi)$ is shown in the lower panel is representative of $\mathbf{Q}_{CO}$ for direct SDW or DDW. (c) Quasiparticle excitation spectra expected from DDW in an optimally doped hole-type cuprate with a realistic bandstructure [178]. The Fermi surface shown in the lower panel reveals a narrow reciprocal phase space associated with the DDW (red lines). The absence of gapped quasiparticle DOS due to DDW was also discussed in Ref. [185]. (d) Representative simulations of the quasiparticle excitation spectra for coexisting d-SC/DDW and d-SC/CDW for $\eta = 0$ (left) and $\eta = 10^{-6}$ (right).

disorder-pinned SDW to coincide with the Fermi surface separation ($\sim 2k_F$) near the anti-nodal regions, as illustrated in Fig. 7.3a. We compare CDW and DDW to determine whether $\mathbf{Q}_{CO} = (\pm\pi, \pm\pi)$ or a value of $\mathbf{Q}_{CO}$ along the Cu-O bonding direction better accounts for experimental observations. (The results for a CDW are equally valid for a disorder pinned SDW, except that $2\mathbf{Q}_{SDW}$=$\mathbf{Q}_{CDW}$ [86]. Additionally, a direct SDW has a wavevector $\mathbf{Q}_{CO}$=(π, π), according to neutron scattering experiments, similar to that of DDW.)

The results of comparison among CDW and DDW are illustrated in Fig. 7.3, where we have assumed $\Delta_{SC} = 0$ to determine which competing orders will exhibit significant gapped quasiparticle spectra to account for empirical results in hole-type Y-123 and Bi-2212. Figure 7.3a shows the resulting quasiparticle DOS for a CDW along the Cu-O bonding direction, revealing sharp peaks in the spectra at $\omega = \pm V_{CO} = \pm V_{CDW}$. We have used a single realistic bandstructure, equivalent to the bonding band in Bi-2212 from Ref. [178], and $\mathbf{Q}_{CO}$ as illustrated below Fig. 7.3a. In Fig. 7.3b, we illustrate the scenario for a DDW under a nearly nested condition [186] condition of the Fermi surface, which reveals sharp peaks at $\omega = \pm V_{CO} = \pm V_{DDW}$. However, we note that the nearly nested condition is not a realistic bandstructure for doped hole-type cuprates because it is in the insulating limit. We then compare the scenario of DDW using a realistic bandstructure in Fig. 7.3c, which shows no features in the quasiparticle spectra due to the limited phase space associated with DDW near the Fermi surface. Finally, we illustrate in Fig.7.2d, the scenarios of coexisting SC/CDW and SC/DDW with and without quantum fluctuations to approximately reproduce the T $\ll$ T$_C$ spectra in hole-type cuprates.

From Fig. 7.3d, we see qualitatively that the coherence peaks and satellite features in Y-123 and the rounded peaks and kinks in Bi-2212 will be difficult to reproduce with a DDW (or direct SDW) because of the limited phase space associated with DDW. In contrast, we find that the features associated with coexisting SC/CDW may be able to reproduce observations of coherence peaks and satellite features in Y-123 and rounded peaks and kink-like low-energy features in Bi-2212, as in Fig 7.2. As a side note, it is possible that the antibonding bands in Y-123 and Bi-2212 may reproduce the nearly nested condition [178] necessary for DDW. However, theoretical two-leg ladder

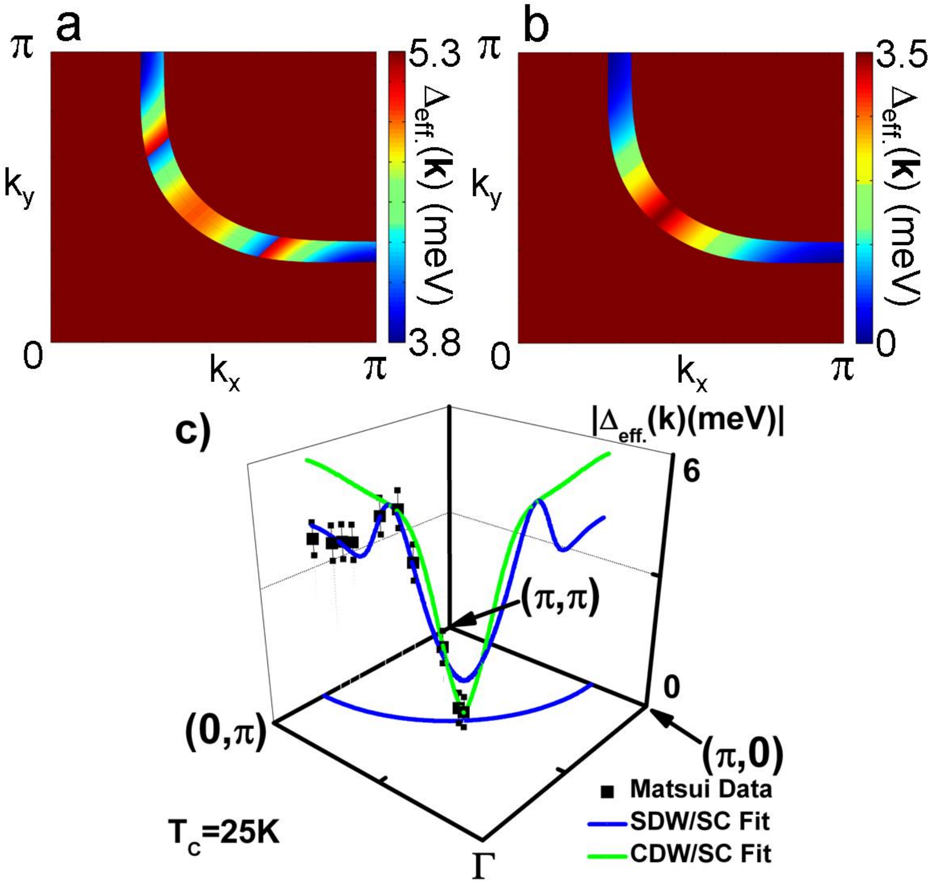

Figure 7.4: Phenomenological SC/CO simulation of Δ_{eff}(k) in the first quadrant of the Brillouin zone of PLCCO at (a) T = 0 and (b) T = 0.9 T_C in a $|\ \xi_{\mathbf{k}}\ | < 75$meV window. (c) The non-monotonic gap observed from momentum dependent ARPES leading edge data (×2) from Ref. [41] are shown as a function of $\phi \equiv \tan^{-1}$(ky/kx) as solid symbols with uncertainties. The phenomenological fit, Δ_{eff}-vs.-θ_k, using COs of CDWs and direct SDWs [176]. For the fits, we assume isotropic Gaussian shapes for both $V_{CO} = V_{CDW}$(k) and V_{SDW}(k) defined by $\mathbf{Q}_{CO}$ and $\delta\mathbf{Q}$. The SDW is fit is shown as a blue line and uses $\mathbf{Q}_{CO} = (\pi, \pi)$, while the CDW is shown as a green line with $\mathbf{Q}_{CO} \parallel (\pi,0)/(0,\pi)$. The SDW fit with $\mathbf{Q}_{CO} = (\pi, \pi)$ more accurately reproduces the ARPES data. The revelation of commensurate SDW fit agrees with the observation of commensurate spin excitations in one-layer electron-type cuprates [12].

simulations appear [187] to rule out DDW as a relevant coexisting CO with SC. Based on these results, we find that disorder-pinned SDWs or CDWs can produce quasiparticle spectra for T $\ll$ T$_C$ consistent with experimental quasiparticle DOS in hole-type cuprates, and it is unlikely that DDWs reproduce empirical observations in hole-type cuprates.

To investigate the scenario in the electron-type cuprates, we cannot rely on discerning two gaps from quasiparticle tunneling DOS data; therefore, we must rely upon results from ARPES to attempt to distinguish among possible relevant COs. To discern the relevant COs, we attempt to fit the non-monontic momentum-dependent gap observed in the one-layer electron-type PLCCO from ARPES measurements [41]. The ARPES measurements of the effective gap are shown in Fig. 7.4c as solid symbols and are based on the leading gap edge ($\times 2$) at the Fermi surface as a function of angle θ_k [41]. Using the values of $\xi_{\mathbf{k}}$ for an electron-type cuprate and the conditions $\xi_{\mathbf{k}}\xi_{(\mathbf{k}+\mathbf{Q})} < 0$ and $\mid \xi_{\mathbf{k}} \mid \simeq \mid \xi_{\mathbf{k}+\mathbf{Q}} \mid$, we generate the values of Δ_{eff}-vs.-θ_k for d-wave SC and either a CDW or a direct SDW in order to differentiate between $\mathbf{Q}_{SDW} = (\pi, \pi)$ or $\mathbf{Q}_{CDW}$ along the Cu-O bonding direction. The results of $\Delta_{eff}(k)$-vs.-θ_k from our simulations are compared with ARPES data for PLCCO in Fig. 7.4c, with SC/CDW as a green line, SC/SDW as a blue line, and the data as black solid symbols. We have used the values, $\Delta_{SC} = 5.5$meV and V$_{CO}$ = 4.2meV. Clearly, the case of a direct SDW fits the experimental observation much better than the case of a CDW. Additionally, this result agrees with the observations in one-layer electron-type cuprates from neutron scattering that show spin collective excitations are commensurate with the lattice and the SDW gap is smaller than the SC gap [9, 12].

In addition to fitting the non-monotonic d-wave gap in PLCCO, we consider the generation of Δ_{eff}-vs.-θ_k in a window of energies $\mid \xi_{\mathbf{k}} \mid < 75$meV in Figs. 7.4a and 7.4b for T = 0 and T = 0.9T$_C$. We show only one quadrant of the Brillouin zone in Figs. 7.4a and 7.4b, as the same results are reproduced in all four quadrants. We assume that both the SC and CO energies follow a BCS-like temperature dependence, and for the case of T = 0.9T$_C$ and with $\Delta_{SC}(T = 0) = 5.5$meV and V$_{CO}(T = 0)$=4.2meV, we expect that the CO will be absent and that SC will remain. Thus, we may account for the observation of a non-monotonic gap from ARPES measurements for T $\ll$ T$_C$

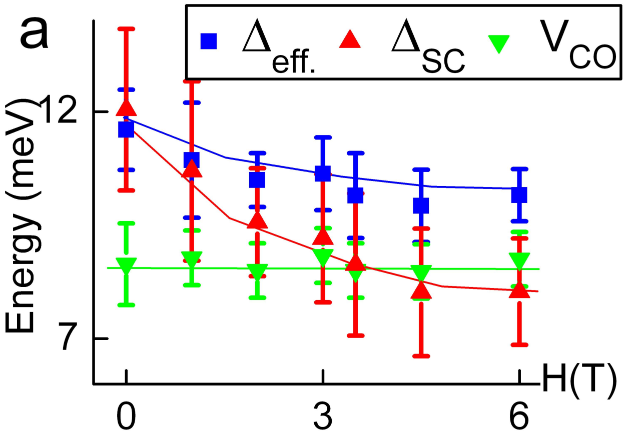

Figure 7.5: Magnetic field evolution of the SC/CO characteristic energies Δ_{eff}, Δ_{SC} and V_{CO} for H = 1, 2, 3, 3.5, 4.5 and 6 T determined from the histograms in Fig. 4.10a. The histograms in Fig. 4.10a were fit with a Lorentzian functional form, and the peak position of the fit determines the location of Δ_{eff} (H) in this figure. The low-energy cutoff of each histogram empirically determines V_{CO}. Finally, the SC gap at each field is defined as $\Delta_{SC}(H) = \frac{\sqrt{\Delta_{eff}^2 - V_{CO}^2}}{cos(2\phi_{AF})}$, where $\phi_{AF} = 25^o$ is an angle associated with the antiferromagnetic hot spots [41]. From the data, we found that V_{CO} was nearly constant as a function of H, and Δ_{SC}(H) decreased with increasing H. The values of Δ_{SC} and V_{CO} become comparable for H ≥ 6T, implying increasing difficulty in achieving contrast of vortices using r_G (Eq. 4.1).

and the absence of either a pseudogap or the Fermi arc in electron-type cuprates above T_C using a direct SDW instead of incommensurate pinned SDW or CDW for the CO, if the CO follows a BCS-like temperature dependence.

To this point, we find that disorder pinned SDW or CDW with $\mathbf{Q}_{CO}$ along the Cu-O bonding direction seem to be the best candidates for fitting hole-type experimental data using our model. In contrast, based on our PLCCO fitting and results from neutron scattering, the electron-type cuprates are best fit by a direct SDW for the CO with commensurate $\mathbf{Q}_{CO} =(\pm\pi, \pm\pi)$ along the nodal direction.

Now that we have established the relevant COs for hole- and electron-type cuprates, we proceed to quantitatively fit experimental quasiparticle DOS. We have already seen in Chapters 4 and 5, that our model of SC and CO may be used to fit the quasiparticle spectra in La-112 and Y-123. Now that we have developed our formalism, we may discuss parameters needed to fit the T ≪ T_C data, shown in Figs. 4.4a and 5.2 for La-112 and Y-123, respectively, in more detail.

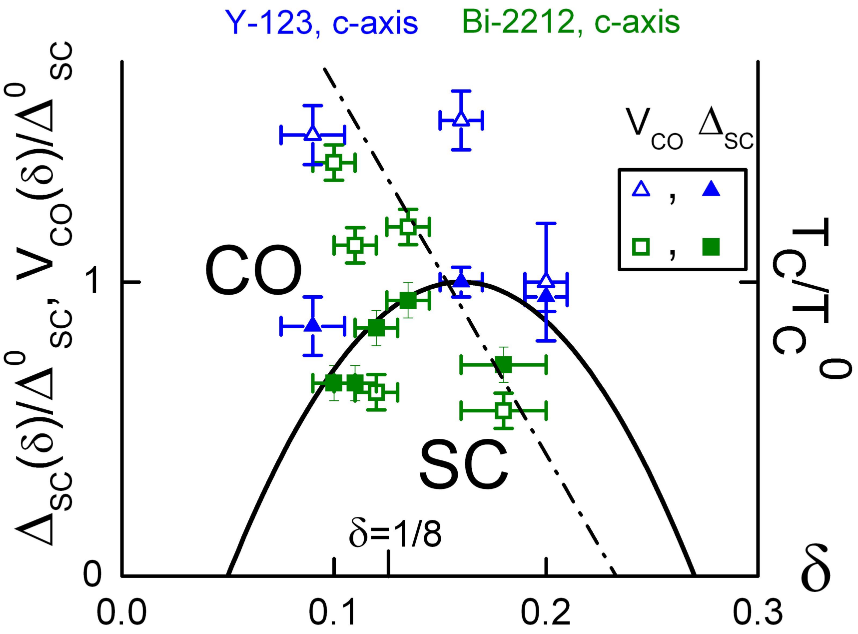

Figure 7.6: Doping dependence of Δ_{SC}, V_{CO} and T_C in the hole-type cuprates Y-123 (blue triangles) and Bi-2212 (green squares). The values of Δ_{SC} and V_{CO} are normalized to the SC gaps at optimal doping, Δ^0_{SC} for Y-123 and Bi-2212, and T_C is normalized to the optimal doping value, T_C^0. The solid black line represents $T_C(\delta)$ normalized to T_C^0, and the dashed line is a guide to the eye. Here, we use the empirical relation $T_C(\delta) = T_C^0(1\text{-}82.6(\delta\text{-}0.16)^2)$ to define the black line.

For Y-123, we fit our experimental quasiparticle spectra, as shown in Fig. 5.2, using coexisting CDW and d-wave or (d+s)-wave SC, with $\mathbf{Q}_{CO} = [\pm(0.25 \pm 0.05)\pi, 0]$ and $[0, (\pm0.25 \pm 0.05)\pi]$ and $\delta\mathbf{Q}= 0.03\pi$. We find that d-wave or (d+s)-wave may account for the experimental quasiparticle spectra due to the orthorhombicity of Y-123. As has been seen from previous experiments in our group [35], the quasiparticle spectra in Y-123 shows evidence for an s-wave component that significantly increases in percentage compared to the dominant d-wave component at or near optimal doping. Therefore, an assumption of d-wave or (d+s)-wave SC fitting in Y-123 near optimal doping is reasonable. For the fitting in Fig. 5.2, the s-wave component of Δ_{SC} is (2.0 ± 2.0)meV, and the maximum d-wave component is equal to $\Delta_{SC}(k = 0) = (18 \pm 2)$meV. The value of $V_{CO} = (32.0 \pm 1.5)$meV. The value of V_{CO} is equivalent to the value of $V_{PG} = (31.5 \pm 2)$meV observed in vortex cores in Y-123, suggesting that a CDW or disorder pinned SDW is revealed inside vortex cores in Y-123. Further, the model value of $\Delta_{eff} = (37.7 \pm 2.3)$meV agrees with the experimentally observed $\Delta_{eff} = (37.8 \pm 1.2)$meV in zero magnetic field.

Furthermore, the T = 77K spectra may be modeled by assuming temperature dependent values for Δ_{SC} ~10meV and V_{CO} ~27meV, utilizing Eq. 2.13 with N(ω)=dI/dV(E) to account for thermal broadening, and assuming the transition temperatures obey T*~T_C = 93K. (Here, Eq. 2.13 approximates the solution expected from a thermal Green's function analysis when quantum phase fluctuations are neglected, which we have assumed is true for T = 77K in Y-123 here.) Only the set of rounded peaks at $\omega = \pm\Delta_{eff}$ is able to be resolved at T =77K due to thermal broadening, and the quasiparticle spectra exhibits the overall appearance that the rounded peaks have not moved in energy as a function of temperature.

For La-112, we fit our experimental spectra using a coexisting direct SDW ($\mathbf{Q}_{CO}$=(π, π), $\delta\mathbf{Q}$=0.043π) and d-wave SC at T = 6K in Fig. 4.4, and we have used Δ_{SC} = (12.0 ± 0.2)meV and V_{CO} = (8.0 ± 0.2)meV. In addition to the parameters (Δ_{SC}, V_{CO}, $\mathbf{Q}_{CO}$, $\delta\mathbf{Q}$), we needed to account for a small amount of quantum fluctuations between the two orders using $\eta = 10^{-7}$ for the fit in Fig. 4.4. We refer to the quantum fluctuations as small because they do not significantly raise the zero-energy ($\omega = 0$) DOS, as would be the case for larger quantum fluctuations. The use of $\eta = 10^{-7}$ better accounts for the observed subgap DOS than $\eta = 0$. More important is the observation that we may account for the CO energy using V_{CO}=(8.0±0.2)meV, which is equal to the pseudogap energy, V_{PG}=(8.5±0.6)meV, and the low-energy cutoff observed in the core of vortices in La-112. Using our analysis of Δ_{eff}-vs.-θ_k in PLCCO and assuming a similar scenario in La-112, we may now analyze Δ_{eff}, $\Delta_{SC}(k = 0)$, and V_{CO} as a function of magnetic field in La-112. For this analysis, we assume that V_{CO} is determined by the low-energy cutoff for each histogram in Fig. 4.10a. The resulting magnetic field dependence for all three gaps is shown in Fig. 7.5. As H→6T, Δ_{SC} and V_{CO} become comparable, and this fact indicates that identifying vortices in La-112 for H $\geq$ 6T will become significantly more difficult due to the lack of contrast expected from r_G(Eq. 4.1).

Based on the fitting of La-112 and Y-123, we may then attribute the presence of satellite features and $V_{PG} > \Delta_{SC}$ in hole-type Y-123 to the fact that $V_{CO} > \Delta_{SC}$. In contrast, electron-type La-112 exhibits no satellite features and $V_{PG} < \Delta_{SC}$ because $V_{CO} < \Delta_{SC}$.

In addition to fitting our experimental data, we fit doping dependent data on hole-type Y-123

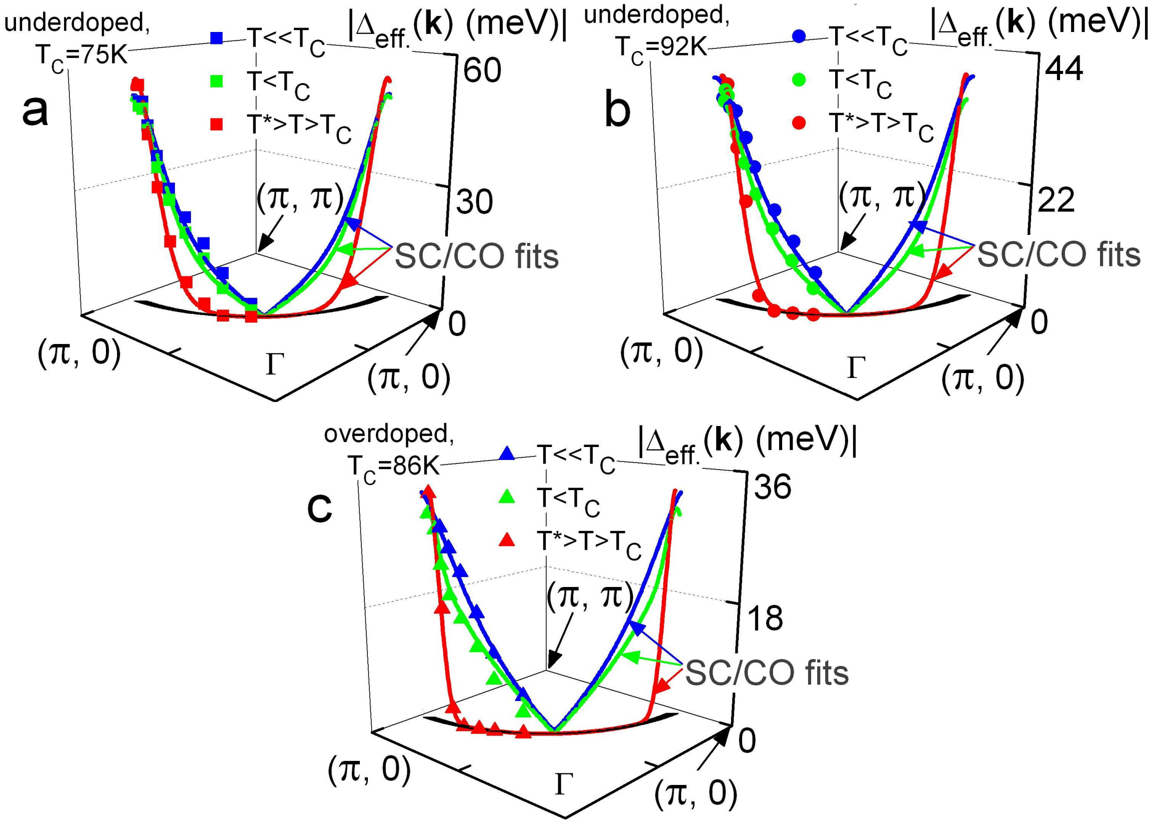

Figure 7.7: Phenomenological fit of Δ_{eff}-vs.-θ_k as a function of doping in Bi-2212 at three doping levels. The ARPES data from Ref. [6] is shown as solid symbols, while the SC/CO phenomenological fitting curves are shown as solid lines: (a) Underdoped Bi-2212 with T_C = 75 K, T* = 210 K, δ = 0.11. The temperature dependent fitting parameters Δ_{SC} and V_{CO} for T = 10, 66, 86 K are given in Fig. 7.9a. The CO fitting wave-vector is $|\mathbf{Q}_{CO}| = 0.16\ \pi$, while $|\delta Q| = 0.21\pi$, 0.19π, 0.14π for T = 10, 66, 86 K. (b) Slightly underdoped Bi-2212 with T_C = 92 K, T* = 150 K, δ = 0.15. The temperature dependent fitting parameters Δ_{SC} and V_{CO} for T = 10, 82, 102 K are given in Fig. 7.9b. The CO fitting wave-vector is $|\mathbf{Q}_{CO}| = 0.2\pi$, while $|\delta Q| = 0.18\pi$, 0.17π, 0.1π for T = 10, 82, 102 K. (c) Overdoped Bi-2212 with T_C = 86 K, T* = 100 K, δ = 0.19. The temperature dependent fitting parameters Δ_{SC} and V_{CO} for T = 18, 73, 93 K are given in Fig. 7.9c. The CO fitting wave-vector is $|\mathbf{Q}_{CO}| = 0.18\pi$, while $|\delta Q| = 0.22\pi$, 0.08π, 0.06π for T = 18, 73, 93 K. Both CDW and pinned SDW yield comparable results. The parameters shown here are for CDWs and fitting to the anti-bonding band, with $\mathbf{Q}_{CO} \parallel \delta\mathbf{Q}_{CO} \parallel (\pi,0)/(0,\pi)$.

taken previously in our lab [97, 35] and published doping dependent data on Bi-2212 [68, 100]. For the hole-type data on Y-123 and Bi-2212, we may either model $\mathbf{Q}_{CO}$ ($\sim 2k_F$) to couple effectively to the anti-bonding or to the bonding band near the anti-nodal direction [178]. For fitting to the experimental data on Y-123 in Fig. 4.4, we have fit $\mathbf{Q}_{CO}$ to the anti-bonding band, and the empirically observed $\mathbf{Q}_{CDW} \simeq 0.28\pi$ for diffraction modes in FT-LDOS in Chapter 5 is approximately equal to $\mathbf{Q}_{CO}$ determined by the antibonding band in Y-123. For comparison, the values for Fig. 7.2 are closer to fits to the bonding band for Y-123, and we find that the values of Δ_{SC} and V_{CO} determined by either band are essentially equivalent and display similar behavior as a function of doping. ARPES measurements are required to distinguish the two fits, but for fitting to quasiparticle DOS data, we are most concerned with the doping dependence of Δ_{SC}, V_{CO}, and Δ_{eff}. The resulting fits of Y-123 and Bi-2212 are shown in Fig. 7.2, along with the relevant fitting parameters. In Fig. 7.2, $\eta = 0$ for all fittings, and the values of $\delta\mathbf{Q} = 0.2\pi$ for Bi-2212 and $\delta\mathbf{Q} = 0.025\pi$ for Y-123. We plot Δ_{SC}-vs-δ and V_{CO}-vs-δ, where δ is the doping value, for Y-123 and Bi-2212 in Fig. 7.6. We find that Δ_{SC}-vs.-δ follows the same non-monotonic behavior as T_C-vs.-δ in Y-123 and Bi-2212 based on our analysis.

We next examine the consistency of our model between ARPES and quasiparticle DOS measurements in Bi-2212 from ARPES [6] and STS [68, 100] data available in the literature. We fit published doping and temperature dependent data of Δ_{eff}-vs.-θ_k from ARPES measurements in Bi-2212 [6], assuming $\eta = 0$, and the published data (symbols) along with our fits (lines) are shown in Fig. 7.7. The data in Fig. 7.7 is fit for samples with T_C=75K, 92K, and 86K, corresponding to underdoped, slightly underdoped, and overdoped Bi-2212 respectively. For each doping, we fit data for Δ_{eff}-vs.-θ_k values for $\mathrm{T} \ll \mathrm{T}_C$, $\mathrm{T} < \mathrm{T}_C$, and $\mathrm{T}_C < \mathrm{T} < \mathrm{T}^*$, and the values of ($\Delta_{SC}$, V_{CO}, $\mathbf{Q}_{CO}$, and $\delta\mathbf{Q}$) are summarized in the caption of Fig. 7.7.

The resulting values of Δ_{SC}-vs-δ and V_{CO}-vs-δ fit from ARPES and quasiparticle DOS data for $\mathrm{T} \ll \mathrm{T}_C$ are shown in Fig. 7.8c, and we observe consistency among the two fits. Furthermore, we consider the quasiparticle DOS that would be generated from the parameters we gathered from fitting the Bi-2212 ARPES data in Fig. 7.8a and the average Bi-2212 quasiparticle DOS observed in

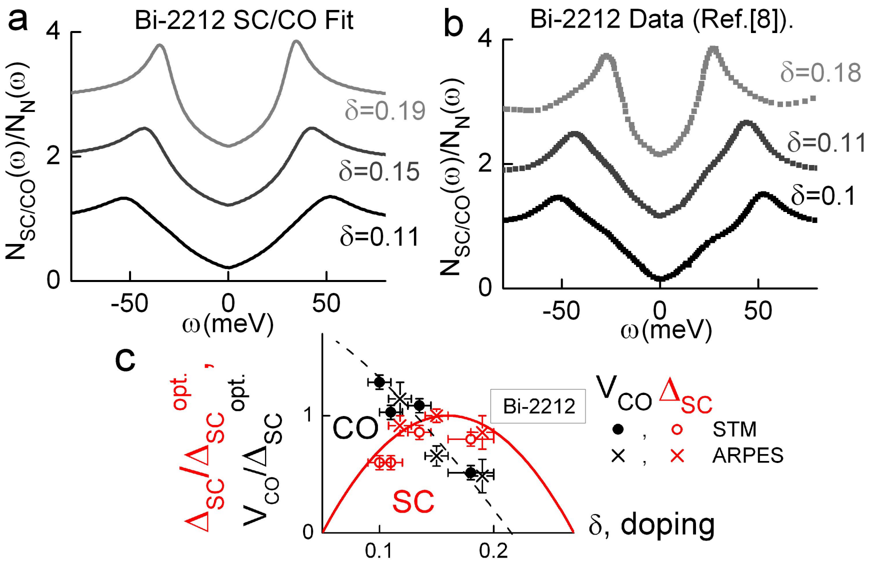

Figure 7.8: (a) Simulations of the quasiparticle excitation spectra at T = 0 in Bi-2212 for three different doping levels. The input parameters to generate the simulated quasiparticle spectra are determined from the ARPES fits in Fig. 7.7. (b) Spatially averaged quasiparticle density of states data of three Bi-2212 samples [68], with doping comparable to the doping in Fig. 7.7. (c) Demonstration of consistency among the SC/CO fitting parameters V_{CO} and Δ_{SC} from fits of ARPES data [6] and from quasiparticle DOS data. The dashed line is a guide to the eye. The solid line represents $T_C(\delta)$ normalized to the optimal doping value, using the empirical relation $T_C(\delta) = T_C^0(1\text{-}82.6(\delta\text{-}0.16)^2)$.

Refs. [68, 100] in Fig. 7.8b. We find that the two results agree, indicating that our model accurately models the ARPES and quasiparticle DOS data consistently.

Interestingly, we find that $\delta\mathbf{Q}{\sim}\mathbf{Q}_{CO}$ in Bi-2212, and this observation, in the case when $V_{CO} > \Delta_{SC}$ is directly responsible for the observance of rounded pseudogap-like peaks at Δ_{eff} and kink-like feature at Δ_{SC} in underdoped Bi-2212. This observed quasiparticle DOS arises because of the enhanced reciprocal space associated with CO due to a large $\delta\mathbf{Q}$ value. Namely, there is a considerable region of reciprocal space associated with coexistence of both SC/CO near the anti-nodes, and a smaller region of reciprocal space associated with SC near the nodes in Bi-2212. In contrast, Y-123 displays smaller values of $\delta\mathbf{Q}$ ($< \mathbf{Q}_{CO}$). Hence, there is less reciprocal space of coexistence between SC/CO in Y-123. The features at Δ_{eff} in Y-123 only appear as shoulder-like features, and the sharp coherence peaks are at Δ_{SC} due to the majority of reciprocal space associated with SC rather than coexisting SC/CO. The differences in Y-123 and Bi-2212 may be attributed to the dimensionality of the two systems and the resulting coupling to disorder. Namely, Bi-2212

($\gamma \sim 50$) is more two-dimensional than Y-123 ($\gamma \sim 5$); therefore, quasiparticles in Bi-2212 are more susceptible to disorder than in Y-123. It is likely that CO are more easily pinned in Bi-2212 due to the dimensionality, and the variations in disorder in Bi-2212 contribute to a large $\delta\mathbf{Q}$ measured by ARPES and from average quasiparticle spectra. The notion of stronger effects of disorder in Bi-2212 is also manifested by the nano-scale spatial inhomogeneity of quasiparticle tunneling spectra, which is in sharp contrast to our findings in Y-123, as discussed in Chapter 5.

In addition to considering the results for T $\ll$ T_C, we examine the temperature evolution of Δ_{SC} and V_{CO} in Bi-2212 determined from fittings in Fig. 7.7. We present the values of Δ_{SC}, V_{CO}, and Δ_{eff} determined as a function of temperature from fitting Δ_{eff}-vs.-θ_k in Fig. 7.9 (a)–(c) for Bi-2212. Interestingly, we find that the value of V_{CO} appears to increase near T_C, when SC is being suppressed, for all fittings. Similar behavior was predicted previously from self-consistent solutions of phonon-mediated coexistence of s-wave SC and CDW gaps [188]. To investigate the scenario of phonon-mediated generation of SC and CDW in Bi-2212, we numerically simulated[1] self-consistent solutions of Δ_{SC} and V_{CO} as a function of temperature following the methods of Ref. [188], and the results are shown in Fig. 7.9d. Similar behavior to empirical results is qualitatively reproduced. However, the phonon cutoff frequency, $\omega_D = 64$meV and the phonon induced attractive electron-electron interaction energies λ_Δ ($\sim$ 330 meV) and λ_G ($\sim$ 870 meV) of the model exceed the values determined in actual cuprates [189, 190]. Consequently, it is unlikely that phonons mediate the occurrence of both SC and CDW in Bi-2212.

Subsequently, we also examine the values of $\delta\mathbf{Q}$(T) and the relation to the Fermi arcs observed in Bi-2212. The values of δQ-vs.-T/T* values determined from the fittings in Fig. 7.7 are shown in Fig. 7.10a, using the values of T* obtained from Ref. [191]. The modeled values of $\delta\mathbf{Q}$ are shown as symbols, and an attempt to fit the data to the power-law dependence,

$$\delta\mathbf{Q}(T) = \delta\mathbf{Q}(0)(1 - T/T^*)^\nu, \tag{7.17}$$

is shown with the data. As was discussed earlier, $\delta\mathbf{Q}$ may be conjectured to be related to a CO

---

[1] Simulations performed by Guglielmo Lockhart

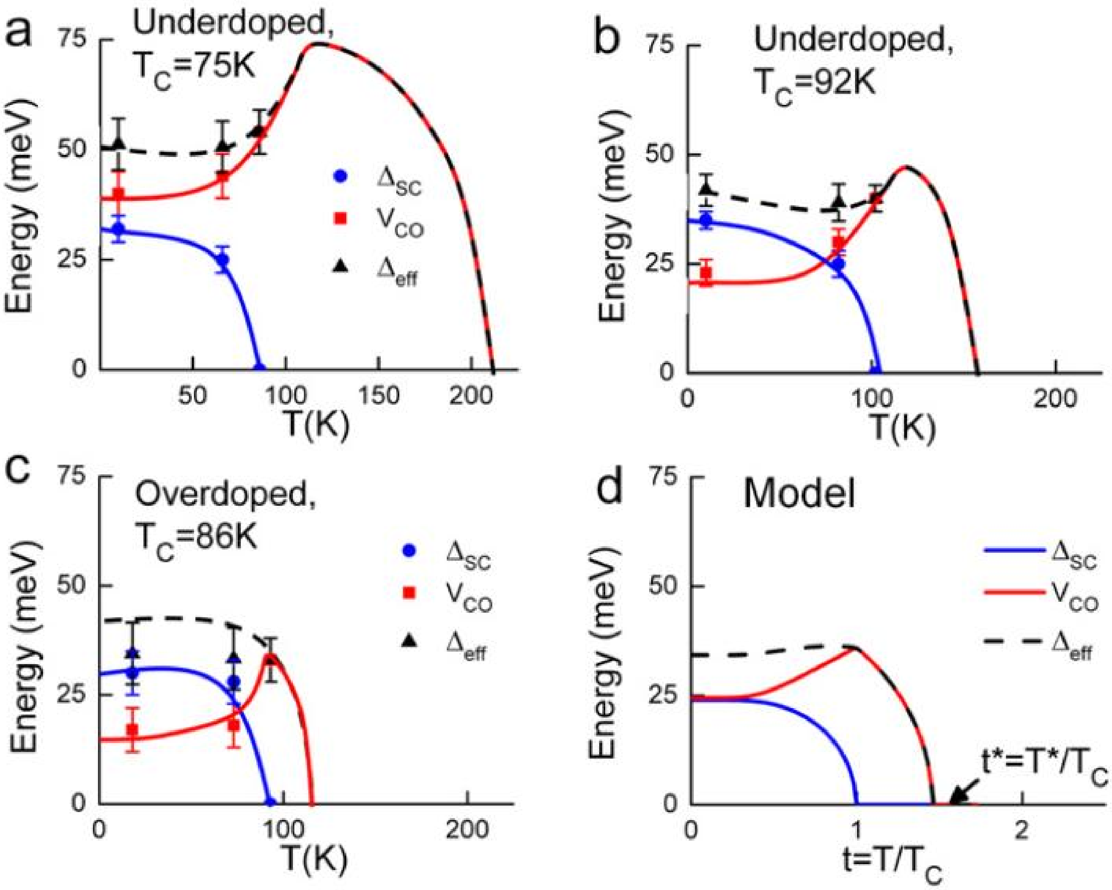

Figure 7.9: The temperature evolution of Δ_{SC} and V_{CO} based on doping dependent fits of ARPES data in Fig. 7.7 and the qualitative expectations based on self-consistent solutions of phonon-mediated SC and CDW in Ref. [188]. (a) The SC/CO phenomenological fitting parameters for underdoped Bi-2212 in Fig. 7.7a: Δ_{SC} = (32±3), (25±3), 0 meV and V_{CO} = (40±5), (44±5), (54±5) meV for T = 10, 66, 86 K. (b) The SC/CO phenomenological fitting parameters for slightly underdoped Bi-2212 in Fig. 7.7b: Δ_{SC} = (35±2), (25±3), 0 meV and V_{CO} = (23±5), (30±5), (40±5) meV for T = 10, 82, 102 K. (c) The SC/CO phenomenological fitting parameters for overdoped Bi-2212 in Fig. 7.7c: Δ_{SC}= (30±3), (28±3), 0 meV and V_{CO} = (17±5), (18±5), (33±5) meV for T = 18, 73, 93 K. (d) Simulation of Δ_{SC}(T), V_{CO}(T) and Δ_{eff}(T) as a function of temperature following the self-consistent solutions of Ref. [188], assuming phonon mediated CDW and s-wave SC. For the simulation, we used a CDW wave-vector $\mathbf{Q}_{CO}$ = (0.2π,0). The phonon-mediation parameters needed to produce gap values comparable to empirical results are unreasonably large compared to known values of the parameters in the cuprates [189, 190]. We used a phonon cutoff energy ω_D = (64.0±0.5) meV and phonon-induced electron-electron attractive energies for SC λ_δ = (328.9±1.1) meV and for CDW λ_G = (672.2±2.9) meV.

correlation length, $\xi_{CO} \sim \delta\mathbf{Q}^{-1}$. We find that $\nu = 0.53$, implying that $\delta\mathbf{Q}$(T) exhibits mean-field behavior expected for a second order phase transition characterized by ξ_{CO}.

Additionally, the values of $\delta\mathbf{Q}$(T < T*) determine the extent of the Fermi arcs observed, and here, we determine how the Fermi arc relates to $\delta\mathbf{Q}$(T < T*). In our numerical simulations, $\delta\mathbf{Q}$ describes the standard deviation from the mean-value of $\mathbf{Q}_{CO}$ as in Eq. 7.16. As a first approximation, we may assume that the CO arises near the $(\pm\pi, 0)$ and $(0, \pm\pi)$ points in the Brillouin zone and extends out from that region of reciprocal space based on the value of $\delta\mathbf{Q}$(T* > T > T$_C$) for Bi-2212. The CO energy gap will extend out 2 to 3 times $\delta\mathbf{Q}$(T* > T > T$_C$) before being undetectable via ARPES measurements. Therefore, we assume the Fermi arc will extend out 2.5$\delta\mathbf{Q}$(T < T*). The Fermi arc may not exceed over a maximum arc length of $\pi/2$; therefore, we define the Fermi arc percentage, $F_{arc,\%}$, from $\delta\mathbf{Q}$ to be equal to

$$F_{arc,\%} = (\pi/2)^{-1}(\pi/2 - 2.5 \times \delta\mathbf{Q}). \tag{7.18}$$

We plot $F_{arc,\%}$-vs.-T/T* determined from Eq. 7.18 and the three doping levels modeled here (red symbols) with other experimental data of $F_{arc,\%}$ in Bi-2212 [191] in Fig. 7.10b. The empirical formula determined from Eq. 7.18 aligns with the other observed data sets so that we may use Eqs. 7.17 and 7.18 to predict Fermi arc percentages.

Finally, we note that the observation of the pseudogap above T$_C$ and Fermi arcs relies on T* > T$_C$. The condition for observing satellite features in quasiparticle DOS data relies on $\mathrm{V}_{CO} > \Delta_{SC}$. Based on the data fit here, we find a nearly doping independent ratio of $(\mathrm{V}_{CO}/\mathrm{k}_B\mathrm{T}^*) = (2.0 \pm 0.2)$. In contrast, the value of $(\Delta_{SC}/\mathrm{k}_B\mathrm{T}_C)$ decreases from 4.9 to 4.0 as δ increases from $\delta = 0.11$ to $\delta = 0.19$, respectively.

7.3 Summary

In summary, we have developed a phenomenological model that describes the quasiparticle spectral density function and DOS expected for coexistence of SC and COs in an attempt to account for the

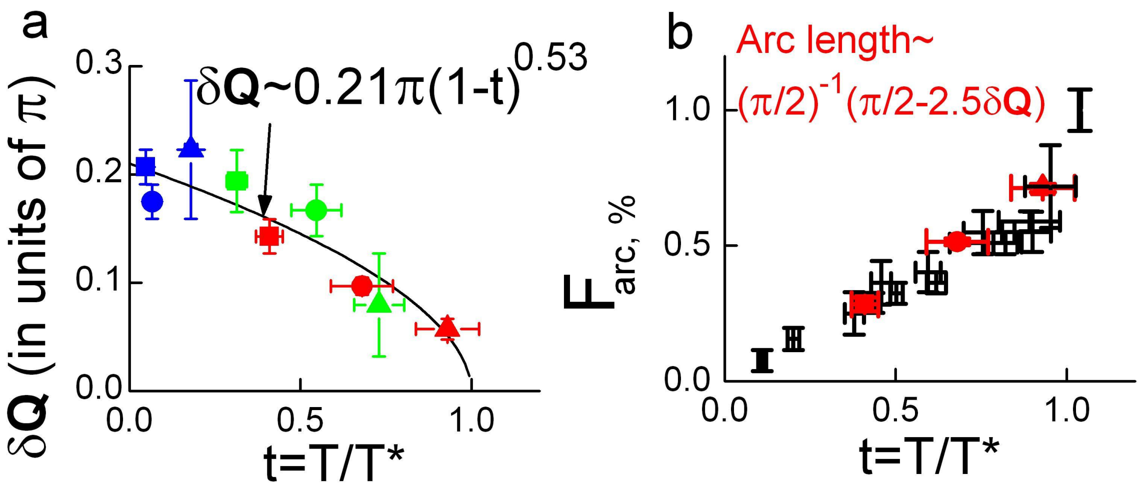

Figure 7.10: (a) $\delta\mathbf{Q}$-vs.-(T/T*) data for Bi-2212 with three doping levels δ = 0.11 (squares), 0.15 (circles) and 0.19 (triangles). The $\delta\mathbf{Q}$ data is generated from fits of the ARPES dispersion data in Ref. [6] and shown in Fig. 7.7, and the colors are correlated with the temperatures in Fig. 7.7. The values of T*(δ) are 210 K, 150 K and 100 K respectively from Ref. [192]. The $\delta\mathbf{Q}$-vs.-(T/T*) data may be fit with a power-law dependence of the form$\delta\mathbf{Q}$(T) = $\delta\mathbf{Q}$(0)[1-(T/T*)]$^{\nu}$, with $\nu \sim 0.53$. (b) $F_{arc,\%}$-vs.-(T/T*), computed from $\delta\mathbf{Q}$ values in (a) and Eq. 7.18 are shown as solid red symbols. The values agree with experimental data (black crosses) from Ref. [191] for other hole-type cuprates.

unconventional behavior of quasiparticles in cuprate superconductors. We find that many phenomena may be accounted by this phenomenological model, if we consider CDWs and SDWs as relevant COs. We find that disorder-pinned SDWs or CDWs, with $\mathbf{Q}_{CO}$ along the Cu-O bonding direction, coexisting with SC may reproduce quasiparticle excitations seen in the hole-type cuprates. In contrast, direct SDWs coexisting with SC may be used to model quasiparticle excitations in electron-type cuprates, and the direct SDWs exhibit $\mathbf{Q}_{CO}$ along the nodal direction with $\mathbf{Q}_{CO}$=(π, π). By using these revelations and fitting our quasiparticle spectra in hole-type Y-123 (electron-type La-112), we could account for the presence (absence) of satellite features for T $\ll$ T_C by modeling the data assuming $V_{CO} > \Delta_{SC}$ ($V_{CO} < \Delta_{SC}$).

Upon fitting the doping dependent quasiparticle DOS in the hole-type cuprates Y-123 and Bi-2212, we found that our model generates values of $\Delta_{SC}(\delta)$ from fits that follow a doping dependence, $\Delta_{SC}(\delta)$-vs.-δ, mimicking the behavior of T_C-vs.-δ observed from bulk measurements. Furthermore, we could account for the quasiparticle spectra in Bi-2212 and Y-123 for all doping levels. We found that Y-123 showed coherence peaks at $\omega = \pm\Delta_{SC}$ and rounded satellite features at $\omega = \pm\Delta_{eff}$, while Bi-2212 showed rounded pseudogap-like peaks at $\omega = \pm\Delta_{eff}$ and low-energy kink-like features at $\omega = \pm\Delta_{SC}$ due to the large values of $\delta\mathbf{Q}$ in Bi-2212 compared to Y-123.

Further, we fit ARPES data as a function of temperature and doping level in Bi-2212 using our phenomenological model. We found that the $\mathrm{T} \ll \mathrm{T}_C$ results of fitting ARPES data produced parameters that agreed with empirically observed quasiparticle DOS in Bi-2212 for $\mathrm{T} \ll \mathrm{T}_C$. We also found that the generated temperature dependence of $\Delta_{SC}(\mathrm{T})$ and $\mathrm{V}_{CO}(\mathrm{T})$ from the ARPES fits could be qualitatively described by the self-consistent solutions of coexisting SC and CDW arising from phonon-mediated pairing of SC and CDW; however, we found that quantitatively the parameters necessary to generate the qualitative fit were unphysical, implying that phonons are unlikely the microscopic mechanism responsible for the occurrence of both SC and CDW in the cuprates. Finally, our additional analysis indicated that the presence(absence) of satellite features and the above-T_C pseudogap and Fermi arc phenomena in the hole-(electron-)type cuprates could be accounted for if $\mathrm{V}_{CO} > \Delta_{SC}$ ($\mathrm{V}_{CO} < \Delta_{SC}$) and $\mathrm{T}^* > \mathrm{T}_C$ ($\mathrm{T}^* < \mathrm{T}_C$), respectively.

Conclusion

In conclusion, the non-universal and unconventional quasiparticle excitations in the hole- and electron-type cuprate superconductors have been investigated both experimentally and theoretically, and the results appear to be consistently explained as being due to a combination of the Bogoliubov quasiparticles from Cooper pairs and collective mode excitations from competing orders. In other words, the low-energy excitations in cuprate superconductors emerge from a ground state of coexisting superconductivity and competing orders.

Specifically, spatially resolved STS studies of the quasiparticle excitations in both hole-type Y-123 and electron-type La-112 appear incompatible with a ground state of superconductivity alone. The intra-vortex spectra of La-112 and Y-123 show no evidence for zero-bias conductance peaks that are salient signatures for conventional superconductivity upon the suppression of superconductivity inside the vortex core. Furthermore, pseudogap-like quasiparticle spectra are observed inside vortex cores for both systems, and an additional subgap energy ($\Delta' \sim 7 - 12meV$) is observed for intra-vortex spectra in Y-123. The pseudogap energy, V_{PG} = (8.5±0.6)meV in La-112 is less than than the zero field effective gap value Δ_{eff} ~12meV. In contrast, the intra-vortex pseudogap energy V_{PG} = (31.5±2)meV is greater than $\Delta_{SC} \sim$ 20meV in Y-123. A model of superconductivity alone cannot be reconciled with such opposite behaviors in hole- and electron-type cuprate superconductors, whereas the model of coexisting superconductivity (SC) and competing orders (CO) may account for this behavior if the conditions of $\Delta_{SC} > \mathrm{V}_{CO}(=\mathrm{V}_{PG})$ in La-112 and if $\Delta_{SC} < \mathrm{V}_{CO}(=\mathrm{V}_{PG})$ in Y-123 are assumed. The origin of the subgap energy remains to be determined but provides further evidence in Y-123 that a model of superconductivity alone is lacking in this system.

Further evidence for competing orders was observed in the Fourier-transformed local density of states (FT-LDOS) of Y-123 as a function of magnetic field for T $\ll$ T_C. In the FT-LDOS analysis, three energy-independent diffraction modes were observed and attributable to a pair-density wave ($\mathbf{Q}_{PDW}$), a charge-density wave ($\mathbf{Q}_{CDW}$), and a spin-density wave ($\mathbf{Q}_{SDW}$) based on the symmetry of the real part of the FT-LDOS at these diffraction modes. While the observation of PDW may be attributed to locally disorder superconductivity in forms of incoherent pair density waves, the findings of distinct SDW and CDW clearly point to the presence of competing orders besides superconductivity. Moreover, the "two-gap" model for coexisting SC/CO is compatible with the notion of preformed pairs suggested by the "one-gap" model. In contrast, the "one-gap model" alone fails to consistently account for empirical observations as functions of hole- or electron-doping, doping level, temperature, and magnetic field.

The interplay of unconventional quasiparticle excitations is further seen to cause significant field-induced quantum phase fluctuations and quantum criticality among all cuprates, based on bulk measurement characterizations of the vortex phase diagrams of many different cuprates. A general trend of the degree of quantum fluctuations has been established as a function of the doping level, the electronic anisotropy, and the number of CuO_2 layers per unit cell. It is plausible from further analysis that quantum criticality and strong field-induced quantum phase fluctuations are induced in cuprates because of their proximity to a quantum critical point related to the coexistence of superconductivity and competing orders in the ground state of cuprates.

Finally, many of the unconventional and non-universal phenomena among all cuprates, such as the pseudogap and Fermi arc phenomena, may be consistently accounted for with a quantitative "two-gap" model of coexisting SC/CO based on Green's function techniques. Phenomena in both hole- and electron-type cuprates are explained by this model, and other features, such as the satellite features and the conductance modulations in the quasiparticle tunneling spectra, that are not accounted for by existing "one-gap" models, may be explained. It is therefore evident that competing orders are necessary to understand the unconventional quasiparticle excitations in the cuprates, and future theoretical developments should incorporate the"two-gap" perspective to account for all experimentally observed phenomena.

Appendix A

Methodologies for STS data processing

In this appendix, the techniques used to normalize the dI/dV data that facilitated the primary findings described in Chapters 4 and 5 are detailed.

A.1 Normalization of differential conductance (dI/dV) data

Locating and studying vortices in cuprate superconductors is more complicated than in conventional type-II superconductors due to the small superconducting coherence length ($\xi_{ab} = 1.5 \sim 2.0$nm for Y-123 and ~5.0 nm for La-112) relative to the average vortex separation $a_B = 1.075\sqrt{\Phi_0/B} \sim 48.91$ nm $/\sqrt{B}$, where the magnetic induction B is measured in Tesla. Given that the cuprates are extreme type-II superconductors, we have B≃H with H being the applied magnetic field. Hence, the vortex separation varies from 35.0nm at H = 2T to 20.0nm at H = 6T. Additionally, the observation of remnant pseudogap-like behavior in the core of vortices further complicates the ability to find and examine vortices because the differential conductance inside and outside a vortex core region does not differ as much as in conventional type-II superconductors, such as $NbSe_2$ [23, 24, 25].

To facilitate the investigation of vortices in Y-123, we employ three techniques to improve our data analysis of spatially resolved differential conductance maps. First, we normalize the differential conductance to remove both the electronic bandstructure effects at high energies ($|\omega| \gg \Delta_{eff}$) and the slight variations in the tunnel junction resistance from pixel to pixel. Second, we subtract out the contribution of a remnant surface layer above the underlying bulk superconductor of interest. Finally, we check to see that the density of states is conserved over our measured energy range. We perform these three procedures for each differential conductance curve in all spatially resolved differential conductance maps to facilitate our study of vortices in Y-123 as a function of magnetic field.

A.1.1 Removal of the variations in tunnel junction resistance and contributions from high-energy electronic bandstructure effects

Slight variations in the tip/sample separation create extrinsic contributions to the differential conductance curves at each pixel in our differential conductance map. The outcome is slight variations in the offset of each differential conductance curve from pixel to pixel. Additionally, the electronic bandstructure of Y-123 dictates the curvature of the differential conductance data for energies $|\omega| \gg \Delta_{eff}$. Any local variation in the electronic properties of the surface layer leads to additional extrinsic contributions to the differential conductance data. We remove both effects simultaneously by fitting the raw differential conductance curves at each pixel to a polynomial, as a function of ω, for energies $|\omega| \gg \Delta_{eff}$. As an example, we show differential conductance data (solid line) and background fitting (dashed line) from our study of Y-123 in Fig. A.1a, and the resulting normalized spectra in Fig. A.1b. The removal of effects due to slight variations in the electronic bandstructure and tip/sample separation, such as in Fig. A.1b, is performed at each pixel to ensure that the resulting differential conductance curves are largely governed by intrinsic properties such as features at Δ_{SC} and Δ_{eff}.

A.1.2 Tunneling into the CuO$_2$ planes through vacuum and a metallic layer in YB$_2$Cu$_3$O$_{7-\delta}$

Unlike Bi$_2$Sr$_2$CaCu$_2$O$_x$, the surface of most cuprates cannot be easily prepared by cleaving. The surface of Y-123 must be chemically etched by 0.5–2% bromine in ethanol solution to remove carbonates and other non-stoichiometric layers that form on the surface of these cuprates [147]. A

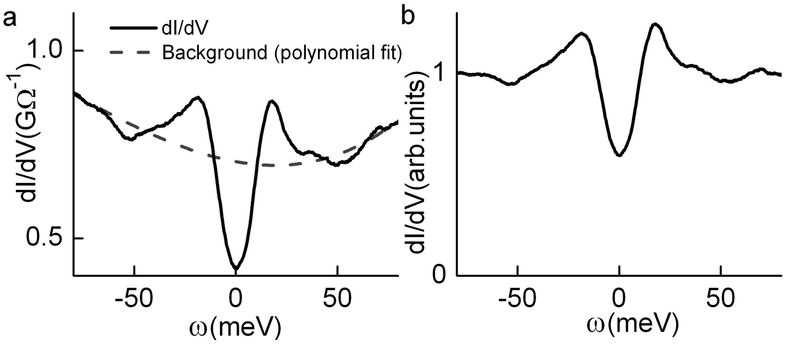

Figure A.1: Procedure to normalize raw differential conductance curves in Y-123: (a) Raw differential conductance data taken from Y-123 (solid line) and the polynomial fit to the high-energy ($|\omega| \gg \Delta_{eff}$) background features (dashed line) due to the electronic bandstructure. (b) The resulting normalized differential conductance curve obtained by dividing the raw differential conductance by the high-energy polynomial fit in (a).

passivated surface layer typically forms after an etching of the surface. The surface layer protects the cuprate for a few hours in air from further degradation of the surface, enabling the sample to be loaded into our STM for long-term measurements under UHV conditions and cryogenic temperatures. Empirically, the surface layer is a metallic CuO_2 plane with a well defined Fermi edge according to X-ray photoemission spectroscopic (XPS) studies [147] and has an ohmic current vs. voltage characteristic. Therefore, the surface layer contributes to a constant offset in the normalized differential conductance in addition to the differential conductance due to the superconducting bulk. We remove the surface layer contribution to the differential conductance in Y-123 by subtracting the H = 0 average differential conductance at zero energy ($\omega = 0$), which we denote as G_M, from all differential conductance maps. For example, we can remove $G_M = 0.575$ from the Y-123 data in Fig. A.2b. The resulting data from this operation is shown in Fig. A.2a. After removing G_M, we must then proceed to check that the density of states is conserved.

A.1.3 Checking for conservation of density of states in $YB_2Cu_3O_{7-\delta}$

To ensure that the density of states is conserved after the removal of G_M, we sum the density of states over the energy range measured. If Y-123 were in the normal state without either superconductivity (SC) or competing orders (CO), the density of state normalized relative to the electronic bandstructure would equal one at all energies, as in Fig. A.2b. Thus, the area under the differential

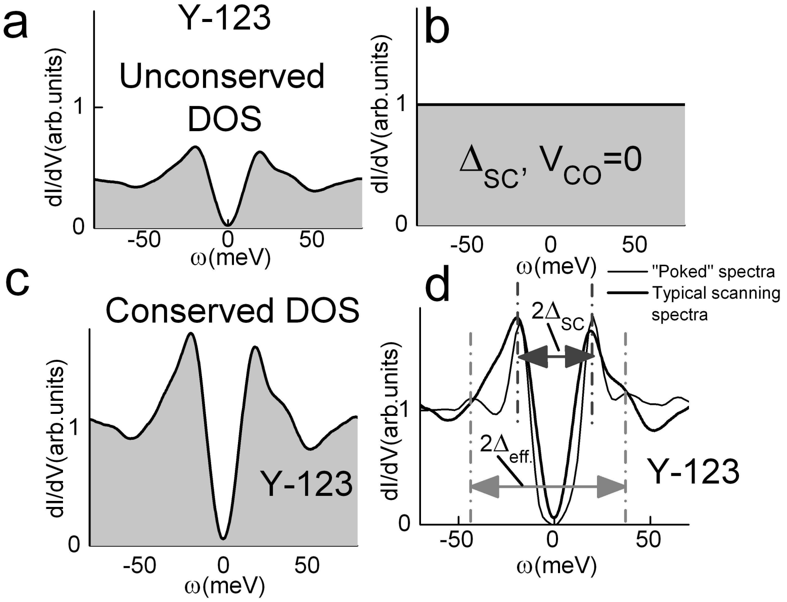

Figure A.2: Conservation of density of states after removing the influence of the metallic layer in Y-123: (a) The normalized differential conductance curve obtained after $G_M = 0.575$ is removed. The density of states is not conserved. (b) The normalized differential conductance curve with Δ_{SC}, V_{CO}=0 is equal to one everywhere. The area under the curve in (b) should equal the area under the curve in (a), which is not true and means we must multiply by a constant to renormalize the data in (a). (c) The resulting renormalized differential conductance curve in Y-123 obtained by multiplying the curve in (a) by a renormalization constant. The area under the curve in (c) is now equal to the area under the curve in (b). (d) A comparison of the curve in (c) to data taken by "poking" the STM tip through the surface metallic layer. Spatially resolved differential conductance map measurements are performed under normal tunneling conditions ($R_{junction}$ ∼1GΩ), without the tip poked into the sample.

conductance curve in Fig. A.2a for $T < T_C$ should then be equal to the area under the curve in Fig. A.2b for $T > T_C$. This condition is not met after the subtraction of the surface layer contribution. Therefore, we must multiply the curve in Fig. A.2b by a renormalization constant to restore the conservation of density of states. The result of multiplying Fig. A.2a by a renormalization constant is shown in Fig. A.2c. We can verify the validity of removing G_M and renormalizing the data by "poking" our STM tip through the surface layer above the CuO_2 planes and measuring the spectra. We find that the normal tunneling spectra, obtained at a junction resistance of about 1GΩ and analyzed with our three data analysis procedures described above, is similar to the "poked" spectra. Both spectra display Δ_{SC} and Δ_{eff} occurring at the same positions, as illustrated by our experimental data for both scenarios in Fig. A.2d. Given that scans cannot be performed with the tip "poked" into the sample at each pixel, we must measure spatially resolved differential conductance maps under normal tunneling conditions, with a tunnel junction resistance of about 1GΩ.

A.2 Fourier-transformed local density of states on etched surfaces

In order to reveal sharp conductance modulation diffraction modes from FT-LDOS-vs.-**k** maps in Y-123 for easier study, the data must be processed to remove the broad diffraction spot at the Γ point (**k**=0) due to the etched surface. The broad diffraction spot at the Γ point arises from a cross-talk effect between the STM tube scanner and the tunneling current. As was mentioned in Chapter 3, spatially resolved STS performed in constant tip-junction resistance mode will eliminate surface roughness features from contributing to the observed conductance maps to lowest order. However, the z-scan voltage of the tube scanner must be changed at each point of an STS map to maintain constant tip-junction resistance, and the z-scan voltage is typically on the order of 100V. While the resistance between the tube-scanner and tip is greater than 1GΩ, it is likely on the order of 100–1000GΩ. Therefore, the measured STM current will be modulated by 0.1% to 1% by the etched surface roughness in Y-123, which is on the order of 5 nanometers. In contrast, this problem is not an issue in Bi-2212 [3], because the surfaces of Bi-2212 for STS studies are nearly atomically flat due to the ease with which the surfaces are cleaved and retain their stoichiometry compared to most other cuprates [147].

We illustrate in Fig. A.3 the process to remove the etched surface contribution to the FT-LDOS. The data shown in Fig. A.3 has been folded onto itself by folding along the Cu-O bonding directions to reduce noise. The data in Fig. A.3 is the raw data of Fig. 5.7 before removal of the etched surface background. In Figs. A.3a and A.3c, the raw differential FT-LDOS, after folding, in Y-123 is shown as a three-dimensional image and a two-dimensional intensity plot respectively. We fit a smooth background function to the raw data such that sharp diffraction peaks are preserved and only the peak at Γ and the broad and gradually varying features around it are considered in the background fit. The smoothed background data is shown in Figs. A.3b and A.3d as a three-dimensional image and a two-dimensional intensity plot, respectively. Finally, we subtract the smooth background from the raw data to obtain our final FT-LDOS, which reveals a flattened set of conductance data in momentum space. We may then investigate the energy dependence of various sharp diffraction modes in momentum space to differentiate between energy-independent conductance modulations and energy-dependent quasiparticle scattering interferences, as discussed in Chapter 5.

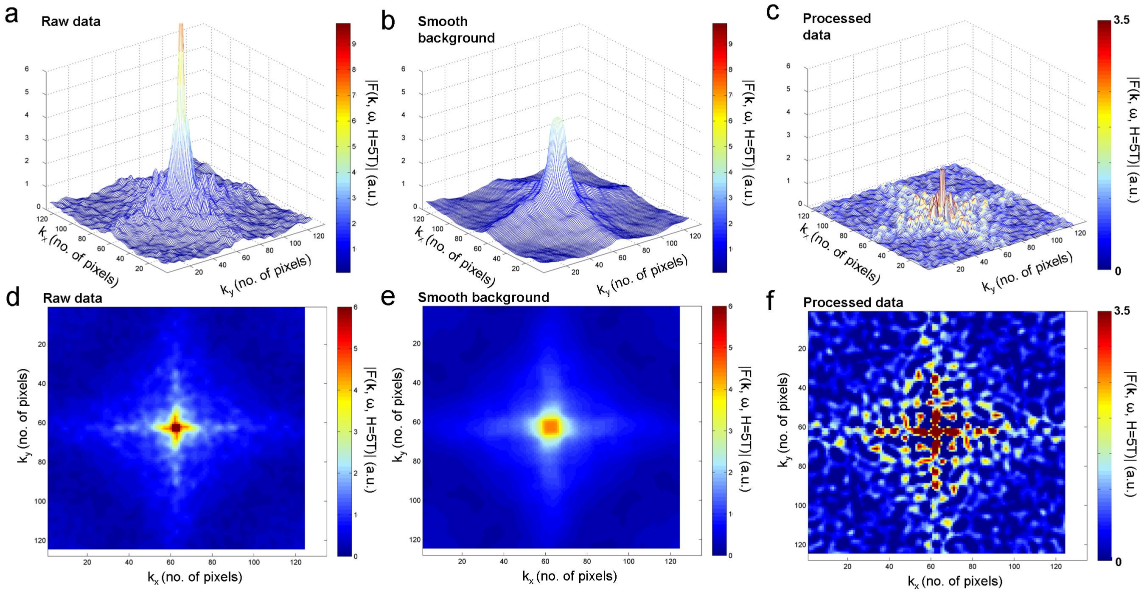

Figure A.3: Background removal in FT-LDOS maps of $YB_2Cu_3O_{7-\delta}$. Here, we illustrate the method to remove the broad background from FT-LDOS maps due to the etched surface, and we illustrate the procedure on the differential FT-LDOS from Fig. 5.7. (a) Three-dimensional mesh plot of the raw data. (b) Two-dimensional intensity plot of the raw data. (c) Three-dimensional mesh plot of the smooth background obtained from fitting broad features in the raw data. (d) Two-dimensional intensity plot of the smooth background obtained from fitting broad features in the raw data. c) Three-dimensional mesh plot of the raw data minus the smooth background, revealing sharp diffraction modes. (d) Two-dimensional intensity plot of the raw data minus the smooth background, revealing sharp diffraction modes

Appendix B

Differential FT-LDOS-vs.-energy in $YB_2Cu_3O_{7-\delta}$

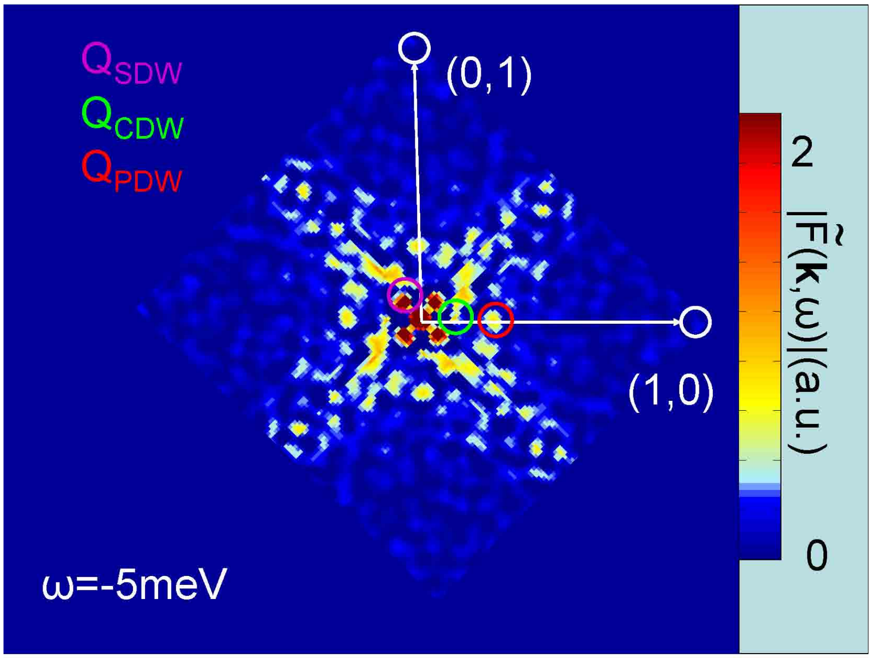

Figure B.1: $\tilde{F}(\mathbf{k},\omega\text{=-5meV},\text{H=5T})$

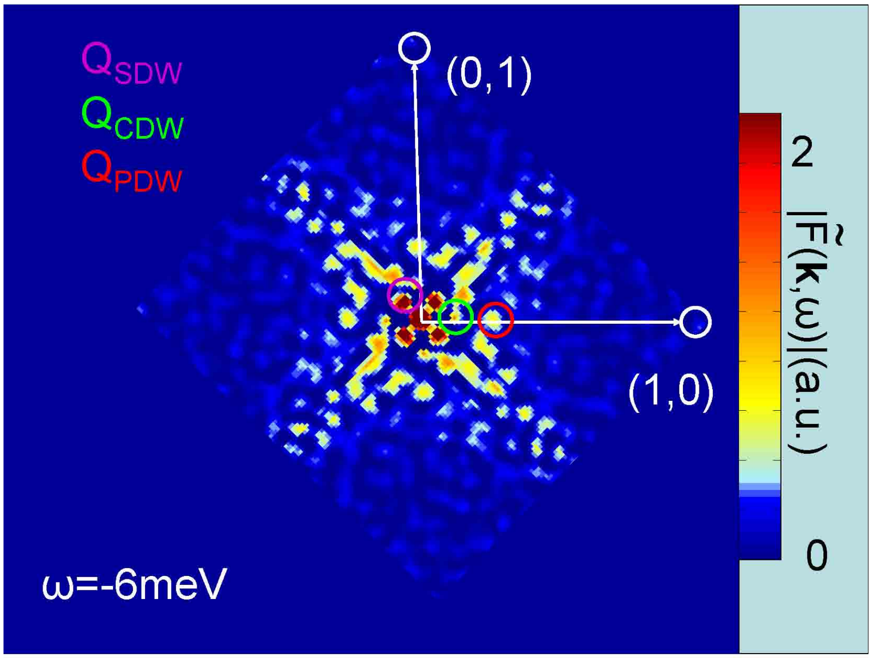

Figure B.2: $\tilde{F}(\mathbf{k}$,ω=-6meV,H=5T)

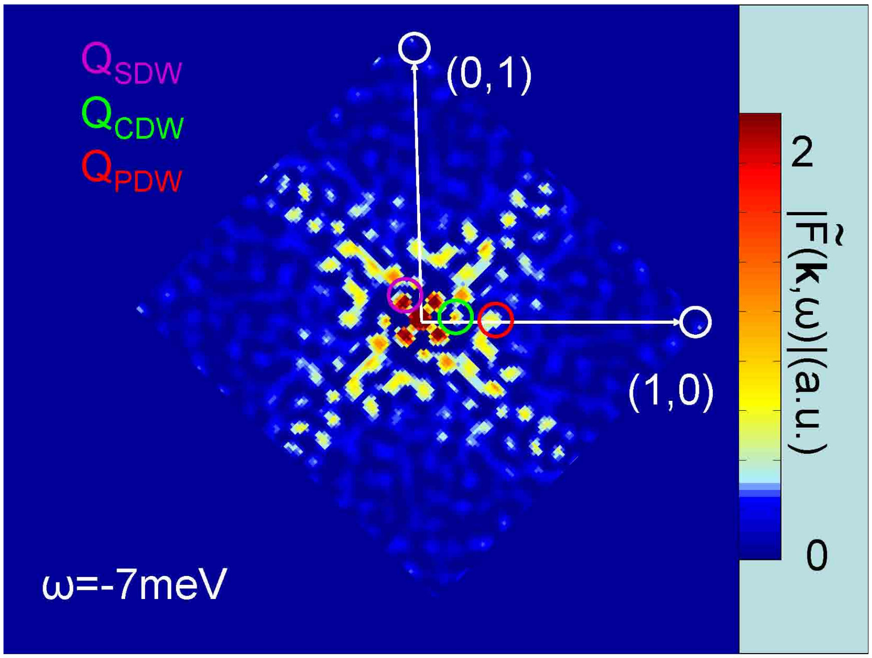

Figure B.3: $\tilde{F}(\mathbf{k}$,ω=-7meV,H=5T)

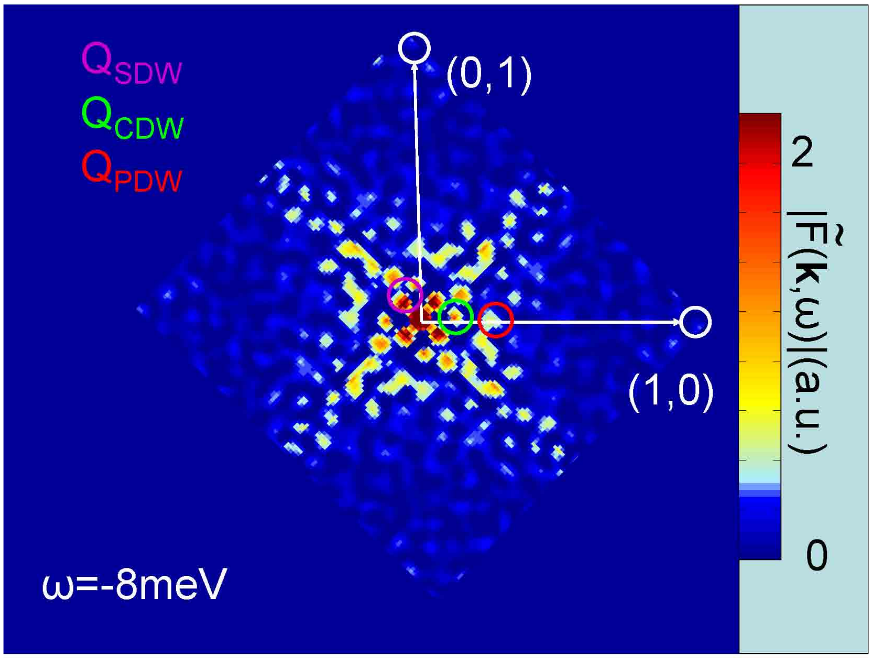

Figure B.4: $\tilde{F}(\mathbf{k}$,ω=-8meV,H=5T)

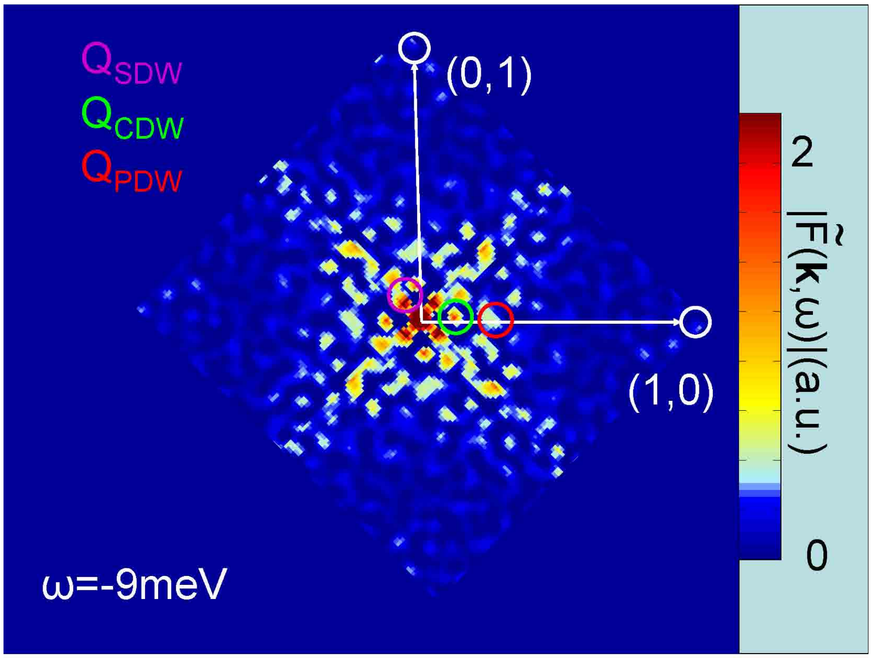

Figure B.5: $\tilde{F}(\mathbf{k}$,ω=-9meV,H=5T)

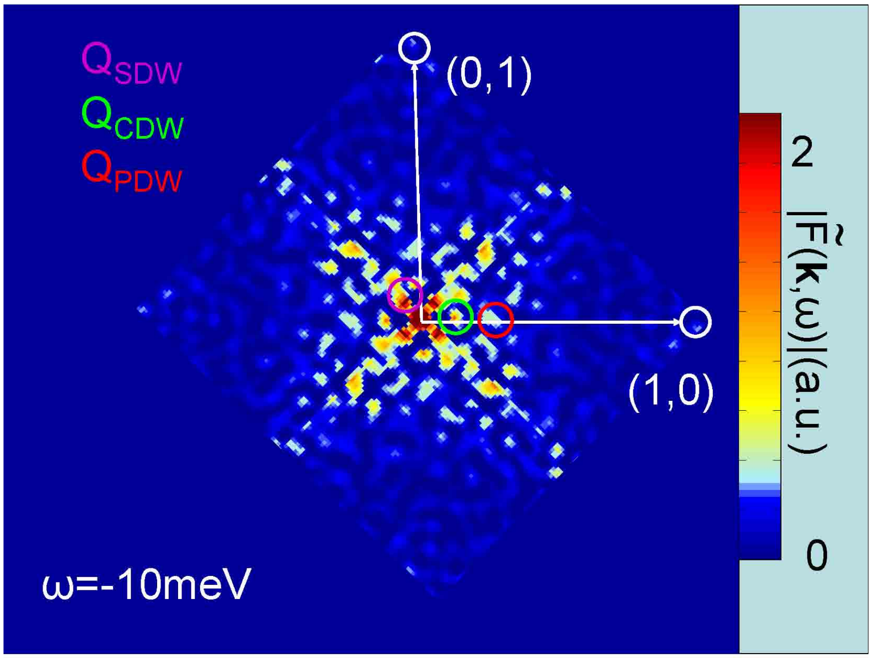

Figure B.6: $\tilde{F}(\mathbf{k},\omega\text{=-10meV,H=5T})$

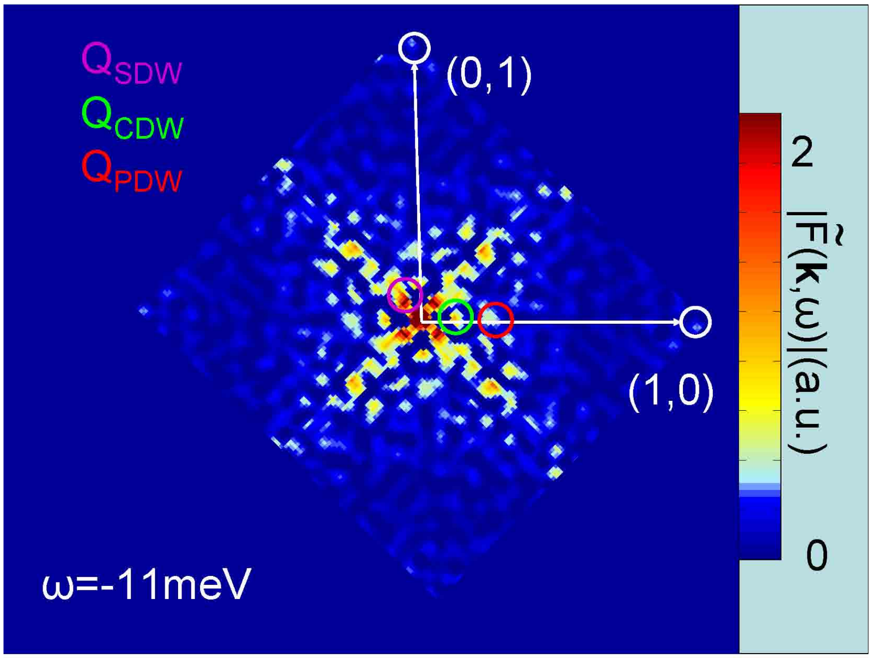

Figure B.7: $\tilde{F}(\mathbf{k},\omega\text{=-11meV,H=5T})$

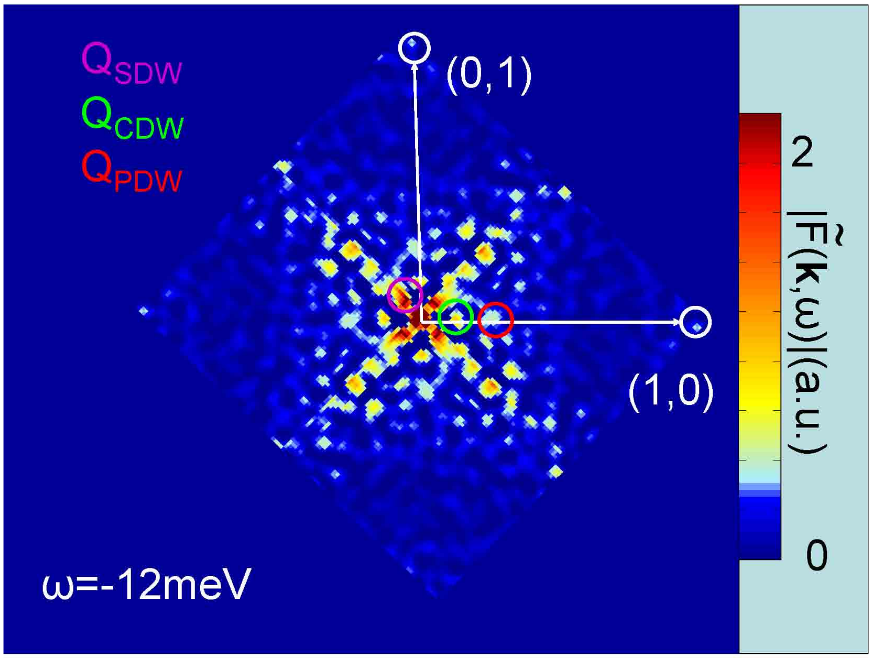

Figure B.8: $\tilde{F}(\mathbf{k}, \omega\text{=-12meV,H=5T})$

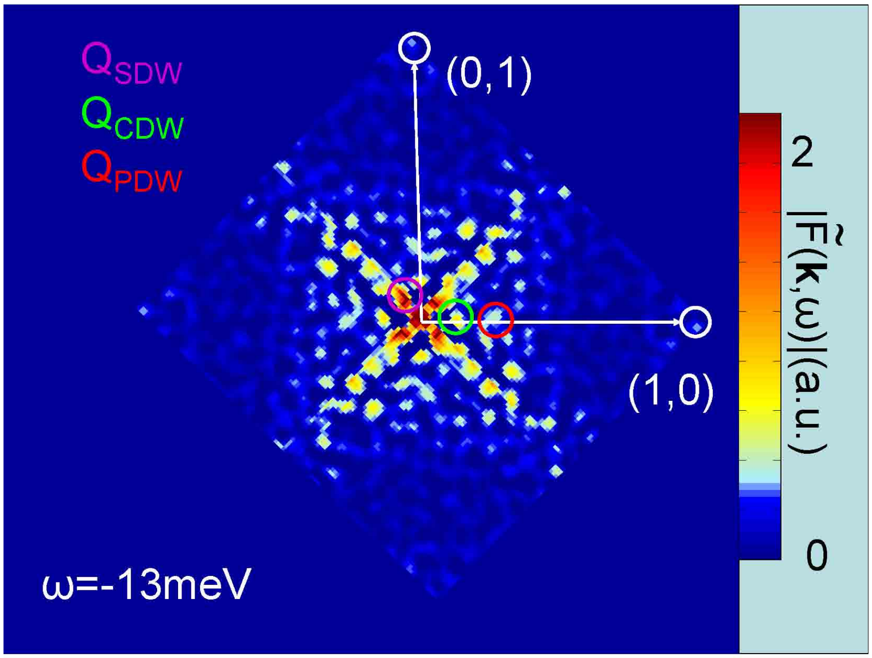

Figure B.9: $\tilde{F}(\mathbf{k}, \omega\text{=-13meV,H=5T})$

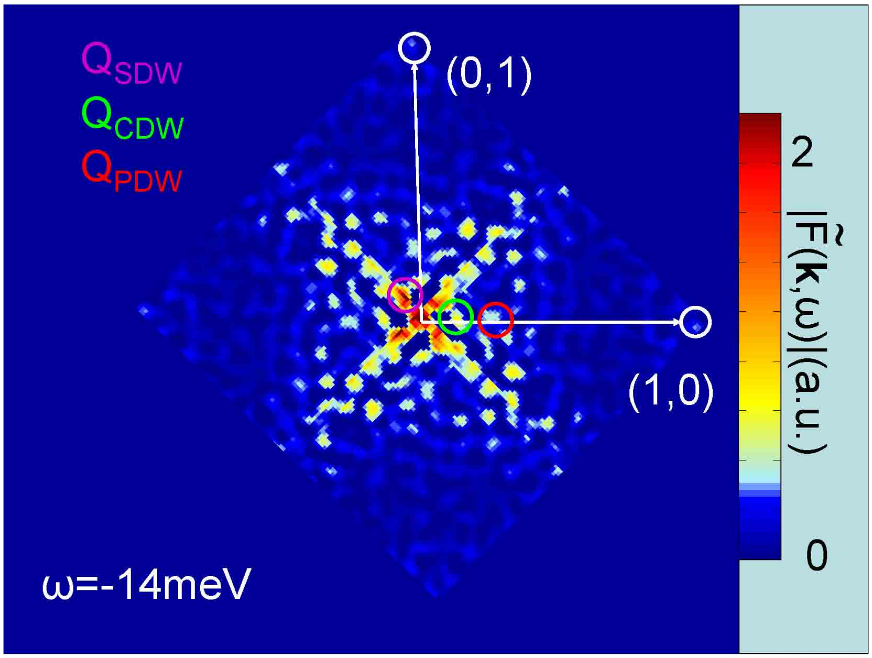

Figure B.10: $\tilde{F}(\mathbf{k}$,ω=-14meV,H=5T)

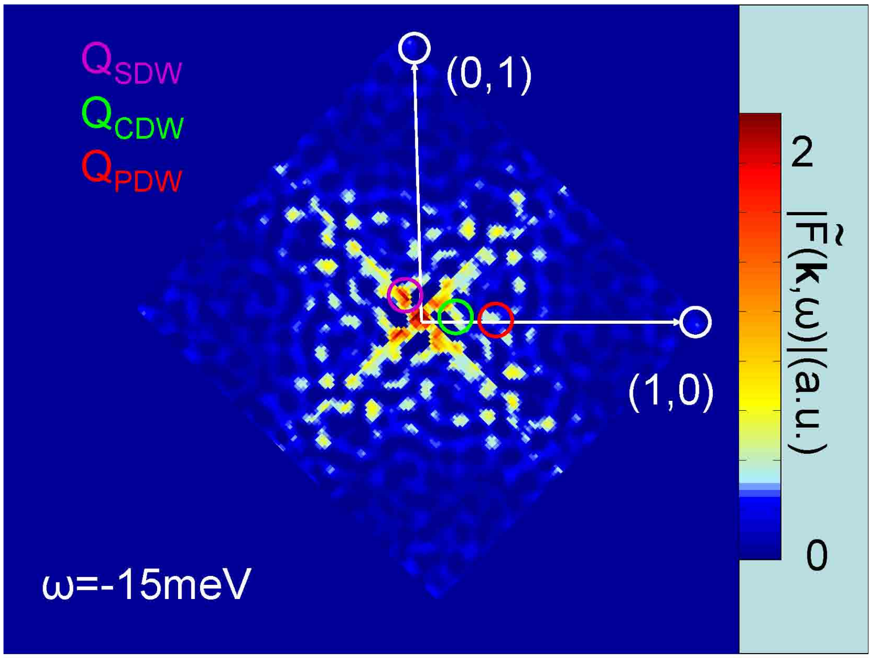

Figure B.11: $\tilde{F}(\mathbf{k}$,ω=-15meV,H=5T)

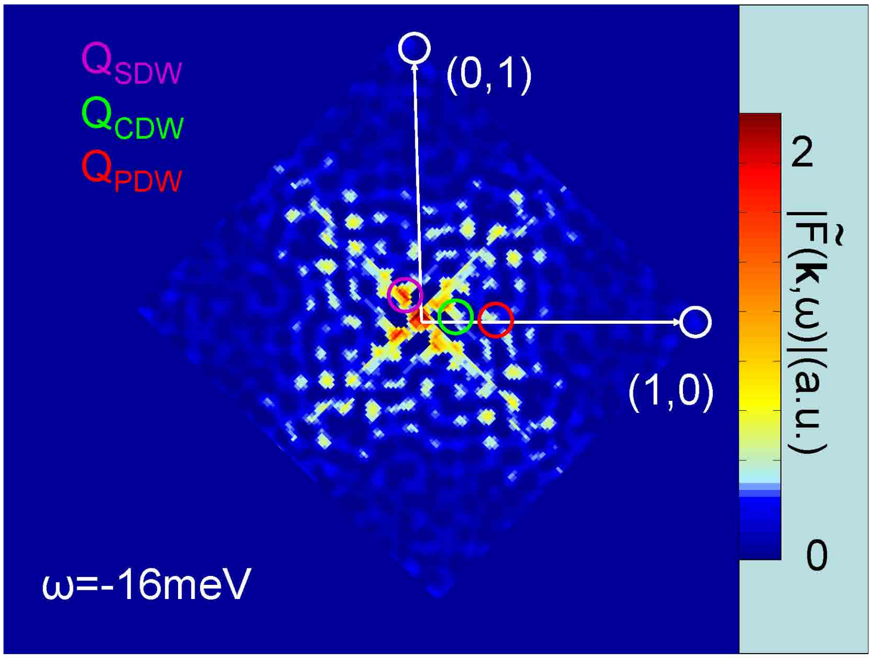

Figure B.12: $\tilde{F}(\mathbf{k}$,ω=-16meV,H=5T)

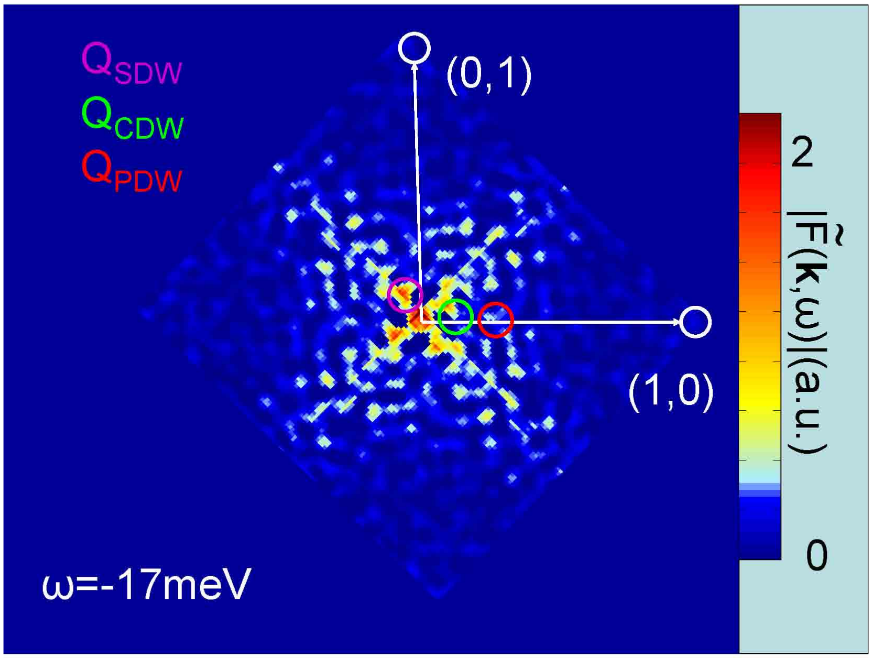

Figure B.13: $\tilde{F}(\mathbf{k}$,ω=-17meV,H=5T)

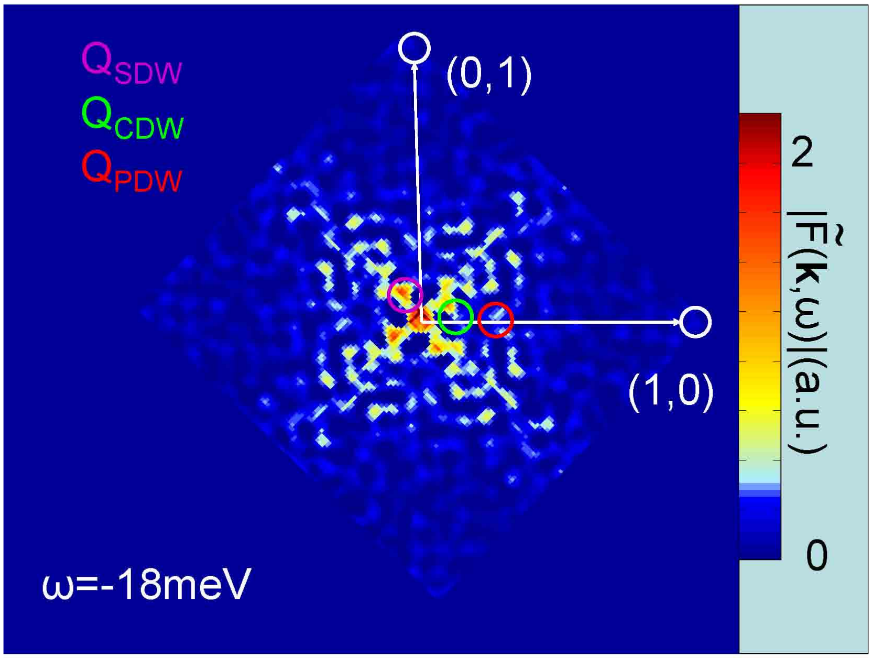

Figure B.14: $\tilde{F}(\mathbf{k},\omega$=-18meV,H=5T)

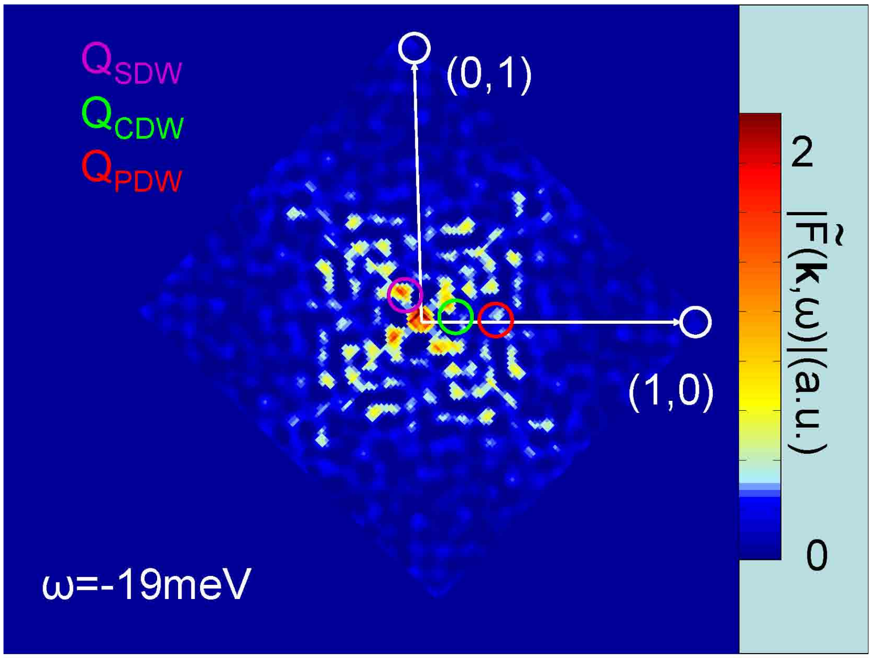

Figure B.15: $\tilde{F}(\mathbf{k},\omega$=-19meV,H=5T)

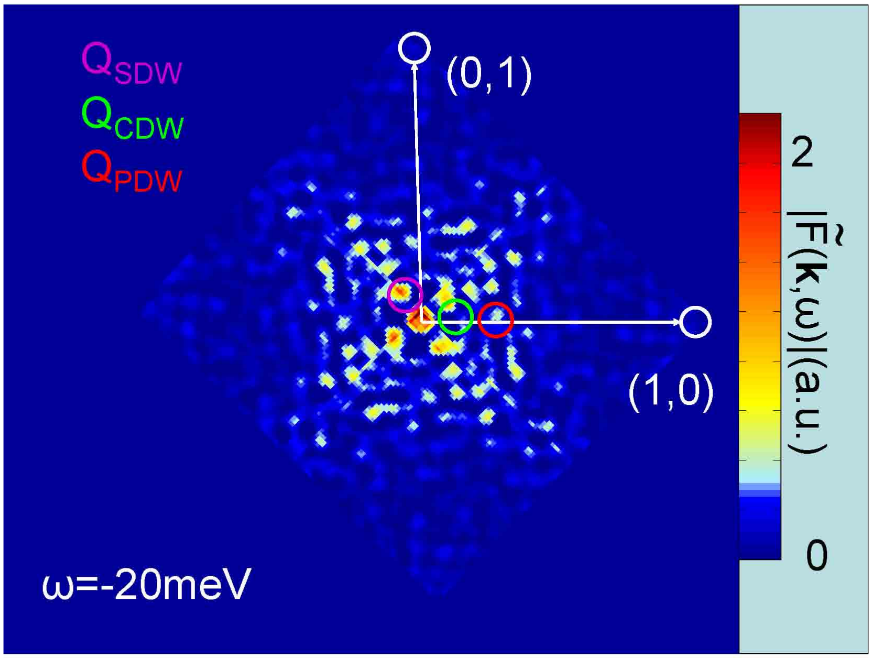

Figure B.16: $\tilde{F}(\mathbf{k}$,ω=-20meV,H=5T)

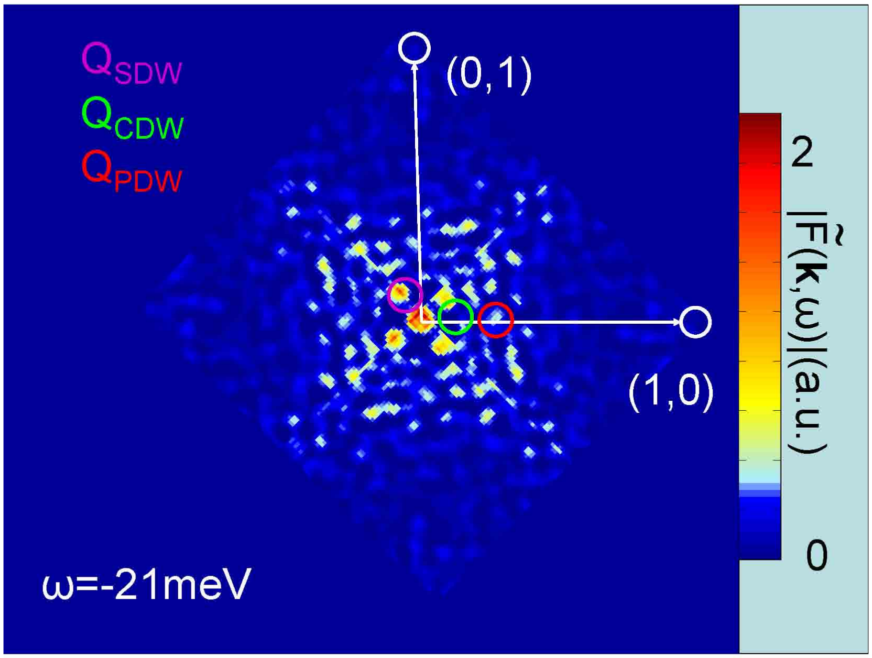

Figure B.17: $\tilde{F}(\mathbf{k}$,ω=-21meV,H=5T)

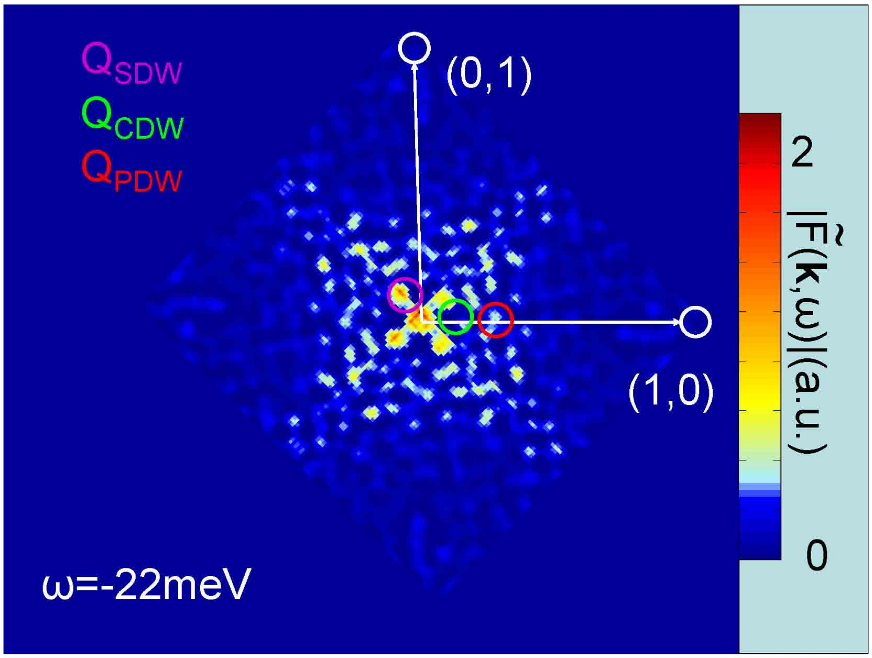

Figure B.18: $\tilde{F}(\mathbf{k}$,ω=-22meV,H=5T)

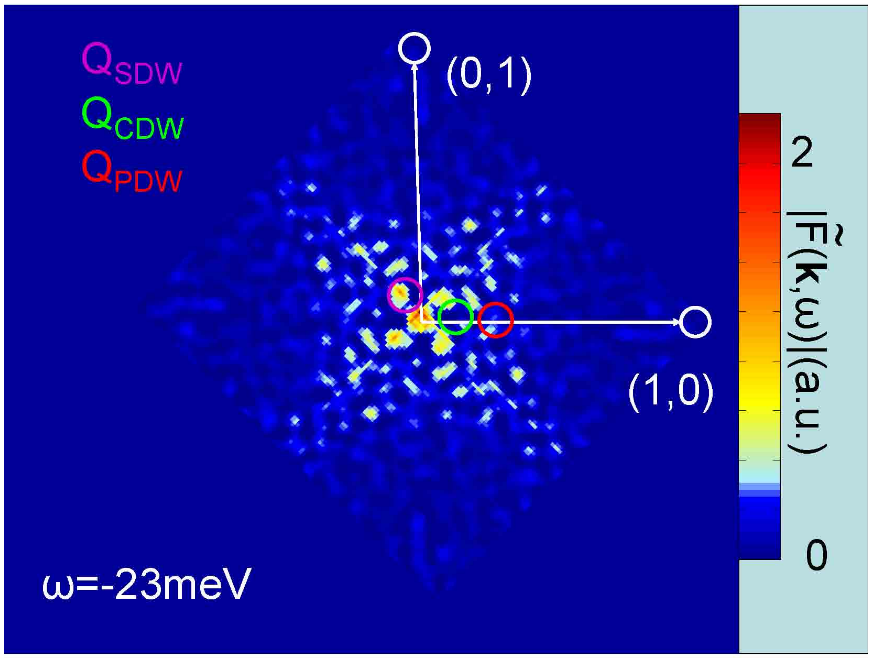

Figure B.19: $\tilde{F}(\mathbf{k}$,ω=-23meV,H=5T)

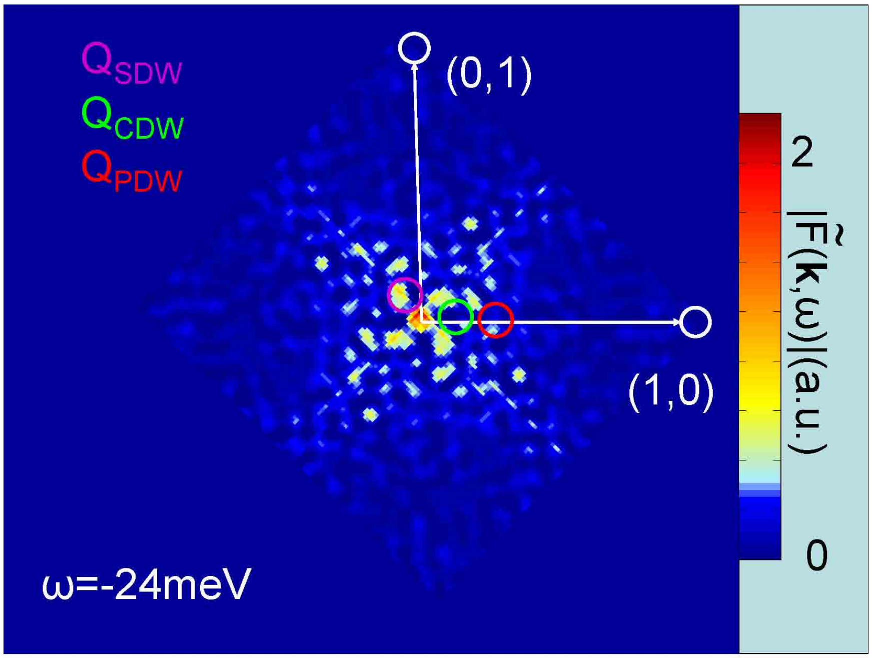

Figure B.20: $\tilde{F}(\mathbf{k}$,ω=-24meV,H=5T)

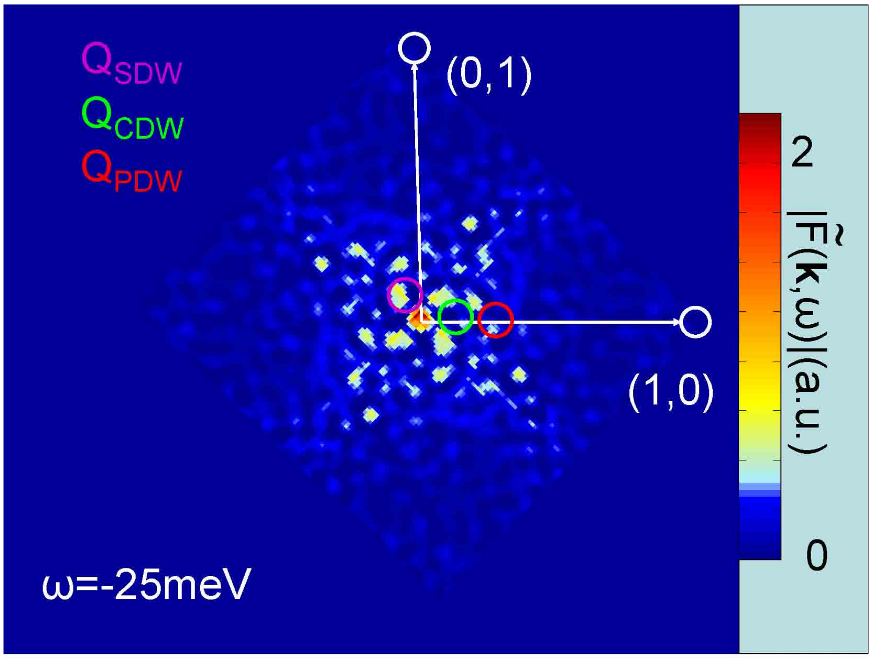

Figure B.21: $\tilde{F}(\mathbf{k}$,ω=-25meV,H=5T)

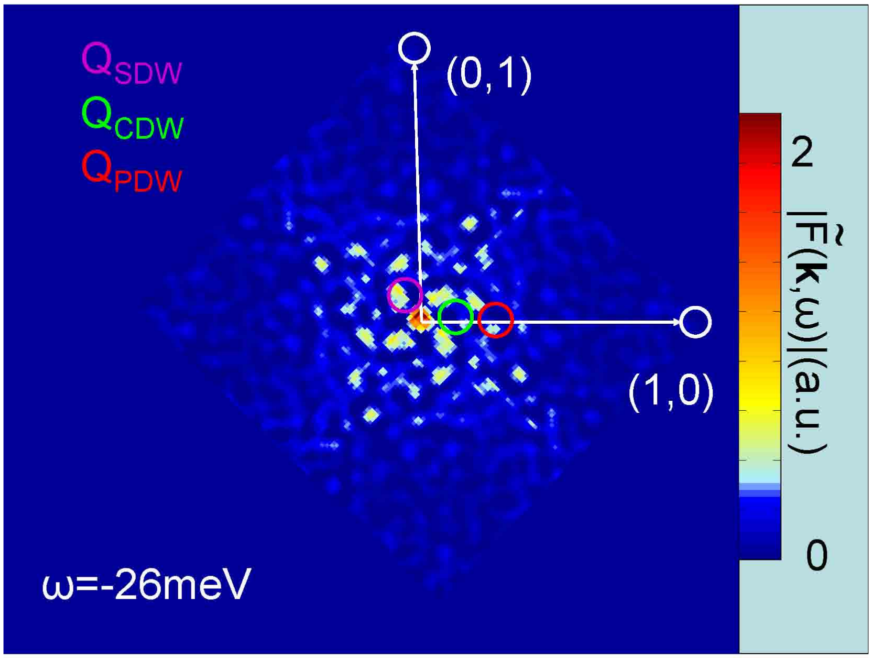

Figure B.22: $\tilde{F}(\mathbf{k},\omega$=-26meV,H=5T)

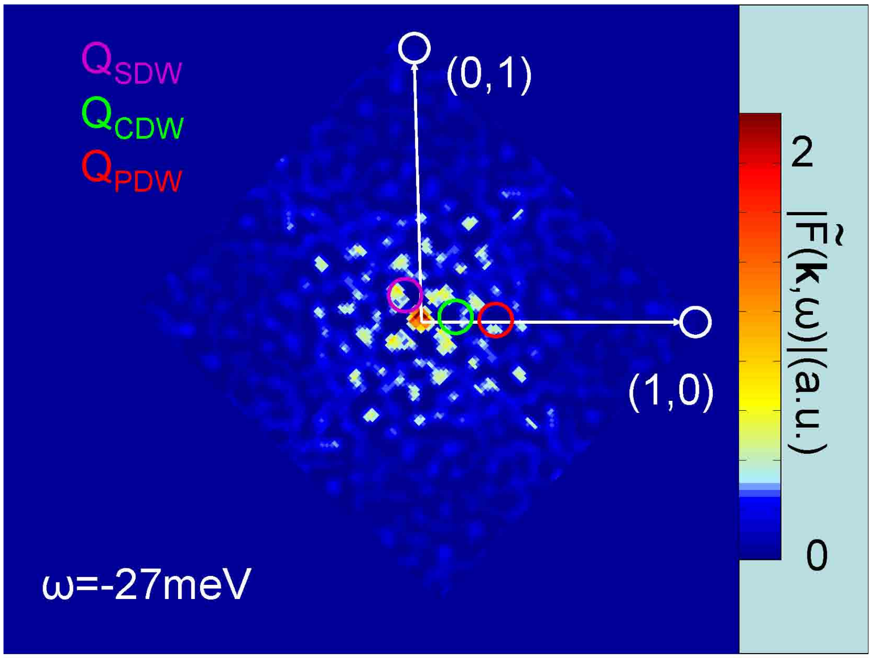

Figure B.23: $\tilde{F}(\mathbf{k},\omega$=-27meV,H=5T)

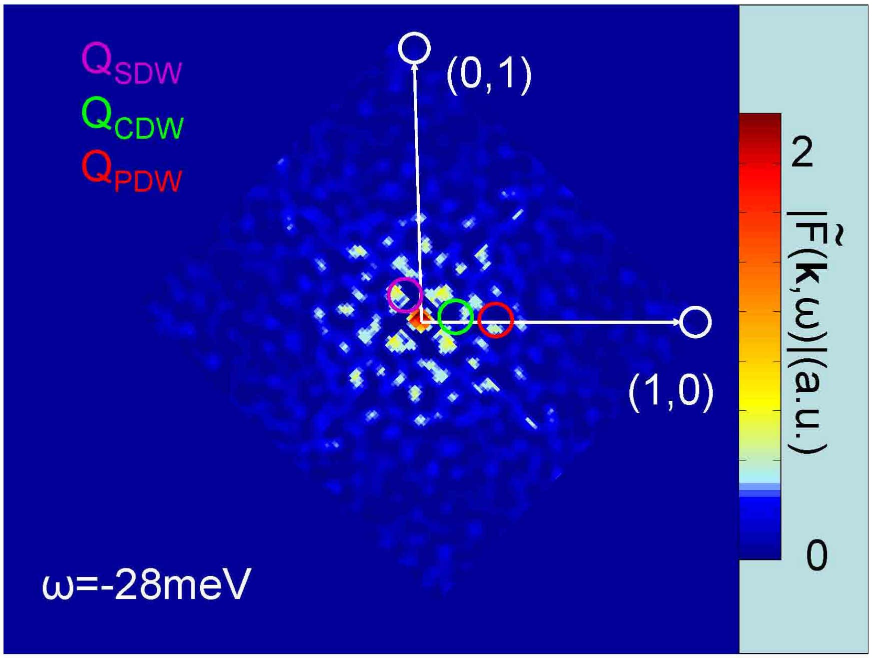

Figure B.24: $\tilde{F}(\mathbf{k},\omega\text{=-28meV,H=5T})$

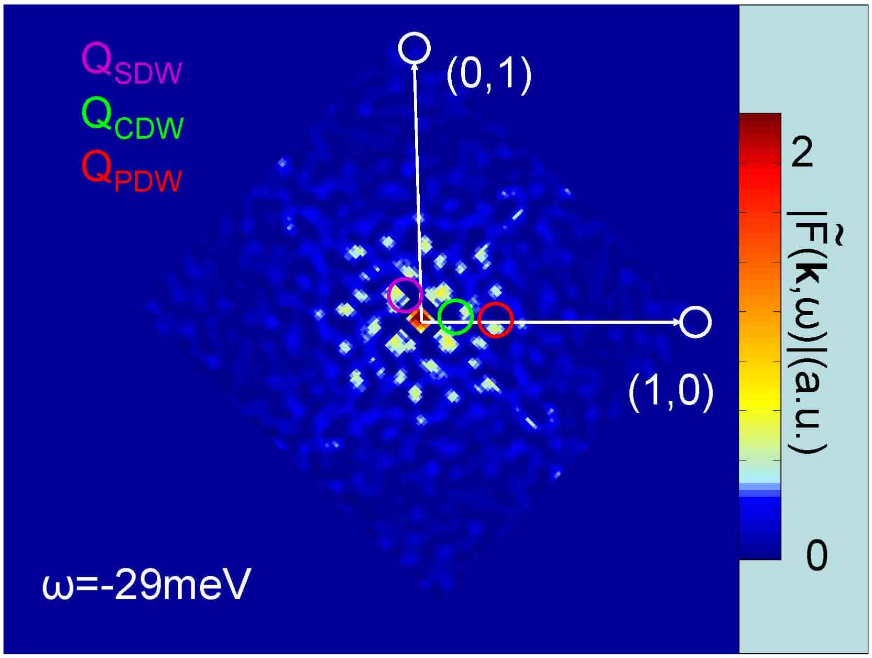

Figure B.25: $\tilde{F}(\mathbf{k},\omega\text{=-29meV,H=5T})$

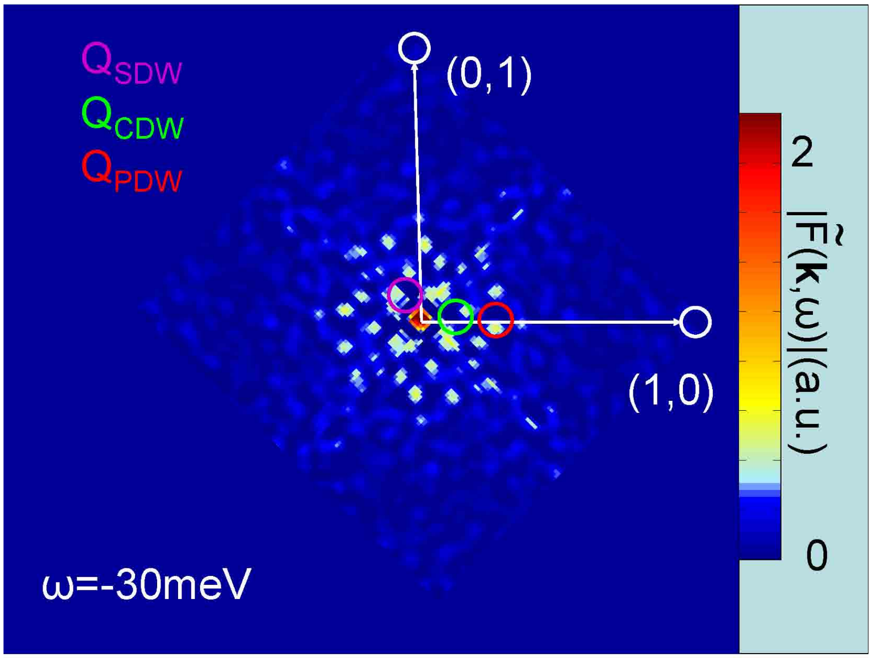

Figure B.26: $\tilde{F}(\mathbf{k}$,ω=-30meV,H=5T)

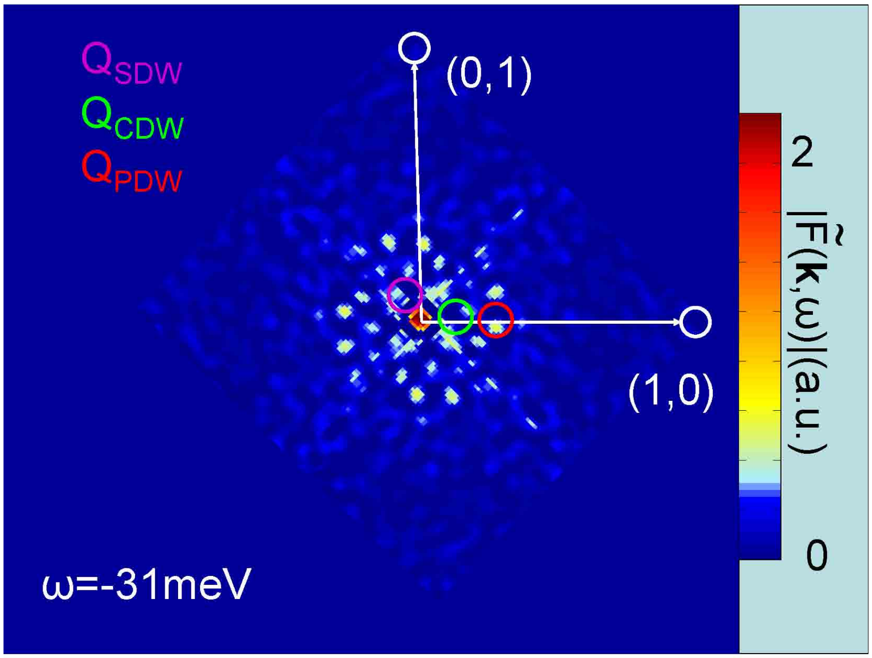

Figure B.27: $\tilde{F}(\mathbf{k}$,ω=-31meV,H=5T)

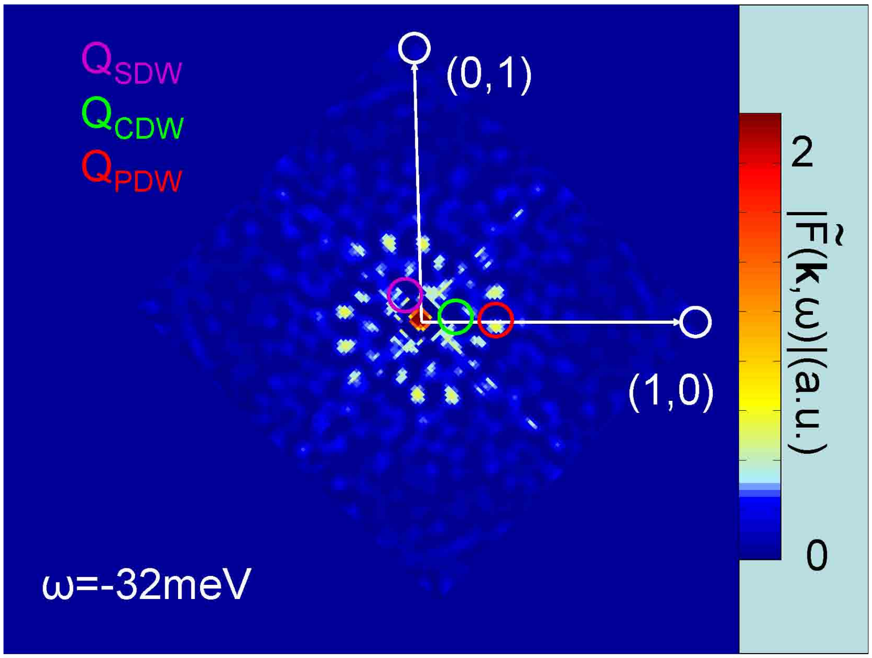

Figure B.28: $\tilde{F}(\mathbf{k}$,ω=-32meV,H=5T)

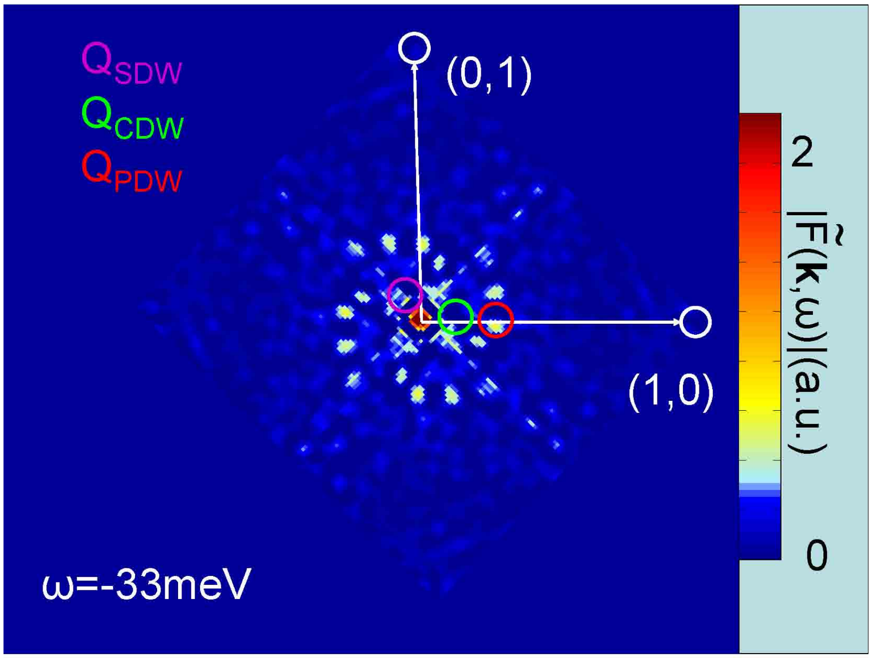

Figure B.29: $\tilde{F}(\mathbf{k}$,ω=-33meV,H=5T)

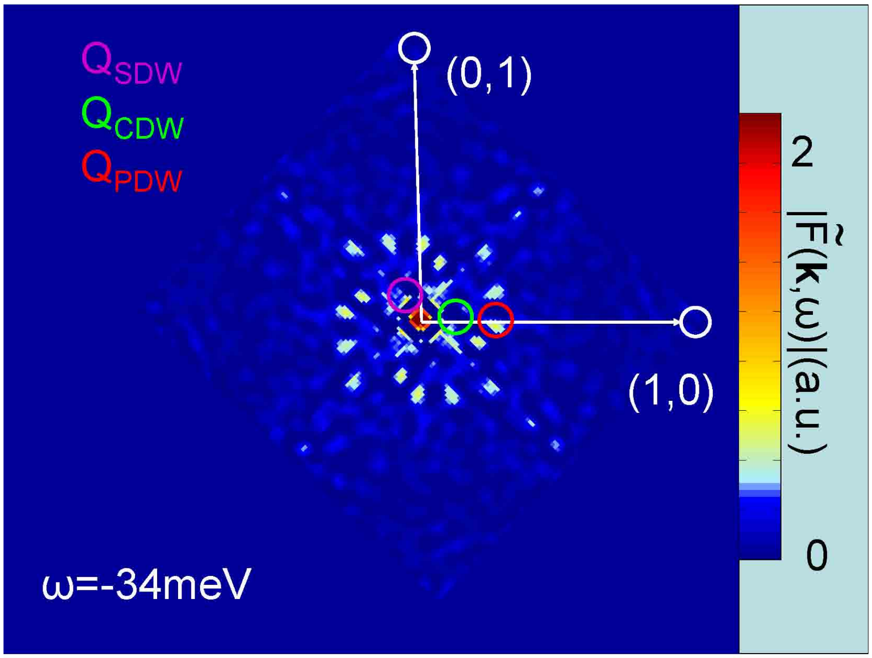

Figure B.30: $\tilde{F}(\mathbf{k},\omega$=-34meV,H=5T)

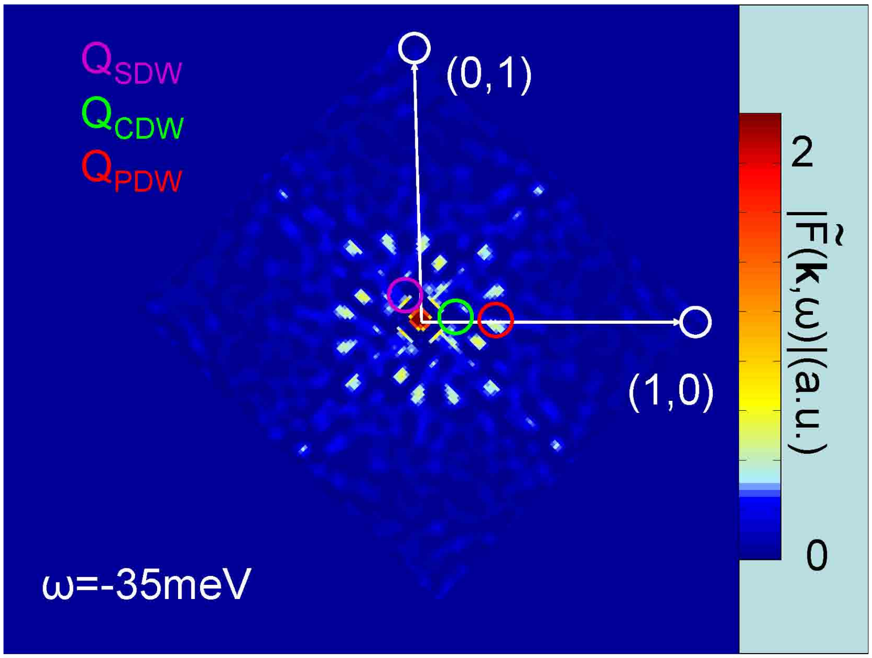

Figure B.31: $\tilde{F}(\mathbf{k},\omega$=-35meV,H=5T)

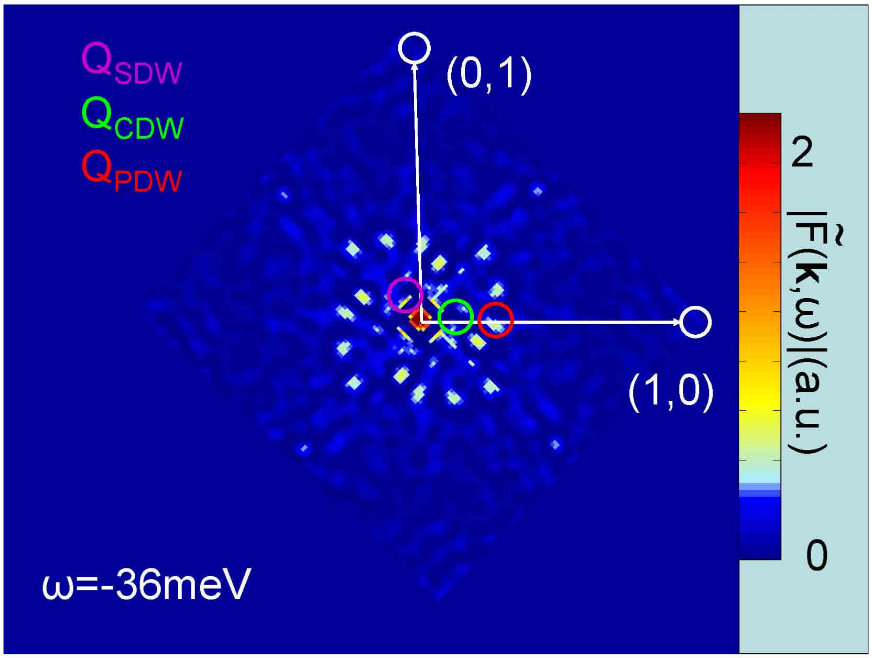

Figure B.32: $\tilde{F}(\mathbf{k},\omega$=-36meV,H=5T)

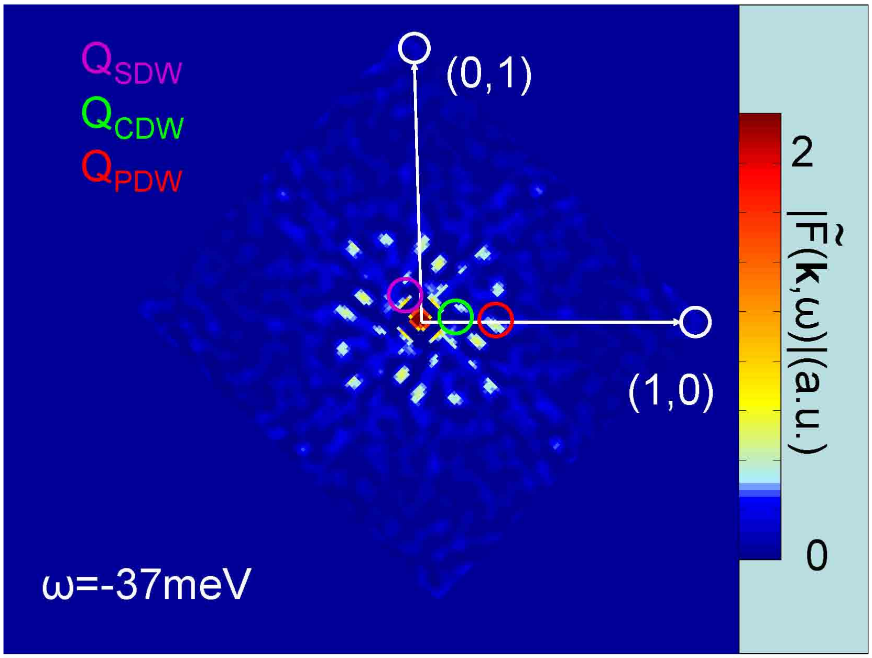

Figure B.33: $\tilde{F}(\mathbf{k},\omega$=-37meV,H=5T)

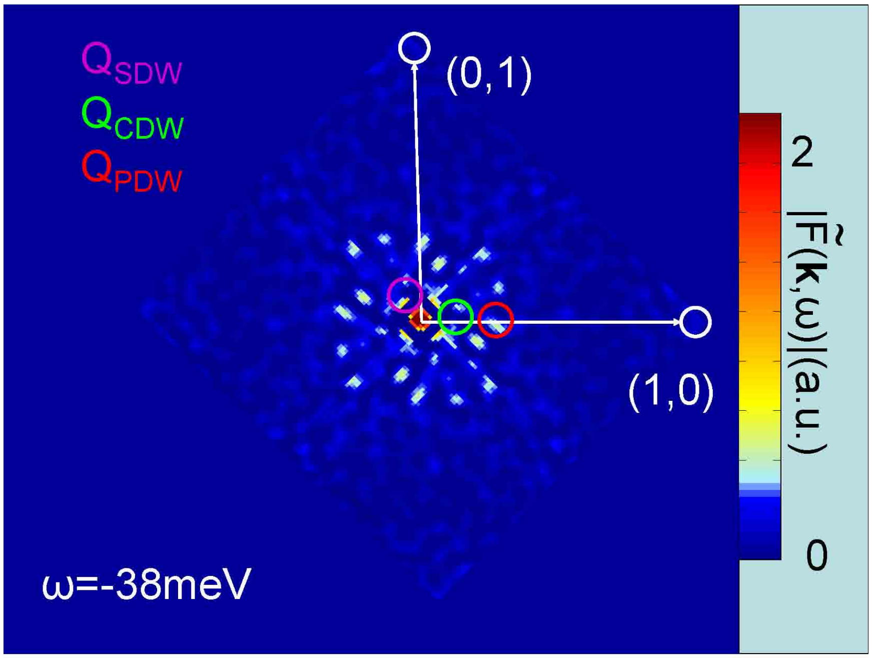

Figure B.34: $\tilde{F}(\mathbf{k}$,ω=-38meV,H=5T)

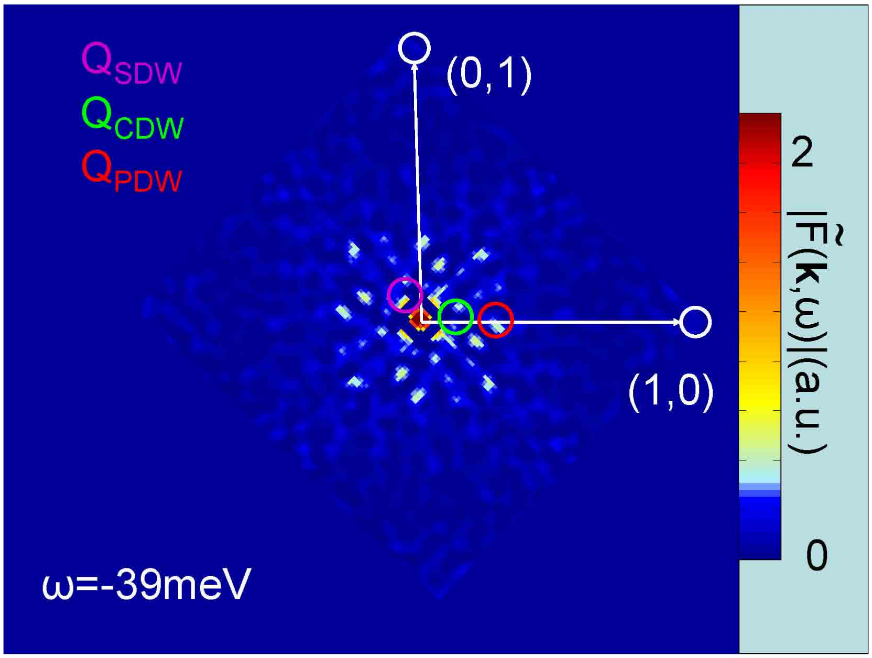

Figure B.35: $\tilde{F}(\mathbf{k}$,ω=-39meV,H=5T)

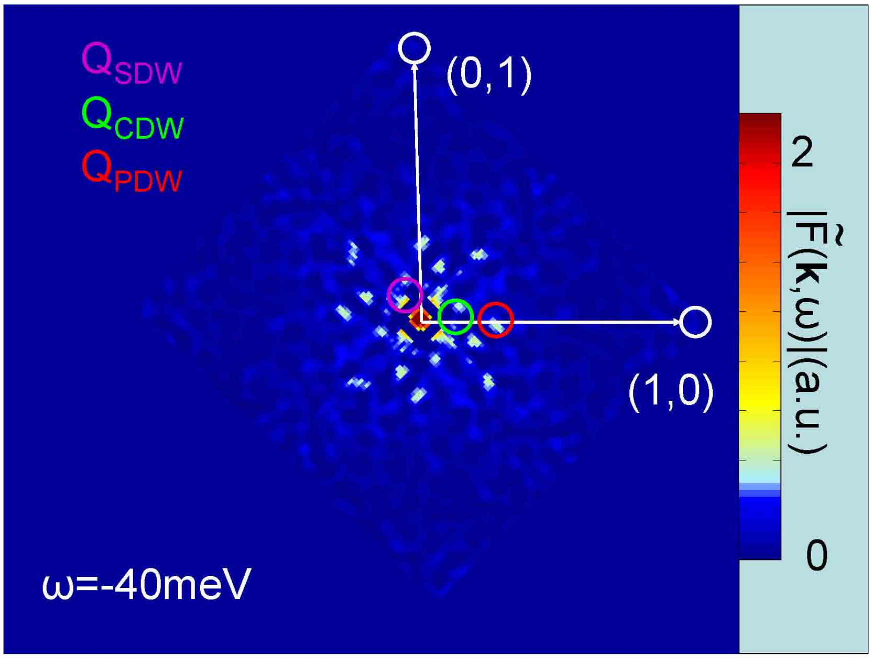

Figure B.36: $\tilde{F}(\mathbf{k}$,ω=-40meV,H=5T)

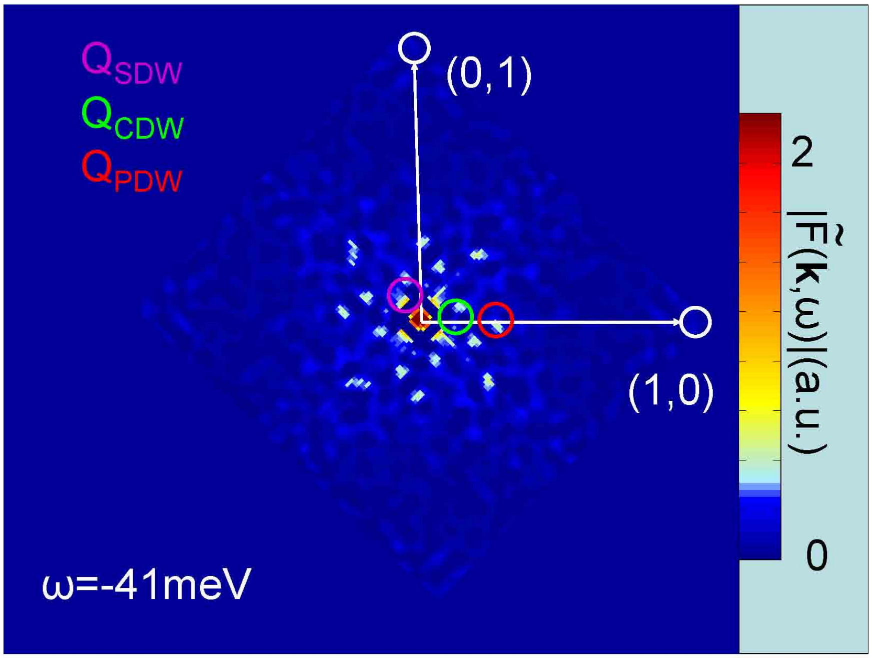

Figure B.37: $\tilde{F}(\mathbf{k}$,ω=-41meV,H=5T)

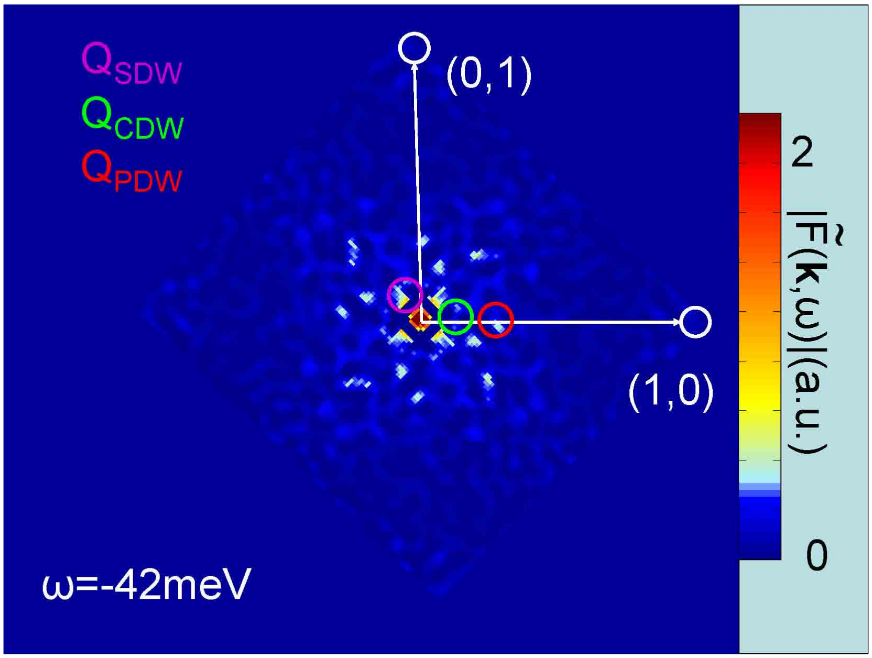

Figure B.38: $\tilde{F}(\mathbf{k},\omega$=-42meV,H=5T)

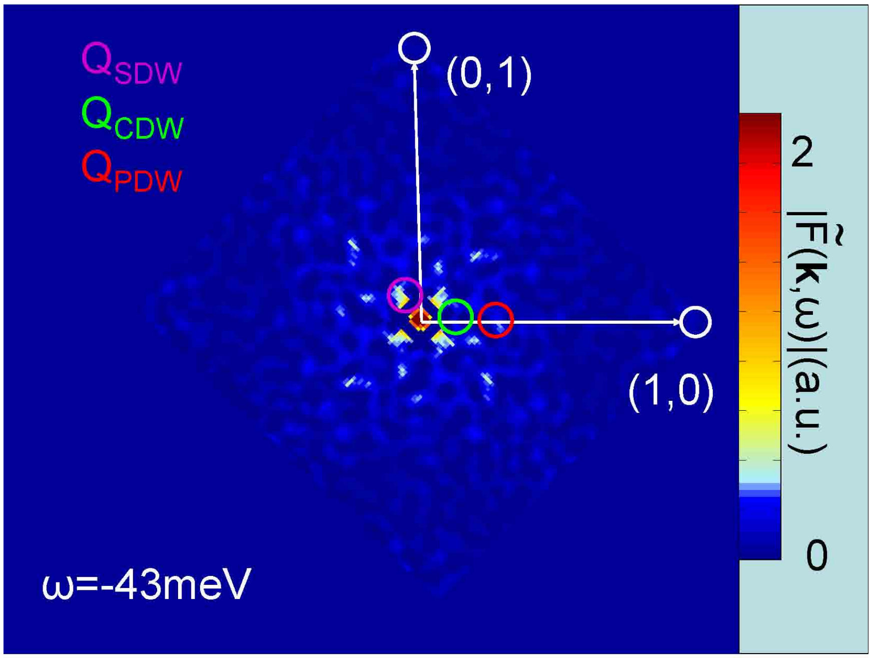

Figure B.39: $\tilde{F}(\mathbf{k},\omega$=-43meV,H=5T)

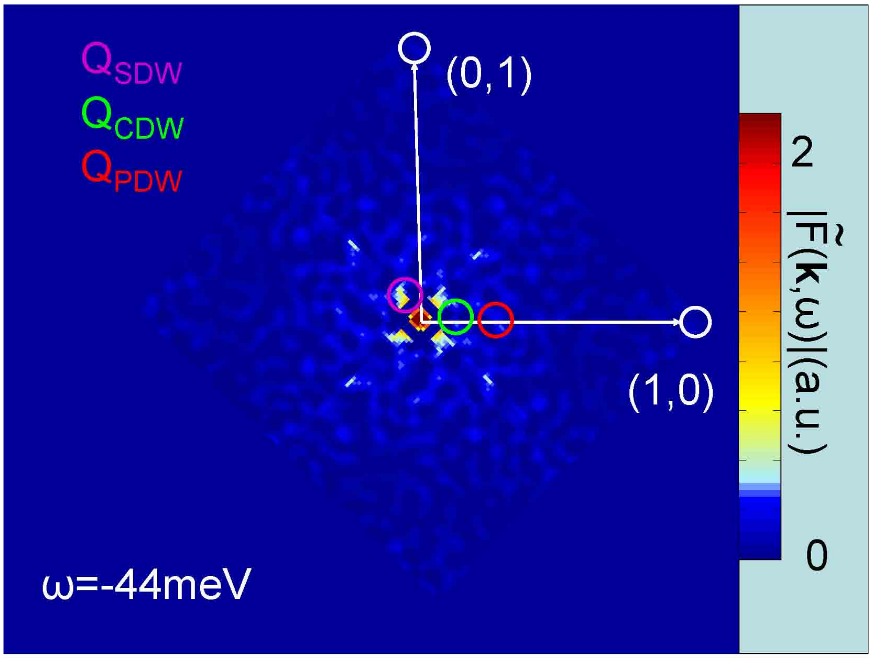

Figure B.40: $\tilde{F}(\mathbf{k}$,ω=-44meV,H=5T)

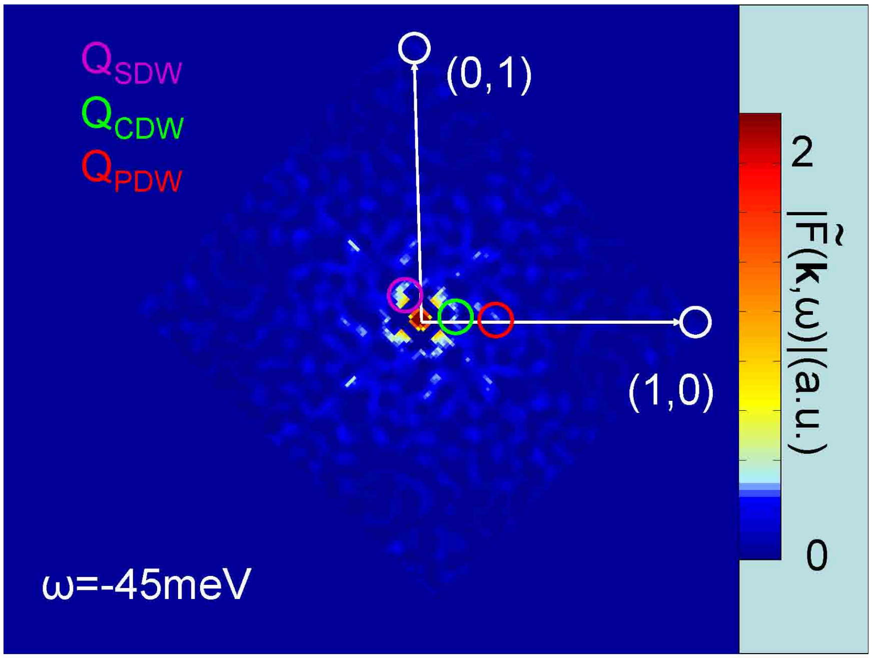

Figure B.41: $\tilde{F}(\mathbf{k}$,ω=-45meV,H=5T)

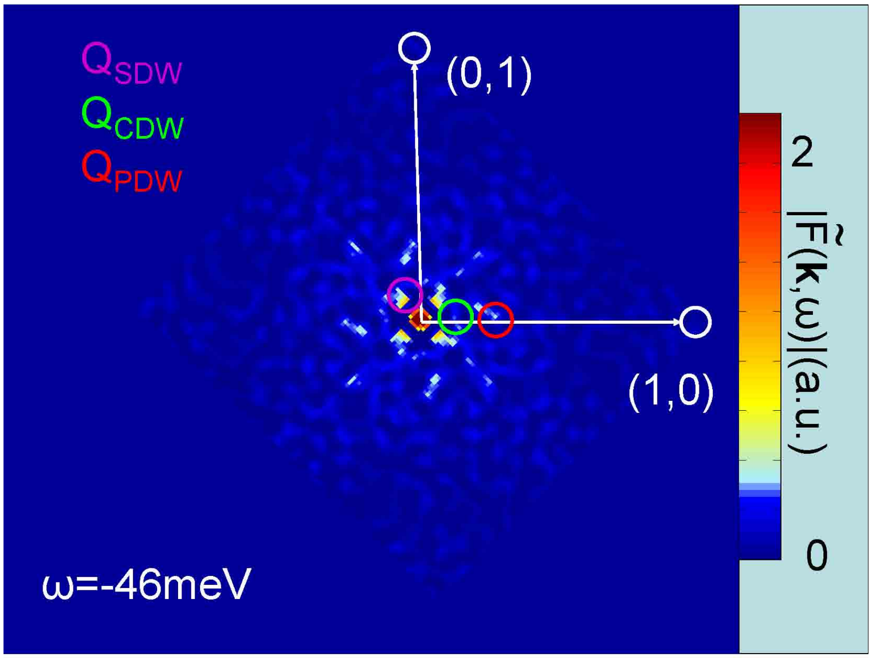

Figure B.42: $\tilde{F}(\mathbf{k},\omega$=-46meV,H=5T)

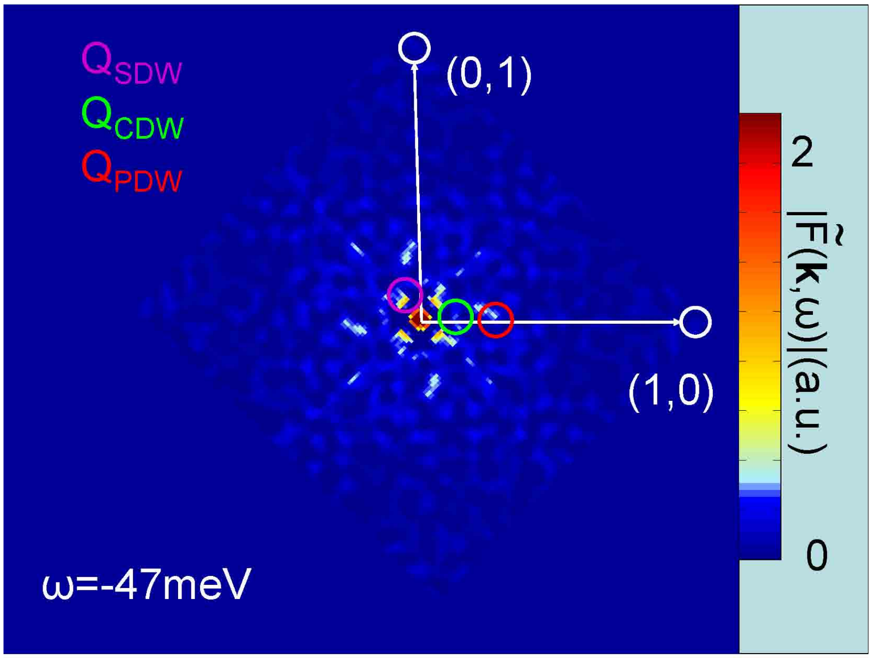

Figure B.43: $\tilde{F}(\mathbf{k},\omega$=-47meV,H=5T)

Appendix C

Progress toward development of a cryogenic scanning tunneling microscope/scanning electron microscope (STM/SEM)

Many challenges arise when performing scanning tunneling microscopy (STM) studies on inhomogeneous samples because of the limited maximum field-of-view ($\sim 10 \times 10\ \mu\mathrm{m}^2$) and slow scanning speed of STM for typical STM designs (∼ minutes or hours to scan the entire maximum field-of-view). However, the atomic scale resolution constant-current imaging and spectroscopy capabilities of STM provide a vital tool for characterizing local surface properties of materials and devices at the atomic scale. In contrast, scanning electron microscopy (SEM) offers fields-of-view ranging from approximately $100 \times 100\ \mathrm{nm}^2$ up to $1 \times 1\ \mathrm{mm}^2$ and can perform entire field-of-view scans in less than a second under ideal circumstances. However, the analytical characterization capabilities of SEM are limited to a maximum resolution of ∼10nm. A combined STM/SEM is expected to reduce the time for locating nano-scale devices and samples of interest within a large area of material from the order of weeks to hours. Additionally, an STM/SEM would allow characterization of samples using both STM and SEM techniques and would enable new studies to be performed by combining both techniques simultaneously. In this Appendix, we present progress to date on the development of a cryogenic scanning tunneling/scanning electron microscope (STM/SEM) for the Kavli Nanoscience Institute at Caltech. The cryogenic STM/SEM is expected to facilitate effective investigations of complicated nano-scale features over an extended spatial area using both STM and SEM techniques.

C.1 Overview and ultra-high vacuum (UHV) components

The cryogenic STM/SEM is designed to perform all operations under ultra-high vacuum (UHV) conditions and follows a design for UHV cryogenic STM operation similar to Ref. [193]. An overview illustration of the instrument is shown in Fig. C.1. As shown in the figure, analysis using both STM and SEM will be performed in the main analysis chamber of the UHV arrangement. The SEM electron column[1], for generating the electron beam for SEM imaging and analysis, and the detector will be inserted into angled conflat flanges near the top of the main analysis chamber to allow SEM imaging and analysis to be performed in the main analysis chamber. An XYZ and rotary manipulator (XYZR)[2] is mounted to the top of the main analysis chamber[3], and a cryo-cooler[4] is mounted through the middle of the XYZR manipulator and attached through a 10" conflat flange in order to provide a cold stage, moveable stage for the STM. The STM head is attached to the end of the cryo-cooler and may be located within the line-of-sight of the SEM column and detector, using the XYZR manipulator, for simultaneous STM and SEM analysis in the main analysis chamber. The XYZR manipulator can also position the STM in the lower section of the main analysis chamber for tip and sample exchange.

The SEM electron column used is a UHV compatible Schottky emission electron column with a variable beam energy from 1keV to 25keV. It is designed to fit into a 4.5" conflat flange on the STM/SEM with a working distance of 2.55". An additional 4.5" conflat flange is provided on the main analysis chamber to put the SEM at working distance of 0" relative to the centerline of the main analysis chamber. A custom flange can then be built and added to this flange to provide another working distance, in the event that a 2.55" working distance is inadequate for operation or if there is a clash of instrumentation. Detectors for backscattered and secondary electron emission will include

---

[1] FEI UHV Subsystem SEM, 2LE Schottky Emission Electron Column

[2] Omniax manipulator from VG Scienta, Inc. Simstep stepper motor and Simstep Motor controller for controlling XYZR motion also from VG Scienta, Inc.

[3] Custom chamber designed by the author and built by VG Scienta

[4] Helitran cryo-cooler from ARS, Inc.

an Everhart-Thornley detector for secondary electrons or a solid-state detector for backscattered electrons. More details on detector types may be found in Ref. [194].

Oxygen free high thermal conductivity (OFHC) thermal radiation shields[5] surround the STM and join it to the cold stages of the cryo-cooler. At the bottom of the main analysis chamber a wobble-stick is attached to provide in-vacuum motion in order to lower the OFHC radiation shields for STM tip or sample exchange. The STM/SEM analysis is performed in the top portion of the main analysis chamber with the OFHC thermal radiation shields raised, and the STM may be lowered to the bottom portion using the XYZ and rotary manipulator to lower the thermal radiation shields and exchange samples or tips. More details of the cryogenic operation and exchange of tips and samples are presented more fully in Section C.4.

An ion pump[6], turbomolecular pump[7], and scroll pump[8] serve to pump out the STM/SEM chambers. To reach UHV conditions, the turbomolecular, the scroll pump, and the ion pump will be used to initially evacuate the main analysis chamber. Upon reaching UHV vacuum conditions, the turbomolecular pump and scroll will be disengaged, and the ion pump will maintain UHV during sensitive measurements using the STM and SEM. The ion pump will also be used to maintain UHV conditions in the main analysis chamber while the turbomolecular and scroll pump evacuate the load-lock chamber for introducing tips and samples for exchange. Gate valves[9] are installed to allow isolation of the pumps from the main analysis chamber as needed. An ion gauge and Pirani gauge[10] will be used for measurements of the pressure near the STM/SEM from atmospheric pressure to UHV conditions.

A load-lock chamber consisting of a six-way cross, optical viewports, 6” gate valve[11], a vacuum carousel[12] for holding tips and samples to be exchanged, and a linear, rotary manipulator[13] for performing exchange of tips and samples is attached to the side of the main analysis chamber. The

---

[5] Constructed from OFHC copper, 0.032” thick

[6] LION 40 Ion Pump with 2 ports, SafeLION Feedthrough and Bakeout heater purchased from Kurt J. Lesker Co.

[7] TMU 071YP TurboDrag Pump with TC 100 on-board electronics purchased from Pfeiffer Vacuum

[8] XDS5 Scroll Pump wired for 115V purchased from Kurt J. Lesker Co.

[9] Two 4.5” copper bonnet gate valve purchased from Kurt J. Lesker

[10] IGC3 ion gauge controller with Pirani Module and adaptor cable purchased from VG Scienta, Inc.

[11] Softshut 6” UHV Gate Valve purchased from VG Scienta, Inc.

[12] Rotary, linear direct drive from MDC Vacuum

[13] Rotary Linear Magnetic Drive, 24” linear travel, 2 3/4” ODCF purchased from VG Scienta, Inc.

load-lock chamber is evacuated with the large gate valve, that separates the load-lock chamber and main analysis chamber, closed ([7] in Fig. C.1), and tips or samples are introduced into the main analysis chamber using the linear, rotary manipulator.

C.2 Design of the STM

The STM for the STM/SEM is designed similarly to the STM described in Chapter 3; however, significant modifications have been made to further optimize the performance at cryogenic temperatures and to reduced the susceptibility of the STM to vibrations. The design of the molybdenum STM head is shown as a 2D image of the solid model in Fig. C.2a and in actuality in Fig. C.2b.

The STM incorporates XY and Z coarse-motion stages with the same working principle and design as described in Fig. 3.2, 3.5, and 3.6. Similarly, the piezoelectric tube scanner that provides fine STM tip scanning motion is the same type of piezo tube scanner as described in Fig. 3.3.

One difference from the previous design is that the body of the STM on the STM/SEM is made out of molybdenum, instead of Macor[14]. An advantage of a molybdenum STM body is that it has more mass ($\sim$ 0.445kg) than a Macor STM body($\sim$ 0.100kg). The larger mass leads to a lower resonant mechanical frequency of the STM head when suspended from the rest of the STM/SEM instrumentation and less susceptibility to mechanical vibrations in general. Further, a molybdenum body will have a larger thermal mass than a similar head made out of Macor, and the enhanced thermal mass will reduce temperature fluctuations during STM measurements. In addition, a molybdenum body, compared to a Macor body, will have a higher thermal conductivity and a smaller thermal gradient between the cold stage of the cryo-cooler and the STM tip and sample stage. Finally, the thermal contraction/expansion coefficient of molybdenum is comparable to that of piezoelectric material, which is ideal for constructing an STM stage.

Due to the fact that the STM body is made out of molybdenum, wires and electrical connections must be electrically isolated from the molybdenum body. Wires were insulated from the STM body

---

[14] Macor is a machineable ceramic available from Corning Inc.

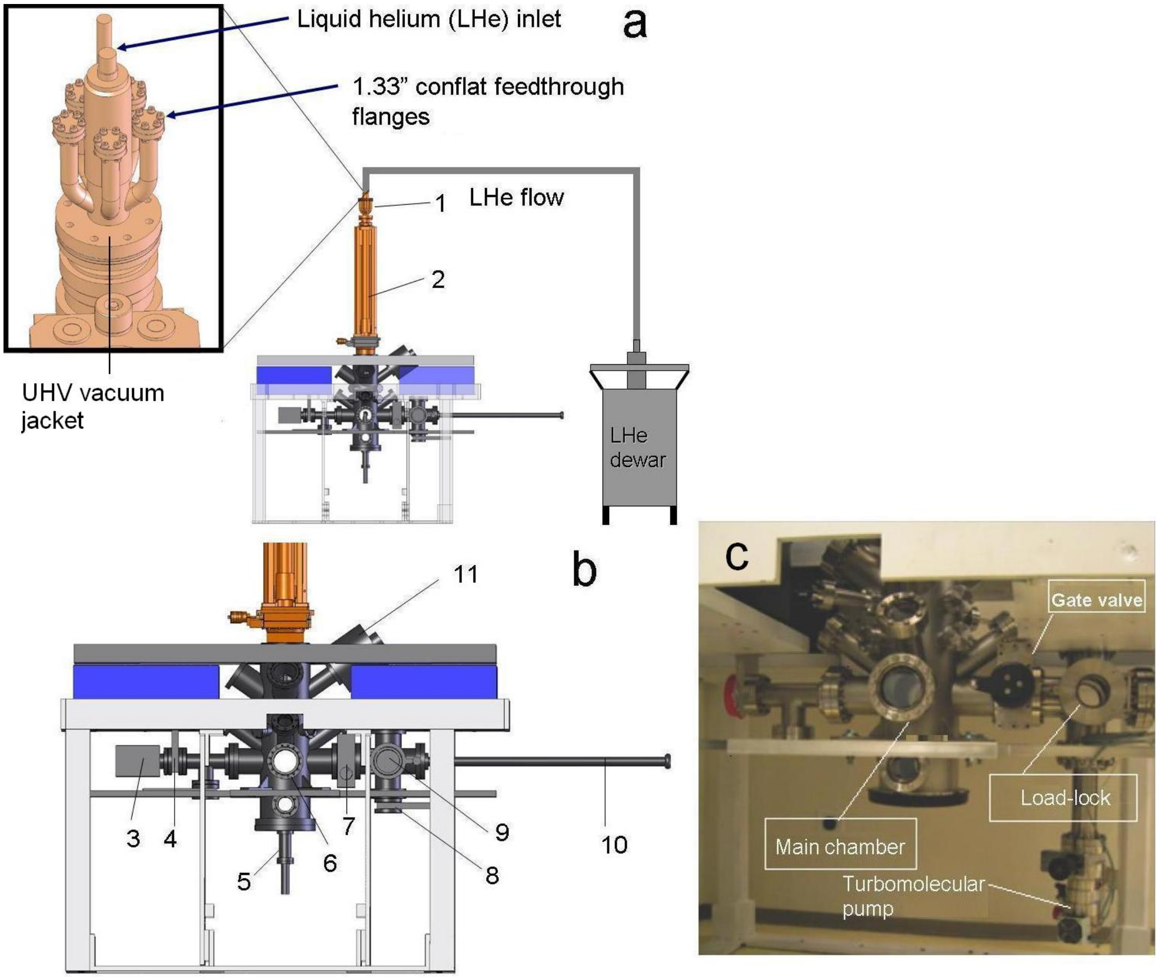

Figure C.1: Schematic illustration of the cryogenic STM/SEM: [1]–Helitran cryo-cooler, [2] Omniax XYZ and rotary (XYZR) manipulator, [3]–LION 40 Ion pump, [4]–Gate valve to isolate ion pump, [5]–Wobble stick, [6]–Main analysis chamber, [7]–Large gate valve separating the load-lock chamber and main analysis chamber, [8]–Gate valve for the turbomolecular pump and scroll pump, [9]–Load-lock door and six way cross for loading tips and samples onto the vacuum carousel, [10]–Linear, rotary manipulator for tip and sample exchange, [11]–UHV 2LE SEM electron column. (a) Schematic overview of the cryogenic STM/SEM system showing a liquid helium dewar attached to the cryo-cooler. Liquid helium flows through the cryo-cooler. The cryo-cooler is designed so that bubbling of liquid helium (LHe) during flow is eliminated in order to reduce vibrations. Five 1.33" conflat flanges are fed through a UHV vacuum jacket along with cryo-cooler cold tip, as shown in the expanded inset. Two BNC connectors and three 10-pin instrumentation electrical feedthrough connections are attached to these conflat flanges, along with wiring, to provide electrical connections to the STM head and temperature control on the STM head. In addition, the LHe dewar may placed onto an additional vibration isolation platform or hung from the ceiling using flexible attachments to further reduce coupling of vibrations to the STM/SEM. (b) Side-view close up model of the cryogenic STM/SEM. (c) Picture of the actual cryogenic STM/SEM.

using ceramic beads[15]. The piezoelectric stack connections were insulated from the molybdenum body by attaching alumina plates[16] to the underside of the pizeo stacks with epoxy[17]. The alumina plates were then attached to thin, square Shapal[18] plates, which were attached to the molybdenum using epoxy[19].

Another difference from the previous STM design is that the new STM body was machined out of a single piece of material so that the XY and Z coarse-motion stages are combined into a monolithic structure for XY and Z coarse-motion capability. In contrast, the STM described in Chapter 3 has separate XY and Z coarse motion stages that interlock together for combined XY and Z coarse-motion capabilities. It is expected that the monolithic design will reduce the susceptibility of the STM to mechanical vibrations between the XY and Z coarse-motion stages.

C.3 Vibration and acoustic noise isolation

The cryogenic STM/SEM required instrumentation to isolate the apparatus from vibrational and acoustic noise sources. Examples of noise sources present in the STM/SEM laboratory space include building vibrations and acoustic and vibrational noise from mechanical pumps. To isolate from these noise sources the STM/SEM was constructed on a concrete slab isolated from the rest of the laboratory, was loaded onto a spring loaded vibration isolation table, and was surrounded by thick plastic curtains to damp acoustic noise[20].

A concrete isolation slab, of dimension $5' \times 5.5'$, was constructed in the STM/SEM laboratory space to reduce the transmission of high frequency vibrations to the apparatus. The isolation slab was constructed by contractors, who dug a pit approximately $4'$. The pit was subsequently filled with compacted fill (95% compaction fill or greater) and topped with a 3” layer of sand to a net height of approximately $2'$. On top of the sand a $2'$ thick concrete slab was poured, and a sealant

---

[15] Fish-spline ceramic beads available from Kurt J. Lesker Co.

[16] 0.020” thick Superstrates manufactured by Coors Ceramic Company

[17] H74 epoxy purchased from Epotek

[18] Shapal is a machineable ceramic with slightly improved thermal conductivity compared to Macor and is available from Ceramic Substrates and Components Ltd.

[19] H74 epoxy

[20] Assembly and testing of the STM/SEM instrumentation for vibration and acoustic noise isolation was performed by the author and Guglielmo Lockhart. The work was performed by Guglielmo Lockhart as his SURF project during the summer of 2008

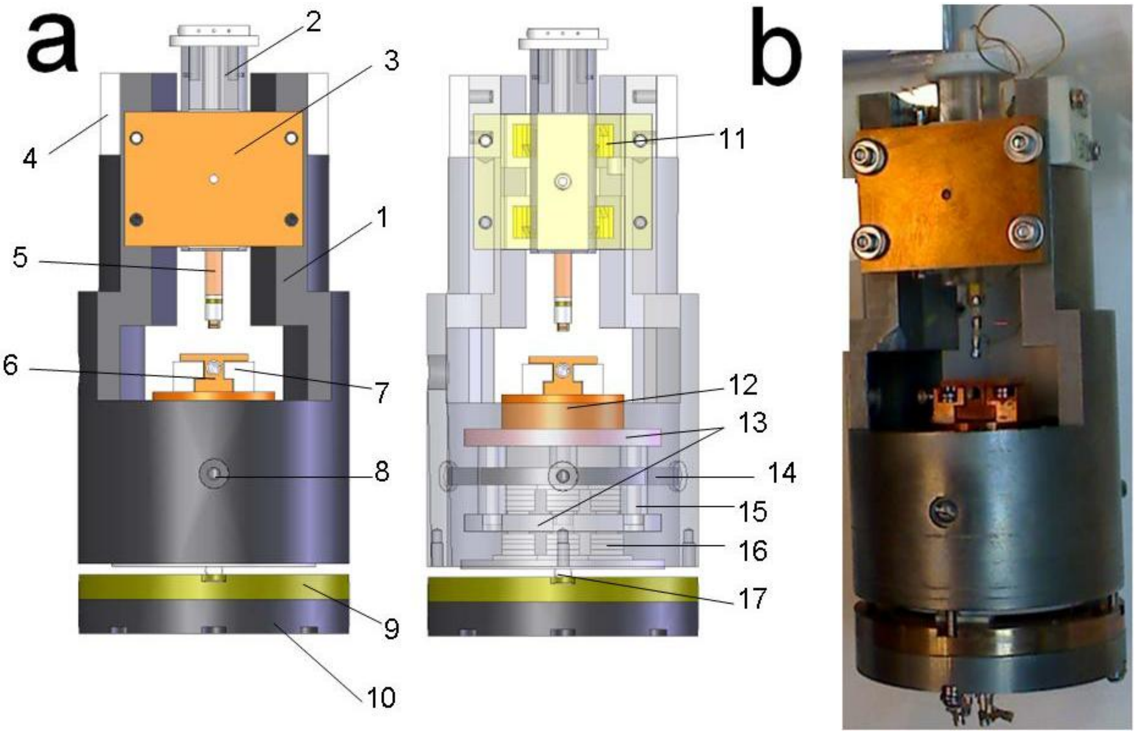

Figure C.2: Molybdenum STM head constructed and designed by the author. (Machining of parts was done by Nils Asplund and by the Physics Department Machine Shop staff under the direction of Richard Paniagua): (a) Left panel is a 2D image of the solid model (created in Solidworks CAD software). Right panel is a semi-transparent model of (a). [1]–Molybdenum body, [2]–Sapphire prism for Z coarse-motion stage, [3]–Copper-beryllium spring for adjusting tightness of piezo shear stacks on the sapphire prism for Z coarse-motion stage, [4]–Shapal electrical feedthrough for Z stage connections, [5]–Piezo tube scanner, [6]–Oxygen free high thermal conductivity (OFHC) removable copper stage, [7]–OFHC fixed copper stage fixed stage, [8]–Through hole for stainless steel (SS) screw to secure [14], [9]–Copper-beryllium spring for adjusting tightness of piezo shear stacks against the sapphire plates for the XY coarse-motion stage, [10]–Molybdenum bottom plate with Shapal electrical feedthrough stages for wiring to the XY coarse-motion stage piezo shear stacks, [11]–Piezo shear stack for Z stage, [12]–OFHC copper base for temperature sensors and heaters, [13]–Sapphire plates for XY coarse-motion stage, [14]–Molybdenum plate for supporting half of the XY stacks, [15]–Sapphire posts that link the two XY sapphire plates together, [16]–Piezo shear stack for XY stage, [17]–Sapphire ball for adjusting the the tightness of the XY coarse-motion stage piezo shear stacks. The functionality of the Z coarse-motion stage is described more fully in Fig. 3.5.

was filled between the isolation slab and the building floor grade. When finished, the concrete slab was flush with the floor of the lab space.

The entire STM/SEM apparatus is mounted to a vibration isolation table to reduce low frequency vibrations, and a 2D image of the solid model of the vibration isolation table arrangement is shown in Fig. C.3. The table is comprised of a steel support table, four vibration isolation platforms, and two aluminum plates. The steel table was designed by the author and built to specifications[21]. It approximately weighs one ton and sits directly on the aforementioned concrete isolation slab. The four vibration isolation platforms[22] are located on the four corners of the steel support table, and the 3"-thick top aluminum plate[23] sits directly on the vibration isolation platforms. The STM/SEM apparatus is mounted to the 3"-thick top plate, and a 1"-thick bottom aluminum plate[24] is suspended from the bottom of the STM/SEM apparatus. The bottom plate is designed to support additional STM/SEM parts and to add structures to support the UHV vacuum chamber parts. For instance, a support structure for the linear/rotary manipulator shown in Fig. C.1 is needed to prevent mechanical stress on this part, and a support structure can be machined and attached to the bottom aluminum plate.

The four vibration isolation platforms act like compression springs, and their effective spring constants are adjusted for optimal performance of the vibration isolation table. The spring constant of each vibration isolation platform may be adjusted using a simple crank mechanisms installed by the manufacturer until the table is supported vertically by the springs. Additionally, two horizontal sets of springs maintain the horizontal orientation of the STM/SEM. Ballast weights may be added to properly load the entire vibration isolation table[25]Upon proper tuning of the spring constants, the mechanical resonant frequency of the vibration isolation table in the vertical and horizontal directions is $\sim$0.5Hz.

To damp acoustic noise, thick plastic curtains on guide rails were installed around the entire

---

[21] Steel table built and welded together by CenterLine Welding, under the direction of Dale Giese

[22] BM-1 Benchtop Vibration Isolation platforms purchased from Minus K technology. Each platform can support up to 700 lbs

[23] 3" aluminum plate designed by author and machined to specification by the D-M-E Co.

[24] 1" aluminum plate designed by the author and machined by the D-M-E Co.

[25] The ballast weights consisted of concrete blocks encased and sealed in plastic boxes

STM/SEM apparatus, and the curtains were designed to prevent transmission of acoustic noise into the STM/SEM measurement area, as shown in Fig. C.3b. Additionally, the walls and doors of the STM/SEM room were designed with a Sound Transmission Class (STC) rating of approximately 45 to prevent the transmission of noise through the laboratory walls. (An STC rating is an ASTM International Classification standard rating that describes the ability of walls and doors to attenuate sound transmission for 16 standard frequencies from 125 Hz to 4000 Hz.)

The acoustic curtains were not found to significantly reduce acoustic noise levels inside the lab space. Calibrated microphone measurements using a condenser microphone and pre-amplifier did not detect a significant difference in acoustic noise levels with and without the acoustic curtains surrounding the instrumentation. The acoustic noise levels in the lab space are already expected to be low due to the STC 45 doors and walls, and it appears as though the curtains provide a negligible improvement. Additionally, an air vent is positioned within the space surrounded by the curtains. The air vent is likely the dominant noise source in the lab space, and curtains are ineffective against this acoustic noise source. Future measurements with the STM/SEM are needed to characterize the susceptibility of STM and SEM measurements to acoustic noise. It is possible that the current acoustic noise levels will not significantly affect actual STM/SEM measurements. Additional measures to reduce acoustic noise[26] may be implemented as needed.

To test the performance of the vibration isolation instrumentation, we performed accelerometer measurements of the vibration levels. The accelerometer measurements were performed by attaching an accelerometer to the support leg of the steel support table (no vibration isolation) and to the bottom aluminum plate of the vibration isolation table (with vibration isolation) for comparison. The results are shown in Fig. C.4. It is found that the vibration levels are significantly reduced over the frequency range up to 125 Hz when measured on the vibration isolation table compared to the steel support leg. Most notably, a significant vibration level above the noise level was detected at a frequency of 11Hz on the steel support leg. This frequency is likely the resonant building vibration frequency, and it is observed that this vibration level was significantly damped by the vibration

---

[26] (a) Acoustic damping blankets could be installed in addition to the plastic curtains. Blankets may be purchased from All Noise Control, for example. (b) Bass absorbing traps could be added as well, and may be purchased from McMaster-Carr, for example

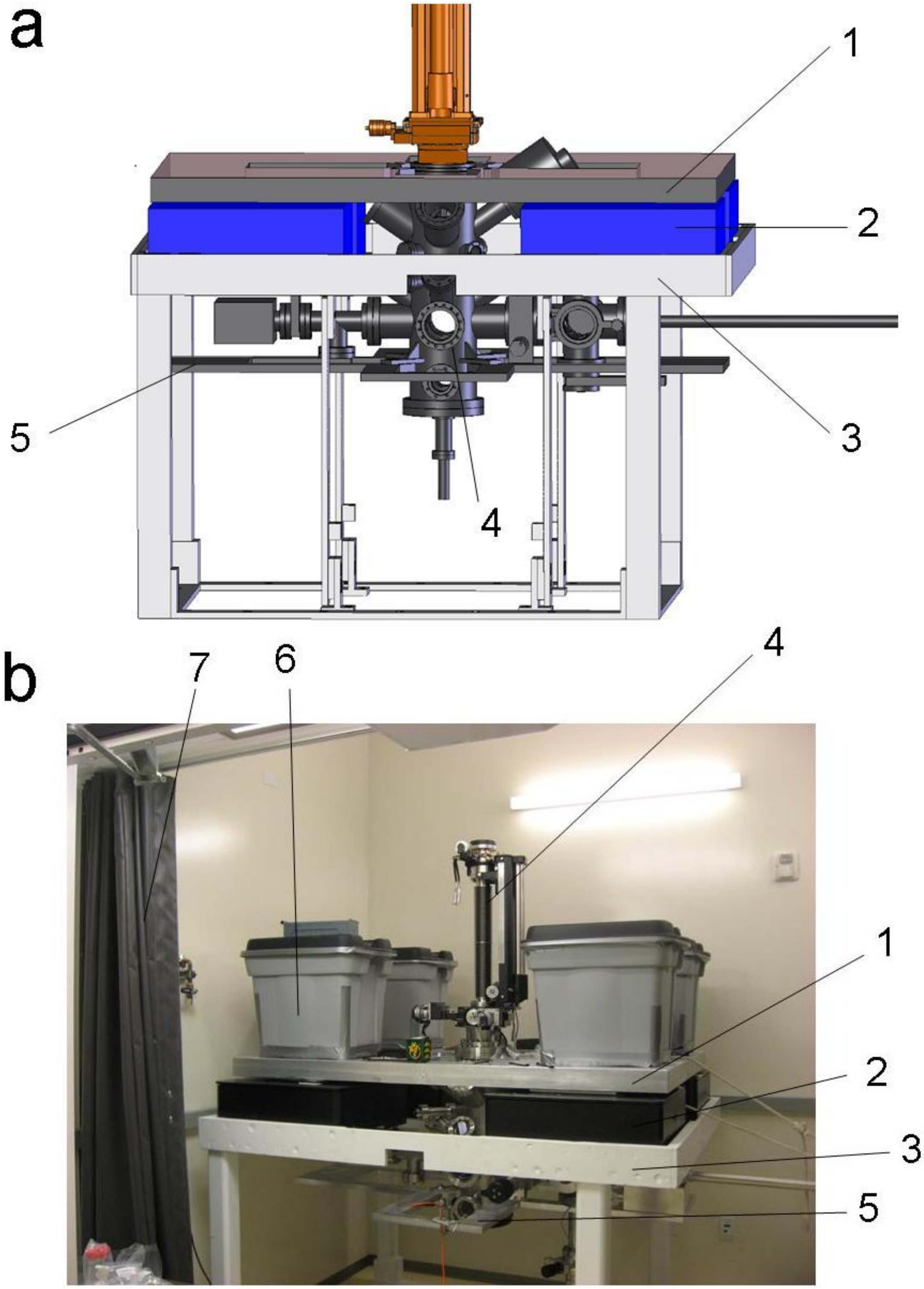

Figure C.3: Vibration isolation table for the cryogenic STM/SEM: [1]–Top 3”-thick aluminum plate, [2]–Vibration isolation spring platforms from Minus K Technology, [3]–Steel support table, [4]–STM/SEM apparatus main analysis chamber, [5]–Bottom 1”-thick aluminum plate. [6]–Ballast weights, [7]–Thick plastic curtains. (a) Two-dimensional image of the solid model of the vibration isolation table and STM/SEM. (b) Actual STM/SEM housed in its laboratory space.

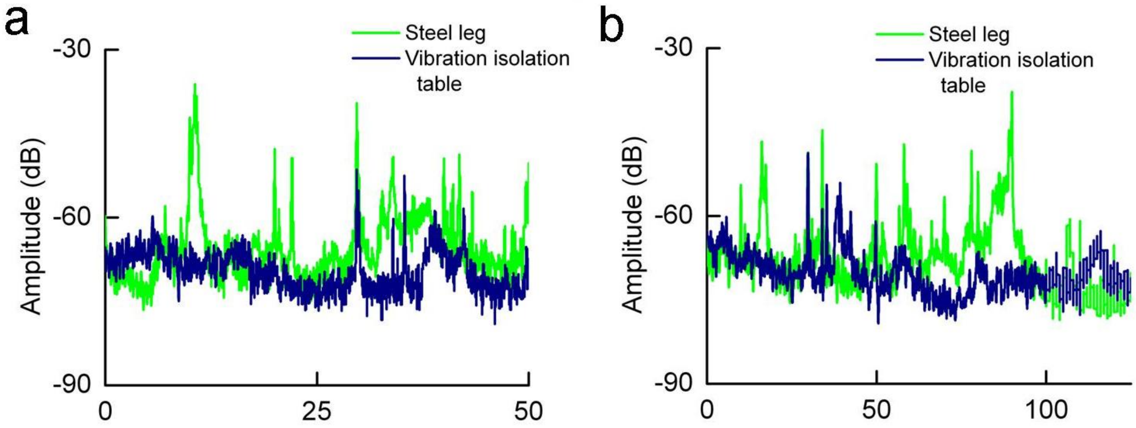

Figure C.4: Vibrational noise characterization for the cryogenic STM/SEM: (a) 0–50Hz vibration levels for the accelerometer attached to the steel leg of the steel support table (no vibration isolation) and for the accelerometer on the bottom aluminum plate of the vibration isolation table (with vibration isolation). (b) 0–125Hz vibration levels for the accelerometer attached to the steel leg of the steel support table (no vibration isolation) and for the accelerometer on the bottom aluminum plate of the vibration isolation table (with vibration isolation).

isolation table.

C.4 Cryogenic operation and STM tip and sample exchange in-situ

Cooling of the STM of the STM/SEM is performed under UHV conditions by a continuous flow cryo-cooler. The cold tip of the cryo-cooler provides the main cooling to the STM head, and the temperature is controlled by adjusting the cryogen flow rate using a fine needle valve on the cold tip and by using a heater wrapped around the cold tip. The cryo-cooler manufacturer also provides a secondary cold connection for an outer thermal radiation shield. The secondary connection point on the cryo-cooler is cooled by helium exhaust gas from the flow of liquid helium internal to the cryo-cooler. Two thermal radiation shields will be used to shield the STM from heat sources. The STM will be linked directly to the cold tip and surrounded by an inner thermal radiation shield connected to the cold tip. An outer thermal radiation shield will be connected to the secondary cold connection and surround the STM and inner radiation shield. Should mechanical vibrations

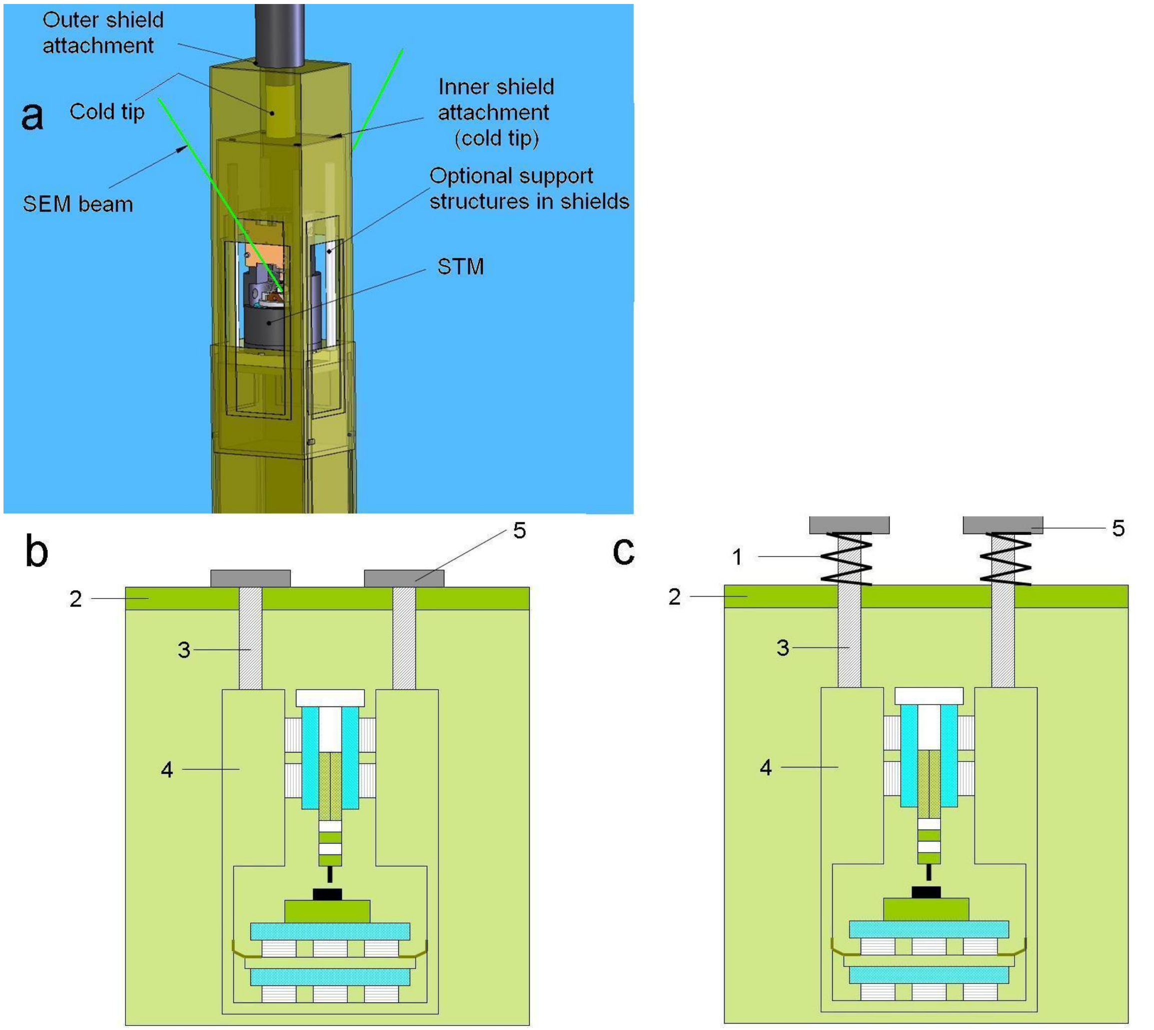

Figure C.5: Illustration of thermal radiation shields for the cryogenic STM/SEM: (a) Two-dimensional image of the solid model for the inner and outer thermal radiation shields of the cryogenic STM/SEM and their attachments to the continuous flow cryo-cooler. The inner radiation shield attaches directly to the cold tip of the cryo-cooler. The outer thermal radiation shield attaches to the secondary cold connection of the cryo-cooler, which is cooled by returning helium gas inside the cryo-cooler. The shields are designed to lower for tip and sample exchange and raise for STM/SEM measurements. Small holes, to allow the SEM beam to reach the STM sample stage and to allow the secondary and backscattered electrons to be detected, will eventually need to be cut into the shields. [1]–Compression springs, [2]–Inner shield attachment: Top plate of the inner radiation shield which attaches directly to the cold tip, [3]–#10-32 Stainless steel (SS) threaded rod. The SS rod is threaded into the STM head. The SS threaded rod fits through a through-hole in the inner shield attachment, and may be secured directly to the inner shield attachment using washers and nuts or compression springs may be added, [4]–STM head inside the inner radiation shield, [5]–Attachment point for design (b) or large washers to hold the compression springs in place for design (c). (b) Current design for attaching the STM head to the inner radiation shield. This design will minimize vibrations between STM and SEM. The STM may not achieve atomic resolution constant-current imaging capability in this design, and it may be necessary to use the secondary design. (c) Secondary design for attaching the STM head to the inner radiation shield and cold tip. Compression springs can be placed between the top of the inner radiation shield and the SS threaded rod to provide local vibration damping to the STM head. The relative vibration between the STM head and the SEM will be increased compared to the current design in the secondary design.

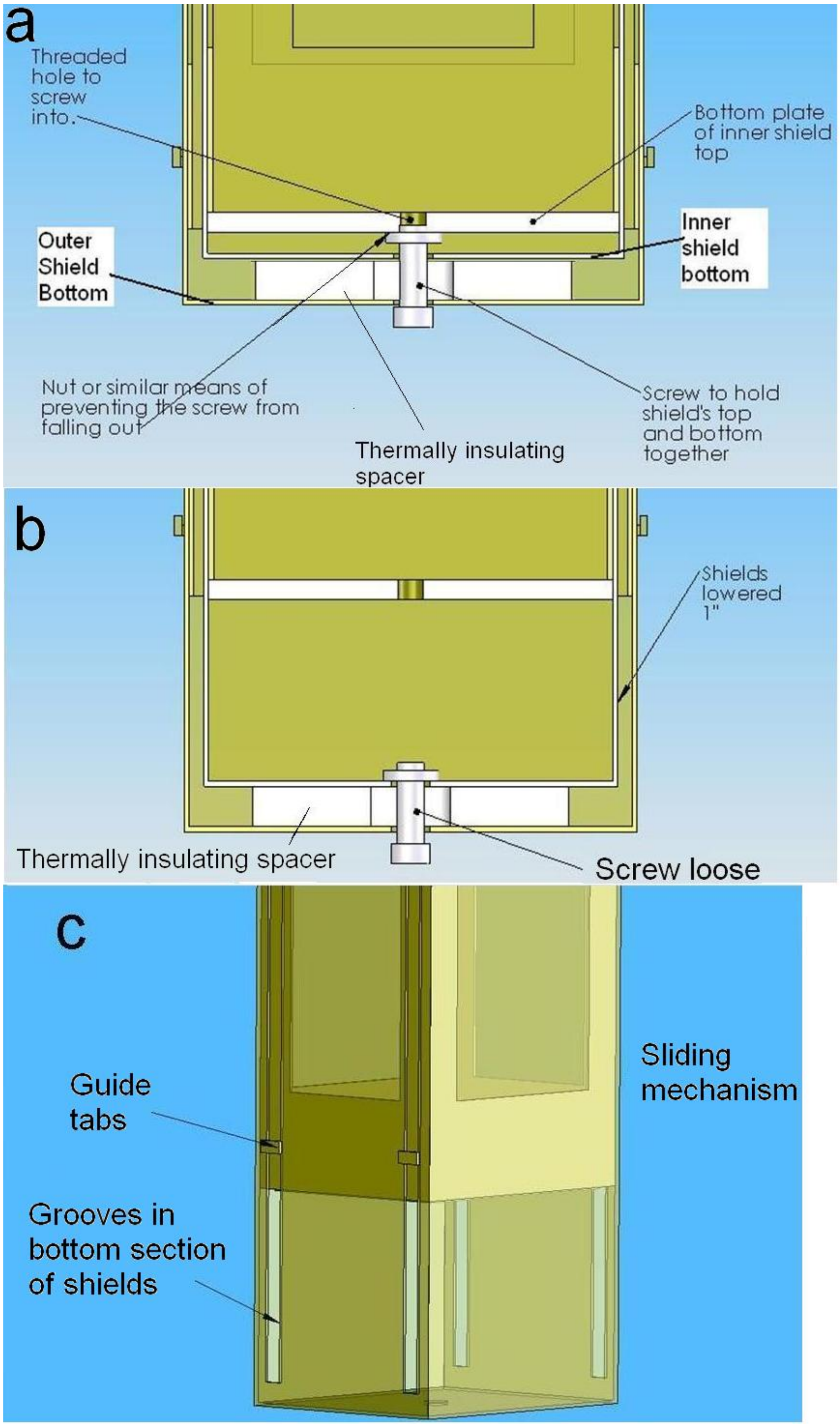

Figure C.6: Illustration of the design of the inner and outer thermal radiation shields: (a) Schematic of the inner and outer thermal radiation shields in the raised position. A screw holds the two shields together in the raised position. (b) Shields lowered by undoing the screw holding them together. The wobble stick ([5] in Fig. C.1) attached to the main analysis chamber of the STM/SEM will be used to manipulate the screw to raise and lower the thermal radiation shields, as shown in Fig. C.7. (c) Illustration of the guiding tabs grooves that comprise the guided sliding mechanism of the thermal radiation shields.

from direct connection of the STM to the cold tip be too large for atomic resolution imaging with the STM, a secondary design, utilizing compression springs between the STM head and the inner thermal radiation shield connection, will reduce mechanical vibrations at the STM head. Both thermal radiation shields and the secondary design for compression spring connections are illustrated in Figs. C.5 and C.6.

In order to exchange samples and tips, the thermal radiation shields must be lowered to provide access to the STM stage. The schematic process for lowering the shields is shown in Fig. C.7. Initially, the radiation shields are in place and raised for STM measurements. The STM and radiation shields are then lowered to the bottom of the main analysis chamber[27] (hidden in Fig. C.7) in order to loosen the set screw holding the thermal shields up. Once the screw has been loosened, the STM is raised up and the thermal radiation shield will lower. Subsequently, the STM may be rotated via the Omniax XYZ and rotary (XYZR) manipulator in order for the tip and sample to be exchanged via the linear, rotary manipulator shown in Fig. C.1. The process is reversed once a tip and sample have been loaded to raise the thermal radiation shields for STM and SEM measurements to be performed in the top portion of the main analysis chamber.

The schematic process of exchanging a tip is shown in Fig. C.8. The linear, rotary manipulator will have a threaded attachment on the end of the manipulator which can be threaded through a removable sample stage ([8] in Fig. C.2). The sample stage may then be interlocked into the fixed OFHC copper stage ([7] in Fig. C.2). The linear, rotary manipulator may then be unscrewed and removed. A special sample stage for holding tips for exchange may also be constructed. A schematic of one design for exchanging tips in this manner is shown in Fig. C.8c,d. A spring loaded tip-grabbing feature on the end of the tube scanner can be used to grab a tip and pull it back for use in such a design.

---

[27] Control of the Omniax XYZR manipulator is performed through stepper motors and the Sim-Step stepper motor controller purchased from VG Scienta, Inc.

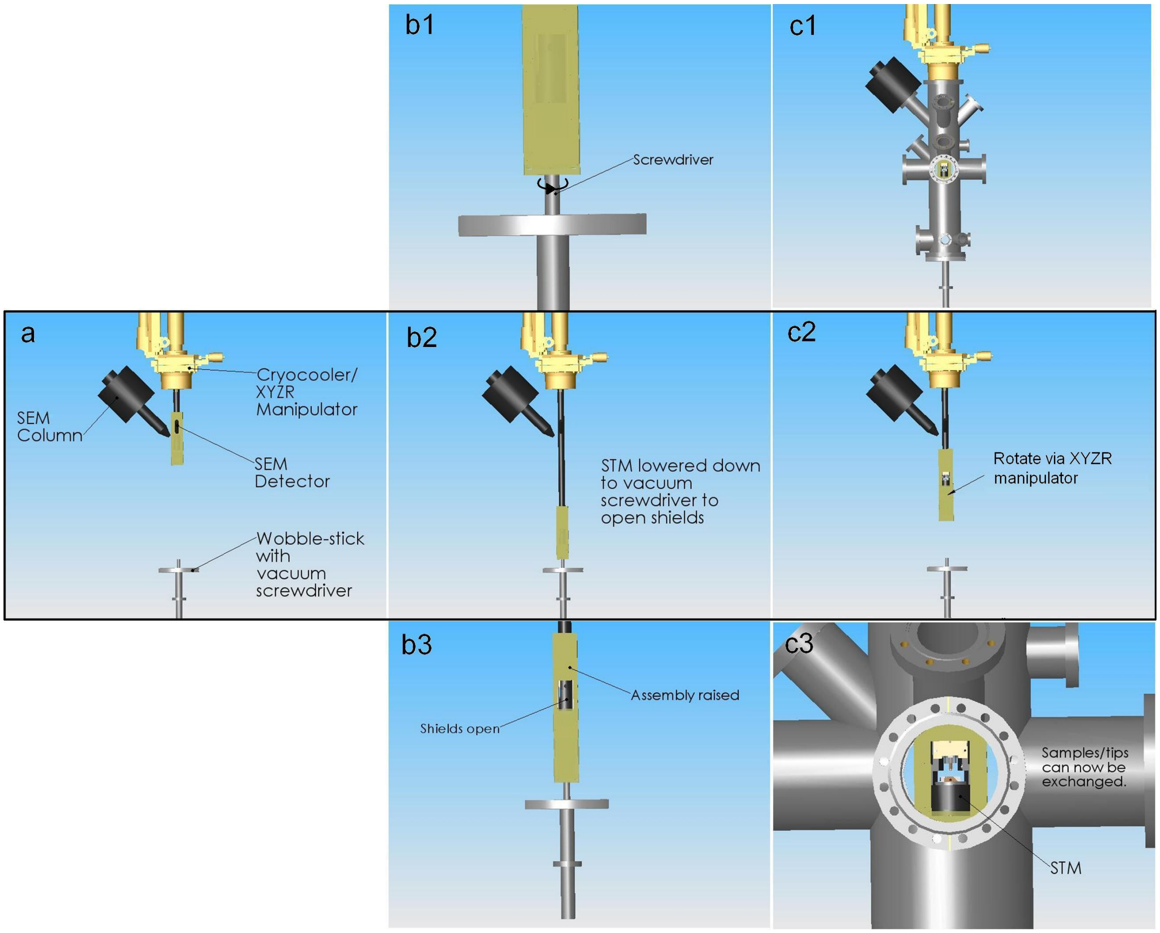

Figure C.7: Schematic illustration of raising and lowering the thermal radiation shields: The images illustrate the parts inside the main analysis chamber. The main analysis chamber is hidden except in (c1) and (c3). (a) The thermal radiation shields are raised and the STM is in the upper portion of the main analysis chamber of the STM/SEM for simultaneous STM and SEM study. (b) The XYZR ([2] in Fig. C.1) manipulator may then be used to lower the radiation shields down to the wobble stick to unscrew the screw shown in Fig. C.6: (b1) Illustrating the wobble stick unscrewing the thermal radiation shield screw. (b2) The thermal radiation shields lowered to the wobble stick using the XYZR manipulator. (b3) After the thermal radiation screw is loose, the entire STM assembly may be raised using the XYZR manipulator, and the shield bottoms will lower due to gravity. (c) The STM assembly may then be rotated and raised to the proper height for tip and sample exchange. (c1) The STM assembly raised to the proper height for tip and sample exchange with the main analysis chamber of the STM/SEM shown. (c2) The STM assembly raised to the proper height for tip and sample exchange without the main analysis chamber of the STM/SEM shown for comparison with (a) and (b). (c3) Zoomed in view of the STM assembly raised to the proper height for tip and sample exchange with the main analysis chamber of the STM/SEM shown. The linear, rotary manipulator can be used to exchange tips and samples. More details are described in Fig. C.8.

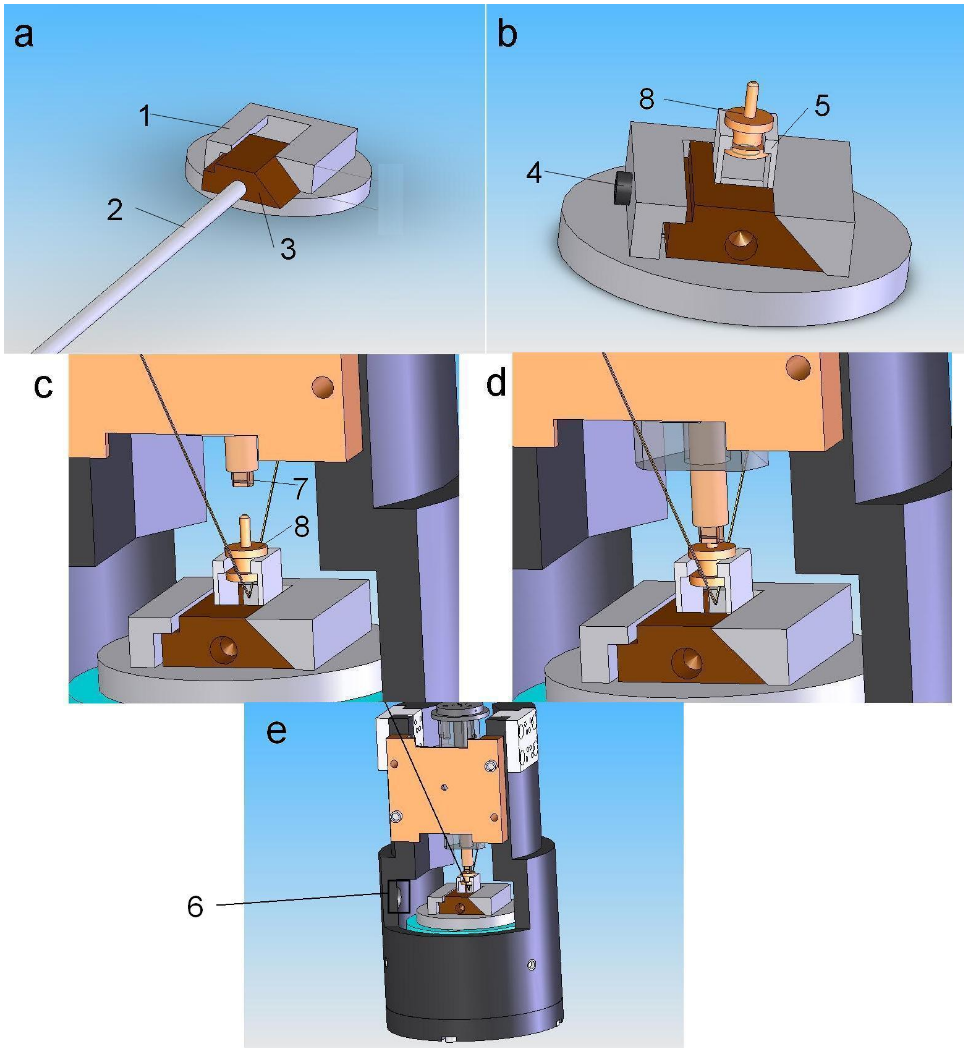

Figure C.8: Schematic of the tip and sample exchange mechanism for the cryogenic STM/SEM: [1]–Schematic of the fixed OFHC sample stage of the STM head ([7] in Fig. C.2)[2]–Linear, rotary manipulator ([10] in Fig. C.1) with a threaded attachment on the end, [3]–Schematic of the removable OFHC sample stage of the STM head ([6] in Fig. C.2). The removable stage has a threaded hole in the center of its face for attachment to the threaded end of the linear, rotary manipulator, [4]–Stainless steel set screw for holding the removable OFHC sample stage in place, [5] Additional attachment for removable OFHC sample stages for tip exchange, [6] Through-hole for the linear rotary manipulator to tighten the set screw to secure the removable sample stage, [7] STM tip grip piece. Initially designed to be a copper-beryllium spring loaded grip piece, [8]–Removable STM tip holder. (a) Schematic illustration of a removable OFHC sample stage ([3]) being inserted into the fixed OFHC sample stage ([1]). Once the removable stage is completely inserted into the fixed stage, the linear, rotary manipulator may be unscrewed from the fixed sample stage. (b) Schematic illustration of an additional attachment for tip exchange and the set screw for securing the sample stage. The STM assembly may be rotated using the XYZR manipulator so that the set screw is accessible through the set screw hole ([6]) in order to secure the removable OFHC sample stages. (c) Schematic illustration of tip exchange. The piezo tube scanner is equipped with an attachment ([7]) that may be used to grab the removable tip holder ([8]). (d) The Z coarse-motion stage may be used to lower the piezo tube scanner to grab the removable tip holder ([8]). (e) Zoomed out view of the STM head for comparison with (c) and (d).

Bibliography

[1] J. G. Bednorz and K. A. MÃŒller, Zeitschrift fÃŒr Physik B Condensed Matter **64**, 189 (1986), URL `http://dx.doi.org/10.1007/BF01303701`.

[2] C. Renner, B. Revaz, J.-Y. Genoud, K. Kadowaki, and O. Fischer, Phys. Rev. Lett. **80**, 149 (1998).

[3] O. Fischer, M. Kugler, I. Maggio-Aprile, C. Berthod, and C. Renner, Reviews of Modern Physics **79**, 353 (pages 67) (2007), URL `http://link.aps.org/abstract/RMP/v79/p353`.

[4] M. C. Boyer, W. D. Wise, K. Chatterjee, M. Yi, T. Kondo, T. Takeuchi, H. Ikuta, and E. W. Hudson, Nat Phys **3**, 802 (2007), ISSN 1745-2473, URL `http://dx.doi.org/10.1038/nphys725`.

[5] M. Vershinin, S. Misra, S. Ono, Y. Abe, Y. Ando, and A. Yazdani, Science **303**, 1995 (2004), `http://www.sciencemag.org/cgi/reprint/303/5666/1995.pdf`, URL `http://www.sciencemag.org/cgi/content/abstract/303/5666/1995`.

[6] W. S. Lee, I. M. Vishik, K. Tanaka, D. H. Lu, T. Sasagawa, N. Nagaosa, T. P. Devereaux, Z. Hussain, and Z. X. Shen, Nature **450**, 81 (2007), ISSN 0028-0836, URL `http://dx.doi.org/10.1038/nature06219`.

[7] A. Damascelli, Z. Hussain, and Z.-X. Shen, Rev. Mod. Phys. **75**, 473 (2003).

[8] M. R. Norman, A. Kanigel, M. Randeria, U. Chatterjee, and J. C. Campuzano, Physical Review B (Condensed Matter and Materials Physics) **76**, 174501 (pages 7) (2007), URL `http://link.aps.org/abstract/PRB/v76/e174501`.

[9] K. Yamada, K. Kurahashi, T. Uefuji, M. Fujita, S. Park, S.-H. Lee, and Y. Endoh, Phys. Rev. Lett. **90**, 137004 (2003).

[10] M. Fujita, M. Matsuda, S. Katano, and K. Yamada, Phys. Rev. Lett. **93**, 147003 (2004).

[11] H. J. Kang, P. Dai, H. A. Mook, D. N. Argyriou, V. Sikolenko, J. W. Lynn, Y. Kurita, S. Komiya, and Y. Ando, Phys. Rev. B **71**, 214512 (2005).

[12] E. M. Motoyama, P. K. Mang, D. Petitgrand, G. Yu, O. P. Vajk, I. M. Vishik, and M. Greven, Physical Review Letters **96**, 137002 (pages 4) (2006), URL `http://link.aps.org/abstract/PRL/v96/e137002`.

[13] K. Yamada, S. Wakimoto, G. Shirane, C. H. Lee, M. A. Kastner, S. Hosoya, M. Greven, Y. Endoh, and R. J. Birgeneau, Phys. Rev. Lett. **75**, 1626 (1995).

[14] C.-H. Lee, K. Yamada, Y. Endoh, G. Shirane, R. J. Birgeneau, M. A. Kastner, M. Greven, and Y.-J. Kim, Journal of the Physical Society of Japan **69**, 1170 (2000), URL `http://jpsj.ipap.jp/link?JPSJ/69/1170/`.

[15] B. Lake, G. Aeppli, T. E. Mason, A. Schrder, D. F. McMorrow, K. Lefmann, M. Isshiki, M. Nohara, H. Takagi, and S. M. Hayden, Nature **400**, 43 (1999).

[16] P. Dai, H. A. Mook, R. D. Hunt, and F. Doğan, Phys. Rev. B **63**, 054525 (2001).

[17] Y. Krockenberger, B. Welter, M. Schonecke, R. Gross, D. Manske, M. Naito, and L. Alff, Nature **422**, 698 (2003).

[18] C. Renner, B. Revaz, K. Kadowaki, I. Maggio-Aprile, and O. Fischer, Phys. Rev. Lett. **80**, 3606 (1998).

[19] B. W. Hoogenboom, C. Renner, B. Revaz, I. Maggio-Aprile, and I. . Fischer, O., Physica C: Superconductivity **332**, 440 (May 2000), scanning tunneling spectroscopy allows us to study the changes in the quasiparticle local density of states due to the presence of vortex cores in Bi2Sr2CaCu2O8+ (BSCCO). The vortex core spectra are characterized by a gap-like structure similar to the...

[20] B. W. Hoogenboom, K. Kadowaki, B. Revaz, M. Li, C. Renner, and O. Fischer, Phys. Rev. Lett. **87**, 267001 (2001).

[21] J. E. Hoffman, E. W. Hudson, K. M. Lang, V. Madhavan, H. Eisaki, S. Uchida, and J. C. Davis, Science **295**, 466 (2002), `http://www.sciencemag.org/cgi/reprint/295/5554/466.pdf`, URL `http://www.sciencemag.org/cgi/content/abstract/295/5554/466`.

[22] S. H. Pan, E. W. Hudson, A. K. Gupta, K.-W. Ng, H. Eisaki, S. Uchida, and J. C. Davis, Phys. Rev. Lett. **85**, 1536 (2000).

[23] H. F. Hess, R. B. Robinson, R. C. Dynes, J. M. Valles, and J. V. Waszczak, Phys. Rev. Lett. **62**, 214 (1989).

[24] H. F. Hess, R. B. Robinson, and J. V. Waszczak, Phys. Rev. Lett. **64**, 2711 (1990).

[25] H. F. Hess, R. B. Robinson, and J. V. Waszczak, Physica B: Condensed Matter **169**, 422 (2 February 1991), the low-temperature scanning tunneling microscope, STM, is capable of measuring the local density of states across a surface with sub-nanometer resolution. This allows vortices and the flux lattice to be imaged by measuring the spatial variations in th..., URL `http://dx.doi.org/10.1016/0921-4526(91)90262-D`.

[26] P. A. Lee, N. Nagaosa, and X.-G. Wen, Reviews of Modern Physics **78**, 17 (pages 69) (2006), URL `http://link.aps.org/abstract/RMP/v78/p17`.

[27] S.-C. Zhang, Science **275**, 1089 (1997), `http://www.sciencemag.org/cgi/reprint/275/5303/1089.pdf`, URL `http://www.sciencemag.org/cgi/content/abstract/275/5303/1089`.

[28] S. Chakravarty, R. B. Laughlin, D. K. Morr, and C. Nayak, Phys. Rev. B **63**, 094503 (2001).

[29] E. Demler, S. Sachdev, and Y. Zhang, Phys. Rev. Lett. **87**, 067202 (2001).

[30] S. Sachdev, Rev. Mod. Phys. **75**, 913 (2003).

[31] S. A. Kivelson, I. P. Bindloss, E. Fradkin, V. Oganesyan, J. M. Tranquada, A. Kapitulnik, and C. Howald, Rev. Mod. Phys. **75**, 1201 (2003).

[32] C. Berthod and B. Giovannini, Phys. Rev. Lett. **87**, 277002 (2001).

[33] J. W. Alldredge, J. Lee, K. McElroy, M. Wang, K. Fujita, Y. Kohsaka, C. Taylor, H. Eisaki, S. Uchida, P. J. Hirschfeld, et al., Nat Phys **4**, 319 (2008), ISSN 1745-2473, URL `http://dx.doi.org/10.1038/nphys917`.

[34] C. C. Tsuei and J. R. Kirtley, Rev. Mod. Phys. **72**, 969 (2000).

[35] N.-C. Yeh, C.-T. Chen, G. Hammerl, J. Mannhart, A. Schmehl, C. W. Schneider, R. R. Schulz, S. Tajima, K. Yoshida, D. Garrigus, et al., Phys. Rev. Lett. **87**, 087003 (2001).

[36] L. Alff, A. Beck, R. Gross, A. Marx, S. Kleefisch, T. Bauch, H. Sato, M. Naito, and G. Koren, Phys. Rev. B **58**, 11197 (1998).

[37] L. Shan, Y. Huang, H. Gao, Y. Wang, S. L. Li, P. C. Dai, F. Zhou, J. W. Xiong, W. X. Ti, and H. H. Wen, Physical Review B (Condensed Matter and Materials Physics) **72**, 144506 (pages 9) (2005), URL `http://link.aps.org/abstract/PRB/v72/e144506`.

[38] B. Stadlober, G. Krug, R. Nemetschek, R. Hackl, J. L. Cobb, and J. T. Markert, Phys. Rev. Lett. **74**, 4911 (1995).

[39] C.-T. Chen, P. Seneor, N.-C. Yeh, R. P. Vasquez, L. D. Bell, C. U. Jung, J. Y. Kim, M.-S. Park, H.-J. Kim, and S.-I. Lee, Phys. Rev. Lett. **88**, 227002 (2002).

[40] C. C. Tsuei and J. R. Kirtley, Phys. Rev. Lett. **85**, 182 (2000).

[41] H. Matsui, K. Terashima, T. Sato, T. Takahashi, M. Fujita, and K. Yamada, Physical Review Letters **95**, 017003 (pages 4) (2005), URL `http://link.aps.org/abstract/PRL/v95/e017003`.

[42] G. Blumberg, A. Koitzsch, A. Gozar, B. S. Dennis, C. A. Kendziora, P. Fournier, and R. L. Greene, Phys. Rev. Lett. **88**, 107002 (2002).

[43] C. M. Varma, P. B. Littlewood, S. Schmitt-Rink, E. Abrahams, and A. E. Ruckenstein, Phys. Rev. Lett. **63**, 1996 (1989).

[44] A. Krol, C. S. Lin, Z. H. Ming, C. J. Sher, Y. H. Kao, C. L. Lin, S. L. Qiu, J. Chen, J. M. Tranquada, M. Strongin, et al., Phys. Rev. B **42**, 4763 (1990).

[45] G. Liang, Y. Guo, D. Badresingh, W. Xu, Y. Tang, M. Croft, J. Chen, A. Sahiner, B.-h. O, and J. T. Markert, Phys. Rev. B **51**, 1258 (1995).

[46] J. M. Tranquada, S. M. Heald, A. Moodenbaugh, and M. Suenaga, Phys. Rev. B **35**, 7187 (1987).

[47] A. Fujimori, E. Takayama-Muromachi, Y. Uchida, and B. Okai, Phys. Rev. B **35**, 8814 (1987).

[48] Z. Tan, S. M. Heald, S.-W. Cheong, A. S. Cooper, and A. R. Moodenbaugh, Phys. Rev. B **47**, 12365 (1993).

[49] K. K. Gomes, A. N. Pasupathy, A. Pushp, S. Ono, Y. Ando, and A. Yazdani, Nature **447**, 569 (2007), ISSN 0028-0836, URL `http://dx.doi.org/10.1038/nature05881`.

[50] T. Timusk and B. Statt, Reports on Progress in Physics **62**, 61 (1999), URL `http://stacks.iop.org/0034-4885/62/61`.

[51] R. L. Corey, N. J. Curro, K. O'Hara, T. Imai, C. P. Slichter, K. Yoshimura, M. Katoh, and K. Kosuge, Phys. Rev. B **53**, 5907 (1996).

[52] Y.-W. Hsueh, B. W. Statt, M. Reedyk, J. S. Xue, and J. E. Greedan, Phys. Rev. B **56**, R8511 (1997).

[53] M.-H. Julien, P. Carretta, M. Horvati, C. Berthier, Y. Berthier, P. Ségransan, A. Carrington, and D. Colson, Phys. Rev. Lett. **76**, 4238 (1996).

[54] R. Stern, M. Mali, I. Mangelschots, J. Roos, D. Brinkmann, J.-Y. Genoud, T. Graf, and J. Muller, Phys. Rev. B **50**, 426 (1994).

[55] R. Stern, M. Mali, J. Roos, and D. Brinkmann, Phys. Rev. B **52**, R15734 (1995).

[56] R. E. Walstedt, R. F. Bell, and D. B. Mitzi, Phys. Rev. B **44**, 7760 (1991).

[57] A. V. Puchkov, P. Fournier, D. N. Basov, T. Timusk, A. Kapitulnik, and N. N. Kolesnikov, Phys. Rev. Lett. **77**, 3212 (1996).

[58] F. Slakey, M. V. Klein, J. P. Rice, and D. M. Ginsberg, Phys. Rev. B **42**, 2643 (1990).

[59] G. Blumberg, M. V. Klein, K. Kadowaki, C. Kendziora, P. Guptasarma, and D. Hinks, Journal of Physics and Chemistry of Solids **59**, 1932 (11 October 1998), for YBa2Cu3O6+ and Bi2Sr2CaCu2O8 superconductors, electronic Raman scattering from high- and low-energy excitations has been studied in relation to the hole doping level, temperature and energy of the incident photons. For underdoped superconductors..., URL `http://dx.doi.org/10.1016/S0022-3697(98)00135-8`.

[60] M. Le Tacon, A. Sacuto, A. Georges, G. Kotliar, Y. Gallais, D. Colson, and A. Forget, Nat Phys **2**, 537 (2006), ISSN 1745-2473, URL `http://dx.doi.org/10.1038/nphys362`.

[61] S. Kleefisch, B. Welter, A. Marx, L. Alff, R. Gross, and M. Naito, Phys. Rev. B **63**, 100507 (2001).

[62] N. Miyakawa, M. Minematsu, K. Ogata, M. Fujita, and K. Yamada, Journal of Physics: Conference Series **150**, 052163 (4pp) (2009), URL `http://stacks.iop.org/1742-6596/150/052163`.

[63] F. C. Niestemski, S. Kunwar, S. Zhou, S. Li, H. Ding, Z. Wang, P. Dai, and V. Madhavan, Nature **450**, 1058 (2007), ISSN 0028-0836, URL `http://dx.doi.org/10.1038/nature06430`.

[64] N. P. Armitage, F. Ronning, D. H. Lu, C. Kim, A. Damascelli, K. M. Shen, D. L. Feng, H. Eisaki, Z.-X. Shen, P. K. Mang, et al., Phys. Rev. Lett. **88**, 257001 (2002).

[65] P. K. Mang, S. Larochelle, A. Mehta, O. P. Vajk, A. S. Erickson, L. Lu, W. J. L. Buyers, A. F. Marshall, K. Prokes, and M. Greven, Phys. Rev. B **70**, 094507 (2004).

[66] P. Richard, G. Riou, I. Hetel, S. Jandl, M. Poirier, and P. Fournier, Phys. Rev. B **70**, 064513 (2004).

[67] G. V. M. Williams, R. Dupree, A. Howes, S. Krämer, H. J. Trodahl, C. U. Jung, M.-S. Park, and S.-I. Lee, Phys. Rev. B **65**, 224520 (2002).

[68] K. McElroy, D.-H. Lee, J. E. Hoffman, K. M. Lang, J. Lee, E. W. Hudson, H. Eisaki, S. Uchida, and J. C. Davis, Phys. Rev. Lett. **94**, 197005 (2005).

[69] I. Maggio-Aprile, C. Renner, A. Erb, E. Walker, and O. Fischer, Phys. Rev. Lett. **75**, 2754 (1995).

[70] J.-H. Ma, Z.-H. Pan, F. C. Niestemski, M. Neupane, Y.-M. Xu, P. Richard, K. Nakayama, T. Sato, T. Takahashi, H.-Q. Luo, et al., Physical Review Letters **101**, 207002 (pages 4) (2008), URL `http://link.aps.org/abstract/PRL/v101/e207002`.

[71] B. W. Hoogenboom, K. Kadowaki, B. Revaz, and . Fischer, Physica C: Superconductivity **391**, 376 (15 September 2003), recently, much attention has been paid to inhomogeneity in samples of the high-temperature superconductor Bi2Sr2CaCu2O8+. In this work it is shown that homogeneous samples can indeed be obtained in the slightly overdoped range. However, the homogeneit..., URL `http://dx.doi.org/10.1016/S0921-4534(03)01087-6`.

[72] A. A. Abrikosov, Sov. Phys. JETP **5**, 1174 (1957).

[73] J. D. Shore, M. Huang, A. T. Dorsey, and J. P. Sethna, Phys. Rev. Lett. **62**, 3089 (1989).

[74] U. Klein, Phys. Rev. B **40**, 6601 (1989).

[75] F. m. c. Gygi and M. Schluter, Phys. Rev. B **41**, 822 (1990).

[76] S. Ullah, A. T. Dorsey, and L. J. Buchholtz, Phys. Rev. B **42**, 9950 (1990).

[77] T. Hanaguri, Y. Kohsaka, M. Ono, M. Maltseva, P. Coleman, I. Yamada, M. Azuma, M. Takano, K. Ohishi, and H. Takagi, Science **323**, 923 (2009), `http://www.sciencemag.org/cgi/reprint/323/5916/923.pdf`, URL `http://www.sciencemag.org/cgi/content/abstract/323/5916/923`.

[78] Q.-H. Wang and D.-H. Lee, Phys. Rev. B **67**, 020511 (2003).

[79] C.-T. Chen and N.-C. Yeh, Phys. Rev. B **68**, 220505 (2003).

[80] C. Howald, H. Eisaki, N. Kaneko, M. Greven, and A. Kapitulnik, Phys. Rev. B **67**, 014533 (2003).

[81] T. Hanaguri, C. Lupien, Y. Kohsaka, D. H. Lee, M. Azuma, M. Takano, H. Takagi, and J. C. Davis, Nature **430**, 1001 (2004), ISSN 0028-0836, URL `http://dx.doi.org/10.1038/nature02861`.

[82] W. D. Wise, M. C. Boyer, K. Chatterjee, T. Kondo, T. Takeuchi, H. Ikuta, Y. Wang, and E. W. Hudson, Nat Phys **4**, 696 (2008), ISSN 1745-2473, URL `http://dx.doi.org/10.1038/nphys1021`.

[83] H.-D. Chen, J.-P. Hu, S. Capponi, E. Arrigoni, and S.-C. Zhang, Phys. Rev. Lett. **89**, 137004 (2002).

[84] H.-D. Chen, O. Vafek, A. Yazdani, and S.-C. Zhang, Phys. Rev. Lett. **93**, 187002 (2004).

[85] V. M. Krasnov, A. Yurgens, D. Winkler, P. Delsing, and T. Claeson, Phys. Rev. Lett. **84**, 5860 (2000).

[86] A. Polkovnikov, M. Vojta, and S. Sachdev, Phys. Rev. B **65**, 220509 (2002).

[87] J.-X. Li, C.-Q. Wu, and D.-H. Lee, Physical Review B (Condensed Matter and Materials Physics) **74**, 184515 (pages 6) (2006), URL `http://link.aps.org/abstract/PRB/v74/e184515`.

[88] J. Bardeen, Phys. Rev. Lett. **6**, 57 (1961).

[89] I. Giaever, Phys. Rev. Lett. **5**, 147 (1960).

[90] J. Nicol, S. Shapiro, and P. H. Smith, Phys. Rev. Lett. **5**, 461 (1960).

[91] J. Tersoff and D. R. Hamann, Phys. Rev. Lett. **50**, 1998 (1983).

[92] J. Tersoff and D. R. Hamann, Phys. Rev. B **31**, 805 (1985).

[93] G. E. Blonder, M. Tinkham, and T. M. Klapwijk, Phys. Rev. B **25**, 4515 (1982).

[94] Y. Tanaka and S. Kashiwaya, Phys. Rev. Lett. **74**, 3451 (1995).

[95] S. Kashiwaya, Y. Tanaka, M. Koyanagi, and K. Kajimura, Phys. Rev. B **53**, 2667 (1996).

[96] S. Kashiwaya, Y. Tanaka, M. Koyanagi, H. Takashima, and K. Kajimura, Phys. Rev. B **51**, 1350 (1995).

[97] J. Y. T. Wei, N.-C. Yeh, D. F. Garrigus, and M. Strasik, Phys. Rev. Lett. **81**, 2542 (1998).

[98] M. R. Norman, H. Ding, M. Randeria, J. C. Campuzano, T. Yokoya, T. Takeuchi, T. Takahashi, T. Mochiku, K. Kadowaki, P. Guptasarma, et al., Nature **392**, 157 (1998), ISSN 0028-0836, URL `http://dx.doi.org/10.1038/32366`.

[99] K. McElroy, R. W. Simmonds, J. E. Hoffman, D. H. Lee, J. Orenstein, H. Eisaki, S. Uchida, and J. C. Davis, Nature **422**, 592 (2003), ISSN 0028-0836, URL `http://dx.doi.org/10.1038/nature01496`.

[100] E. W. Hudson, S. H. Pan, A. K. Gupta, K.-W. Ng, and J. C. Davis, Science **285**, 88 (1999), `http://www.sciencemag.org/cgi/reprint/285/5424/88.pdf`, URL `http://www.sciencemag.org/cgi/content/abstract/285/5424/88`.

[101] G. Binnig and H. Rohrer, Rev. Mod. Phys. **59**, 615 (1987).

[102] G. Binnig, H. Rohrer, C. Gerber, and E. Weibel, Applied Physics Letters **40**, 178 (1982), URL `http://link.aip.org/link/?APL/40/178/1`.

[103] S. H. Pan, E. W. Hudson, and J. C. Davis, Review of Scientific Instruments **70**, 1459 (1999), URL `http://link.aip.org/link/?RSI/70/1459/1`.

[104] H. J. Hug, B. Stiefel, P. J. A. van Schendel, A. Moser, S. Martin, and H.-J. Guntherodt, Review of Scientific Instruments **70**, 3625 (1999), URL `http://link.aip.org/link/?RSI/70/3625/1`.

[105] B. L. Rogers, J. G. Shapter, W. M. Skinner, and K. Gascoigne, Review of Scientific Instruments **71**, 1702 (2000), URL `http://link.aip.org/link/?RSI/71/1702/1`.

[106] I. Spielman, Ph.D. thesis, California Institute of Technology, Department of Physics (2004).

[107] C.-T. Chen, Ph.D. thesis, California Institute of Technology, Department of Physics (2006).

[108] D. S. Reed, N.-C. Yeh, M. Konczykowski, A. V. Samoilov, and F. Holtzberg, Phys. Rev. B **51**, 16448 (1995).

[109] D. S. Reed, N.-C. Yeh, M. Konczykowski, A. V. Samoilov, and F. Holtzberg, Phys. Rev. B **51**, 16448 (1995).

[110] D. Reed, Ph.D. thesis, California Institute of Technology, Department of Physics (1995).

[111] J. S. Brooks, M. J. Naughton, Y. P. Ma, P. M. Chaikin, and R. V. Chamberlin, Review of Scientific Instruments **58**, 117 (1987), URL `http://link.aip.org/link/?RSI/58/117/1`.

[112] M. J. Naughton, J. P. Ulmet, A. Narjis, S. Askenazy, M. V. Chaparala, and A. P. Hope, Review of Scientific Instruments **68**, 4061 (1997), URL `http://link.aip.org/link/?RSI/68/4061/1`.

[113] N. P. Armitage, D. H. Lu, C. Kim, A. Damascelli, K. M. Shen, F. Ronning, D. L. Feng, P. Bogdanov, Z.-X. Shen, Y. Onose, et al., Phys. Rev. Lett. **87**, 147003 (2001).

[114] C. Caroli, P. G. D. Gennes, and J. Matricon, Phys. Lett. **9**, 307 (1964).

[115] G. Levy, M. Kugler, A. A. Manuel, O. Fischer, and M. Li, Phys. Rev. Lett. **95**, 257005 (2005).

[116] J. D. Jorgensen, P. G. Radaelli, D. G. Hinks, J. L. Wagner, S. Kikkawa, G. Er, and F. Kanamaru, Phys. Rev. B **47**, 14654 (1993).

[117] T. Siegrist, S. M. Zahurak, D. W. Murphy, and R. S. Roth, Nature **334**, 231 (1988), URL `http://dx.doi.org/10.1038/334231a0`.

[118] M. G. Smith, A. Manthiram, J. Zhou, J. B. Goodenough, and J. T. Markert, Nature **351**, 549 (1991), URL `http://dx.doi.org/10.1038/351549a0`.

[119] C. U. Jung, J. Y. Kim, M.-S. Park, M.-S. Kim, H.-J. Kim, S. Y. Lee, and S.-I. Lee, Phys. Rev. B **65**, 172501 (2002).

[120] R. P. Vasquez, C. U. Jung, J. Y. Kim, M.-S. Park, H.-J. Kim, and S.-I. Lee, Journal of Physics: Condensed Matter **13**, 7977 (2001), URL `http://stacks.iop.org/0953-8984/13/7977`.

[121] M.-S. Kim, C. U. Jung, J. Y. Kim, J.-H. Choi, and S.-I. Lee, Solid State Communications **123**, 17 (1 July 2002), the infinite-layer compound ACuO2 (A=alkaline-earth ions) is regarded as the most suitable material for exploring the fundamental nature of the CuO2 plane because it does not contain a charge-reservoir block, such as a rock-salt or a fluorite like bloc..., URL `http://dx.doi.org/10.1016/S0038-1098(02)00202-8`.

[122] A. Biswas, P. Fournier, M. M. Qazilbash, V. N. Smolyaninova, H. Balci, and R. L. Greene, Phys. Rev. Lett. **88**, 207004 (2002).

[123] J. A. Skinta, M.-S. Kim, T. R. Lemberger, T. Greibe, and M. Naito, Phys. Rev. Lett. **88**, 207005 (2002).

[124] L. Alff, S. Meyer, S. Kleefisch, U. Schoop, A. Marx, H. Sato, M. Naito, and R. Gross, Phys. Rev. Lett. **83**, 2644 (1999).

[125] B. Chesca, M. Seifried, T. Dahm, N. Schopohl, D. Koelle, R. Kleiner, and A. Tsukada, Physical Review B (Condensed Matter and Materials Physics) **71**, 104504 (pages 7) (2005), URL `http://link.aps.org/abstract/PRB/v71/e104504`.

[126] J. A. Skinta, T. R. Lemberger, T. Greibe, and M. Naito, Phys. Rev. Lett. **88**, 207003 (2002).

[127] M.-S. Kim, J. A. Skinta, T. R. Lemberger, A. Tsukada, and M. Naito, Phys. Rev. Lett. **91**, 087001 (2003).

[128] R. Prozorov, R. W. Giannetta, P. Fournier, and R. L. Greene, Phys. Rev. Lett. **85**, 3700 (2000).

[129] A. Snezhko, R. Prozorov, D. D. Lawrie, R. W. Giannetta, J. Gauthier, J. Renaud, and P. Fournier, Phys. Rev. Lett. **92**, 157005 (2004).

[130] V. S. Zapf, N.-C. Yeh, A. D. Beyer, C. R. Hughes, C. H. Mielke, N. Harrison, M. S. Park, K. H. Kim, and S.-I. Lee, Phys. Rev. B **71**, 134526 (2005).

[131] R. C. Dynes, V. Narayanamurti, and J. P. Garno, Phys. Rev. Lett. **41**, 1509 (1978).

[132] N. C. Yeh, C. T. Chen, R. P. Vasquez, C. U. Jung, S. I. Lee, K. Yoshida, and S. Tajima, Journal of Low Temperature Physics **131**, 435 (2003), URL `http://dx.doi.org/10.1023/A:1022934832360`.

[133] A. Kanigel, U. Chatterjee, M. Randeria, M. R. Norman, G. Koren, K. Kadowaki, and J. C. Campuzano, Physical Review Letters **101**, 137002 (pages 4) (2008), URL `http://link.aps.org/abstract/PRL/v101/e137002`.

[134] H. B. Yang, J. D. Rameau, P. D. Johnson, T. Valla, A. Tsvelik, and G. D. Gu, Nature **456**, 77 (2008), ISSN 0028-0836, URL `http://dx.doi.org/10.1038/nature07400`.

[135] T. Valla, A. V. Fedorov, J. Lee, J. C. Davis, and G. D. Gu, Science **314**, 1914 (2006), `http://www.sciencemag.org/cgi/reprint/314/5807/1914.pdf`, URL `http://www.sciencemag.org/cgi/content/abstract/314/5807/1914`.

[136] M. Vojta, Y. Zhang, and S. Sachdev, Phys. Rev. B **62**, 6721 (2000).

[137] E. Demler, W. Hanke, and S.-C. Zhang, Rev. Mod. Phys. **76**, 909 (2004).

[138] K. Shibata, M. Maki, T. Nishizaki, and N. Kobayashi, Physica C: Superconductivity **392-396**, 323 (2003), ISSN 0921-4534, proceedings of the 15th International Symposium on Superconductivity (ISS 2002): Advances in Superconductivity XV. Part I, URL `http://www.sciencedirect.com/science/article/B6TVJ-48XSHHJ-B/2/13c905156386553e9eba3540439c6269`.

[139] M. Kugler, O. Fischer, C. Renner, S. Ono, and Y. Ando, Phys. Rev. Lett. **86**, 4911 (2001).

[140] M. F. Limonov, A. I. Rykov, S. Tajima, and A. Yamanaka, Phys. Rev. B **61**, 12412 (2000).

[141] R. P. Vasquez, B. D. Hunt, and M. C. Foote, Applied Physics Letters **54**, 2373 (1989), URL `http://link.aip.org/link/?APL/54/2373/1`.

[142] R. P. Vasquez, M. C. Foote, and B. D. Hunt, Applied Physics Letters **55**, 1801 (1989), URL `http://link.aip.org/link/?APL/55/1801/1`.

[143] D. J. Derro, E. W. Hudson, K. M. Lang, S. H. Pan, J. C. Davis, J. T. Markert, and A. L. de Lozanne, Phys. Rev. Lett. **88**, 097002 (2002).

[144] D. H. Lu, D. L. Feng, N. P. Armitage, K. M. Shen, A. Damascelli, C. Kim, F. Ronning, Z.-X. Shen, D. A. Bonn, R. Liang, et al., Phys. Rev. Lett. **86**, 4370 (2001).

[145] H. L. Edwards, J. T. Markert, and A. L. de Lozanne, Phys. Rev. Lett. **69**, 2967 (1992).

[146] H. L. Edwards, A. L. Barr, J. T. Markert, and A. L. de Lozanne, Phys. Rev. Lett. **73**, 1154 (1994).

[147] R. P. Vasquez, Journal of Electron Spectroscopy and Related Phenomena **66**, 209 (28 January 1994), photoemission signals which are characteristic of high quality surfaces of high temperature superconductors are briefly reviewed. Criteria for assessing surface quality are determined, and these criteria are then used to evaluate the various surface pr..., URL `http://dx.doi.org/10.1016/0368-2048(93)01850-E`.

[148] H. Safar, P. L. Gammel, D. A. Huse, D. J. Bishop, J. P. Rice, and D. M. Ginsberg, Phys. Rev. Lett. **69**, 824 (1992).

[149] M. Tachiki, M. Machida, and T. Egami, Phys. Rev. B **67**, 174506 (2003).

[150] I. Maggio-Aprile, C. Renner, A. Erb, E. Walker, B. Revaz, J.-Y. Genoud, K. Kadowaki, and y. Fischer, Journal of Electron Spectroscopy and Related Phenomena **109**, 147 (August 2000), during past years, scanning tunneling spectroscopy (STS) investigations of high temperature superconductors have revealed unusual characteristics of the superconducting gap. We present here the temperature dependence of the tunneling conductance spectr..., URL `http://dx.doi.org/10.1016/S0368-2048(00)00113-4`.

[151] M. P. A. Fisher, Phys. Rev. Lett. **62**, 1415 (1989).

[152] G. Blatter, M. V. Feigel'man, V. B. Geshkenbein, A. I. Larkin, and V. M. Vinokur, Rev. Mod. Phys. **66**, 1125 (1994).

[153] N.-C. Yeh, W. Jiang, D. Reed, U. Kriplani, F. Holtzberg, M. Konczykowski, C. Tsuei, and C. Chi, Physica A: Statistical Mechanics and its Applications **200**, 374 (1993), ISSN 0378-4371, URL `http://www.sciencedirect.com/science/article/B6TVG-46X9KRG-B5/2/9cb44bdd4f3b68974e3af21816024e37`.

[154] L. Balents and D. R. Nelson, Phys. Rev. Lett. **73**, 2618 (1994).

[155] T. Giamarchi and P. Le Doussal, Phys. Rev. B **52**, 1242 (1995).

[156] G. Kotliar and C. M. Varma, Phys. Rev. Lett. **77**, 2296 (1996).

[157] J. Kierfeld and V. Vinokur, Phys. Rev. B **69**, 024501 (2004).

[158] N.-C. Yeh, C.-T. Chen, V. S. Zapf, A. D. Beyer, and C. R. Hughes, International Journal of Modern Physics B **19**, 285 (2005).

[159] D. S. Fisher, M. P. A. Fisher, and D. A. Huse, Phys. Rev. B **43**, 130 (1991).

[160] F. Onufrieva and P. Pfeuty, Phys. Rev. Lett. **92**, 247003 (2004).

[161] H. Kotegawa, Y. Tokunaga, K. Ishida, G.-q. Zheng, Y. Kitaoka, H. Kito, A. Iyo, K. Tokiwa, T. Watanabe, and H. Ihara, Phys. Rev. B **64**, 064515 (2001).

[162] H. Kotegawa, Y. Tokunaga, K. Ishida, G. q. Zheng, Y. Kitaoka, K. Asayama, H. Kito, A. Iyo, H. Ihara, K. Tanaka, et al., Journal of Physics and Chemistry of Solids **62**, 171 (January 2001), we report 63Cu-Knight shift measurement on multilayered high-Tc cuprate oxides that include inequivalent outer (OP) and inner (IP) CuO2 planes in a unit cell with number of planes n=35. Using an experimental relation between the spin part of Knight sh..., URL `http://dx.doi.org/10.1016/S0022-3697(00)00122-0`.

[163] N.-C. Yeh, W. Jiang, D. S. Reed, A. Gupta, F. Holtzberg, and A. Kussmaul, Phys. Rev. B **45**, 5710 (1992).

[164] J. L. O'Brien, H. Nakagawa, A. S. Dzurak, R. G. Clark, B. E. Kane, N. E. Lumpkin, R. P. Starrett, N. Muira, E. E. Mitchell, J. D. Goettee, et al., Phys. Rev. B **61**, 1584 (2000).

[165] L. Krusin-Elbaum, T. Shibauchi, and C. H. Mielke, Phys. Rev. Lett. **92**, 097005 (2004).

[166] M.-S. Kim, S.-I. Lee, S.-C. Yu, I. Kuzemskaya, E. S. Itskevich, and K. A. Lokshin, Phys. Rev. B **57**, 6121 (1998).

[167] A. Iyo, Y. Tanaka, Y. Kodama, H. Kito, K. Tokiwa, and T. Watanabe, Physica C: Superconductivity **445-448**, 17 (2006), ISSN 0921-4534, proceedings of the 18th International Symposium on Superconductivity (ISS 2005), Proceedings of the 18th International Symposium on Superconductivity (ISS 2005), URL `http://www.sciencedirect.com/science/article/B6TVJ-4JW7WX2-J/2/26bb8f4f2eb11fd81cc717970eaa1022`.

[168] C. Mielke, J. Singleton, M.-S. Nam, N. Harrison, C. C. Agosta, B. Fravel, and L. K. Montgomery, Journal of Physics: Condensed Matter **13**, 8325 (2001), URL `http://stacks.iop.org/0953-8984/13/8325`.

[169] H. Kotegawa, Y. Tokunaga, Y. Araki, G.-q. Zheng, Y. Kitaoka, K. Tokiwa, K. Ito, T. Watanabe, A. Iyo, Y. Tanaka, et al., Phys. Rev. B **69**, 014501 (2004).

[170] H. Kotegawa, H. Okumoto, T. Imamura, S. Mikusu, K. Yuasa, W. Higemoto, K. Nishiyama, A. Iyo, Y. Tanaka, and T. Watanabe, Int. J. Mod. Phys. B **17**, 3540 (2003).

[171] M.-S. Kim, C. U. Jung, S.-I. Lee, and A. Iyo, Phys. Rev. B **63**, 134513 (2001).

[172] *We assume a value similar to that in hg-1234.*

[173] D. Zech, J. Hofer, H. Keller, C. Rossel, P. Bauer, and J. Karpinski, Phys. Rev. B **53**, R6026 (1996).

[174] C. Nayak, Phys. Rev. B **62**, 4880 (2000).

[175] J. M. Tranquada, H. Woo, T. G. Perring, H. Goka, G. D. Gu, G. Xu, M. Fujita, and K. Yamada, Nature **429**, 534 (2004), ISSN 0028-0836, URL `http://dx.doi.org/10.1038/nature02574`.

[176] J. R. Schrieffer, X. G. Wen, and S. C. Zhang, Phys. Rev. B **39**, 11663 (1989).

[177] M. C. Schabel, C.-H. Park, A. Matsuura, Z.-X. Shen, D. A. Bonn, R. Liang, and W. N. Hardy, Phys. Rev. B **57**, 6090 (1998).

[178] B. W. Hoogenboom, C. Berthod, M. Peter, O. Fischer, and A. A. Kordyuk, Phys. Rev. B **67**, 224502 (2003).

[179] O. K. Andersen, A. I. Liechtenstein, O. Jepsen, and F. Paulsen, Journal of Physics and Chemistry of Solids **56**, 1573 (December 1995), we describe the LDA band structre of YBa2Cu3O7 in the F 2 eV range using orbital projections and compare with YBa2Cu4O8. Then, the high-energy and chain-related degrees of freedom are integrated out and we arrive at two, nearest-neighbor, orthogonal..., URL `http://dx.doi.org/10.1016/0022-3697(95)00269-3`.

[180] H.-J. Kwon and A. T. Dorsey, Phys. Rev. B **59**, 6438 (1999).

[181] R. Shankar, Rev. Mod. Phys. **66**, 129 (1994).

[182] H.-J. Kwon, A. T. Dorsey, and P. J. Hirschfeld, Phys. Rev. Lett. **86**, 3875 (2001).

[183] T. Kondo, T. Takeuchi, A. Kaminski, S. Tsuda, and S. Shin, Physical Review Letters **98**, 267004 (pages 4) (2007), URL `http://link.aps.org/abstract/PRL/v98/e267004`.

[184] X. J. Zhou, T. Yoshida, D.-H. Lee, W. L. Yang, V. Brouet, F. Zhou, W. X. Ti, J. W. Xiong, Z. X. Zhao, T. Sasagawa, et al., Phys. Rev. Lett. **92**, 187001 (2004).

[185] D. K. Morr, Phys. Rev. Lett. **89**, 106401 (2002).

[186] C. Bena, S. Chakravarty, J. Hu, and C. Nayak, Phys. Rev. B **69**, 134517 (2004).

[187] U. Schollwöck, S. Chakravarty, J. O. Fjærestad, J. B. Marston, and M. Troyer, Phys. Rev. Lett. **90**, 186401 (2003).

[188] R. S. Markiewicz, C. Kusko, and V. Kidambi, Phys. Rev. B **60**, 627 (1999).

[189] F. W. de Wette and A. D. Kulkarni, Phys. Rev. B **46**, 14922 (1992).

[190] R. Abd-Shukor, Solid State Communications **142**, 587 (June 2007), URL `http://dx.doi.org/10.1016/j.ssc.2007.04.012`.

[191] A. Kanigel, M. R. Norman, M. Randeria, U. Chatterjee, S. Souma, A. Kaminski, H. M. Fretwell, S. Rosenkranz, M. Shi, T. Sato, et al., Nat Phys **2**, 447 (2006), ISSN 1745-2473, URL `http://dx.doi.org/10.1038/nphys334`.

[192] J. C. Campuzano, H. Ding, M. R. Norman, H. M. Fretwell, M. Randeria, A. Kaminski, J. Mesot, T. Takeuchi, T. Sato, T. Yokoya, et al., Phys. Rev. Lett. **83**, 3709 (1999).

[193] B. C. Stipe, M. A. Rezaei, and W. Ho, Review of Scientific Instruments **70**, 137 (1999), URL `http://link.aip.org/link/?RSI/70/137/1`.

[194] P. J. Goodhew, J. Humphreys, and R. Beanland, *Electron microscopy and analysis* (Taylor and Francis (New York and London), 2001), 3rd ed.